EVALUATION OF SURFACE AND SUB-SURFACE DEFECTS IN FRICTION STIR WELDING THROUGH EXPERIMENTS AND COUPLED EULERIAN AND LAGRANGIAN BASED FINITE ELEMENT MODEL

Debtanay Das

Department of Mechanical Engineering

Indian Institute of Technology Guwahati, Assam

August 2023

Evaluation of Surface and Sub-Surface Defects in Friction Stir Welding through Experiments and Coupled Eulerian and Lagrangian based Finite Element Model

A thesis submitted in partial fulfilment for the award of the degree of

Doctor of Philosophy

by

Debtanay Das

(186103014)

Under the supervision

of

Prof. Swarup Bag

and

Prof. Sukhomay Pal

Department of Mechanical Engineering

Indian Institute of Technology Guwahati, Assam

2023

Dedicated to

“My mother and father”

“Life”

“Ma” and “Tarak”

“Agartala”

“Collegetilla”

“24”

“07”

“93”

“NERIST”

“35”

“01, 05, 04”

“NITA”

“02”

“235”

“Ansys APDL”

“IITG”

“186103014”

“S-204”

“GF-5”

“AWJL”

“FSW”

“Abaqus”

“CIF”

“FESEM”

“PSBDKMTMMJASPMSTBVJDN”

“Shyamnagar”

“14/06/2023”

“14/12/2023”

“2023”

“My journey from DTD to DDTD”

***“2D** was here to become **3D**”*

Department of Mechanical Engineering
Indian Institute of Technology Guwahati
Guwahati, Assam – 781039
INDIA

CERTIFICATE

It is cetified that the woek contained in the thesis entitled ***"Evaluation of surface and sub-surface defects in friction stir welding through experiments and coupled eulerian and lagrangian based finite element model"*** submitted by **Mr. Debtanay Das** to the Indian Institute of Technology Guwahati for the award of the degree of Doctor of Philosophy has been carried out under our supervision in the Departmetn of Mechanical Engineering, Indian Institute of Technology Guwahati. This work has not been submitted elsewhere frfo the award of any other degree or diploma.

The thesis, in our opinion, has reached the strandard fulfilling the requirements for the award of degree of Doctor of Philosophy in accordance with the regulations of the Institute.

Date: 14th December 2023

Prof. Swarup Bag
Department of Mechanical Engineering
Indian Institue of India Guwahati
Guwahati – 781039
Assam, India

Prof. Sukhomay Pal
Department of Mechanical Engineering
Indian Institue of India Guwahati
Guwahati – 781039
Assam, India

Declaration

I declare that the present written submission is my thoughts in my own words. I have adequately cited and referenced the original sources, where other's ideas have been involved. I also declare that I have followed to all principles of academic morality and honesty and have neighther fabricated nor falsified any idea/data in the present thesis. I realize that any defilement of the above will be cause for disciplinary action by the Institute and can also induce disciplinary action from the sources which have thus not been properly cited.

Date:

DEBTANAY DAS

(186103014)

Department of Mechanical Engineering

Indian Institute of Technology Guwahati

Guwahati – 781039

Assam, India

Acknowledgement

I am also thankful to god almighty for providing me with this opportunity.

First and foremost, I would like to thank my father ***Mr. Debabrata Das*** *and mother* ***Mrs. Kaberi Das*** *for making me capable enough to pursue and complete my Ph. D degree. They have been my biggest support system all my life.*

I would like to express my sincere gratitude to ***Prof. Swarup Bag*** and ***Prof. Sukhomay Pal***, Department of Mechanical Engineering, Indian Institute of Technology Guwahati, for accepting me as their research scholar. I am also thankful to them for allowing me to work in their lab. I was under their constant guidance and had their support throughout my research work. I am especially thankful to both of my supervisors for putting in significant effort to finalize and submit my thesis within the deadline, so that I can easily apply for a post-doctoral position. I really appreciate this selfless deed from both of my supervisors. I will forever be grateful to them.

I am indebted to ***Prof. Bidyut K. Bhattacharya*** and my M. Tech supervisor ***Dr. Vidyut Dey***, Assistant Professor, Production Engineering Department, National Institute of Technology, Agartala, for introducing me to research, publication, simulation, and Latex.

I am immensely grateful to *Mr. Dhaneswar Khaklary, Mr. Gakul Das, Mr. Gwmchar Baro, Mr. Joykrishna Saikia, Mr. Mrinal Sarma, Mr. Saiffudin Ahmed, Mr. Sanjib Sarma,* and *Mr. Amal Kalita* sir for their help, guidance and support during experimental work. I am thankful to them for having to listen to my novice queries and respectfully providing suggestions and solutions. I am especially thankful to **Mr. Dilip Chetri** for being my troubleshooter in the Mechanical Workshop.

I am really grateful to my seniors, batchmates, and juniors for their support and encouragement. They have been supportive throughout my Ph. D. tenure, especially during my 1st year coursework saga and 5th year of Ph. D completion and thesis writing. Thank you, Dr. Uttam Kumar Tarai, Dr. Bikash Kumar, Dr. Ajit Kumar Sahu, Mr. Ankan Mishra, Mr. Swagat Dwibedi, Mr. Vivekananda Haldar, Mr. Sunil Biswal, Mr. Dipankar Saha, Mr.

Avadh Kishore Prasad, Mr. Arnab Sarmah, Mr. Ritam Sarma, Mr. Alok Trivedi, Mr. Amritesh Kumar, Mr. Hritaban Acharya, Mr. Umesh Melkani, Mr. Akshay Kumar Soni, Mr. Gaurav Prakash, Mr. Vikas Bhushan, and Mr. Sourabh Mishra.

Lastly, I am thankful to all my family members and friends for their constant support.

Debtanay Das

Abstract

The manufacturing industry widely accepts friction stir welding (FSW) as an environment friendly technology since it can produce a joint with almost zero emissions to the environment. Moreover, this green technology operates without the need for any shielding gas or filler material. FSW produces good quality weld joint at temperatures lower than the melting point. The welds produced by FSW are free from fusion welding defects such as porosity, distortion, spatter, etc. However, the FSW process is not circumscribed from deleterious defects such as tunnel defects, flash formation, and residual stresses. Extensive research has already been conducted to understand the physical process and material flow in FSW process. A significant amount of research has focused on optimizing the process parameters and tool geometry using experiments and mathematical models. However, there remains a lack of any predictive model to estimate the defect formation and its impact on the weld quality. The successful prediction of weld quality in terms of defect formation will aid to reduce the material wastage and trial-and-error cost for producing a defect free weld. In the present work, a 3D thermo-mechanical model is developed following the Coupled Eulerian-Lagrangian (CEL) approach to evaluate the varying surface morphology, material flow, and defect formation in FSW process. The similar and dissimilar combinations of AA6061 and AZ31B materials are extensively investigated by solid-state FSW process. The tool wear is also estimated to account its influence on the defect formation viz. weld quality. Proper selection of mass scaling factor eliminates the high computational time associated with the CEL approach. The influence of mass scaling technique on the total computational time, weld quality, thermo-mechanical responses, and defect prediction are extensively investigated. Any adverse effect of the artificial mass scaling is kept under check by maintaining the kinetic energy (KE) to internal energy (IE) ratio below 10%. The KE to IE ratio varies as the tool moves from a sound weld region to a defective weld region, but it remains constant if the weld quality is sound or defective for the complete weld length. Therefore, the KE to IE ratio variation cannot be conclusively used to determine the weld quality and can only be used to check any adverse effect of mass scaling. The developed numerical model is validated by comparing the experimentally measured temperature evolution, volumetric defects, and residual stress data. The model can accurately predict the different surface and sub-surface defects, viz., the tunnel defect, flash formation, failed joints, exit hole, and other surface defects, while considering the tool rotation speed, traverse speed, pin height, plunge depth,

pin geometry, tool condition and plate position as the process variables. Further, the developed model can estimate the material mixing and weld interface location specifically for dissimilar welding. All these process variables influence the magnitude and distribution of residual stress of FSW joints. However, the residual stress is more generous during dissimilar FSW due to the non-uniformity of the heat flow and material properties. This makes the residual stress estimation more complicated in dissimilar FSW. Hence, the CEL based mechanistic model is coupled with the machine learning (ML) algorithms to predict the temperature distribution and residual stress in dissimilar AA6061-AZ31B FSW. This approach essentially reduces the prediction time of the final result involving large amount of data. Different ML algorithms are compared to estimate their prediction accuracy. The extra tree regressor, XGBoost, and random forest regressor models predict the temperature evolution and residual stress with a maximum deviation of less than 8% for temperature and 10.3% for residual stress, respectively. Essentially, the physics-informed ML algorithm is a reliable process model for predicting the transient state of thermal and mechanical responses during the FSW process, which is more appealing to apply for any other industrial problem of interest.

Keywords: CEL approach, Defects in FSW, Dissimilar FSW, Extra tree, FESEM-EDS, Finite element modelling, Flash formation, Improper joint, Machine learning, Mass scaling factor, Micro-FSW, Random forest, Residual stress, Similar FSW, Solid state joining, Substrate position in dissimilar FSW, Surface defects, Surface morphology, Tool-material interaction, Tool wear, Tunnel defect, XGBoost, XRD

CONTENTS

List of Figures

List of Tables

List of acronyms

Acronyms	Description
FSW	Friction stir welding
CEL	Coupled Eulerian-Lagrangian
KE	Kinetic energy
IE	Internal energy
KE to IE	Kinetic to internal energy
ML	Machine learning
AS	Advancing side
RS	Retreating side
LoP	Lack of penetration
LoF	Lack of fill
CT	Computed tomography
MLR	Multi-linear regression
SVM	Support vector machine
ANN	Artificial neural network
GPR	Gaussian process regression
ALE	arbitrary Lagrangian and Eulerian
CEL	coupled Eulerian and Lagrangian
FESEM	Field emission scanning electron microscope
EDX	energy dispersive X-ray
XRD	X-ray diffraction
FSSW	Friction stir spot welding
SZ	Stir zone
TMAZ	Thermo-mechanically heat affected zone
HAZ	Heat affected zone
JLR	Joint Line Remnant
EF	excessive flash
GMAW	Gas metal arc welding
FEM	Finite element modelling
IMCs	Intermetallic compounds
TIG	Tungsten inert gas
HAGBs	High angle grain boundaries
CAD	Computer aided design
SPH	Smoothed particle hydrodynamics
CFD	Computational fluid dynamics
CSM	Computational solid mechanics
HTZ	High temperature zone
EVF	Eulerian volume fraction
RFR	Random forest regressor
SVR	Support vector regression
DTR	Decision tree regression
PR	Polynomial regression
KNN	k-nearest neighbor
ANFIS	Adaptive neuro-fuzzy inference systems
CS	Concave shoulder
THCS	Three-helix concave shoulder
THFS	Three-helix flat shoulder

FCC	Face-centered cubic
HCP	Hexagonal close-packed
WEDM	Wire electrical discharge machining
SD	Shoulder diameter
PD	Pin diameter
JC	Johnson-Cook
ALLSE	Elastic strain energy
ALLPD	Plastic strain energy
ALLAE	Artificial strain energy
FD	Frictional energy
AE	Artificial energy
PD	Plastic energy
SE	Elastic strain energy

Nomenclature

Symbol	Description
ϕ	Arbitrary variable
u	Material velocity
ρ	Density
σ	Cauchy stress
b	Body force
e	Total energy per unit volume
D	Velocity strain
Φ	Flux
S	Source term
$\bar{\sigma}_s$	Flow stress from JC model
m	Thermal softening coefficient
$\bar{\varepsilon}$	Effective plastic strain
$\dot{\bar{\varepsilon}}$	Effective plastic strain rate
$\dot{\varepsilon}_0$	Reference strain rate
A, B, C	Material constants
n	Work-hardening exponent
$T_{r,}$	Reference room temperatures
T_m	Melting temperatures
$\Delta\bar{\varepsilon}^{pl}$	Increment in the effective plastic strain
$\bar{\varepsilon}_f^{pl}$	Plastic strain in failure
$d_1 - d_5$	Failure parameters measured at the material transition temperature
p	Pressure
q	Von-Mises stress
R_s	Radius of the shoulder
R_p	Radius of the pin
μ_f	Coefficient of friction
τ	Contact stress
ω_v	Angular velocity
P	Contact pressure

H_{plas}	Plastic heat generated
η	Thermal conversion efficiency
σ_d	Deviatoric stress
$\dot{\varepsilon}_{plas}$	Plastic strain rate
k	Thermal conductivity
C_p	Specific heat capacity
h_{conv}	Convective heat coefficient
σ_{sb}	Stefan-Boltzmann constant
T	Temperature variable
T_{amb}	Ambient temperature
$\dot{\varepsilon}$	Strain rate tensor
$\bar{\varepsilon}^{pl}$	Equivalent plastic strain
$\bar{\varepsilon}^{pl}\|_0$	Initial equivalent plastic strain
$\dot{\bar{\varepsilon}}^{pl}$	Equivalent plastic strain rate
R	Yield stress ratio
σ^{eq}	Von Mises equivalent stress
S	Deviatoric stress tensor
σ	Stress
I	Matrix
$\dot{\varepsilon}^{el}$	Elastic components of the strain rate
$\dot{\varepsilon}^{pl}$	Plastic components of the strain rate
$\dot{\varepsilon}^{ae}$	Artificial components of the strain rate
v	Velocity field vector
Δs	Incremental slip
Δt	Incremental slip
t	Time
$[N]$	Elemental shape function
$[B]$	Spatial derivatives of the elemental shape function
$[C]$	Lumped capacitance matrix
H	Enthalpy
$[M]$	Diagonal lumped nodal mass matrix
$\{\ddot{u}\}$	Nodal acceleration at the beginning of the increment

$\{f\}$	Resultant force vector
n	Number of increments
ω_{max}	Highest frequency
v_w	Function of the dilatational wave
L_e	Element length
λ_l and μ_l	Lame's constants
L_{min}	Smallest element in the domain with length
Δt_{mech}	Time step increment for the mechanical analysis
$\Delta t_{thermal}$	Time step increment for the Thermal analysis
κ	Mass scaling factor
ρ^*	Artificial density
$C_p^{'}$	Artificial specific capacity
ν	Poisson's ratio
E	Modulus of elasticity
α	Coefficient of thermal expansion
T_m	Melting temperature

Chapter 1

Introduction

1.1 General Background

Welding and joining of similar and dissimilar materials are extremely important in the manufacturing industry. The welding of various Aluminium alloys, Magnesium alloys, steels, and Ni-based alloys has ensured wide application in the aerospace, automobile, rail, and shipbuilding industries (Thomas and Nicholas, 1997; Liu *et al.*, 2018; Singh, Singh and Singh, 2018). Over the years, there has been a remarkable development of different fusion and solid-state welding processes to address several metallurgical issues for advance materials and difficult-to-weld materials. During world war II, arc welding was used to weld steel sheets for faster production of ships. The welding process was found to be more reliable than the widely adapted riveting technology at the time. But many of the welded ships started failing due to the fracture and crack propagation. The failure of liberty ships is well documented in history (Kobayashi and Onoue, 1943). The main reason for the failure of these ships is the ductile-to-brittle transition of the steel when cooled through a critical range of temperatures. This led to serious concern for extensive study of the imperfections or defects formed during the arc welding procedures throughout the late 20^{th} century and early 21^{st} century. Even a proven welding method may produce a defective weld for several reasons. Irrespective of the type of welding processes, the defects can be either mechanical or metallurgical in nature. The probablity of defect formation is deleterious when joining dissimilar materials. The main reason for such a study is to identify the primary causes of defect formation to eliminate them. Hence, predicting

defective welds is practically significant to understanding the obstacles to producing sound welds.

In 1991, when the TWI (The welding institute) patented a novel welding technique for the solid-state joining of Aluminium and its alloys, it effectively provided a means to eliminate the defects associated with conventional arc welding techniques (Thomas, W.M.; Nicholas, E.D.; Needham, J. C.; Murch, M.G.; Templesmith, P.; Dawes, 1991). The friction stir welding (FSW) process joins the materials due to material plasticization below the material melting point. Moreover, it proved a suitable method to weld other difficult-to-weld metals like magnesium and its alloys, MMCs, polymers, etc. Since different materials behave differently to the tool-workpiece interaction and temperature evolution, the optimal temperature and process parameters for FSW are material-specific and need to be investigated individually. Although various welding defects associated with the conventional arc welding techniques are absent in FSW; however, it is not completely absent of defects itself. The FSW process can observe various surface and sub-surface defects. Void defects and tunnel defects are commonly occurring sub-surface defects in FSW. The absence of material due to the void or tunnel defect significantly deteriorates the welding quality (Morisada, Imaizumi and Fujii, 2015; Zeng, Xue, Wang, Ni, Xiao, Wang, *et al.*, 2018). The surface defects include excessive flash formation that can reduce the cross-sectional area of the welded sample. The reduced cross-section and region of stress concentration at the flash root can weaken the welded sample significantly (Ranjan *et al.*, 2016). These defects can be either localized or present in the complete weld length. The reasons for defect formation are broadly identified as improper material mixing, improper heat generation, relative position and movement of the tool, improper choice of process parameters, improper design of the tool, and tool wear. Therefore, finding an optimal mix of process parameters is crucial to achieving a sound-quality weld.

1.2 Current Status

There are several ways to investigate defect formation in the similar and dissimilar FSW of the Aluminium alloys. The defects can be investigated through direct experimental trials or analysis of signals by suitable mathematical models or visualization of defects through phenomenological modeling approaches. Although the results achieved with the direct experiment are very accurate, these methods are primarily destructive in nature and involve considerable material, manpower, and analysis costs. A few non-destructive testing techniques for weld defect identification are eddy current probes (Rosado *et al.*, 2014), X-

radiography (Malarvel and Singh, 2021), X-ray computed tomography (CT) (Raguvarun *et al.*, 2015), Ultrasonic C-scan testing (Santos and Santos, 2010), Ultrasonic phased array inspection (Huggett *et al.*, 2017) and fluorescent penetrating fluid inspection (Li, Shen and Hu, 2011). The eddy current probes method employs the concept of electromagnetism to generate and pass eddy current through the inspection region. The presence of any discontinuity is detected and characterized in the form of an output voltage. The eddy current probe technique can detect defects to a depth of about 60 μm (Rosado *et al.*, 2010). The X-ray technique utilises a radioactive source that emits X-rays on a specimen. As the X-rays penetrates into the test specimen an image is generated to evaluate the formed defect. The defect is genrally analysed as a discontinuity in the otherwise continuous sample. This technique provides an accurate and fast imaging of the defects. The CT scans can have some discrepencies due to the resolution of the CT apparatus while analysing the defective welds (Hamade and Baydoun, 2019). The CT technique can detect defects, discontinuities, wall thickness, etc., for different types of materials (Du Plessis and Rossouw, 2015; Moura *et al.*, 2015; Petit *et al.*, 2017; S. Zheng *et al.*, 2017). This is a preferred technique for the estimation of volumetric defects (Ditchburn, Burke and Scala, 1996). However, this technique suffers a huge drawback as the surface of the specimen, i.e., the top and the bottom surface, needs to be easily accessible for this technique to perform efficiently. Such a scenario might not always be possible in real-life applications, and therefore ultrasonic technique is preferred over X-ray technique. Moreover, this technique cannot precisely detect the planar defects, unlike ultrasonic techniques. The ultrasonic technique is found to be more accurate than X-ray radiography (Ditchburn, Burke and Scala, 1996). The ultrasonic technique was used as a non-destructive defect detection technique as early as the 1960s. As the ultrasonic technique can detect both planar and volumetric defects, it gained huge acceptance as a non-destructive testing technique. The ultrasonic waves passing through the workpiece are disturbed by the presence of both the planar and the volumetric perturbations. As a consequence, the different types of defects are easily detected using this method. However, the interaction of the ultrasound with various defects needs to be precisely studied to utilize this technique as a defect detection means. The passing of the ultrasound through the different types of materials, the wave propagation through complicated geometry, and any effect of microstructural influences on the wave propagation also need to be comprehended (Ditchburn, Burke and Scala, 1996). Most non-destructive techniques suffer from a common drawback of less inspection depth. On the other hand, the fluorescent penetrating fluid inspection technique can be utilized for

detecting root flaw defects (Li, Shen and Hu, 2011); however, the fluorescent penetrating fluid technique requires access to the back end of the welded sample (Tabatabaeipour *et al.*, 2016). This might not always be practically feasible.

Although the above-mentioned non-destructive testing techniques are gaining acceptance; however, their application gets restricted due to the need for complicated equipment, trained personnel to operate those equipment, easy access to either side of the workpiece, the study of the interaction of the probing mechanism, and the workpiece material etc. With the improvement in computational power in the last couple of decades, numerical modeling and signal processing for defect detection are becoming viable options (Das, Pal and Bag, 2017b, 2018; Guan *et al.*, 2021). Moreover, it is easy to incorporate any changes to the model for further study and improve the process. The real-time monitoring is a proven approach for detecting the defect generated in FSW (Mishra *et al.*, 2020). Various researchers have proposed the measurement of signals in the form of welding force and torque to use normalization techniques, neural network approaches, or machine learning (ML) approaches to detect defect formation (Dewan *et al.*, 2016; Du, Mukherjee and DebRoy, 2019; Guan *et al.*, 2021; Hartl *et al.*, 2021). Multiple ML based methods are also used to either classify a joint as defective or sound quality or to predict the output response such as the cross-sectional morphology, and mechanical strength (Bhat *et al.*, 2015; Krutzlinger *et al.*, 2019; Nie, Wu and Gong, 2020; Elsheikh, 2023). The multi-linear regression (MLR) approach may not always be practically feasible when the relation between input and output parameters is highly non-linear. The support vector machine (SVM) approach minimizes the generalization error and is also less computationally expensive than the artificial neural network (ANN) technique. The Gaussian process regression (GPR) technique sorts multiple random variables and correlates each variable with the adjacent variable. It maps a function to each data point and also assigns a probability to each of these functions. The advantage of the GPR over the SVM technique is that the GPR is truely probabilistic in nature and also estimates the output uncertainity (Markov and Matsui, 2014). The GPR approach is also found to produce a better result than the SVM and the MLR approaches (Verma, Gupta and Misra, 2018; Verma *et al.*, 2021). Furthermore, the image processing technique is also investigated to detect defect formation in FSW (Sinha *et al.*, 2008; Sinha, Muthukumaran and Mukherjee, 2008; Ranjan *et al.*, 2016). The experimental image is digitally converted to a grayscale image for further analysis by the image processing techniques (Wang, 2014; Das, Pal and Bag, 2016c; Sudhagar, Sakthivel and Ajith Arul Daniel, 2020). The image processing techniques cannot

efficiently detect the sub-surface defects without preparation of welded sample. Even the analysis of image is computationally intensive. Although the signal processing approach is a very reliable method to detect the defects associated with FSW; however this is a laggi ng approach, i.e., the welding needs to be performed first to employ the signal processing approach. This can also lead to the loss of material and time. The advantage of the numerical model is that they can model the complete process and aid to detect defects before the welding is performed. This leads to an accurate defect prediction and a reduction in the cost incurred during production. The numerical models can act as the simulators for this joining process. The proficeincy of the simulator (i.e., the numerical model) is based on the severity of the model. The most basic FSW models are capable of predicting the thermal profile of the workpiece. This model can be improved by incorporating the mechanical responses of the system, thus giving rise to the thermo-mechanical model of the process. Further improvement will incorporate the material flow to predict the various surface and subsurface defects. The model can further be extended to incorporate the metallurgical effect to the thermo-mechanical response. Another significant component of the FSW is the accurate measurement of the tool responses. Assembling all the aforementioned physics can lead to the development of a dedicated FSW simulator. The said simulator can also act as a stepping stone for incoporating the digital twin tool and thus the Industry 4.0 into the FSW manufacturing process.

The numerical modeling allows for the easy study of the FSW process to obtain the various thermo-mechanical responses and also observe the various surface and sub-surface defects (Chauhan *et al.*, 2018; Choudhary and Jain, 2022; Iqbal *et al.*, 2022). The Lagrangian and Eulerian methods are the conventional methods used for numerical modeling. The mesh nodes in the Lagrangian method coincide with the material points. As a load is applied to the assembly, the nodes and material points deform simultaneously. This allows for easy tracking of material, especially in contact body problems. The Lagrangian approach is primarily used to model problems that observe negligible or minor material deformation. Alternatively, the Eulerian approach is used to model severe deformation problems. The mesh nodes, unlike the Lagrangian technique, are fixed in space, for the Eulerian approach. The material flows through the fixed mesh nodes in the Eulerian approach and is represented as velocity. The issue of severe mesh distortion is easily solved with Eulerian approach as the mesh is fixed spatially. The primary disadvantage of the Eulerian approach is its inability to model the free boundary surface. This approach can only be used to model the free boundary surface when the deformed

surface is known beforehand (Jain, Pal and Singh, 2017). The conventional Lagrangian and the Eulerian methods are coupled to capture the advantages of both these methods, to develop the newer arbitrary Lagrangian and Eulerian (ALE) and coupled Eulerian and Lagrangian (CEL) techniques. The main difference between the ALE and CEL technique lies in the fact that there is no mesh deformation in the case of the CEL technique, whereas the zone with severe deformation is modelled with re-meshing criterion in the case of the ALE technique. The re-meshing of old mesh into new mesh and re-mapping of solution into the new mesh is an integral component of the ALE technique (Bakroon *et al.*, 2019). However, the severe mesh distortion and the simultaneous re-meshing strategy can be a computationally cumbersome process for ALE. The CEL on the other hand can be easily applied to severe deformation and fluid structure interaction problems as there is not any mesh distortion. A new Lagrangian based meshless approach, i.e., the SPH technique is gaining popularity to model the FSW process efficiently. The meshless approach allows for easy and efficient interface tracing, large deformations, void formation, defect detection, and thermo-mechanical response estimation (Tartakovsky *et al.*, 2006; Wang *et al.*, 2016). However, the SPH method inherently suffers from stability issues the particles are subjected to tensile stresses (Mao, Liu and Dong, 2017; Askour, Mesmoudi and Braikat, 2020). The inclusion of artificial terms helps to resolve these issues; however, the accuracy of the results may get affected due to the artificial terms.

It is understood that the FSW process is a complex manufacturing process with multi-body interactions of wide differences in strength involving multiple process parameters. In the majority of the cases, the optimum process window is obtained by trial and error method to achieve a good quality weld. Researchers have also embarked on designing mathematical approaches to optimise the process parameters required to produce a defect free weld. In most cases, the analysis is confined to the workpiece only by neglecting the interaction of the FSW tool and its influence on the process condition. Often the approach involves a huge amount of experimental data to develop a data driven model. The deformed shape of the workpiece and the material flow at the intricate part of the domain are indicative of any surface and subsurface defect formation, which is difficult to analyze by simple experimental measurement. Hence, the physics based model considering tool-material interaction using the CEL approach can inherently predict the quality of weld for a similar or dissimilar FSW process. The present research work is oriented towards the development of the CEL method in the case of the FSW process for the visualization of several types of

defects. Even the model predicts that the choice of proper process parameters can eliminate the defective weld.

Currently, the researchers are exploring the possibility of miniaturizing the FSW process for the joining of sheets of a thickness of 1 mm or less (Park, Joo and Kang, 2020; Verma and Saha, 2023). The welding of such thin sheets is widely recognized as micro-FSW (μ-FSW). The key issues for the downscaling of the FSW process are the proper fixturing of the workpieces during welding and selection of optimal process parameters (Ahmed and Saha, 2020). The μ-FSW joining is genrally performed with the conventional milling or CNC milling machines (Ahmed, Verma and Saha, 2021). Further, the fixtures and clamps necessary for restraining the workpieces are modified as required (Ahmed and Saha, 2018). The μ-FSW requires the downsizing of the tool, which can significantly affect the heat generation and thus the optimal process parameters compared to the conventional FSW. However, barring a few publications, there is a lack of published articles in the literature discussing the modelling of the μ-FSW process (Mohan, Jayadeep and Manu, 2021). Various key issues of the process such as the material flow, defect formation, weld quality estimation, etc. are not keenly investigated. The use of a conventional FSW setup can cause significant waste of energy and needless use of heavy machinery for extremely thin sheet welding. Hence, the design and development of a portable μ-FSW can be beneficial for joining very thin sheets at different locations.

1.3 Significance of Present Study

The discussion in the literature indicates the fact that the FSW process is gradually replacing the fusion welding processes and is gaining more importance in the manufacturing industry because of clean and environment friendly process. A lot of development in the FSW joining a domain is still going on. The good quality joints produced by the FSW process have resulted in it being applied for the joining of similar and dissimilar combinations of Aluminium alloys, Magnesium alloys, steel, Titanium alloys, Copper alloys, Nickel alloys, MMCs, etc. However, the ever-increasing applicability of the FSW process highlights a new set of problems for the process. The foremost issue is the determination of the optimal process window for a sound quality weld through numerical simulation and experimental measurement. In the current work, the FSW process is analyzed from the scope of the formation of different surface and sub-surface defects. The determination of the process conditions leading to the formation of a certain

type of defect is paramount for the successful elimination of the defect and formation of the sound quality joint. Further, the numerical process model helps to reduce the requirement of multiple experiments and expeditiously estimate the various thermo-mechanical responses of the system. Numerical modelling of the FSW process allows in-depth analysis of the process without incurring any significant material or manpower costs. The CEL technique is chosen for the current investigation due to its ability to model high deformation problems. Essentially the computational model suffers from a significant issue of high computational time. Moreover, the available investigations of the FSW process and its modelling approach primarily deal with the thermal or mechanical responses. There is a dearth of published literature discussing the modelling of the various defects occurring during the welding process. In the current work, this issue is addressed in detail and with a comprehensive experimental investigation. The CEL approach works efficiently with the FSW process for the accurate prediction of the various responses and defect formation. However, it is realized from the literature that the prediction using the numerical process model is generally more computationally expensive compared to the ML approaches. Alternatively, the ML algorithms suffer due to the need for multiple data points for the training of the model. To find a balance between the computational time and the accurate prediction of the process, a physics informed ML modelling strategy is employed for the FSW process. To employ this strategy, initially, a 3D model based on the CEL technique is developed and solved. The solution of the CEL model then serves as the input parameters for training the ML algorithms. This strategy is substantially capable of predicting any sudden variation or changes in the output response. Further, the ML models can accurately predict the spatial and temporal distribution of the various thermo-mechanical responses. However, the utility of the numerical models cannot be fully ignored in favour of the ML approaches. Firstly, the ML models require significant data points for the training purpose and the same is being provided by the solution of the CEL model. Moreover, the visualization and estimation of the various volumetric defects is quite realistic with the CEL approach.

Besides the industrial application, the aluminium alloys have also become an integral part of our everyday lives. Because of very good electrical and thermal conductivity, and diffusivity is making them suitable for both cooking utensils, heat sinks in the electronics industry, and door and window panels for stable oxide layer on the surface. These applications require the welding of thin sheet Aluminium alloys. This generates the need for the FSW process in the micro scale where the sheets thickness is about 1 mm or less.

Further, the applicability of the μ-FSW can reach its full potential with the help of a portable μ-FSW setup. Although various researchers have embarked on a journey to investigate the μ-FSW process, they primarily use a dedicated FSW or modified milling machine to weld the samples. This do not solve the portability issue faced by the conventional machines that are inherently bulky in nature. Moreover, the use of such heavy machinery for micro-scale welding can cause waste of power and resources. Therefore, the current work is focused on developing a setup that is capable of performing both butt and lap welding at micro scale level. At the same time, the setup is developed in a manner that it can be easily transported between different workstations.

1.4 Problem Statement

To summarise the current work, the FSW process is investigated primarily in three verticals. Firstly, a three dimensional CEL based model is developed to predict the various thermo-mechanical responses of the welded joint and the quality of the weld with an option to predict the geometric features of the various surface and volumetric defects. The heat generation in the body is governed by Coulomb's friction law whereas the non-Newtonian fluid flow is accomplished following the Johnson-Cook material model. Temperature dependent thermo-physical properties are utilised to accurately predict the process. The CEL model is divided into three components, i.e., one Lagrangian domain and two Eulerian domains. The Lagrangian domain is defined as the tool, whereas one of the Eulerian is used as the workpiece material domain. The other Eulerian domain is kept void and is placed on top of the workpiece domain. The inclusion of the void Eulerian domain is done primarily to capture the flash formation. The mass scaling approach keeps the total computational time within check using the CEL technique. For the mass scaling apporach to perform efficiently, the density of the workpiece is artificially increased while ensuring the dynamic responses are not adversely affecting the model. As the time increment for the explicit scheme of solution for the CEL approach is a function of mesh size and material density, the increase in the density increases individual time increments, thus reducing the total computational time. A set of experimental investigations on different Al-alloys and Mg-alloys are utilized for the sake of validation of the numerical model. The present model offers several advantages such as the accurate estimation of the thermo-mechanical response within the complete computational domain, visualization of material flow, and defect formation. The computational model is further advanced by integrating ML

algorithms for the defect evolution. This second vertial aims to develop a physics informed ML model primarily to reduce the experimental counts. Several ML algorithms are used in the current work to predict the temperature and residual stress evolution. A set of experimental measurements on residual stress data facilitates the two-step validation of the physics informed ML model.

The third vertical is focussed on the development of the μ-FSW setup. The basic mechanisms of the conventional and μ-FSW are similar that usually leads to using the same conventional setup for the μ-FSW welding. However, a keen observation of both processes highlights some key distinguishing features, such as the tool geometry, a reduced frictional contact area between the tool and the workpiece, and tool working conditions such as the rotation speed, traverse speed, etc. Further, it is realized that the usage of conventional machinery for μ-FSW limits the application remotely. The optimal welding conditions for both processes can be significantly different due to the reduction in the frictional contact area for the μ-FSW process. This may warrant a need for a higher rotation speed compared to the conventional FSW. All these factors motivate the development of a dedicated μ-FSW setup which is portable in nature and capable of performing the micro-scale FSW in various welding configurations.

1.5 Research Objectives

The primary objective of the current research work is to perform experimental and computational investigations to model the FSW process with a keen interest to predict various thermo-mechanical responses aligned to define the surface and sub-surface defects that appeared during similar and dissimilar materials joining. The thermo-mechanical responses and defect formation are investigated using both the CEL model and the ML algorithms. The effect of the tool wear and substrate positions are also investigated for dissimilar FSW process. The different defects prediction using the developed models are the tunnel defect, flash formation, exit hole, and partially and completely failed joints. Further, the principles of the conventional FSW process are utilized to develop a portable μ-FSW setup. The developed setup is further used to perform various μ-FSW in lap weld configuration. To achieve the stated objective the complete work is divided into several segments.

- **Finite element based thermo-mechanical modelling of similar and dissimilar FSW process following CEL approach**

The model predicts the temperature distribution at different stages of the FSW process. The model estimates the different mechanical responses such as the stress evolution, strain, strain rate, and material flow field. The thermo-mechanical responses estimate various surface and volumetric defects for similar and dissimilar FSW process. It exclusively explains the prediction of tunnel defect, excessive flash formation, failed joints, exit hole, tool wear on weld quality, and the substrate position on the weld quality.

- **Physics informed ML algorithm for the prediction of thermo-mechanical responses and residual stresses in dissimilar FSW process**

The thermal and mechanical responses from the CEL solution are considered as input datapoints for the training of the ML algorithms. Different ML algorithms are compared based on R^2 and mean square error (MSE). The three best ML algorithms are used to predict the residual stress for an independent set of process parameters.

- **Experimental investigation on conventional and μ-FSW processes**

A set of experiments are performed to validate the numerical models. The complete work is focussed on the similar and dissimilar FSW of AA6061 and AZ31B. The developed model is validated for temperature evolution using an IR camera. Secondly, the geometric dimensions of the volumetric defects are measured using an optical microscope. Thirdly, the residual stress evaluation is performed for different locations of the welded sample with XRD measurement. The microstructural characterization of the samples is performed using the optical microscope (OM), field emission scanning electron microscope (FESEM), energy dispersive X-ray (EDX) analysis, and X-ray diffraction (XRD) techniques.

Finally, an in-house μ-FSW setup is developed. The key tasks performed for the setup development are the design and fabrication of the welding bed, assembly of the welding bed with the tool spindle, and the integration of the welding bed with the stepper driver and micro-controller to provide CNC control to the motion of the bed. The main objectives for the development of the μ-FSW setup are the availability of a dedicated setup of ultra thin sheet FSW and the portability of the setup. The welding of 1 mm thickness AA5052 and AA1200 is performed using μ-FSW process.

1.6 Layout of Thesis

The thesis comprises ***seven*** chapters. ***Chapter 1*** introduces the issues investigated in the current work. A brief of the current research status in the published literature, problem statement, objective, and the layout of the thesis are presented in this chapter. ***Chapter 2***

presents a comprehensive survey of the existing literature. The primary focus is on experimental investigation and numerical modelling of various surface and sub-surface defects appearing during FSW for various materials and varying process parameters. The physics-informed ML models are also surveyed for the accurate prediction of the FSW. Further, the μ-FSW process is also reviewed in detail to realize the scarcity of dedicated welding setup for the micro-scale FSW process. ***Chapter 3*** deals with the experimental procedures, identification of process parameters, and selection of tools and materials for comprehending the research work. The details for the design and development of the μ-FSW setup are also included here. ***Chapter 4*** describes the finite element modelling of thermo-mechanical analysis using the CEL approach with a proper discussion on the mass scaling factor. The material behavior is assumed to follow the Johnson-Cook material model. The development of the physics-informed ML models including the data collection, data processing, model training, and evaluation is explained in this chapter. A comparative analysis of the prediction accuracy of ML algorithms is also performed. ***Chapter 5*** outlines the evaluated results and validation for the numerical and physics-informed ML models. The model validation is performed using the temperature evolution, and residual stress data for different welding conditions. The effect of the tool geometry, tool wear, rotation speed, traverse speed, plunge depth, and substrate positions on the weld quality is investigated for both similar and dissimilar FSW. The ML models are used to predict the temperature and stress evolution for an independent set of process parameters. Finally, multiple sets of experiments are performed and analyzed using the in-house developed μ-FSW setup to ascertain the weldability of the developed setup. Lastly, ***Chapter 6*** highlights the conclusions drawn from the entire work. Further, the future scope of work and the list of references in the context of this thesis are presented.

Chapter 2

Literature Survey

2.1 General background

The basic FSW process comprises two components, i.e., the tool and the workpiece. The workpiece can be divided into three zones based on microstructural differences, i.e., the stir zone (SZ), the parent material (PM), and the transitional zone (TZ) between SZ and PM. The TZ comprises the thermo-mechanically affected zone and the heat-affected zone. The tool is both rotating and translating while moving through the faying edges of the workpiece clamped tightly together leading to the joining of the two plates. The tool rotation raises the temperature of the material due to friction. It also promotes the mechanical mixing of the materials. The material mixing can be further improved by the tool shoulder and the tool pin profiles like square pin, triflute, grooved shoulder. The material mixing is a very important feature of the welding process as the temperature in this case remains below the melting point of the material. FSW offers various advantages over the fusion welding techniques such as the defects associated with melting, solidification, reduction is shrinkage, and distortion, no filler material, flux or shielding gases are required. Materials welded using FSW do not require any special edge preparations. These advantages have lead to the introduction of the FSW technique to weld other materials such as Magnesium, Copper, Steel, Titanium, Inconel, and MMCs. The FSW process is primarily applied to the aerospace, automotive and the maritime industries.

The FSW process has gained widespread application in the manufacturing industry due to the absence of multiple welding defects, viz., spatter, porosity, solidification cracking, etc. Moreover, this process is widely regarded as an environment friendly and sustainable manufacturing process. The FSW is capable of welding a wide variety of metals, such as Aluminium, Magnesium, Steel, etc., in various lap and butt weld configurations for both similar and dissimilar combinations of materials. The frictional contact between the tool and workpiece is primarily responsible for the heat generation during FSW. Additionally,

the tool pin plasticizes, rotates, and mixes the material at the faying edges of the workpiece. The frictional heat and plastic deformation due to the tool action leads to the formation of various thermo-mechanical zones. Essentially FSW process is a transition between joining and hot metal working process with the resultant microstructure and metal flow features similar to typical metal extrusion and forging processes (Mishra and Ma, 2005).

Although this solid-state welding process eliminates most of the difficulties associated with fusion welding processes, it is not completely free from defect formation. The common defects associated with the FSW process include different variants of processes like hybrid FSW, friction stir spot welding (FSSW), and additive FSW handling similar or dissimilar materials joining. In general, the different types of defects are segregated by differences in mechanism in terms of material flow, temperature, and thermo-mechanical properties of the materials.

Figure 2.1 depicts typical metallurgical zones associated with the FSW process (Mishra and Ma, 2005). These zones are termed as preheating zones, initial deformation zones, extrusion zones, forging zones, and post-heat or cooled down zones. In the extrusion zone, the material flows around the rotating tool and moves from the front to the back of the tool. Simultaneously, the extruded material is forged to the back of the tool to fill the cavity in the forging zone.

The solid-state nature of the FSW process ensures that the highest temperature during welding is within the recrystallization and melting point of the material. The conventional extrusion process is associated with direct, indirect, impact, and hydrostatic segments. The selection of improper process parameters may lead to the development of funnel defect, fir tree cracking, pipe or fish tail, center burst, and cracks during the extrusion process (Ko and Kim, 2000; Morsi, McShane and McLean, 2000; Saanouni *et al.*, 2004). The funnel defect is a commonly occurring flow related defect in the direct extrusion process (Balasundar and Raghu, 2010). Forging is a widely used manufacturing process where the reduction in production time is a great advocate from cold to hot working processes (Forcellese and Gabrielli, 2000). The state of temperature mainly dictates various defects such as underfilling, cracks, surface defects, the material flow related forging defects which can significantly degrade the product quality (Abdullah *et al.*, 2013; Hawryluk and Jakubik, 2016; Gao *et al.*, 2019). Since the FSW process inherently resembles the forging and extrusion of the materials at variable thermo-mechanical conditions, it is associated with various geometric and flow related defects. Therefore, it is of utmost importance to perform an in-depth analysis of the different types of defects associated with materials, joint

configurations, and methods to find the feasible condition for producing a sound quality weld.

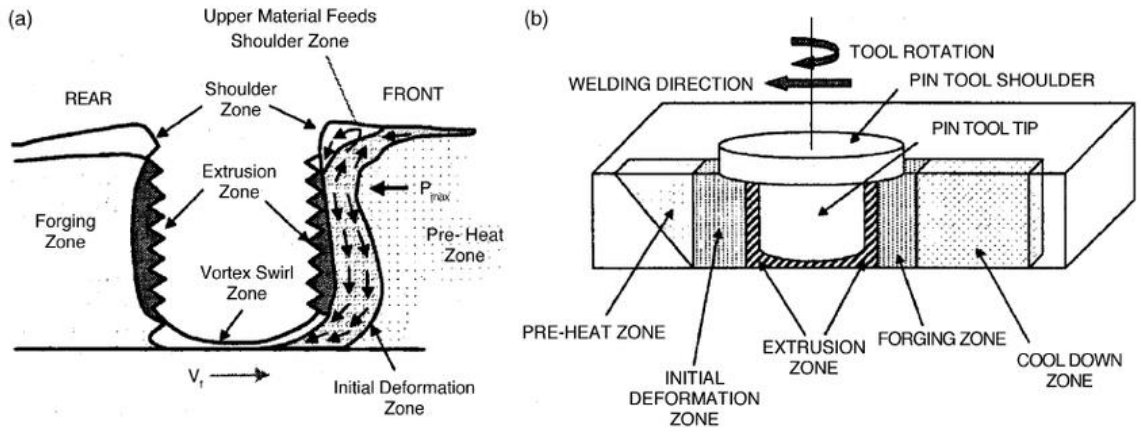

Fig. 2.1 Depiction of the (a) material flow and (b) metallurgical processing zones developed during FSW (Mishra and Ma, 2005)

The FSW comprises of four primary zones namely the stir zone (SZ) or nugget zone (NZ), the thermo-mechanically heat affected zone (TMAZ), the heat affected zone (HAZ) and the base material (BM) as shown in Fig. 2.2 (Heidarzadeh *et al.*, 2020). The SZ is the region observing maximum material mixing and heat generation. This zone observes maximum strain and is prone to recrystallization (Moreira *et al.*, 2009). The zone immediately next to the SZ is the TMAZ. This zone is affected by both the heat and the straining due to the action of the tool pin. However, the material straining experienced by the TMAZ is lesser than the SZ. The zone immediately next to TMAZ is the HAZ (Woo *et al.*, 2006). The effect of mechanical straining is not observed within the HAZ. The zone immediately next to HAZ is the BM which does not observe any thermal or straining effect. The SZ is almost symmetric about the weld centreline. The SZ is the most prominent feature of the FSW.

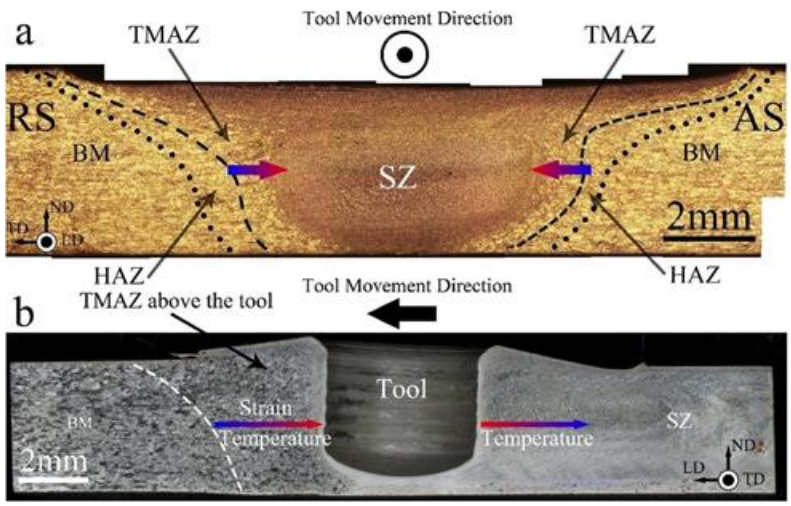

Fig. 2.2 Typical macrostructure and different zones of FSW (Heidarzadeh et al., 2020)

The SZ presents a much smaller and equiaxed grain compared to the BM. The dynamic recrystallization at the SZ is primarily responsible for the change in the grain size (Scialpi, De Filippis and Cavaliere, 2007). The microstructure of the TMAZ is similar to that of the SZ whereas the microstructure of the HAZ is similar to that of the BM. The welded components mostly fracture due to the local and heterogenous deformation in the material (Liu *et al.*, 2003). The welding parameters significantly affect the weld quality and the fracture location. The mechanical strength of the welded product also significantly depends on the welding defects and material flow, which is in turn dependent on the process parameters (Zeng, Xue, Wang, Ni, Xiao and Ma, 2018).

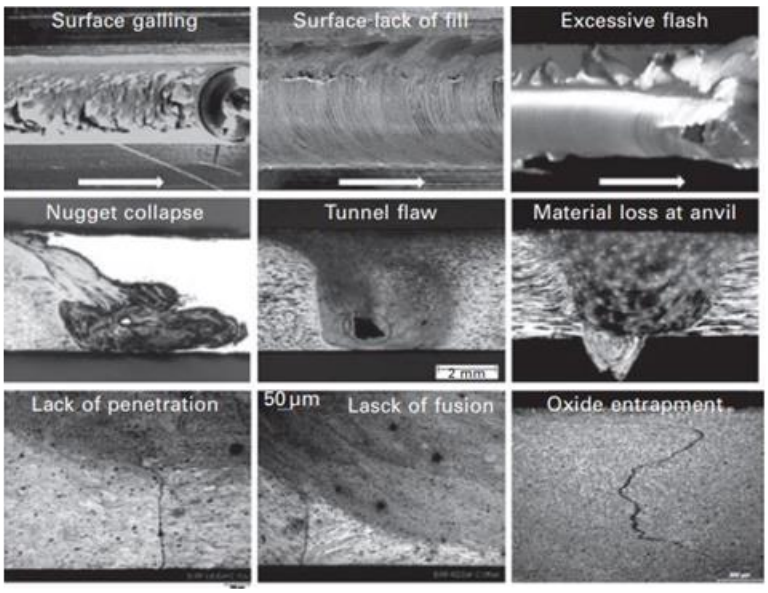

Fig. 2.3 Different defects observed in FSW (Lohwasser, D.; Chen, 2009)

Defects or flaws are the discontinuities arising in the weld generally due to improper welding process parameters. The factors responsible for defect generation have been discussed in the subsequent sections. FSW is a thermo-mechanical process and the effects of both the temperature and material movement are important to produce a sound quality weld. As FSW is a solid-state welding technique, the rise in temperature cannot produce a good quality weld, single-handedly. This makes the joining of parts by FSW a temperature dependent, tool-workpiece interactive event. The most notable advantage of the FSW process is the elimination of defects associated with conventional arc welding such as porosity, weld distortions, oxidation, spattering, etc. (Fande, Taiwade and Raut, 2022). Although the FSW process is void of conventional weld defects, however, this solid-state welding technique also observes some surface or sub-surface defects such as tunnel defect, micro and macro cracks, excessive flash formation, kissing bond defect, exit hole defect, etc. (Al-Moussawi and Smith, 2018; Guan *et al.*, 2022).

The defects can be surface or body defects, depending on their position of occurrence. The welding defects occur either due to improper heat generation or improper material

plasticization. Thus to produce a defect free joint optimum process parameters need to be maintained. The weld formation during FSW is a two-step process. The first step comprises of the workpiece getting heated due to frictional heat and plastic deformation. The contribution of the plastic heat to the total temperature input is minimal compared to the frictional heat generated (Bastier *et al.*, 2006). The highest temperature rise during FSW is about 70- 90% of the melting point temperature of the base material (Chao, Qi and Tang, 2003; Chalurkar and Shukla, 2022). The temperature rise to the realm of hot working conditions helps to significantly soften the material. In the second step with the rotation of the tool, the material in contact with the tool shoulder and pin is rotated about an axis and deposited from the leading edge to the trailing edge.

The possibility of defect generation arises during the material rotation stage. If the material deposition behind the traversing tool is not proper then void like defect generates. If the void defect continues throughout a continuous length of the workpiece, it can be termed as tunnel defect. The void or tunnel defect can be scalloping also, i.e., intermittent void or tunnel defect may also be present. Due to improper process parameters and improper tool design the kissing bond or weld root defect is observed. The presence of oxide layers can lead to the formation of defects as their chemical composition is different from that of the parent materials. Severe material expulsion due to high plunge depth or excessive heating will lead to the formation of flash defect.

The last three decades of investigation have revealed the successful implementation of the FSW process albeit to a specific set of metallic alloys. However, with the ever evolving manufacturing industry, the welding of similar materials is not sufficient anymore. As a result, several dissimilar combinations of materials need to be welded together. The Al-Mg (Yao *et al.*, 2012; Jiang, Wu and Shi, 2022), Al-Cu (Yaduwanshi, Bag and Pal, 2018; Shankar *et al.*, 2019), Al-Steel (Ogawa *et al.*, 2019; Kaushik and Dwivedi, 2021), Mg-steel (Kasai, Morisada and Fujii, 2015) are some of the popular dissimilar combination of materials to be welded using FSW. However, the welding of dissimilar materials poses a severe difficulty due to the disparity in their thermo-mechanical properties. Different hybrid welding techniques are now being devised to reduce material property discrepancies.

The hybrid welding approach has two heat sources, the secondary heat source is used to heat the stronger material or the higher melting point material and then after an optimal period of time the primary welding technique, i.e., FSW is initialized to complete the welding. The commonly used types of secondary heat sources with FSW are plasma

(Yaduwanshi, Bag and Pal, 2014, 2015), TIG (Bang *et al.*, 2020, 2021), ultrasound (Thomä *et al.*, 2018; S. Chen *et al.*, 2019), laser (Fei *et al.*, 2016; Ahmad, Galloway and Toumpis, 2019), induction (Álvarez *et al.*, 2014; Kaushik and Kumar Dwivedi, 2021) etc. The application of a secondary heat source for the pre-heating purpose leads to the improvement in material plasticization. Bang et al. (Bang *et al.*, 2013) showed that a TIG welding heating source was used to pre-heat the higher melting point Ti6Al4V alloy whereas the tool was offset towards the lower yield point AA6061 to provide better material plasticization. The said arrangement of the tool and the secondary heat source led to a significant improvement in tensile strength and elongation of the welded sample for the TIG assisted FSW compared to the conventional FSW. Insufficient heat penetration and material plasticization were observed near the weld root in the case of conventional FSW. The unwelded zone near the bottom of the workpiece can act as a crack initiation site, thus degrading the mechanical strength of the component. Multiple independent researchers have reported an improvement in the mechanical strength of welded samples when heat assisted FSW is employed for dissimilar FSW (Joo, 2013; Liu, Lan and Ni, 2015a; Mehta and Badheka, 2017). However, for the dissimilar FSW of Cu-SS, the conventional FSW produces a better weld than the heat assisted FSW due to the formation of oxide layers and significant dispersion of the SS particles in the Cu matrix (Joshi and Badheka, 2017).

The plate positioning also plays an important role during dissimilar FSW. The placing of the stronger plate on the Advancing side (AS) produces a good quality weld (Sahu *et al.*, 2016). The high heat input on the plate positioned at the AS leads to better material plasticization and mixing (Muthu and Jayabalan, 2015). The tool offset to either the AS or the Retreating side (RS) is another critical process parameter to control the weld quality (Liang *et al.*, 2013). The offest of tool to the low yield strength material leads to an improvement in weld quality by allowing for easy material movement and mixing (Watanabe, Takayama and Yanagisawa, 2006).

2.2 Types of defects in conventional FSW

Since the advent of FSW technology, the study of defect formation in solid-state welding has been a widely pursued topic. Many researchers opined that categorizing defects would help to understand and study them. One of the biggest challenges is the physics of defect evolution in FSW, which is significantly different from the other arc welding processes. This happens primarily due to the difference in the heat generation mode and the amount of heat input in the FSW process. The material plasticization and rotation,

which is an integral characteristic of FSW can also be responsible for defect generation. Thus, the defects observed in FSW cannot be easily correlated with the defects observed in other commonly practiced welding techniques.

Defects in FSW can appear due to the resistance to deformation and microstructural changes, which is a function of the material properties and chemical composition. The defect can be either due to geometric misalignment, or flow defect (Arbegast, 2008). The geometric defects are those originating due to geometric misalignment such as tool offset, tool plunge depth, tool tilt, tool design, etc. The flow related defects arise due to excessive hot or cold-welding conditions. Too hot welding conditions can lead to the formation of excessive flash or nugget collapse in the SZ. Alternatively, the too cold-welding condition can lead to volumetric non-bonding leading to the formation of either voids or tunnels (Lohwasser, D.; Chen, 2009). The presence of foreign particles such as the oxide layer on the abutting surfaces can lead to the generation of the joint line remnant defect. Although there are multiple methods to define and understand defect formation in FSW, one of the easiest and most inclusive ways is the mass balance flow model proposed by Arbegast (Arbegast, 2008). In this model, the defect is observed as a volume of missing mass in the material. This missing mass can be either on the surface or inside the workpiece. The commonly occurring defects during FSW are shown in Fig. 2.3.

2.2.1 Tunnel defect

Tunnel defect or wormhole is one of the most commonly encountered defects in FSW, formed primarily due to improper selection of process parameters as shown in Fig. 2.4. Inappropriate tool design or insufficient axial force are recognized as the secondary reasons for the formation of the tunnel defect (Dehghani, Amadeh and Akbari Mousavi, 2013; Liu and Wu, 2016). A significant issue encountered for dealing with tunnel defect is that it generates inside the workpiece. This makes detection of the tunnel defect impossible without post-processing. The tunnel defect forms when there is an insufficient flow of material from the RS to the AS with the rotation of the tool (Liu and Wu, 2016). It is observed that for similar FSW, the tunnel defect is generally observed in the AS of the

workpiece (Arbegast, 2008; Tutunchilar *et al.*, 2012). However, in the case of dissimilar welding of aluminium and steel, the tunnel defect is produced in the RS (Dehghani, Amadeh and Akbari Mousavi, 2013). The tool is generally offset towards the high strength material on the AS during dissimilar FSW. The excessive tool offset towards AS can cause improper material deposition on the RS thus leading to the formation of tunnel defect in the RS, i.e., the weaker material side. The tunnel defect is significantly reduced or removed by proper heat input, heat dispersal on both sides of the joint, and with proper material deposition behind the traversing tool. The presence of tunnel defect in the weld cross-section leads to the scarcity of material in the defect location and thus acts as a region for stress concentration. This adversely affects the tensile properties of the weld, making it weak for mechanical applications.

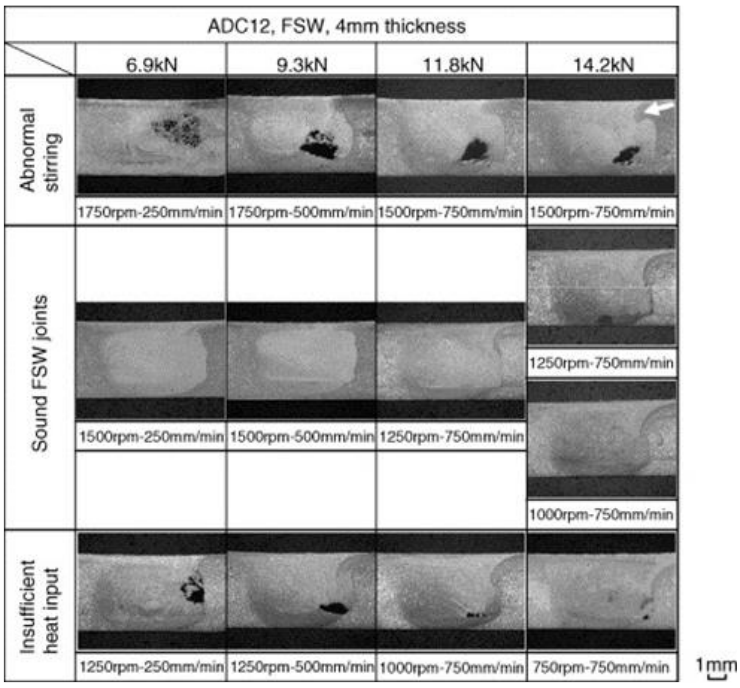

Fig. 2.4 Sub-surface defects at various process parameters for ADC12 FSW (Kim et al., 2006)

2.2.2 Kissing Bond and Joint Line Remnant defect

The Kissing Bond (KB) defect is recognized as the presence of base material remnants in the weld zone (Fig. 2.5) (Sato *et al.*, 2005). In other words, KB defect is the presence of previously separate workpiece materials in the weld zone with negligible bonding between them. Mechanical properties, including fatigue life and impact strength of the weld, can be severely reduced due to the presence of the KB defect (Oosterkamp, Oosterkamp and Nordeide, 2004). The primary reason for the formation of the KB defect is the presence of metallic oxides on the abutting edges of the workpiece. When the applied temperature and strain cannot breakup the oxide layer, the joint formed does not have proper bonding, and the individual material remains in the weld zone. Although the metallic oxides are the primary reason for the formation of the KB defect, this defect can also occur due to unsuitable tool pin design or less plunge depth (Oosterkamp, Oosterkamp and Nordeide, 2004; Khan *et al.*, 2015). Shear stress plays an important role in material mixing and bond

formation. When the shear stress generated is insufficient to break up the metallic oxides, proper bonding cannot occur in the weld zone. Continuous layers of oxides can get deposited in the SZ, leading to the degradation of the mechanical properties (Sato *et al.*, 2005). KB defect is observed near the bottom surface of the workpiece because plunge depth plays an important role in the KB defect formation. With insufficient plunge depth, proper metallic oxide breakup does not occur, leading to KB defect formation. Higher rotation speed and lower traverse help to reduce the formation of KB defects as higher heat input causes better material mixing.

The occurrence of a line at the root of the weld where the workpiece touches each other is often visible as shown in Fig. 2.6. It is referred to as the joint line remnant (JLR) condition. Although this is a visible line at the bottom of the weld, it is not considered a defect as it does not adversely affect the mechanical strength of the weld. JLR formation occurs due to partially dispersed visible surface oxide layers (Gibson *et al.*, 2014). A joint line remnant can also be referred to as a remnant oxide layer. The oxide layer present in the SZ can be in a lazy S or zig-zag pattern (Sato *et al.*, 2004). Modifying the heat input and the process parameters can help eliminate the oxide layer's continuous run or zig-zag line by dispersing the oxide particles throughout the weld zone. The dispersed oxides do not hinder the bonding of metals, and thus the mechanical properties of the weld are not affected (Sato *et al.*, 2005).

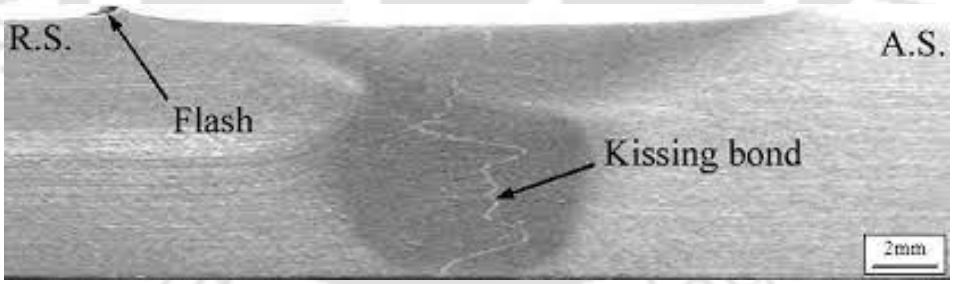

Fig. 2.5 Cross-sectional representation of kissing bond defect during AA5083 FSW (Zhou, Yang and Luan, 2006)

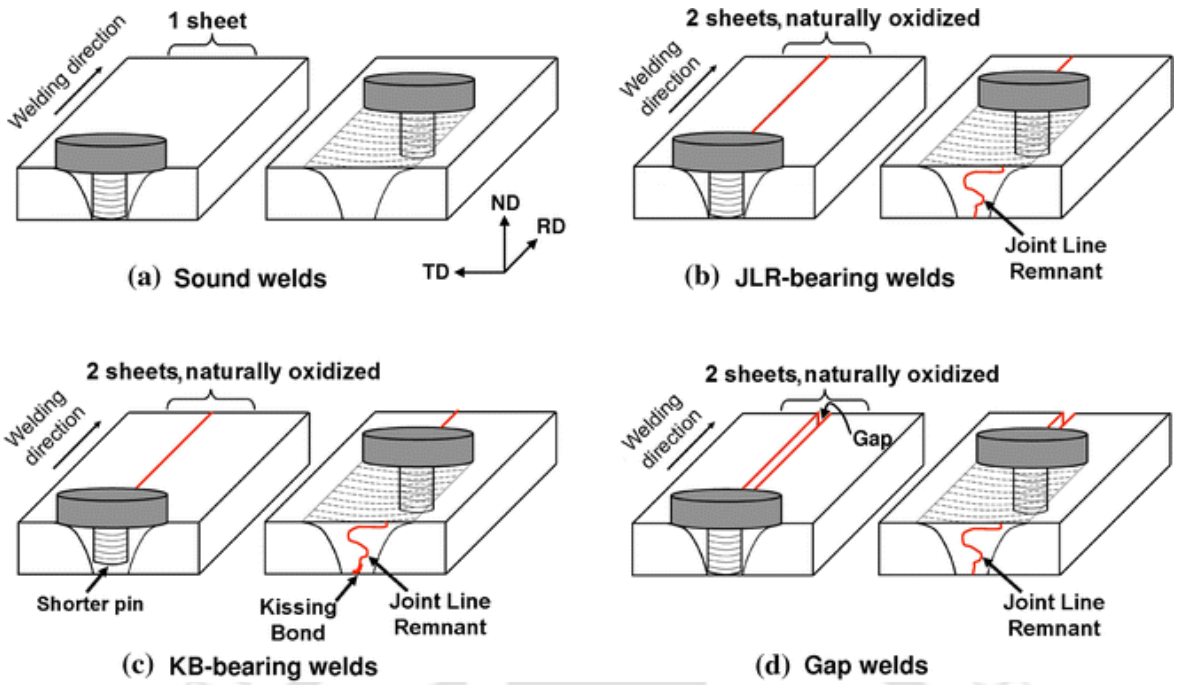

Fig. 2.6 Schematic representation of the difference between the (a) sound weld, (b) JLR defect and (c) kissing bond defect (Le Jolu et al., 2014)

2.2.3 Excessive flash as defect

All the defects discussed earlier are generated inside the material and, therefore, cannot be seen with the naked eye. Alternatively, the excessive flash (EF) formation, is a very commonly occurring surface defect during FSW (Fig. 2.7). The elimination of the flash is a difficult task, as in many practical instances, the flash is used to detect proper contact between the tool and the workpiece. EF formation takes place due to excessive heat generation and large plunge depth. The high heat input severely plasticizes the material and aids in easy material movement out of the workpiece. When the plunge depth is more, the volume of the workpiece material that is plastically deforming is also more. This deforming material tries to move up around the tool. When the tool shoulder cannot contain the upward-flowing material, the EF is generated. The EF takes up the space around the periphery of

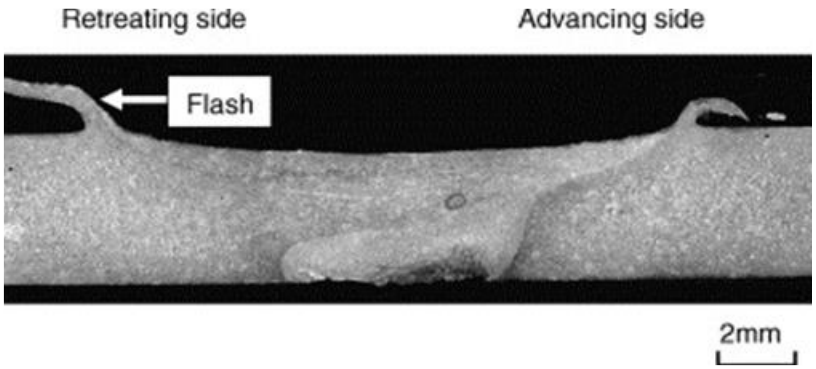

Fig. 2.7 Excessive flash defects at various process parameters for ADC12 FSW (Kim et al., 2006)

the tool shoulder. The EF formation leads to less material available to fill the nugget zone. Therefore, the tunnel defect is also a possibility with EF formation.

As the material flows from the AS to the RS in FSW, more material in the form of flash comes out of the RS (Kumar and Kailas, 2008). Due to EF flowing out of the workpiece, the height of the workpiece cross-section reduces, thus weakening the joint (Mishra and Ma, 2005). Some notch formations can also be observed near the root of EF. These notches can act as regions of stress concentration, thus having a detrimental effect on the tensile properties of the joint. Concave shoulder tools and tilt angle have proved beneficial in containing flash formation (Mishra, De and Kumar, 2014).

2.2.4 Surface galling

The defect like surface galling is defined as the presence of a series of voids on the workpiece surface (Jain *et al.*, 2015). Surface galling is commonly observed in various metal forming processes. The surface galling defect can significantly degrade the surface quality and increase tool wear. It forms due to excessive heat generation leading to sticky welding conditions (Wang *et al.*, 2019). In general, galling is a phenomenon by virtue of which the frictional forces abruptly increase under specific working conditions leading to several microscopic welding (Dohda *et al.*, 2021). The general measure to eliminate surface galling is by reducing the heat supplied per unit area to the workpiece. Figure 2.8 highlights the formation of the surface galling during dissimilar FSW of AZ31 with SS316.

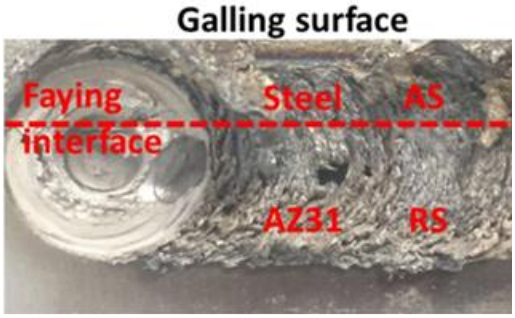

Fig. 2.8 Experimental investigation of surface galling defect for dissimilar FSW (Wang et al., 2019)

2.2.5 Lack of penetration (LoP)

One of the most commonly occurring defects in FSW is the lack of penetration (LoP) which is generally observed near the bottom surface of the joint during butt welding. Figure 2.9 shows the presence of both the LoP and kissing bond defects near the weld root for the FSW of AA 2024. The origin of the root defect is due to the lack of plastic material flow below the tool pin (Santos, Miranda and Vilaça, 2014). The LoP defect arises due to improper tool pin geometry (Aliha *et al.*, 2016). Khalilbad et al. (Masoumi Khalilabad *et al.*, 2018) co-related the tool pin diameter to the plate thickness to identify the formation of

LoP defect. The tool pin with a minimum diameter of dimension equal to half of plate thickness leads to the formation of LoP, alternatively, increasing the minimum tool pin diameter to plate thickness leads to the elimination of LoP. The LoP is responsible for improper material mixing beneath the tool pin (Eslami *et al.*, 2015). The improper material flow below the tool pin can also occur due to some oxide layers. The oxide layers of various metals are stable and have different physical properties than the base material, thus causing difficulty in material flow.

The mechanical properties of the joint are severely affected by the LoP. The LoP defects can be of the order of micron and therefore cannot be observed without specialized tools. The esteemed literature discusses the application of eddy currents to determine the root defects of about 60 μm depth (Rosado *et al.*, 2010). The size of the LoP defect can be significantly reduced by the application of the electrical joule effect (Santos, Miranda and Vilaça, 2014). The external heat source can be used to locally heat the material near the weld root and improve material plasticity to reduce the LoP.

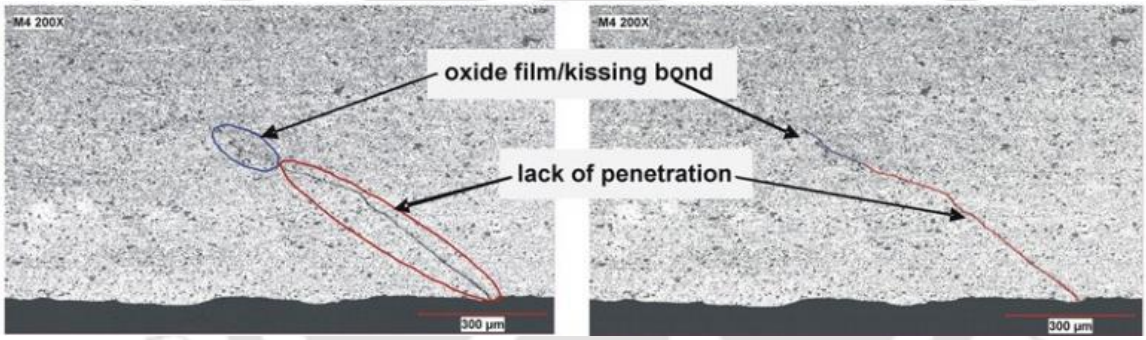

Fig. 2.9 Representation of the simultaneous presence of the LoP and KB defects at the root of AA 2024 butt FSW (Mandache et al., 2012)

2.2.6 Nugget collapse

Nugget collapse is a form of defect that is found explicitly in FSW as shown in Fig. 2.10. It occurs due to excessive heat generation leading to severe plasticization and flow into the SZ. At very hot processing conditions, the torsion applied by the rotating tool is responsible for the excessive material flow leading to the nugget collapse within the SZ (Arbegast, 2008). The nugget collapse originates when the material

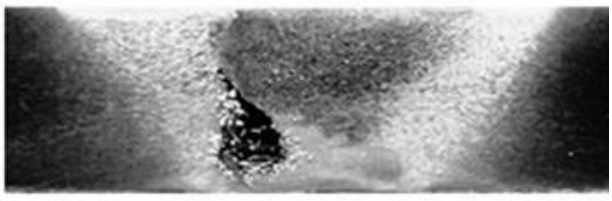

Fig. 2.10 Experimental investigation of tunnel defect and nugget collapse at 1300 rpm and 90 mm/min (Lakshminarayanan, Malarvizhi and Balasubramanian, 2011)

just below the tool shoulder is pushed downwards to the SZ excessively (Arbegast, 2008). This defect is more noticeable on the RS of the SZ, suggestive of the material flow direction. This defect can be eliminated using proper process parameters and tool geometry (Jain *et al.*, 2015).

2.2.7 Micro and macro cracks

Microcracks are another form of defect appearing during FSW (Fig. 2.11). The process parameters, the microstructure of the parent material, and thermal stresses determine the formation of the microcracks (Liu and Wang, 2009). Further, the grain boundary, interface between hard phase particles and matrix, and coarse impurity particles may lead to the formation of microcracks (Jian *et al.*, 2021). The presence of the impure particles, due to poor compatibility with the surrounding matrix leads to stress concentration at the interface between the particle and the matrix leading to the formation of the microcracks. The welding method also significantly affects the formation of microcracks (Chen *et al.*, 2013). Cladding of steel with pure copper with gas metal arc welding (GMAW) produces significant microcracks, which got reduced during FSW due to lower heat input (Shen *et al.*, 2015). The microcracks investigation is important due to its influence on the fracture mechanism of the welded joint. Under straining conditions such as tensile loading, the microcracks grow and connect to produce main cracks (Yazdipour and Heidarzadeh, 2016a).

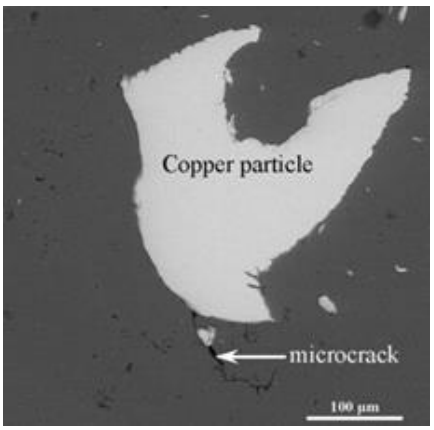

Fig. 2.11 SEM image of microcrack formed during FSW of AA 1060 at 1180 rpm and 90 mm/min (Saeid, Abdollah-zadeh and Sazgari, 2010).

During dissimilar welding, the IMCs inhomogeneity significantly influences the formation and propagation of the microcracks (Xia *et al.*, 2022). The cracks can be present both on the surface, and the cross-section of the weld. At higher tool rotational speed, the cracks appear at the material interfaces due to higher deformation and intense mixing of materials. A reduction in the microcracks is observed at higher traverse speeds due to the reduction in the intense mixing of material (Saeid, Abdollah-zadeh and Sazgari, 2010). The accumulation of alloying elements and intermetallic layers due to the temperature rise during welding is also a possible reason for the crack origination (Ouyang, Yarrapareddy and Kovacevic, 2006). However, the use of appropriate interlayer can reduce the formation of the IMCs and thus the crack formation (Kumar and Wu, 2021). An improper tool offset can also be responsible for the crack formation (Yazdipour and Heidarzadeh, 2016b), whereas the use of no tool offset significantly reduces the microcrack formation (Zandsalimi, Heidarzadeh and Saeid, 2019). The application of ultrasonic vibrations can eliminate the formation of microcracks (You *et al.*, 2023).

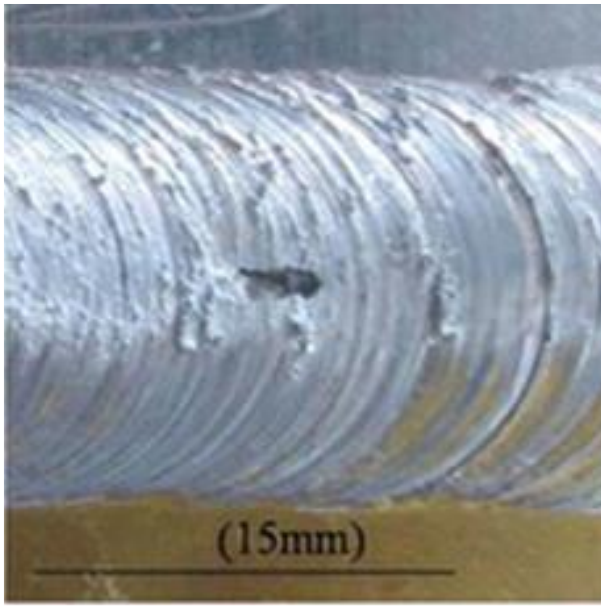

Fig. 2.12 Generation of macrocrack at a low rotation speed of 200 rpm (Esmaeili, Besharati Givi and Zareie Rajani, 2012).

The macrocracks can appear due to improper material flow in the SZ as shown in Fig. 2.12. The slow tool rotation, lack of heat generation, and improper material plasticizations are some of the factors responsible for the formation of the macrocracks (Mehta and Badheka, 2016). During the modelling of the FSW, the occurrence and behaviour of macro cracks in both similar and dissimilar materials are often addressed by implementing appropriate damage models (He, Dawson and Boyce, 2008). These damage models are designed to capture the initiation, propagation, and evolution of cracks within the material during the FSW process (Simar *et al.*, 2012). The interface tracking models such as the level set and phase field models can accurately track the crack interface (Stolarska and Chopp, 2001; Esmaeilzadeh *et al.*, 2020). Other than finite element modelling (FEM), extended finite element methods are also employed to analyze crack growth (Sedmak *et al.*, 2022). They consider factors such as the applied loads, stress distribution, and material

properties to determine the likelihood and progression of crack formation. This allows for the identification of critical locations and conditions for crack propagation.

2.2.8 Lack of fill (LoF) on surface

Lack of fill (LoF) generates primarily due to the negligible material deposition at the trailing side of the tool. Unlike the lack of penetration defect, the lack of fill defect can be present near the top surface. This defect generally originates at low rotation speed and high traverse speed (Shah *et al.*, 2022). As the defect is visible on the top surface (Fig. 2.13), it can also be referred to as a lack of bonding (Kim *et al.*, 2006). Instead of considering the LoF as a separate defect, it can also be considered as a worsened case of the tunnel defect (Sinclair *et al.*, 2010). The LoF is attributed to improper and localized plastic flow of material. A reduction in the material plastic flow and low interface temperature due to improper process parameters contributes to the formation of LoF defects (Pei and Dong, 2017). At the weld initiation, the high workpiece gap can lead to the formation of a LoF defect. Chiuzuli et al. (Chiuzuli *et al.*, 2021) recommend a maximum gap of about 50% of the workpiece thickness for a defect free weld.

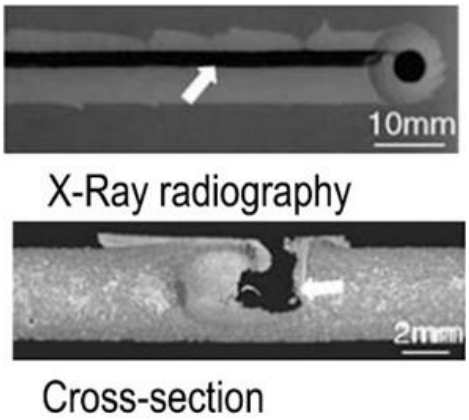

Fig. 2.13 Representation of the lack of fill defect from the top-surfaec by X-Ray radiography and cross-section (Pei and Dong, 2017).

2.2.9 Hook defect

Hook defect is generally observed in the case of lap joints in FSW (Fig. 2.14). This defect originates when the material from the bottom workpiece forces its way into the top workpiece due to the plunging action of the tool (Li *et al.*, 2014). This stirring up of the material at the interface leads to the formation of a notch in the workpiece. The hook defect is either observed in the AS (Dubourg, Merati and Jahazi, 2010) or both AS and RS (Rajesh and V. J. Badheka, 2018).

Hook defect is a loose term for the hook-up effect where the material moves into the top workpiece creating a notch. Although the hook-down effect is very limited, it is still observed in some instances. Rajesh et al. (Rajesh and V. J. Badheka, 2018) observed a hook-down defect at low spindle speed, i.e., the material moves down into the bottom workpiece instead of pushing up. The size of the hook defect increases if a thinner workpiece is used as the top plate compared to the bottom workpiece (Rajesh and V. J. Badheka, 2018). In such cases, more material will be displaced by the tool pin from the thicker bottom plate leading to an increase in the size of the hook. The hook defect is generally observed in TMAZ, beyond this zone, plastic deformation is not observed in FSW. Therefore hook defects cannot form beyond TMAZ.

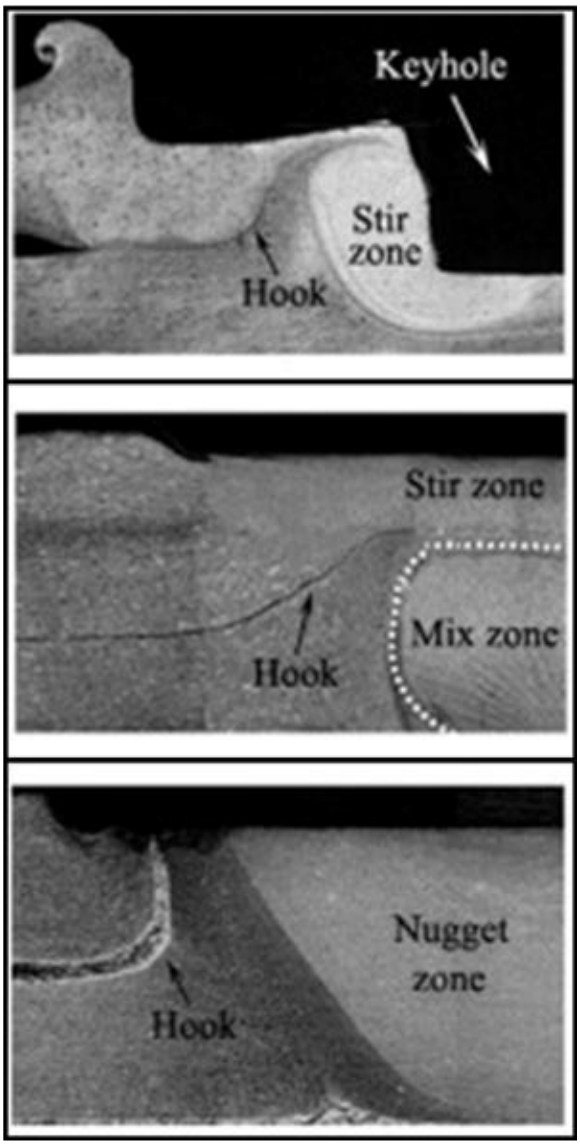

Fig. 2.14 Representation of the Hook and keyhole defect in FSSW of AA2024 (Li et al., 2014)

Modifying the welding parameters, such as the tool rotation speed, can modify the heat input and material plasticization, thereby reducing the hook defect size. Further, the multi-pass welding adjacent to the previous weld line and changing the direction of rotation have proven beneficial in eliminating the defect (Rajesh and V. Badheka, 2018; Rajesh and V. J. Badheka, 2018). Hook defect severely affects the joint's mechanical properties, such as fatigue strength.

2.2.10 Exit hole

One of the most common features of the FSW with the conventional tool is the exit hole defect (Malik *et al.*, 2014). This defect is also referred to as a keyhole defect. This defect is unavoidable with the conventional FSW tool that appears only at the end of the SZ when the tool is plunging out of the workpiece. The exit hole defect is formed by the plunging out action of the tool. As the tool moves out of the SZ, no material movement is possible within the SZ to fill the hole left behind (Fanelli, Vivio and Vullo, 2012). Eliminating the exit hole by post processing is currently the only option to disregard the defect. However, researchers are also proposing to fill the exit hole with the help of a consumable or semi-consumable tool (Behmand *et al.*, 2015) or using the self-refilling technique with a non-consumable tool as shown in Fig. 2.15 (Zhou *et al.*, 2012; Mehta *et al.*, 2020, 2021). Furthermore, the refilling technique employing a semi-stationary bobbin tool is also explored in the literature (Reimann *et al.*, 2017). Although refilling the exit hole seems a viable option, however, the refilling operation is a post-processing approach and it cannot prevent the formation of the defect.

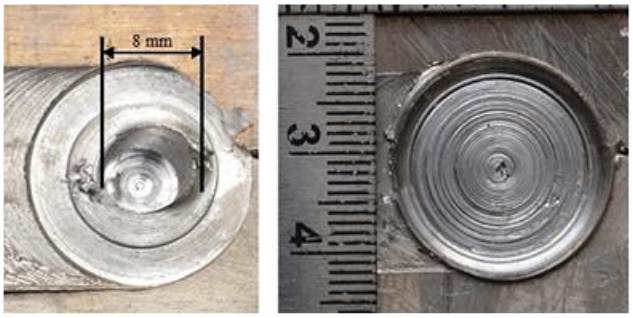

Fig. 2.15 Experimental representation of the (a) exit hole and, (b) repaired exit hole (Mehta et al., 2020)

2.2.11 Residual stress

Residual stress and distortion are common material related defects observed in FSW. The residual stress is developed in the welded sample due to the accumulation of thermo-mechanical strains during welding. The residual stresses are understood by the stresses remaining within a stationary body and at equilibrium with its surrounding when an external load is removed (Withers and Bhadeshia, 2001a). The subsequent non-uniform heating and cooling of the body leads to the generation of residual stresses. The residual stress can act over an extended macroscopic domain, intragranular region, or inter-atomic levels (Withers and Bhadeshia, 2001b). The macroscopic residual stresses can superimpose with the externally applied loads and, therefore, significantly influence the life of the welded component.

The residual stress can have three components, i.e., the longitudinal stress in the welding direction, traverse stress perpendicular to the welding direction, and the normal

stress in the plate thickness direction. The material below the tool shoulder and in front of the tool pin has a high temperature resulting in the expansion of the material. The cooler material in contact with the hot material resists its expansion leading to the formation of compressive stresses in front of the tool pin. Alternatively, the material behind the tool pin contracts due to material cooling. This results in the generation of tensile residual stresses due to the resistance offered by the surrounding materials. It is a common observation that the longitudinal residual stresses are the highest, whereas the normal residual stresses are minimal. This occurs due to a lack of significant temperature difference and opposing forces in the thickness direction due to a low flow gradient. However, for thick plate welding, the normal residual stress cannot be ignored. It is a common belief that FSW is a low distortion process; however, it is not void of either distortion or residual stress.

The primary process parameters affecting the formation of the residual stresses are tool rotation speed, traverse speed, tool design, and clamping devices (de Giorgi *et al.*, 2009; Tutum and Hattel, 2010; Richter-Trummer *et al.*, 2012). Unlike the various defects encountered in FSW, the residual stress cannot be visualized directly with the naked eye, and specialized techniques or modelling approaches are needed to accurately estimate the residual stress. The residual stress demonstrates a non-uniform distribution in the transverse and longitudinal directions (Salih, Ou and Sun, 2022). For instance, the AS is observed to have higher residual stress compared to the RS (Fig. 2.16). This non-uniform residual stress distribution is due to non-uniform temperature distribution and asymmetry material flow field between AS and RS of FSW. The various experimental effort and numerical modelling approaches for the estimation of residual stress are reviewed in detail in the published literature (Woo *et al.*, 2011; Hattel, Sonne and Tutum, 2015).

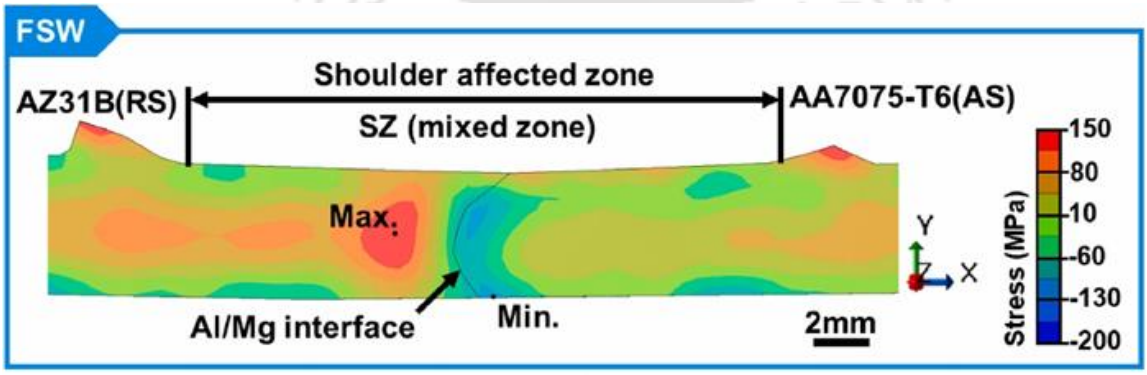

Fig. 2.16 Residual stress distribution for the AA7075-T6 and AZ31B dissimilar FSW at 500 rpm and 50 mm/min (Muhammad et al., 2023).

2.2.12 Intermetallic compounds

The intermetallic compounds (IMCs) generally appear in case of dissimilar FSW (Liu, Ji and Meng, 2018b; Meng *et al.*, 2018; V. P. Singh *et al.*, 2019). The IMCs formation occurs due to the partial melting and intermixing of the constituent materials during the welding process (Sen and Puri, 2022). The probability of the IMCs formation increases when welding immiscible dissimilar materials (Tan, Wu and Shi, 2023). During the cooling phase of the welding, brittle IMCs develop leading to the formation of microcracks (Tan *et al.*, 2013; Beygi *et al.*, 2021). These IMC layers typically have high hardness and low ductility properties. The use of interlayers can prevent the formation of brittle IMCs and thus improve the mechanical properties of the joint (Sahu, Pal and Pal, 2017; Abdollahzadeh *et al.*, 2018). The application of the interlayers prevents the formation of the IMCs. A comprehensive review for the formation of the IMCs and their mitigation strategies is provided in the published literature (Hussein, Tahir and Hadzley, 2015; Sen and Puri, 2022).

The formation of the IMCs can be controlled by reducing the heat input (Pourali *et al.*, 2017; Heidarzadeh *et al.*, 2020; Jabraeili *et al.*, 2021). The application of ultrasonic vibrations can also reduce the IMC thickness (You *et al.*, 2023; Zhao *et al.*, 2023). The underwater FSW also produces thinner IMCs due to a higher cooling rate compared to the FSW in the open air (Lader, Baruah and Ballav, 2023). Figure 2.17 shows the variation of the IMC layer thickness for conventional FSW and tungsten inert gas (TIG) assisted FSW. It is evident from the figure that with the application of a second heat source, the average size of the IMC layer increases due to the increase in heat input. A recent publication by Ahmed et al. (Ahmed *et al.*, 2021) indicates a complete elimination of IMCs when welding AA2021 and AISI1018 by moderating the process parameters to optimize the heat input. However further investigation regarding the complete elimination of IMCs is required, specially for different combinations of metallic alloys. Different types of defects, their location of appearance, and reasons for formation are summarised in Table 2.1.

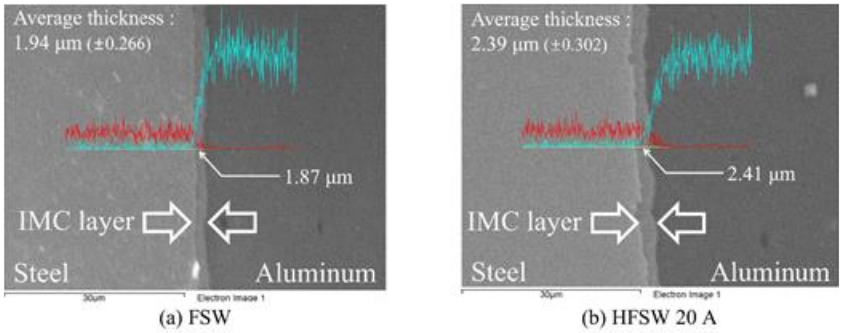

Fig. 2.17 SEM-EDS analysis of IMC formation during (a) FSW; TIG-FSW at (b) 20 A, (c) 30 A, (d) 40 A (Bang et al., 2020)

Table 2.1 Commonly occuring defect during similar, dissimilar and hybrid FSW

Defect	Heat application	Location	Causes	Dissimilar FSW	Hybrid FSW
Tunnel defect or wormhole	Insufficient heating and material mixing	Generally, AS between NZ and TMAZ	➢ Low rotation speed ➢ High traverse speed ➢ Improper tool offset ➢ Improper plunge depth ➢ Improper tool geometry	➢ Present in dissimilar FSW of AA5083 and AA6063 (Khan *et al*., 2015) ➢ Present in dissimilar FSW of AA2024 and SS 304 (Jabraeili *et al*., 2021)	➢ Defect can be eliminated by the Ultrasonic vibration assisted FSW for AA2024 (Liu and Wu, 2016)
Flash formation	Excessive heating and high plunge depth	On the workpiece surface and dominant on RS	➢ High rotation speed ➢ Low traverse speed ➢ High plunge depth	➢ Present in dissimilar FSW of AA6061 and AISI304 (Mahto, Kumar and Pal, 2020) ➢ Present in the dissimilar FSW of AA6061 and AZ31B (Liu, Ji and Meng, 2018a)	➢ Defect can be reduced by the use of Induction heated tool assisted FSW for thermoplastics (Vijendra and Sharma, 2015)
Hook Defect	Excessive heat generation	TMAZ	➢ High plunge force	➢ Present in dissimilar lap FSW of AA6082 and AA5754 (Infante *et al*., 2016) ➢ Present in dissimilar lap FSW of AZ31 and steel	-

				(Jana and Hovanski, 2012)	
Kissing Bond	Presence of metallic oxides	Interface of workpiece	➢ Inept workpiece preparation ➢ Low rotation speed ➢ High traverse speed	➢ Present in dissimilar FSW of AA2198 and AA2024 (Masoumi Khalilabad *et al.*, 2018) ➢ Present in dissimilar FSW of AA5083 and AA7B04 (Chen *et al.*, 2017)	-
Surface galling	Excessive heat	Weld surface	➢ Improper process parameter	➢ Present in dissimilar FSW of AZ31 and SS316 and WE43 and SS316 (Wang *et al.*, 2019)	-
Lack of penetration	Insufficient heat	Bottom half of workpiece	➢ Short pin length ➢ Low plunge depth	➢ Present in dissimilar FSW of AA6061 and AA7277 (Aliha *et al.*, 2016)	➢ Defect can be reduced with the help of electrical heat assisted FSW for AA6082 (Santos, Miranda and Vilaça, 2014)
Root defect	Excessive heat and material plasticization	Weld root touching the backing plate	➢ Improper tool design ➢ High plunge depth	➢ Present in dissimilar lap FSW of Polystyrene and Polypropylene (Eslami *et al.*,	➢ Defect can be eliminated with the help of TIG assisted FSW for

				2015)	AA6063 pipes (Senthil, Nathan and Parameshwaran, 2021)
Joint line remnant	-	Workpiece interface at the bottom surface	➢ Improper process parameters	-	-
Nugget collapse	Excessive heat generation and material flow	Nugget zone	➢ High rotation speed ➢ Large shoulder diameter	-	-
Micro-cracks	High heat input and dissimilar material	Nugget Zone	➢ High rotational speed ➢ Low traverse speed	➢ Present in dissimilar FSW of AA5083 and 316L (Yazdipour and Heidarzadeh, 2016b, 2016a) ➢ Present in dissimilar lap FSW of AA 1060 and copper (Saeid, Abdollah-zadeh and Sazgari, 2010)	-

2.3 Aberration in mechanical properties and material defects

One of the significant issues of the FSW process is the difference in the process responses along the length and depth of the weld nugget. For instance, the temperature distribution between the AS and the RS is different as more heat is generated on the AS compared to the RS, unlike the arc welding techniques. A reduction in temperature and strain rate is also observed along the depth direction during FSW of SAF2507 DSS (Cao *et al.*, 2022). This results in the difference of mechanical properties along the depth direction. The location near the top surface of the plate produces better tensile strength, yield strength, and elongation compared to the bottom surface when welding a 20 mm thick AA7075 (Mao *et al.*, 2018). The difference in the properties is due to the presence of finer grains and more high angle grain boundaries (HAGBs) near the top surface. The difference in the grain size during FSW can be attributed to continuous shearing, extrution, and material mixing accompanied by significant temperature differences. Moreover, the top surface is under tremendous heat and pressure due to the larger profile of the tool shoulder which reduces in the depth direction with the reduction in the tool pin profile. Figure 2.18 shows the grain sizes at various depths of SZ for single side FSW.

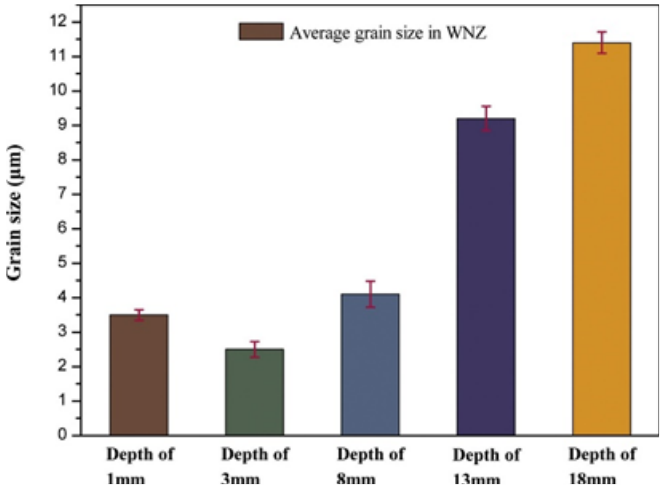

Fig. 2.18 Variation of grain sizes along the thickness of the SZ (Mao et al., 2018)

Along the transverse direction the tensile and the fatigue sample tends to fail near the TMAZ and HAZ interface on the AS (Wan *et al.*, 2014; Y. Chen *et al.*, 2019). This occurs due to the softening effect near this region caused by the thermal cycle during the welding process. However, the fracture location and the mechanical strength of the welded sample can vary if welded under different conditions (Rui-dong *et al.*, 2011). The hardness of the welded sample varies significantly along the depth direction. The dynamic recrystallization and the grain size variations within the SZ is responsible for the varying hardness value. The hardness value was observed to reduce till half of the plate thickness, whereas the

highest hardness value was observed near the top and the bottom surface of the plate (Li *et al.*, 2020). The top surface is in contact with the tool shoulder, resulting in frictional heat generation and material straining. However, as one moves along the depth direction, the temperature rise is only due to the heat conduction and plastic deformation due to the tool pin. Moreover, the top and bottom surface has a relatively higher cooling rate due to contact with the ambient. A similar reduction in hardness value was observed in the depth direction during FSW of 80 mm thick AA6082 plate. A simultaneous reduction in grain size and hardness was observed till half of the plate thickness followed by an increase of both as shown in Fig. 2.19 (Yang *et al.*, 2020). The creep property of the FSW joint was also observed to reduce along the thickness direction for a 12 mm 7B50-T7451 Aluminium alloy (Wang *et al.*, 2022).

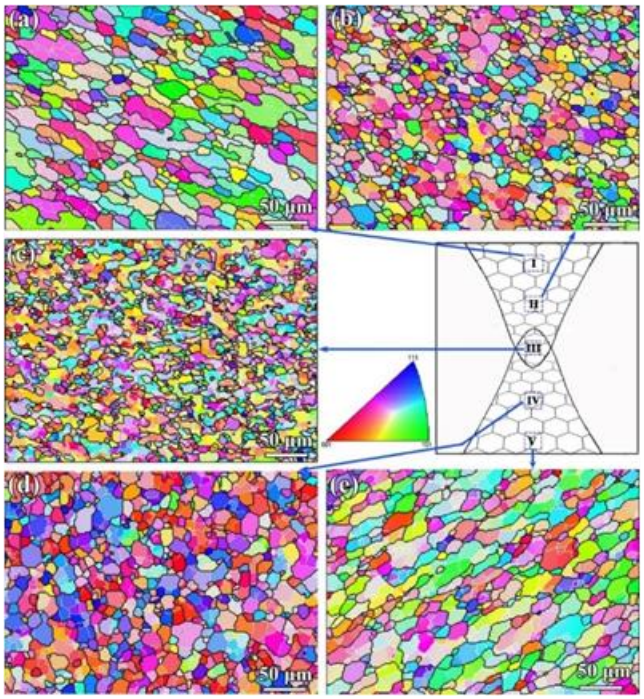

Fig. 2.19 EBSD map of different regions in SZ: (a) top and (b) middle region in the double pass FSW, (c) overlapped region, (d) middle and (e) top region in the single pass FSW (Yang et al., 2020)

2.4 Numerical modelling of FSW

It is realized that several aspects of the modelling technique need to be precisely defined to model a problem with close symbiosis with the actual operation. Some key aspects that need to be considered while modelling the defects in the FSW process are the thermo-physical properties, proper geometrical domain, contact interaction, boundary conditions, and mesh generation. Researchers have indicated that the solution of a more precise result is possible when temperature-dependent material properties are utilized. Thus, the determination of the different material properties as a function of temperature has become an interesting field of research of its own accord (T. Nishi *et al.*, 2003; Tsuyoshi Nishi *et al.*, 2003). Multiple researchers have also employed the velocity and radius dependent values of slip rate (Nandan *et al.*, 2006; Z. Zhang *et al.*, 2011) and temperature and slip rate dependent frictional coefficient (Jamshidi Aval, Serajzadeh and Kokabi, 2011)

for the modelling of FSW process. Table 2.2 summarizes the temperature dependent properties and other attributes essential for the FSW process.

Table 2.2 Different attributes to be defined for the modelling of the FSW process.

Type	Properties	References
Thermal	Density, thermal conductivity, Specific heat capacity, Latent heat of phase transformation	(Ahmad, Galloway and Toumpis, 2018; A. K. Singh *et al.*, 2019)
Mechanical	Density, modulus of elasticity, Poisson's ratio, thermal expansion coefficient, strain hardening exponent	(Sun and Wu, 2018; Iqbal *et al.*, 2022)
Material model *(either one)*	Norton-Hoff model	(N. Dialami, Cervera, *et al.*, 2017)
	Sheppard-Wright model	(Lin *et al.*, 2011)
	Johnson-cook model	(Grujicic *et al.*, 2012)
	Heutier model	(Heurtier *et al.*, 2006; Jacquin *et al.*, 2011)
	Hansel-spittel model	(Assidi *et al.*, 2010)
Friction model *(either one)*	Norton's law	(Fourment and Guerdoux, 2008; Narges Dialami *et al.*, 2017)
	Modified Norton's law	(Assidi and Fourment, 2009)
	Coulomb's law	(Al-Badour *et al.*, 2013; Yaduwanshi, Bag and Pal, 2016)
	Modified Coulomb's law	(Zhang and Chen, 2008)
	Tresca's law	(Jacquin, Desrayaud and Montheillet, 2007; Jacquin *et al.*, 2011)
	Orowan's law	(Aydin *et al.*, 2000)

Different friction models are used to represent the frictional heat generation between the tool and the workpiece (Jacquin, Desrayaud and Montheillet, 2007; Nandan *et al.*, 2007; Zhang and Chen, 2008; Assidi *et al.*, 2010; N. Dialami, Chiumenti, *et al.*, 2017). Proper

geometrical modelling of the various components involved in the welding process is outright mandatory. For instance, the tool can be of any shape and size. The tool pin can have various features such as threads, taper, square, pentagon, hexagon, grooves, etc. Most commercial software packages provide geometrical modelling capabilities; however, these capabilities might not always be sufficient. Therefore, the complex geometries need to be modelled in computer aided design (CAD) packages and then imported into the numerical modelling packages. The modelling of the FSW process primarily consists of thermal and mechanical boundary conditions. The thermal boundary condition consists of the convection and the radiation heat losses from the tool and workpiece to the ambient. There is also thermal contact resistance between the workpiece bottom surface and the backing plate. The modelling of the backing plate is essential as it also contributes to controlling the welding temperature and, thus, the quality of welding (Ghetiya and Patel, 2018).

The meshing of the designed geometric part is directly related to the quality and computational cost of the results. Furthermore, the element size plays a significant role in capturing the intricate details of the micro or macro defect. Generally, the 2D elements are triangular or quadrilateral and the 3-D elements are tetrahedral or hexahedral in shape. The hexahedral or brick elements provide a more accurate result at lower element counts; however, tetrahedral mesh size is a better option if complex geometries and surface interaction between different parts are involved. The features of the FSW components interacting physically during the welding process are the tool shoulder and pin with the SZ of the workpiece. Therefore, mesh sizing of these regions becomes paramount. The SZ is generally meshed finely, whereas the rest of the workpiece meshes coarsely. This is done as the SZ experiences most of the temperature and strain gradients and material movement. The coarser mesh is used away from the weld centreline to keep the total computational cost within balance.

Literature indicates that a much finer mesh size can be modelled in the computational fluid dynamics (CFD) approach compared to the computational solid mechanics (CSM) approaches due to its fixed grid formulations (Meyghani and Wu, 2020). The CSM approaches generally use an explicit scheme to converge to a solution. The computational time of an explicit scheme is a function of the smallest element size. Therefore, significantly reducing the element size in CSM approaches can make the total process computationally expensive (Nicholson, 2008). Some of the commonly chosen elements for the commercially available software are summarised in Table 2.3. The CSM approach primarily comprises of the Lagrangian, Eulerian, ALE, and CEL techniques. A newer

smoothed particle hydrodynamics (SPH) technique based on the Lagrangian approach is gaining importance for the modelling of the FSW process. All these numerical approaches are vastly investigated in the literature (Nandan *et al.*, 2006; Dialami, Cervera and Chiumenti, 2020; Iqbal *et al.*, 2020; Jiang, Wu and Su, 2022; Salih, Ou and Sun, 2022; Yang, Wu and Gao, 2022). In FSW and allied processes, the material behaviour is either visco-plastic or elastic-plastic, or perfectly plastic (Zhang, Zhang and Chen, 2007; Buffa *et al.*, 2020). Accordingly, the CFD approach assumes the fluidic or viscous nature of the material (Hasan *et al.*, 2017; Mohan, Jayadeep and Manu, 2021). The solution domain is either deformable mesh with appropriate remeshing strategy as with the Lagrangian and ALE approaches or fixed mesh as with Eulerian and CEL approaches.

Table 2.3 Various commonly used elements for thermo-mechanical modelling reported in the literature for different commercially available packages.

Element Name	Software	Capabilities	References
Solid 70	Ansys	Thermal	(Prasanna, Rao and Rao, 2010; Yau *et al.*, 2013)
Solid 45	Ansys	Structural	(Prasanna, Rao and Rao, 2010)
Solid 226	Ansys	Thermo-mechanical	(Abhilash, Apeksha and Acharjee, 2018)
C3D8RT	Abaqus	3D coupled temperature displacement	(Mandal, Rice and Elmustafa, 2008; Aval, Serajzadeh and Kokabi, 2012)
C3D4T	Abaqus	4 noded thermal element	(Ragab *et al.*, 2021)
EC3DRT	Abaqus	Eulerian element	(Ahmad, Galloway and Toumpis, 2018)

The final step to obtain a result is to solve the problem with the help of an appropriate solver for a linear system of equations. The numerical solvers can be categorized as direct and iterative solvers. The direct linear equation solver uses a direct, sparse, and Gauss elimination approach to get a solution (Systèmes, 2007). Some software packages also offer a direct frontal solver (Noreika and Tarvydas, 2007). The iterative solver offers a large

number of alternatives compared to the direct solvers. The iterative solvers use the conjugate gradient method, Jacobi conjugate gradient solver, Jacobi conjugate gradient out-of-memory solver, preconditioned conjugate gradient solver, preconditioned conjugate gradient out-of-memory solver, incomplete Cholesky conjugate gradient solver, and the Newton-Raphson iterative methods to solve a problem (Kwan, 2003; manuel, 2004; Ansys, 2005; Chen *et al.*, 2007). Once the complete model is developed, initiating from geometric modelling to the selection of solvers, the commercial packages allow for parallelization of RAM, cores, CPUs, and GPUs to reduce the total computational time with the help of parallel RAM, cores, GPUs, etc. More details about parallelization can be found in the published literature (Pantalé, 2005; Krawezik and Poole, 2009; Li *et al.*, 2015; Tang *et al.*, 2020).

2.5 Constitutive material flow models

The FSW process observes high temperature and strain rate variations; therefore, the constitutive equations adapted for the workpiece must depend on both parameters. The majority of these changes are observed in the SZ of the workpiece. The stress tensor σ can be split into volumetric and deviatoric components as (Ulysse, 2002)

$$\boldsymbol{\sigma} = p\boldsymbol{I} + \boldsymbol{S} \tag{2.1}$$

where p is the pressure field and $\boldsymbol{S}$ is the deviatoric stress tensor. It is a common practice to consider a rigid visco-plastic material behavior using a rate-dependent law as given by (Santiago *et al.*, 2004)

$$\boldsymbol{S} = 2\mu_{eff}\dot{\boldsymbol{e}} \tag{2.2}$$

where μ_{eff} is the effective viscosity of the material and $\dot{e} = dev(\dot{\varepsilon})$ is the deviatoric part of the total strain rate $\dot{\varepsilon}$. In the FSW process, it is a common practice to neglect the elastic and the volumetric strain, and thus the total strain rate is purely deviatoric, such that

$$\dot{\varepsilon} = dev(\dot{\varepsilon}) = \dot{e} \tag{2.3}$$

Therefore, the deviatoric stress tensor can be modified as

$$\boldsymbol{S} = 2\mu_{eff}\dot{\varepsilon} \tag{2.4}$$

The definition of effective viscosity, μ_{eff}, determines the different constitutive characterizations to be adopted (Chiumenti *et al.*, 2013). The visco-plastic constitutive Norton-Hoff, Sheppard-Wright, and Johnson-Cook material models are widely used (de Saracibar *et al.*, 2014; N. Dialami, Cervera, *et al.*, 2017; Dialami, Cervera and Chiumenti,

2018). Most of the literature reports the application of the path-independent constitutive models for FSW modeling (Kuykendall, Nelson and Sorensen, 2013).

2.5.1 Norton-Hoff model

The Norton-Hoff model considers the μ_{eff} as a function of temperature as

$$\mu_{eff}(\dot{\varepsilon}_{eq}, T) = \mu(\sqrt{3}\,\dot{\varepsilon}_{eq})^{m-1} \tag{2.5}$$

and the equivalent plastic strain rate is evaluated as

$$\dot{\varepsilon}_{eq} = \sqrt{\frac{2}{3}}\|\dot{\varepsilon}\| = \sqrt{\frac{2}{3}(\dot{\varepsilon}:\dot{\varepsilon})} \tag{2.6}$$

where $0 \leq m(T) \leq 1$ is the temperature-dependent rate-sensitivity parameter. The m ranges between 0.1 and 0.3 in the case of FSW (Chiumenti *et al.*, 2013).

The Norton-Hoff model is an elastic-viscoplastic material model (Vakhrushev *et al.*, 2022). The Norton-Hoff model is widely used in the field of manufacturing (Eckerson, Liechty and Sorensen, 2008; Khan *et al.*, 2016). The Norton-Hoff model can be defined as (Zhang *et al.*, 2012)

$$\bar{\sigma} = p_2 \exp\{-p_1\varepsilon\}\sqrt{3}(\sqrt{3}\dot{\varepsilon})^{p_3}\varepsilon^{p_4} \tag{2.7}$$

where p_1, p_2, p_3 and p_4 are the material constants, $\bar{\sigma}$ is the flow stress, ε is the strain and $\dot{\varepsilon}$ is the strain rate. The term $(-p_1\varepsilon)$ incorporates the material softening behavior and the value constant value of p_1 can be varied to model the same. However, the effect of strain also needs to be incorporated for accurate estimation of the material flow. Therefore the modified Norton-Hoff model is given by (Zhang *et al.*, 2012)

$$\bar{\sigma} = \sigma_{0.2} + p_2 \exp\left(-p_1\frac{\varepsilon-\varepsilon^*}{\varepsilon^*}\right)\sqrt{3}(\sqrt{3}\dot{\varepsilon})^{p_3}\varepsilon^{p_4} \tag{2.8}$$

$$p_1 = A_0 + A_1T + A_2\dot{\varepsilon} + A_3 ln\dot{\varepsilon} \tag{2.9}$$

$$p_2 = A_4 + A_5T + A_6 ln\dot{\varepsilon} \tag{2.10}$$

$$p_3 = A_7 + A_8\dot{\varepsilon} + A_9 ln\dot{\varepsilon} + A_{10} lnT \tag{2.11}$$

$$p_4 = A_{11} + A_{12}T + A_{13} ln\dot{\varepsilon} + A_{14} exp\dot{\varepsilon} \tag{2.12}$$

where $\sigma_{0.2}$ is the yield stress and is assumed to be equal to the flow stress at which the stress-strain curve is no more linear. The material constant is determined with the help of

tensile test at different temperature strain rate ranges. The material constant for the Ti-6Al-4V is provided in Table 2.4.

Table 2.4: Material constants for Ti-6Al-4V for the Norton-Hoff model (Zhang et al., 2012)

p_1	p_2	p_3	p_4
$A_0 = 10.225$	$A_4 = 557.748$	$A_7 = -10.595$	$A_{11} = 10.237$
$A_1 = -0.008$	$A_5 = -0.457$	$A_8 = -5.424$	$A_{12} = -0.004$
$A_2 = -16.967$	$A_6 = 16.388$	$A_9 = 0.048$	$A_{13} = 0.068$
$A_3 = 0.272$		$A_{10} = 1.545$	$A_{14} = -4.833$

2.5.2 Sheppard-Wright model

The Sheppard-Wright model is a temperature and strain rate-dependent material deformation behavior based on the effective deviatoric flow stress proposed by Sellars and Tegart and modified by Sheppard and Wright (Sheppard and Wright, 1979; Lin *et al.*, 2011). The Sheppard-Wright model can be easily applied to the mechanical processes by incorporating the Arrhenius term comprising the free activation energy and the temperature term to accommodate the temperature variations encountered during various forming and machining processes. For the Sheppard-Wright model, the effective viscosity of the non-Newtonian fluid can be evaluated as (Dialami, Cervera and Chiumenti, 2018)

$$\mu_{eff} = \frac{\bar{\sigma}(T,\dot{\varepsilon})}{3\dot{\varepsilon}} \tag{2.13}$$

where $\bar{\sigma}$ is the flow stress, and $\dot{\varepsilon}$ is the strain rate. In this case the $\bar{\sigma}$ can be expressed as

$$\bar{\sigma} = \frac{1}{\alpha}\sinh^{-1}\left[\left(\frac{Z}{A}\right)^{\frac{1}{n}}\right] = \frac{1}{\alpha}\ln\left[\left(\frac{Z}{A}\right)^{\frac{1}{n}} + \sqrt{1+\left(\frac{Z}{A}\right)^{\frac{2}{n}}}\right] \tag{2.14}$$

where Zener-Holloman parameter Z is expressed as

$$Z = \dot{\varepsilon}\exp\left(\frac{Q}{RT_A}\right) \tag{2.15}$$

where α, A, and n are material-specific constants. T_A is the temperature on an absolute scale, Q is the activation energy, and R is the universal gas constant.

The Sheppard-Wright model allows for precisely calibrating the material properties between the ambient and the melting point temperature. This provides a significant advantage over the Norton-Hoff model as the temperature dependency in Norton-Hoff is introduced by temperature-dependent viscosity. However, neither of these models considers the thermo-elastic strains. As a result, these constitutive models cannot predict the workpiece's residual stress during the cooling cycle to the ambient (Chiumenti *et al.*, 2013). The material constants for various other materials as present in the published literature is provided in Table 2.5.

Table 2.5: Material constants for different materials reported in the literature for the Sheppard-Wright model.

Materials	Material constant				References
	$\ln A$ (s^{-1})	α (MPa^{-1})	n	Q (kJ/mol)	
Magnesium AZ31	20.47	-	4.36	129.00	(Tello, Gerlich and Mendez, 2010)
Titanium Ti6Al4V	15.18	-	3.60	176.00	(Tello, Gerlich and Mendez, 2010)
AISI 304	37.32	-	4.69	441.00	(Tello, Gerlich and Mendez, 2010)
Aluminium AA7050	22.85	0.0269	2.86	151.50	(Sheppard and Jackson, 1997)
Aluminium AA5083	23.11	0.015	4.99	171.40	(Sheppard and Jackson, 1997)
Aluminium AA6063	22.50	0.04	5.385	141.55	(Sheppard and Jackson, 1997)

2.5.3 Johnson-Cook material model

The Johnson-Cook model is a multiplicative model that follows the von-Mises flow stress (Johnson and Cook, 1985). The strain, strain-rate, temperature-dependent visco-plastic Johnson-Cook material model is expressed as

$$\bar{\sigma} = [A + B\,\bar{\varepsilon}^{n}]\left[1 + C\ln\left(\frac{\dot{\bar{\varepsilon}}}{\dot{\varepsilon}_0}\right)\right]\left[1 - \left(\frac{T - T_{room}}{T_{melt} - T_{room}}\right)^{m}\right] \quad (2.16)$$

where $\bar{\sigma}$ is flow stress, $\bar{\varepsilon}$ is the plastic strain, $\dot{\bar{\varepsilon}}$ is the effective strain rate, $\dot{\varepsilon_0}$ is reference strain rate ($1s^{-1}$), T_{room} is room temperature, T_{melt} is melting temperature, A is the yield stress of the material, B is strain hardening modulus, n is work-hardening exponent, C is strain rate hardening, and m is the thermal softening coefficient.

The determination of the material constants for the Johnson-Cook model is a herculean task and requires multiple experiments for torsion, tensile, and Hopkinson test data at various temperatures (Jain, Pal and Singh, 2017). However, this model can be easily incorporated into various numerical models. This law can fit over a wide range of strain, strain rate, and temperature values. The material constant varies for different materials (Kuykendall, Nelson and Sorensen, 2013). Moreover, the Johnson-cook model is developed, assuming the effects of thermal softening, strain, and strain rate hardening on the material flow are independent of each other. Certain modifications must be made to the conventional Johnson-Cook material model to predict the coupled effect of the temperature, strain effectively, and strain rate on the flow behavior during various manufacturing processes (Grujicic *et al.*, 2012; Wang *et al.*, 2020). The Johnson-cook material constant for some of the commonly used metallic alloys is provided in Table 2.6.

Table 2.6: Material constants for different materials reported in the literature for the Johnson-cook model

Materials	Material constant					Reference
	***A* (MPa)**	***B* (MPa)**	***n***	***C***	***m***	
Titanium VT6	900	509.75	0.506	0.03	-	(Buzyurkin, Gladky and Kraus, 2015)
Titanium OT4	600	528	0.386	0.03	-	(Buzyurkin, Gladky and Kraus, 2015)
Titanium OT4-0	500	353.9	0.508	0.04	-	(Buzyurkin, Gladky and Kraus, 2015)
Aluminium A356	270	155	0.28	0.018	1.43	(Gupta, Abotula and Shukla, 2014)
Aluminium A357	313	184	0.27	0.014	1.55	(Gupta, Abotula and Shukla, 2014)

Aluminium F357	319	203	0.27	0.022	1.55	(Gupta, Abotula and Shukla, 2014)

2.5.4 Heurtier law

Heurtier's law is a thermo-mechanical material model capable of predicting the temperature strain and strain-rate variations during FSW (Valvi *et al.*, 2016). The kinematical modeling is performed considering three types of material flows in the SZ, namely, the circumventing, vortex, and torsion velocity fields. Therefore, the velocity field is obtained as (Heurtier *et al.*, 2006)

$$u = V\left[1 - a^2\frac{x^2-y^2}{(x^2+y^2)^2}\right] - \frac{kz}{T^2+z^2}\frac{(\cos\phi)1}{\sqrt{x^2+y^2}} - yV_{tor2}\frac{z}{L_2} \tag{2.17}$$

$$v = V\left[-\frac{2xya^2}{(x^2+y^2)}\right] - \frac{kz}{T^2+z^2}(sin\phi)\frac{1}{\sqrt{x^2+y^2}} + xV_{tor2}\frac{z}{L_2} \tag{2.18}$$

$$w = -\frac{kT}{T^2+z^2}\frac{1}{\sqrt{x^2+y^2}} \tag{2.19}$$

The heat generation due to the frictional heating is determined as

$$q = \frac{2\Pi}{3}\mu p\omega R_S^3 \tag{2.20}$$

where μ is the coefficient of friction, p is the normal pressure, ω is the angular velocity, and R_s is the tool shoulder radius. The heat generation due to the plastic heating is modeled as

$$\Delta T = \frac{K}{\rho C}\dot{\varepsilon}^{m+1}\exp\left(\frac{mQ}{R_G T}\right) \tag{2.21}$$

The value for σ is expressed as

$$\sigma = K\dot{\varepsilon}^{m}\exp\left(\frac{mQ}{R_G T}\right) \tag{2.22}$$

The material properties such as σ and K are determined by performing the conventional torsion tests.

2.5.5 Hansel-Spittel constitutive model

The Hansel-Spittel constitutive model is a multiplicative exponential model. The Hansel-Spittel thermo-viscoplastic material model is commonly used to model the bulk forming processes (Martínez, Coupard and Girot, 2006). The flow stress can be related to the temperature, strain, and strain rate as (Assidi *et al.*, 2010)

$$\bar{\sigma} = Aexp(m_1, T)\bar{\varepsilon}^{m_2}\dot{\bar{\varepsilon}}^{m_3}\exp\left(\frac{m_4}{\bar{\varepsilon}}\right) \quad (2.23)$$

$$\bar{\sigma} = \sqrt{\frac{3}{2}S:S} \quad (2.24)$$

$$\dot{\bar{\varepsilon}} = \sqrt{\frac{2}{3}\dot{\varepsilon}_{vp}:\dot{\varepsilon}_{vp}} \quad (2.25)$$

$$\bar{\varepsilon} = \int_0^t \dot{\bar{\varepsilon}}\, dt \quad (2.26)$$

where $\bar{\sigma}$ is the equivalent flow stress, S is the deviatoric stress component, $\dot{\bar{\varepsilon}}$ is the equivalent strain rate, $\dot{\varepsilon}_{vp}$ is the visco-plastic strain rate, $\bar{\varepsilon}$ is the equivalent strain, A_1,m_1, m_2, m_3, and m_4 are the material constants. The Hansel-Spittel material constants for some of the commonly used materials are provided in Table 2.7.

Table 2.7: Material constants for different materials reported in the literature for the Hansel-Spittel model

Materials	A (MPa)	m_1	m_2	m_3	m_4	References
42CrMo	2136.313	-0.00243	0.2315	0.1215	0.0001	(Chadha, 2018)
AA 6061	352.400	-0.00450	0.066	0.13	0.0024	(Assidi *et al.*, 2010)
HNi55-7-4-2	25900	-3360	-0.268	0.119	-0.016	(Liang *et al.*, 2020)

2.5.6 Discussion

Different constitutive models, such as the Sheppard-Wright, Norton-Hoff, and Johnson-Cook, allow for easy temperature-dependent material behavior adjustment. However, the Norton-Hoff model's temperature dependency is based on the utilization of temperature-dependent material viscosity. Moreover, neither the Sheppard-Wright nor the Norton-Hoff model considers the thermo-elastic strains. Therefore, neither of these models can predict the residual stresses in the body after the completion of the weld (Chiumenti *et al.*, 2013). The residual stress prediction becomes possible with the help of thermo-elasto-plastic models such as the Johnson-Cook and the Hansel-Spittel models (Aziz *et al.*, 2018). However, the Hansel-Spittel model over-predicts the temperature range close to the solidus temperature. It needs to be simplified to a Norton-Hoff viscoplastic model to eliminate the

constraints imposed by the Hansel-Spittel model and for good prediction of results under hot and cold conditions (Guerdoux and Fourment, 2009; Assidi *et al.*, 2010). To the best of the author's knowledge, the most commonly used material model for FSW modeling is the Johnson-Cook model due to its good result output, easy application, and availability with commercial software.

2.6 Friction models for FSW

The highest temperature observed during the FSW process is between 70-90% of the melting point temperature. Frictional heating generates 80-90% of the total heat generated. The transient heat conduction equation is expressed as (Sahu and Bag, 2021)

$$\boldsymbol{\nabla} \cdot (k(T)\boldsymbol{\nabla}T) = \rho C_p \frac{\partial T}{\partial t} \tag{2.27}$$

while the convective and radiative heat losses are governed by Eq. 2.28 (Fraser, Kiss and St-Georges, 2016)

$$q = h_{conv}(T - T_{amb}) + \omega\sigma_{sb}(T^4 - T^4{}_{amb}) \tag{2.28}$$

where k is thermal conductivity, C_p is specific heat capacity, h_{conv} is convective heat coefficient, ω is emissivity, σ_{sb} is Stefan-Boltzmann constant, T is the temperature variable, T_{amb} is ambient temperature. The heat is generated at the interface of the tool and the workpiece. The heat generation equation during FSW is given by (Fraser, 2014)

$$\partial Q = \omega_v \partial M = \omega_v r \tau_{contact} dA = \omega_v r^2 \tau_{contact} d\theta dr \tag{2.29}$$

$$Q = \int_0^{2\pi} \int_{R_p}^{R_s} \omega_v r^2 \tau_{contact} d\theta dr \tag{2.30}$$

where R_s is the radius of the shoulder, R_p is the radius of the pin, μ_f is coefficient of friction, ω_v is the angular velocity in rad^{-1}. The interfacial contact can be of sliding or sticking in nature. Most numerical models consider either fully sliding or fully sticking conditions (N. Dialami, Chiumenti, *et al.*, 2017). A fully sticking condition assumes shearing in the layer below the contact surface. During fully sticking conditions, the workpiece material may stick to the tool surface, provided that the frictional shear stress exceeds the yield shear stress (Durdanović *et al.*, 2009). Alternatively, a fully sliding condition assumes shear in the contact surface and is generally described by a friction law, viz. Norton's law, the modified Norton's law, the Coulomb's law, the modified Coulomb's law, the Tresca's law, the Orowan's law.

2.6.1 Norton's Friction Law

Norton's friction law is a visco-plastic friction law. Norton's law is widely accepted to model the manufacturing processes under hot forming conditions. Simultaneously, this law has found its application in FSW also (Fourment and Guerdoux, 2008; Assidi *et al.*, 2010; Narges Dialami *et al.*, 2017). The literature presented an excellent agreement of welding forces while modeling using Norton's friction law (Guerdoux, 2008; Guerdoux and Fourment, 2009). Norton's friction law can be expressed as (Guerdoux, 2008)

$$\boldsymbol{\tau}_s = -\alpha_f K(T, \bar{\varepsilon}) \|\Delta \boldsymbol{v}_s\|^{q-1} \Delta \boldsymbol{v}_s \tag{2.31}$$

where $\boldsymbol{\tau}_s$ is the frictional shear stress, $\Delta \boldsymbol{v}_s$ is the sliding velocity, α_f is the friction coefficient, q is the sensitivity to the sliding velocity. The material parameters, i.e., α_f and q are temperature dependent. The sliding velocity $\Delta \boldsymbol{v}_s$ is expressed as (Assidi and Fourment, 2009)

$$\Delta \boldsymbol{v}_s = (\boldsymbol{v} - \boldsymbol{v}^t) - [(\boldsymbol{v} - \boldsymbol{v}^t) \cdot \boldsymbol{n}]\boldsymbol{n} \tag{2.32}$$

Norton's law depends upon the tool's sliding velocity over the workpiece. Thus the $\boldsymbol{\tau}_s$ is proportional to the distance from the tool rotational axis.

2.6.2 Modified Norton's Friction Law

The need to modify the conventional Norton's Friction Law arises because the pressure distribution around the tool is non-uniform. However, there is no parameter in the conventional model to account for the same. Therefore, the modified model considers a consistency parameter that is a function of the actual position of each point at the tool-workpiece interface with respect to the rotation axis and the traverse velocity. The modified Norton's Friction Law, as presented by Dialami et al. (N. Dialami, Chiumenti, *et al.*, 2017), is represented as

$$\boldsymbol{\tau}_s = a(x, T) \|\Delta \boldsymbol{v}_s\|^q \boldsymbol{n} \tag{2.33}$$

The consistency parameter a is expressed as

$$a(x, T) = 0.5 \left(a_{max}(T) + a_{min}(T) + \left(a_{max}(T) - a_{\min}(T)\right) \tanh \frac{x}{\frac{R}{6}} \right) \tag{2.34}$$

where R is the shoulder radius, x is the distance of each point located at the tool-workpiece interface from the tool rotation axis.

2.6.3 Coulomb's Friction Law

Coulomb's law is one of the most widely used friction laws to model engineering problems. The law states that when two solid bodies are in contact and are sliding with respect to each other, the frictional shear stress is directly proportional to the normal compressive force. The constant of proportionality is termed the coefficient of friction. Coulomb's law can be expressed as

$$\tau_s = \mu p \tag{2.35}$$

where τ_s is the frictional shear stress, μ is the constant of proportionality and p is the normal compressive force. The coefficient of friction in the published literature is defined as either constant, temperature-dependent, a function of slip rate, or a function of radial distance from the tool rotation axis (Nandan *et al.*, 2007; Alfaro *et al.*, 2009; Aziz *et al.*, 2016; Constantin, Nițu and Bădulescu, 2019; Iordache *et al.*, 2021). Some of the commonly used Coulomb's friction factors in published literature are provided in Table 2.8.

Table 2.8 Various friction factors reported in the literature for Coulomb's law

Material	μ	References
AA 1100 - Cu	0.60 - 0.20	(Yaduwanshi, Bag and Pal, 2016)
AA 6061	0.30, 0.58, 0.80	(Al-Badour *et al.*, 2013)
AA 6061 – AA 5083	0.80	(Al-Badour *et al.*, 2014)
AA 6061 – Cu	0.5	(Karrar *et al.*, 2022)

2.6.4 Modified Coulomb's Friction Law

The modified Coulomb's law professes the introduction of a critical shear stress limit (τ_{CRSS}) to limit the maximum frictional stress (τ_s). The modified law ensures that beyond the τ_{CRSS} value, the τ_s is constant and not a product of the friction coefficient and contact pressure. Conventionally, the τ_{CRSS} is calculated as (Zhang and Chen, 2008; Meyghani, Awang and Wu, 2020)

$$\tau_{CRSS} = \frac{\sigma_s}{\sqrt{3}} \tag{2.36}$$

where σ_s is the yield strength of the material.

2.6.5 Tresca's Friction Law

Tresca's Friction Law is a rigid plastic constitutive law. The frictional shear stress is related to the von Mises equivalent shear yield stress (σ_y) as (Jacquin *et al.*, 2011)

$$\boldsymbol{\tau}_s = \bar{m}\frac{\sigma_y}{\sqrt{3}} \tag{2.37}$$

where $\boldsymbol{\tau}_s$ is the frictional shear stress, and $\bar{m}$ is the shear friction factor. As the shear stress depends on the yield stress only, the heat generated by friction, in this case, is dependent only on the material yield strength (Tongne *et al.*, 2015). Jacquin et al. (Jacquin, Desrayaud and Montheillet, 2007) investigated that Tresca's law quantifies the shear stress at the tool-workpiece interface better than Coulomb's law. Some of the commonly used Tresca's friction factors in published literature are provided in Table 2.9.

Table 2.9 Various friction factors reported in the literature for Tresca's law

Material	$\bar{m}$	References
AA 7449	0.3	(Jacquin, Desrayaud and Montheillet, 2007)
AA 7075	0.46	(Buffa, Fratini and Shivpuri, 2008)
AZ 91	0.4	(Asadi, Mahdavinejad and Tutunchilar, 2011)
Copper	0.4	(Pashazadeh and Teimournezhad, 2014)

2.6.6 Orowan's Law

Orowan's friction law combines Tresca's and Coulomb's friction laws. The graphical representation of the different friction laws is presented in Fig. 2.20. The modeling of the FSW process with Orowan's law allows for a material slip at the tool-workpiece interface. The shear stress imposed at the interface can be evaluated as (Maekawa, Kubo and Childs, 2001)

$$\boldsymbol{\tau}_s = \bar{m}k\left[1 - e^{-\left(\frac{\mu\sigma_n}{k}\right)^a}\right]^{\frac{1}{a}} \tag{2.38}$$

where $k = \frac{\sigma_y}{\sqrt{3}}$, σ_n is the normal stress, μ is the coefficient of friction, and a is a constant.

Assuming that the normal forces are large, Eq. 2.38 simplifies to Tresca's law, whereas, considering a small normal force, Eq. 2.38 gets modified to represent Coulomb's law. This indicates that the sliding between the bodies starts due to Coulomb's friction, whereas as the traction increases, the flow continues due to Tresca's friction (Aydin *et al.*, 2000). Orowan's law allows for simultaneous high and low shear stress regions in the model, i.e., the regions with significant and negligible material flow (Liechty and Webb, 2008). The notable advantage of Orowan's law is the prediction of friction value close to the non-linear friction (Fig. 2.20c). This friction law is successfully modeled other manufacturing processes such as steel machining (Maekawa, Kubo and Childs, 2001), extrusion process (Aydin *et al.*, 2000), and drilling (Bonnet, Pottier and Landon, 2021). The combined Tresca and Coulomb's law can be summarised as provided in Table 2.10.

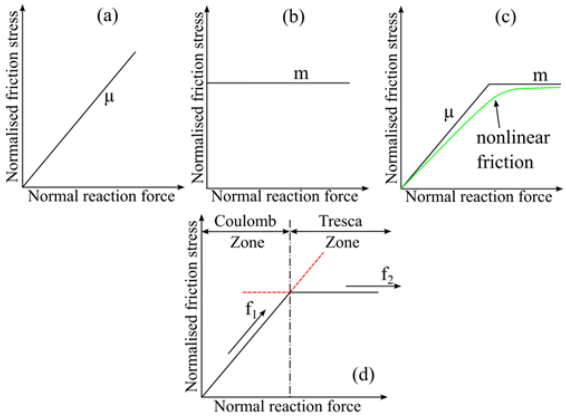

Fig. 2.20 Representation of the friction laws, (a) Coulomb's Law, (b) Tresca's Law, (c) Orowan's Law, (d) Transition between Coulomb's law and Tresca's law (recreated from (Aydin et al., 2000))

Table 2.10 The combination of Tresca's and Coulomb's law (Guerdoux, 2008)

Possibilities	If	Then
Case 1	$\lvert\mu\sigma_n\rvert < \bar{m}\frac{\sigma_y}{\sqrt{3}}$	$\boldsymbol{\tau}_s = -\mu\sigma_n$
Case 2	$\lvert\mu\sigma_n\rvert \geq \bar{m}\frac{\sigma_y}{\sqrt{3}}$	$\boldsymbol{\tau}_s = -\bar{m}\frac{\sigma_y}{\sqrt{3}}$

2.6.7 Discussions

The key difference between the various friction laws resides within the parameters that each law considers. Tresca's law is dependent on the shear strength of the material, whereas Norton's law is focused on the sliding velocity (Murillo-Marrodán, García and Cortés, 2017). Alternatively, Coulomb's law relates the normal force with the tangential contact force. The normal compressive stress in sheet metal forming is much smaller than in the bulk forming process. Therefore, Tresca's law provides a better result in bulk forming

processes, whereas Coulomb's law is preferred for sheet metal operations (Jain, Pal and Singh, 2017). The application of Coulomb's law with the critical shear stress allows to bound of the ever-increasing frictional shear stress with the conventional Coulomb's law. Moreover, the combination of multiple laws such as Orowan's law also allows to closely predict the nonlinear behavior of friction that may be encountered in nature. However, the combination of Coulomb and Norton's law does not produce a feasible result (Assidi *et al.*, 2010).

2.7 Role of tool and tool wear on defect formation

The welding tool is one of the integral components of FSW. The tool is in continuous contact with the workpiece and both the chemical and mechanical degradation of the tool is possible (De, Bhadeshia and Debroy, 2014). The tool used to weld stronger materials such as Steel, Titanium, and Inconel observed more wear compared to the tool used to weld Aluminium and Magnesium (Prater, 2011). Further, the FSW of the composites such as the SiCp/Al also causes serious tool wear due to the interaction of the hard carbide particles with the tool (Zuo *et al.*, 2022). Different types of tools with various shoulder and pin designs can be used for FSW (Rai *et al.*, 2011). The tool pin has a smaller dimension compared to the tool shoulder and therefore wears out easily compared to the tool shoulder. Sahlot and Arora (Sahlot and Arora, 2018) predicted the tool pin profile and tool wear using numerical modeling based on Archard's wear equation. The tendency of the tool to fail can be estimated with the help of a durability factor (Buchibabu, Reddy and De, 2017). Although different coating strategies have been employed on the FSW tool to improve its work life, however, the tool wear cannot be completely eliminated (Emamian *et al.*, 2020; Lacki *et al.*, 2020).

The tool wear can be either in the form of variation in the tool dimensions or in the form of tool material eroding due to friction. The material eroding out of the tool, mixes with the base material in the SZ, thus acting as a foreign particle inclusion with severely different material properties. These inhomogeneous particles cause severe microstructural changes in the SZ (Fall *et al.*, 2016). This can be responsible for the weakening of the joint and also the formation of defects in FSW. Alternatively, the change in the tool pin dimensions will significantly affect the material flow within the SZ. The pin dimension may vary due to the various forces acting on it during plunging in and welding stages or due to material adhesion. These factors significantly distort the shape of the tool primarily causing shoulder bulging, cup formation, groove formation, and mushrooming effect

(Siddiquee and Pandey, 2014; Ragu Nathan *et al.*, 2016). The change in the tool dimension at real time is difficult to be investigated experimentally.

Hasan et al. (Hasan, Bennett and Shipway, 2015) developed a CFD based model to predict the change in the material flow when a tool with and without wear is used. They observed a severe variation in the strain rate and velocity of the material near the weld root. They opined that this location can potentially act as a defect origination site. Moreover, other numerical strategies have also been devised to predict the tool wear evolution during FSW (Hasan *et al.*, 2017). However, it is realized from the literature that the investigation of the defect evolution due to tool wear is lacking and a conscious effort is made within the scope of the current work to fill this gap.

2.8 Characterization of defects through numerical simulation

There is considerable work done for the assessment of defects associated with FSW and allied processes through numerical simulation. Even the simulation techniques are capable of modeling the elimination of defects through the proper selection of process parameters. The sensitivity of the parameters to the weld quality acts as an indicator to define the feasible domain of defect-free weld. All these numerical models are calibrated to verify the experimental results. Hence, the development of simulation techniques based on the fundamental understanding can act as a mathematical tool or simulator for the prediction of process windows of defect-free weld. The process window to achieve a sound quality weld for ADC12 is depicted in Fig. 2.21. It is obvious that it needs a considerable amount of experiments and post-processing of the samples to define this process window.

The FSW defects are categorized primarily in three groups and critical reasons for the generation of these defects are identified. Excessive heat generation can lead to excessive material plasticization and material removal in the form of flash. The material removal can also

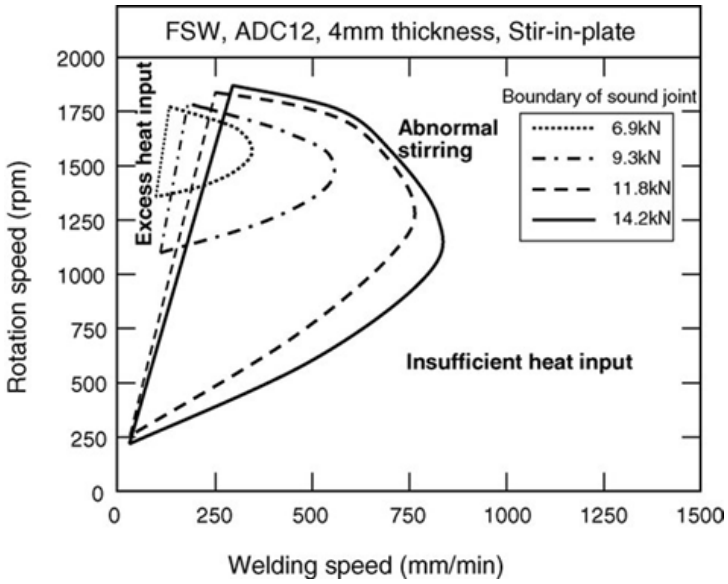

Fig. 2.21 Process window to achieve a sound quality FSW joint for ADC12 (Kim *et al.*, 2006)

lead to tunnel defect formation. Insufficient heat generation can lead to the formation of a cavity or groove-like defect and tunnel defect due to improper material deposition behind the tool. Abnormal stirring also leads to the formation of a cavity (Kim *et al.*, 2006). In general, the mechanism of defect formation is illustrated in Fig. 2.21 where a clear boundary between defective and non-defective weld is defined. The typical characteristics of FSW defects are presented in Fig. 2.22 (Arbegast, 2008). This experimental investigation of the FSW process can be financially daunting due to the requirements of materials and machinery. In contrast, the numerical modeling scheme can be a roundabout to this issue. However, the accuracy of defect prediction advances with the fundamental understanding of the cause and implementation of the same through advanced modeling techniques. Since the defect formation is associated with the thermo-mechanical behavior of the FSW process, there is a need to understand the material flow in the FSW process.

2.8.1 Material flow in FSW

The material flow within the SZ is probably the most important reason behind the formation of any type of defect. The ideal plastic or visco-plastic flow of the material is influenced by several factors such as tool pin geometry, tool rotation speed, traverse speed, and tool tilt angle. Moreover, the material flow is observed both above and within the workpiece surface. The flow of material at different elevations along the workpiece thickness is shown in Fig. 2.23 Either the flow can be out of the workpiece domain to form the flash or it can be deposition of the material behind the traversing tool to produce the weld. Fig. 2.24 shows the material flow at the tool periphery, i.e., the material in direct contact with the tool following the CEL approach. The flow of material around the tool and out of the workpiece domain can serve as important prediction criteria to determine the formation of defects such as flash due to material expulsion, tunnel, void, and cavity type defects due to the improper material flow and deposition behind the tool.

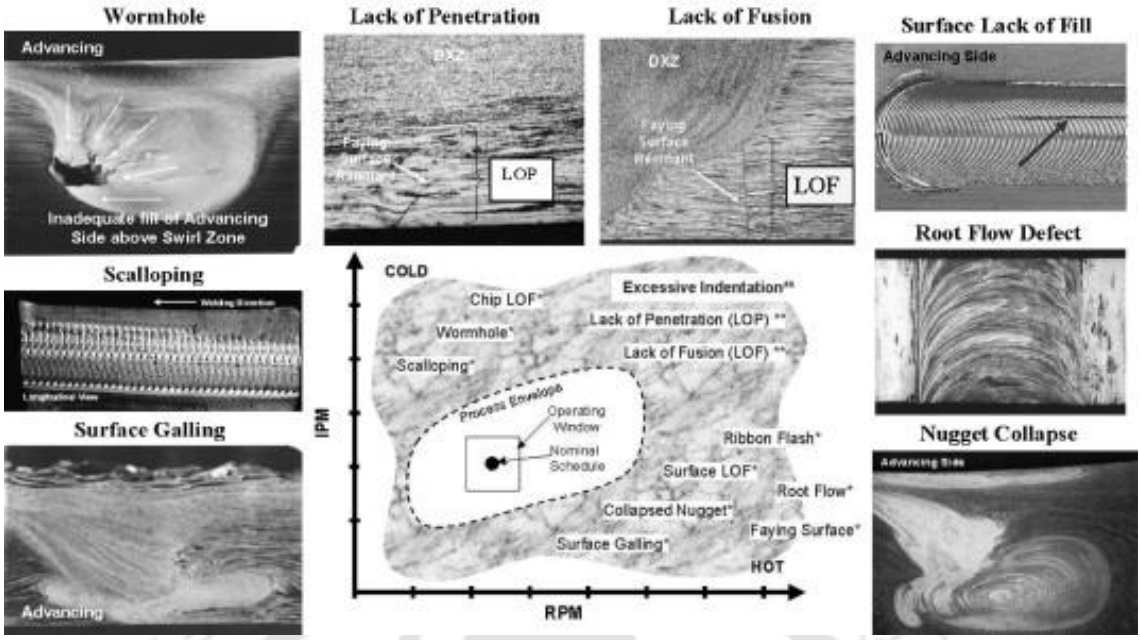

Fig. 2.22 Different defects of FSW (Arbegast, 2008)

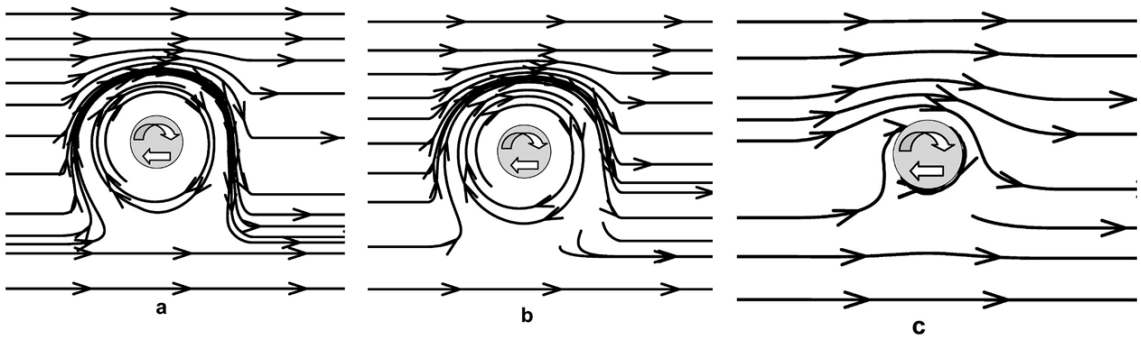

Fig. 2.23 Material flow at (a) z = 5.72mm, (b) z = 4.02 mm, and (c) z = 0.64 mm at 450 rpm and 0.42 mm/s (Nandan et al., 2007)

The CEL approach is used to model the flow of the material within the workpiece domain by Zhu et al. (Zhu *et al.*, 2017). The velocity of the material flow at the tool pin is higher in the case of the threaded and the threaded tri-flat tool pin (Fig. 2.25). The left-hand thread on the tool pin should be accompanied with a

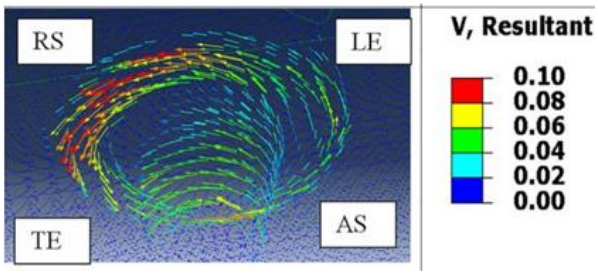

Fig. 2.24 Numerical representation of material flow velocity at the periphery of the tool where LE is the leading edge and TE is the trailing edge (Ajri and Shin, 2017). The velocity is measured in m/s.

clockwise rotation; otherwise, a reverse material movement would lead to more material expulsion (Jain, Pal and Singh, 2018).

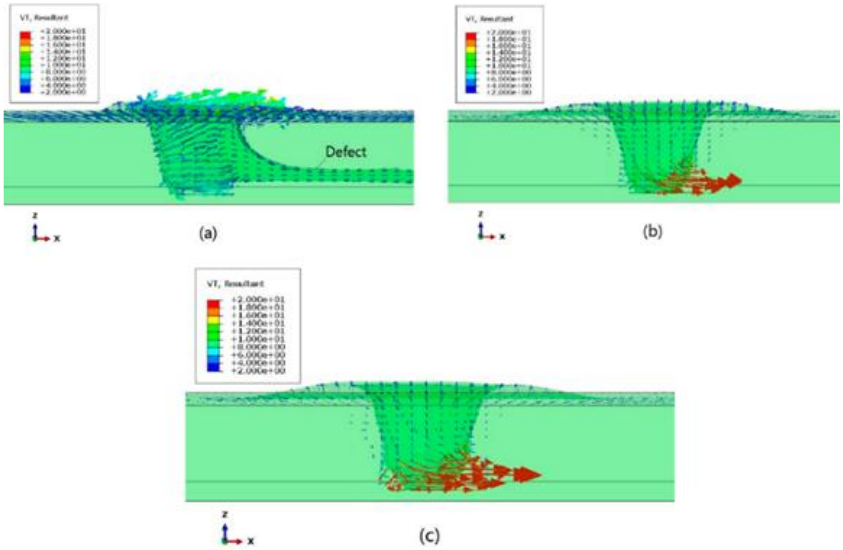

Fig. 2.25 Material velocity (mm/s) around the FSW tool using (a) smooth tool pin, (b) threaded tool pin, and (c) threaded tri-flat tool pin (Zhu et al., 2017).

The higher material flow in the case of the featured pins leads to a reduction in the defect size. Elangovan and Balasubramanian (K Elangovan and Balasubramanian, 2007) investigated the effect of the straight cylindrical, taper cylindrical, threaded cylindrical, square, and triangular pin on the weld quality and observed that the square pin produces the best quality weld. Further, the pulsating effect due to the shape of the pin also play a significant role in the efficient material movement (Jain, Pal and Singh, 2019). The pin profiles with flat surfaces viz. the triangular, square, and triflate pins produce a pulsating effect which is absent in the case of the cylindrical pins. The pulsating effect helps in better material movement and sound quality weld (K Elangovan and Balasubramanian, 2007; Khodaverdizadeh, Heidarzadeh and Saeid, 2013).

The tracer particles technology (Fig. 2.26) and ALE (Fig. 2.27) is used for predicting the material flow in the SZ at different process parameters. Fig. 2.26 shows the material flow and temperature distribution at the tool-workpiece interface. The observation of the tracer particles reveals the highest temperature just below the tool due to severe frictional heating and the temperature reduces near the periphery of the tool. Furthermore, it is revealed that the surface material in front of the tool is moved towards

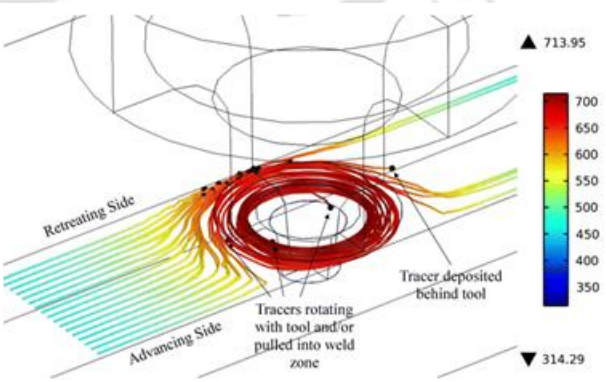

Fig. 2.26 Flow and temperature (K) behaviour of tracer particles when welding at 400 rpm (Hamilton et al., 2013).

the RS. The tracer particles can observe primarily three types of movements, i.e., the material can move along the tool shoulder and be deposited on the AS, deposited behind the traversing tool, or the material is trapped below the tool and is forged in the workpiece thickness direction. The temperature of the surface material is much higher than the mid plane materials. Moreover, the action of the tool on the workpiece material at the top surface is more predominant and the material observes a displacement in the thickness direction. However, the mid-plane material is found to rotate in the same plane indicating marginal movement of the mid plane material in the downward direction (Hamilton *et al.*, 2013). The flow of material as a function of the tool tilt angle is somehow different (Fig. 2.27). The effect of tool tilt is more evident near the tool-workpiece interface. The tool tilt ensures that the material is trapped below the tool and rotates easily with the tool. The material flows around the tool pin and is deposited behind the tool. The tool tilt has an accelerating effect on the workpiece material that is difficult to achieve without a tilt angle. The higher temperature and easy flow of the material due to the tool tilt angle can help to reduce the defect formation behind the traversing tool (Dialami, Cervera and Chiumenti, 2019).

2.8.2 Tunnel defect

The void defect is a commonly occurring sub-surface defect in FSW. The void defect can be defined as a loss of material within the workpiece bulk at a specified location. Unitary void defect or multiple voids are a possibility during FSW. The void defect with a continuous length is referred to as the tunnel or wormhole defect. The presence of the tunnel defect can be for a certain distance in the weld length or for the complete duration of welding. The tunnel defect mainly occurs due to a lack of material flow aided by insufficient heat generation leading to improper plasticization of materials. The defect is represented by the restriction of the velocity potential line.

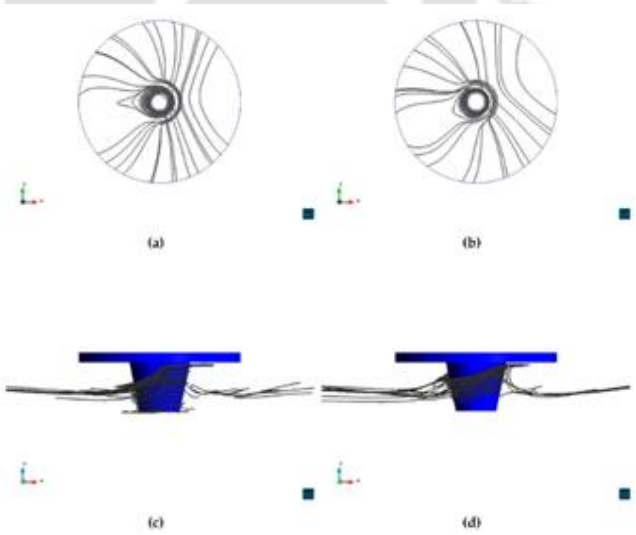

Fig. 2.27 Material flow paths in top and front view at depth of 3 mm for (a) and (c) tilt angle =0°; (b) and (d) tilt angle = 2.5° (Dialami, Cervera and Chiumenti, 2019)

Zhao et al. (Zhao *et al.*, 2019) developed a 3D CFD model based on Coulomb's friction law and the Sheppard-wright material model to predict the tunnel defect at cold welding conditions and cavity type defects at hot welding conditions for 12 mm thick 7N01 alloy. It was realized that improper material flow is a more predominant factor than the maximum temperature to develop the cavity defects. The formation of tunnel defect is explained by the high temperature zone (HTZ) bounded by the recrystallization temperature. A significant change in the HTZ size with variation in rotational speed could lead to the development of tunnel defects (Fig. 2.28). The widely adapted tracer particle technology is used to investigate the material flow in the computational domain that effectively leads to identifying any flow related defects. Multiple tracer particles were introduced in the computational domain to investigate any difference in the material flow in the workpiece, as shown in Fig. 2.29. However, the mass of the tracer particles is neglected to eliminate the effect of the tracer particle on the material flow field (Zhao *et al.*, 2019).

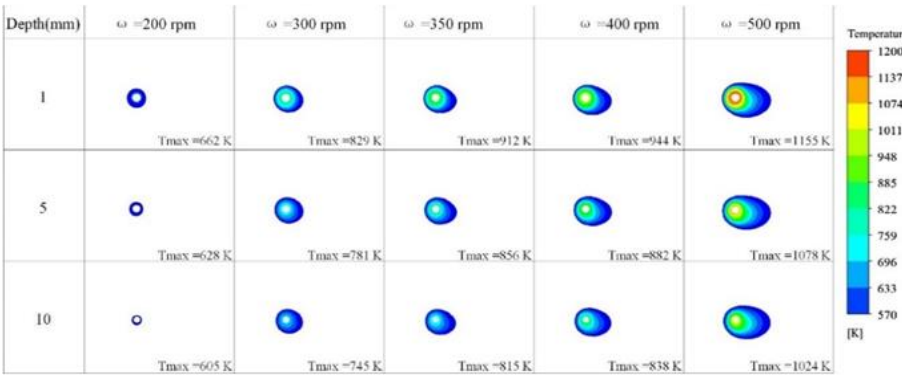

Fig. 2.28 Variation of HTR zone and peak temperature as a function of tool rotation speed (Zhao et al., 2019)

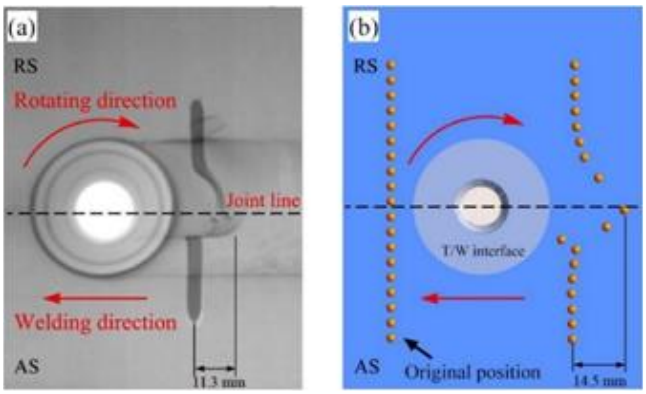

Fig. 2.29 Comparison of the marker material after welding by (a) computed tomography method and (b) CFD modeling (Zhao et al., 2019).

The tracer particle technology is also commonly used with the CFD, ALE, and CEL approaches (Grujicic *et al.*, 2010; Zhai, Wu and Su, 2020; Chu *et al.*, 2021; Kumar *et al.*, 2021) where the tracer particle path is defined based on the streamlines or directly from the velocity field. The tracer particles can be inserted either on one side of the workpiece or on both the AS and RS as per the need for tracking (Grujicic *et al.*, 2011).

Zhu et al. (Zhu *et al.*, 2016) observed the tunnel defect formation following a CFD model using Coulomb's friction law and the Sheppard-Wright material model. The location near the tool pin tip is predicted to be the most probable position for the generation of the tunnel defect. Due to the reduction in the frictional force near the tool pin tip; there is a reduction in the material flow. The reduced velocity leads to inappropriate material deposition and may increase the possibility of tunnel defect formation. To predict void defect formation, Coulomb's friction law and the Sellars-Mctegart constitutive model was employed in a self-reacting FSW process (Zhao and Liu, 2020, 2021). The TMAZ shifts towards the tool centre with an increase in the traverse speed, i.e., there is a significant reduction in the material flow in the TMAZ with an increase in traverse speed. The developed CFD model successfully predicts void defect formation when the traverse speed increases from 100 mm/min to 250 mm/min (Zhao and Liu, 2021). The void defect is generally observed to the AS of the weld centreline (Jia, Wu and Sun, 2022). However, there are instances in the published literature where the defect is observed on the RS (Fig. 2.30) due to rapid cooling and improper deposition of material to the RS. The formation of defects on the AS side is due to improper material flow, whereas the defect appearing near the joint root is due to reduced heat generated (Al-moussawi *et al.*, 2017; Huang *et al.*, 2018). The tracer particle with CFD elucidates the fact that most of the material is deposited behind the tool (Fig. 2.29). Only a small region on the AS near the tool pin experiences forward material movement whereas the complete RS observes negative material movement. A small amount of material is also observed to have moved in the depth direction (Zhao *et al.*, 2019).

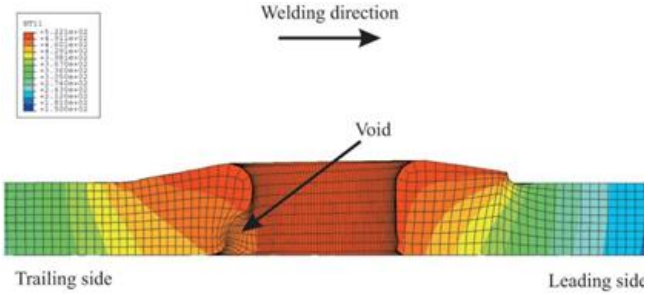

Fig. 2.30 Prediction of the void defect on the RS of the welding (Schmidt and Hattel, 2005).

Although the CFD approach predicts the flow behaviour directly from governing equations, the thermo-mechanical model also predicts the velocity field indirectly where the lack of material flow is relatively easier to represent. Schmidt and Hattel (Schmidt and Hattel, 2005) presented one of the initial examples of thermo-mechanical modelling of the FSW process using the ALE technique. Johnson-Cook material model and Coulomb's friction law for FSW of AA2024 aluminium alloy are used. The void defect was predicted on the RS of the workpiece, as shown in Fig. 2.30. The defect formation is affected by the heat loss coefficient from the bottom surface of the backing plate (Schmidt and Hattel,

2008). The heat loss coefficient of 1000 and 2000 $W\ m^{-2}K^{-1}$ was used in the investigation. The void defect was detected when modeling with the higher heat loss coefficient due to the formation of a colder matrix near the weld root. The higher convection coefficient rapidly cools down the material and restricts the proper material movement and deposition, leading the formation of the void defect.

The void defect was modelled using the CEL approach by Zhu et al. (Zhu *et al.*, 2017). The position of the void defect is shown in Fig. 2.31, which represents well with the experimental result. However, there is a discrepancy in the prediction of the shape of the void defect as it relies on several factors. The mesh size and material properties are the prime factors. The pin height is also responsible for the void defect formation near the bottom surface of the workpiece (Chauhan *et al.*, 2018). It was observed that a larger pin height removes the material, as limited volume is present for the material deposition. However, the void defect due to pin height can be reduced with the use of optimum pin height.

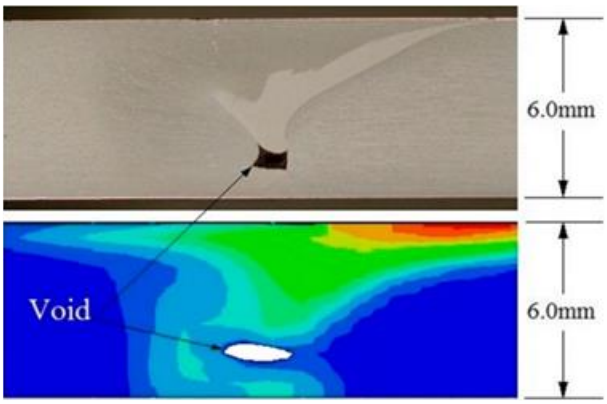

Fig. 2.31 Experimental and numerical comparison of the void defect estimation (Zhu et al., 2017).

2.8.3 Lack of penetration

The CEL approach is further extended to model the cavity (Fig. 2.32) and the root defects (Fig. 2.33) in dissimilar FSW. The cavity defect at a 1° tilt angle appears due to inadequate forging pressure (Choudhary and Jain, 2022). The inadequate pressure leads to insufficient plastic deformation and improper material flow. The cavity defect may look similar to the tunnel defect. The space left for material deposition due to the difference in the shoulder and pin driven flows leads to the formation of the cavity defect (Ajri and Shin, 2017). Zhao et al. (Zhao *et al.*, 2019)

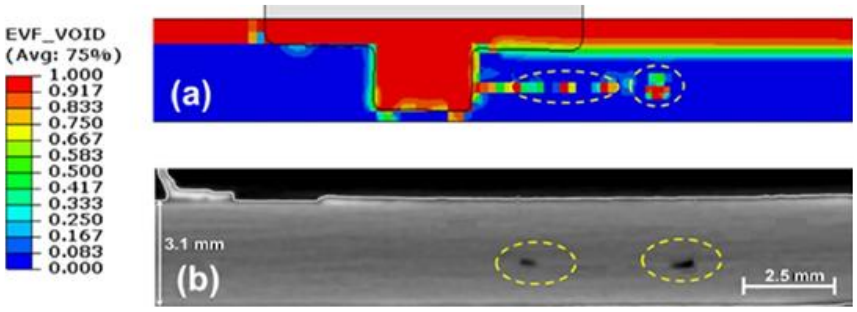

Fig. 2.32 (a) Numerical and (b) Experimental comparison of cavity defect formed at 900 rpm, 60 mm/min and 1° tilt angle (Choudhary and Jain, 2022).

investigated the formation of cavity defects as a difference in the rotational and longitudinal flow of material around the tool. As the difference in the flow is compensated by the tool shoulder compaction in the top half of the workpiece, the cavity defect is more likely to appear in the bottom half. They also concluded that the cavity defect occurs in hot welding conditions. The weld root defect originates between the end of the tool pin and the bottom surface of the workpiece.

The possible cause of root defect generation is improper plunge depth and pin height leading to a lack of filled material. The appearance of the root defect can also be traced to a low tilt angle. The main culprit for the formation of the root defect is the reduction in the material flow between the pin tip and the workpiece bottom surface. This can be rectified with the help of varying the tool shoulder and pin design. The use of a concentric circle flute shoulder reduces the occurrence of root defect (Ji *et al.*, 2012). Simultaneously, the use of a half screw and taper flute pin also reduces the root defect (Ji *et al.*, 2013).

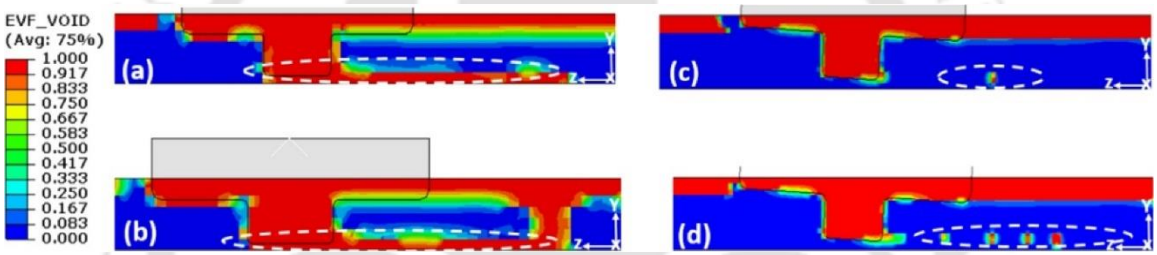

Fig. 2.33 Development of root defects at (a) 900 rpm, (b) 1200 rpm with a constant traverse speed of 90 mm/min and 0° tilt angle, (c) 600 rpm, 60 mm/min, 3° tilt angle and (d) 1200 rpm, 90 mm/min, 3° tilt angle (Choudhary and Jain, 2022)

2.8.4 Joint line remnant

Dialami et al. (Dialami *et al.*, 2019) pioneered the prediction of the JLR defect using the ALE approach with the help of the tracer particles. The tracer particles were introduced into the model as an oxide layer. Following their position after the welding completion helps predict the JLR defect, as shown in Fig. 2.34. Further, different tool geometries were also introduced to understand the effect of tool geometry on defect formation. The prediction of the JLR defect is a significant advancement in the study of defect prediction. The study is one of the first attempts to predict a defect due to a foreign impurity.

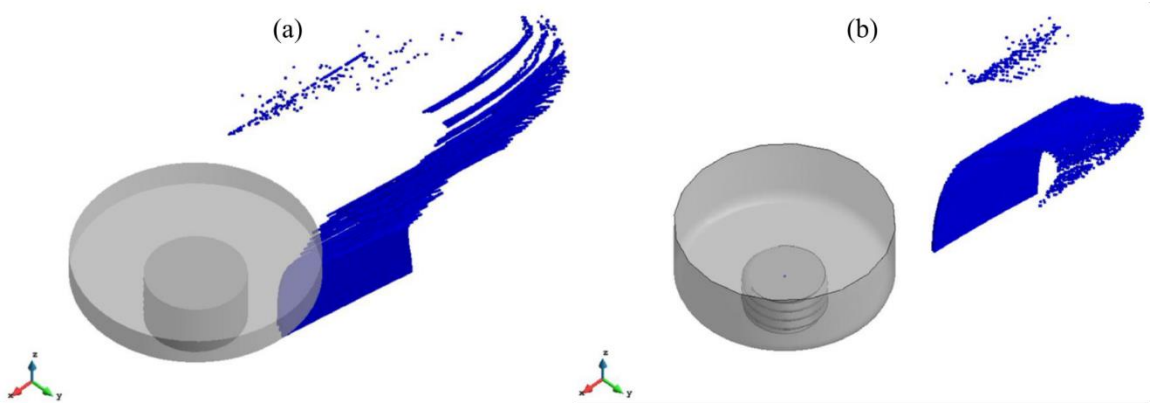

Fig. 2.34 The final position of the tracer particles post moving past (a) the conventional featureless FSW tool and (b) the cylindrical threaded tool (Dialami et al., 2019)

2.8.5 Hook defect

The hook defect appears predominantly in the friction stir lap welding. The numerical modelling of a typical hook defect is presented in Fig. 2.35. The CEL technique is used to model the material flow in both the top and the bottom plates. The Eulerian Volume Fluid (EVF) methodology coupled with the CEL technique is used to determine the partially and completely filled regions (Chu *et al.*, 2018). This in turn helps in the determination of the hooking defect. The effect of the process parameters such as dwell time is investigated numerically on the formation of the hook defect (Rana, Narayanan and Kailas, 2021). The literature review indicates that the CEL approach is a commonly used approach to model the FSSW process (Cao *et al.*, 2017; Wen, Li, Wang, *et al.*, 2019; Buffa *et al.*, 2020).

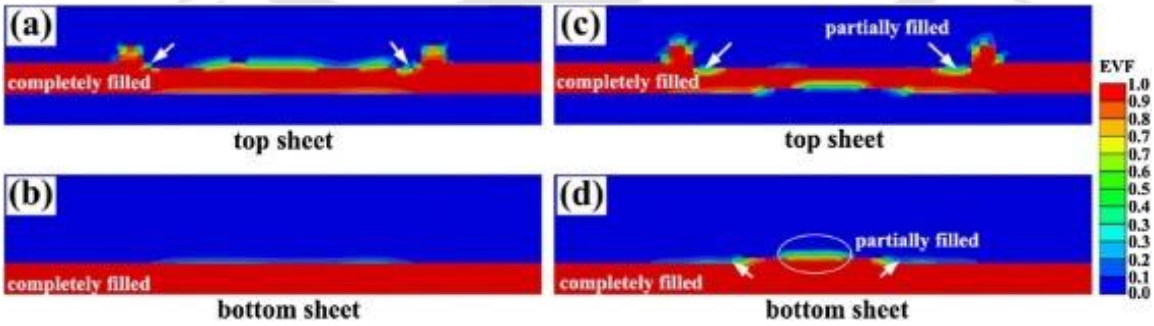

Fig. 2.35 Region of partially and completely filled materials at the top and bottom sheets at (a, b) 0.6 sec in the plunge stage, and (c, d) 6 sec in the dwell stage (Chu et al., 2018)

2.8.6 Other surface irregularities

The banded structure on the top surface of the SZ is a commonly occurring phenomenon in FSW. The periodic bands are a function of the rotation and the traverse

speed (Gratecap *et al.*, 2012). Many times the banded structure on the top surface is related to the onion rings observed at the weld cross section (Dialami, Cervera and Chiumenti, 2020). However, the onion rings are not always visible after FSW and their appearance depends on the welding conditions (Lee, Yeon and Jung, 2003). Although, some attempts have been made in the literature to numerically predict the cross-sectional banded structure as shown in Fig. 2.36 (Wen, Li, Gao, *et al.*, 2019; Dialami, Cervera and Chiumenti, 2020). However, sufficient progress has not been made towards the prediction of the surface banded structure.

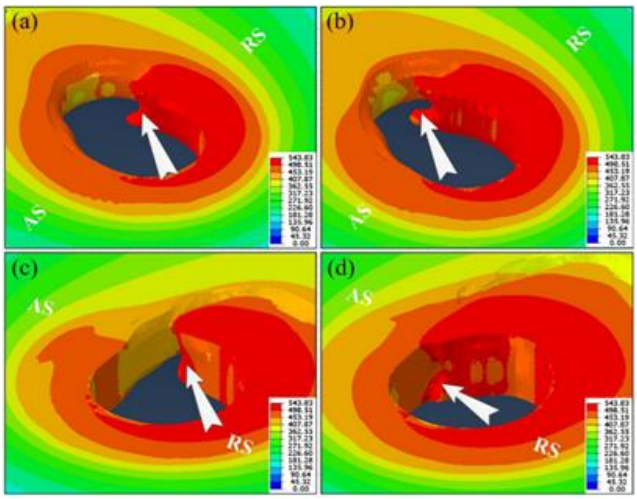

Fig. 2.36 Banded structure along the weld cross-section at different weld durations (Wen, Li, Gao, et al., 2019).

2.8.7 Residual stress

Residual stresses are the self-equilibrating forces remaining in the workpiece when all the external thermo-mechanical forces have been removed. The residual stress in the body varies due to the application of the various process parameters (Bachmann *et al.*, 2017).

Camilleri et al. (Camilleri, Micallef and Mollicone, 2015) developed a numerical model to investigate the distortion in 6 mm thin DH36 mild steel sheets due to the effect of the residual stresses. They concluded that the distortion increases with the increase in the welding speed due to the increased thermal gradient along the thickness direction and higher plunge forces. The hyperbolic parabolic shape of the distortion after FSW can also be correctly predicted (Paulo *et al.*, 2017). However, in FSW, while residual stresses can be present in the welded structure, the associated residual distortion is generally minimal (Zina *et al.*, 2019). The material deformation with elastic spring back and residual stresses can be modelled in the computational domain with the application of any of the viscoplastic, elasto-plastic, or elasto-viscoplastic material models (Guerdoux and Fourment, 2009; De Saracibar, 2019).

An ALE model is developed to investigate the effect of the varying process parameters on the residual stress distribution within a AA6061 plate (Riahi and Nazari, 2011). Furthermore, the novel SPH technique is also used to model the residual stresses at varying

process parameters as shown in Fig. 2.37 (Eivani *et al.*, 2021). The increase in the tool rotation speed increases the maximum temperature, thus resulting in a marginal decrease in the residual stress value from about 431 MPa to 405 MPa. The literature discloses the prediction of residual stress in different combinations of similar, dissimilar, and metal to composite sheets FSW (Nie, Wu and Gong, 2020; Zamani *et al.*, 2021). Further, the effect of the residual stresses on the mechanical properties is also estimated in the literature (Fratini, Macaluso and Pasta, 2009). The increase in the maximum temperature due to higher tool rotation speed causes a higher cooling rate and results in an increase in the residual stress (Geng *et al.*, 2022). However, the axial force and the welding speed have a more prominent effect on the residual stress compared to the tool rotation speed (Nie, Wu and Gong, 2020). When a tool offset is applied, it results in a shift in the location of maximum residual stress within the welded material. Specifically, the maximum residual stress moves towards the plate along which the tool was offset (Hou *et al.*, 2018). However, in case of no offset the maximum stress is generally observed towards the AS.

Figure 2.38 shows the stress distribution at the weld interface of AA5052-DP590 during lap FSW using the CEL approach (Geng *et al.*, 2022). A significant drop is observed between the aluminium to the steel side for the equivalent and longitudinal stress. However, the drop is not as significant in the case of transverse stresses. The laser peening strategy can be used to increase the strength of the FSW welded sample. A numerical modelling strategy is disclosed in the esteemed literature capable of predicting the residual stress in the body for the FSW and LP hybrid manufacturing process (Li *et al.*, 2022). The majority of the models discussed till now primarily consider the thermo-mechanical modelling approach; however, these models can be further improved by incorporating the metallurgical changes to the applied load. Feng et al. (Feng *et al.*, 2007) developed a thermo-metallurgical-mechanical model to predict the residual stress formation and its resulting effects on the microstructure of the base material. They considered the similar FSW of AA6061 plates having a thickness of 6.35 mm. They observed that both the transverse and longitudinal stresses are tensile in nature, and the location of the peak stress falls in the HAZ. The longitudinal residual stress is more dominant compared to the transverse residual stress (Zhang and Zhang, 2009). The developed thermo-metallurgical-mechanical model was further used to predict the behaviour of the welded samples under different loading conditions.

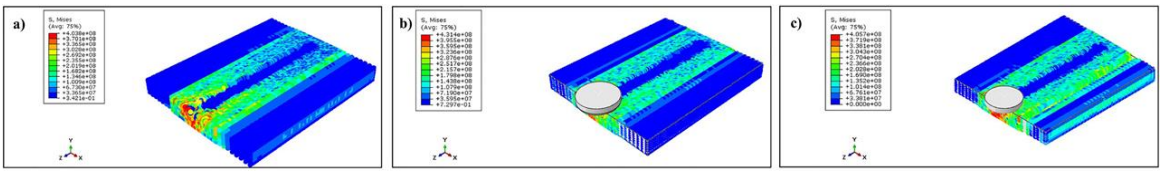

Fig. 2.37 Predicted residual stress in the welded sample at a traverse speed of 100 mm/min and rotation speed of (a) 100 rpm, (b) 50 rpm, and (c) 150 rpm (Eivani et al., 2021)

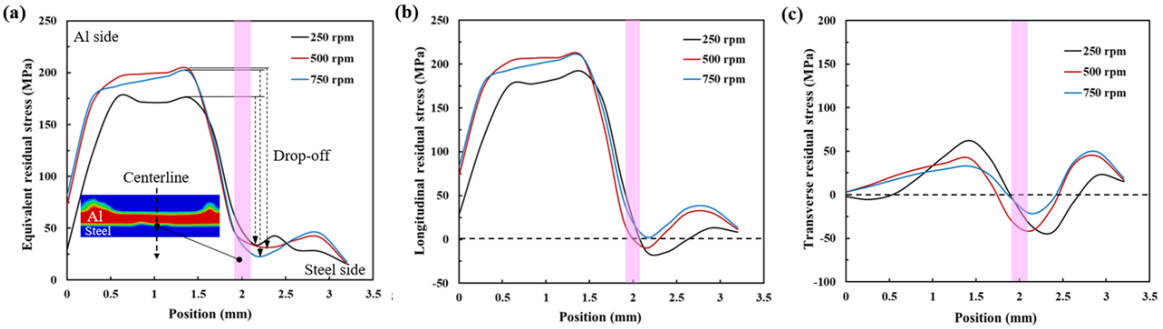

Fig. 2.38 The effect of varying process parameter on the residual stress distribution at the interface of dissimilar Al-Steel lap FSW for (a) equivalent stress, (b) longitudinal stress, and (c) transverse stress (Geng et al., 2022)

2.8.8 Intermetallic compounds

The formation of the IMCs and their primarily brittle nature is one of the most commonly occurring defects in dissimilar FSW affecting the weld quality. Moreover, the functionality of the welded sample can be further affected due to the varied material properties of the IMCs (Chen *et al.*, 2021). The common thermo-mechanical modelling of the FSW process is incapable of predicting the IMCs formation. However, coupling of the thermo-mechanical macro model can be done with the diffusion based micro model to numerically predict the formation of the IMCs during dissimilar FSW of Al and Mg (Yang, Wu and Zhao, 2021). The variation in the predicted thickness of the IMCs during FSW at different process parameters is shown in Fig. 2.39. It was observed that the dislocation density played the dominant role in IMCs formation during the plastic deformation stages. In contrast, the temperature is the principal factor for IMCs generation at the conclusion of the plastic deformation.

Grujicic et al. (Grujicic *et al.*, 2019) postulated that the conventional thermo-mechanical models are adequate for similar FSW; however, such modelling technique is not sufficient to obtain a clear picture of the dissimilar FSW joints. Therefore, they strategized a multi-scale approach that combines the output of a thermo-mechanical model with quantum-mechanical, atomistic, and thermodynamic analysis to predict the formation and growth of IMCs in dissimilar FSW of pure aluminum and AISI 1005 low carbon steel.

The thermo-mechanical model provides information about the temperature distribution, stress, and strain in the welded materials during the FSW process. This data serves as a precursor for the subsequent analysis of the IMC formation. The quantum-mechanical analysis focuses on the electronic structure and bonding behaviour at the atomic level, providing insights into the thermodynamic stability of the IMCs. The atomistic analysis considers the interactions between individual atoms and their arrangement in the IMCs. This helps in understanding the nucleation and growth mechanisms of the IMCs. Additionally, the thermodynamic analysis assesses the interfacial energy, growth rate, and volume fraction of the different IMCs formed during the dissimilar FSW process. Figure 2.40 represents the presence, spatial distribution, and concentration of different Fe_mAl_n IMCs formed during dissimilar Fe-Al FSW.

An indirect approach is also disclosed in the literature wherein the thermal output of the FEM approach is used to determine the temperature in the body and is coupled with the binary phase diagram to predict the IMCs formation (Karrar *et al.*, 2022). The majority of the IMCs prediction models disclosed in the literature are classical diffusion based models. These models can provide accurate prediction results for conventional welding processes however, these models will face limited success while predicting the IMCs during dissimilar FSW due to ignoring the effect of the significant material velocity encountered during FSW. Consequently. Momeni and Ni (Momeni and Ni, 2020) propose an approach where the diffusion model is coupled with the material flow velocity to accurately predict the IMCs layer thickness.

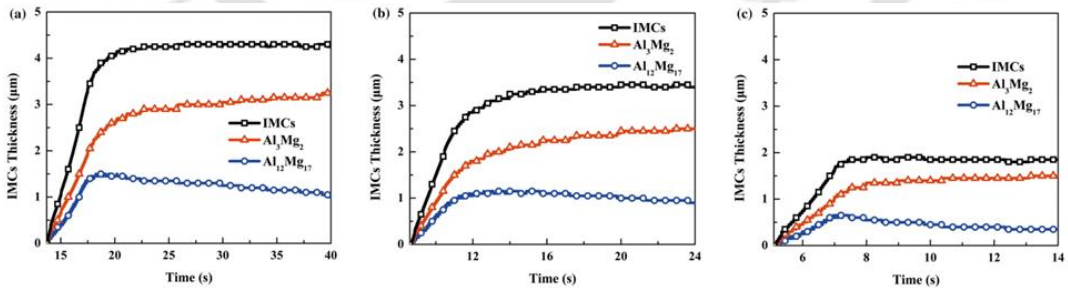

Fig. 2.39 Numerical prediction of the IMCs thickness variation for Al/Mg FSW at 800 rpm and (a) 30 mm/min, (b) 50 mm/min, and (c) 80 mm/min (Yang, Wu and Zhao, 2021)

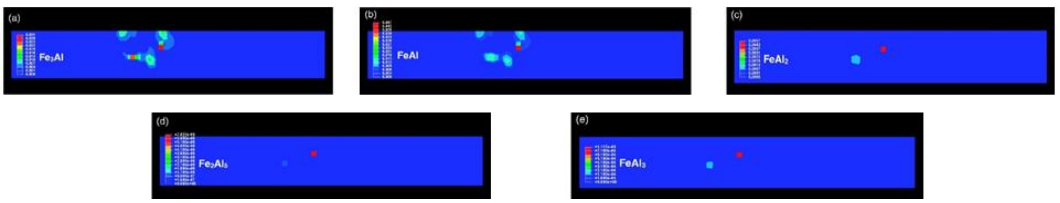

Fig. 2.40 Representation of the spatial distribution of the volume fraction of the (a) Fe_3Al, (b) $FeAl$, (c) $FeAl_2$, (d) Fe_2Al_5, and (e) $FeAl_3$ (Grujicic et al., 2019)

2.8.9 Exit hole

The appearance of the exit hole can be different for different types of FSW tools. The exit hole is a circular region of dimensions similar to that of a tool pin when a conventional tool is used, whereas a region of abruptly filled material is formed both at the entry and exit regions when using a bobbin tool. Although the exit hole defect is a commonly occurring feature in FSW, very few numerical investigations discuss the modelling and mitigation strategies of this defect. The exit hole defect is an immitigable defect during the welding process; however various post processing approaches are used to eliminate the defect. Chen et al. (G. Chen *et al.*, 2019) developed a CFD model to analyse the proficiency of the retractable pin tool FSW technique to eliminate the exit hole defect. Further, the CFD model can also be utilised to study the flow behaviour and deposition of material between the AS and RS around the exit hole (Chen *et al.*, 2018). Fraser et al. (Fraser, 2014) employed the SPH technique to model the entry and exit defects during FSW with the bobbin tool as shown in Fig. 2.41. The modelling of this defect with the bobbin tool is of special significance as the bobbin tool generates this defect both at the initiation and conclusion of FSW. As the only way around this defect is the elimination of the unfilled region, a significant portion of the weld length is rendered unusable leading to significant material wastage.

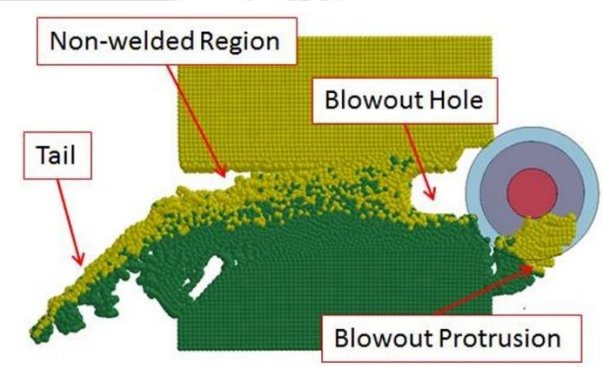

Fig. 2.41 Numerical investigation of entry and exit defects with bobbin tool (Fraser, 2014).

2.8.10 Excessive flash

The flash formation is one of the most commonly occurring phenomena during FSW. Due to the material removal in the form of a flash, the thickness of the actual workpiece reduces, thus weakening the final joint. The tool plunging action at the initiation of the FSW is responsible for pushing the material out of the workpiece domain to form the flash around the tool. High tool rotation speed and reduced tool traverse speed also aid in the flash formation due to the generation of excessive heat (Fig. 2.42). The optimal geometry of the tool shoulder plays a keen role in limiting the material flowing out of the SZ (Malik and Kailas, 2021). Further, featured shoulder designs such as the concave tool shoulder temporarily act as an expelled material reservoir and direct the material towards the tool

pin thus restricting the flash formation (Scialpi, De Filippis and Cavaliere, 2007; Kunnathur Periyasamy, Perumal and Kunnathur Periyasamy, 2019). Aval et al. (Jamshidi Aval *et al.*, 2011) investigated the effect of different tool pin geometry on the surface finish and flash formation to observe that pin design does not significantly affect the flash formation.

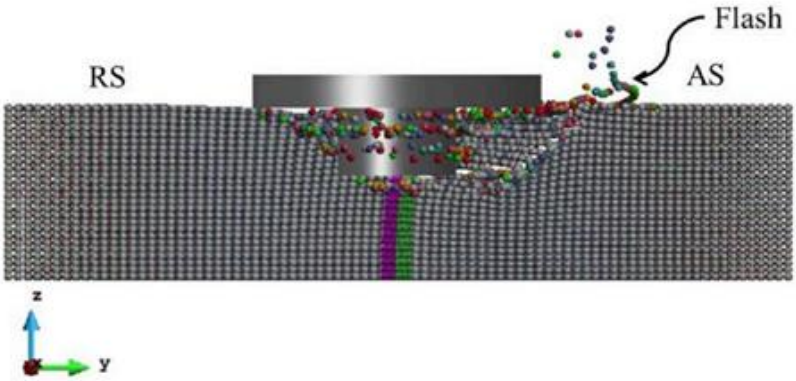

Fig. 2.42 Flash formation due to excessive heat generation on the AS (Dialami, Cervera and Chiumenti, 2020).

2.9 Characterization of defects through ML algorithms

The most beneficial advantage of the solid-state FSW process is the low range of temperature and, thus, a small amount of residual stress evolution compared to fusion welding processes (Carlone and Palazzo, 2015). Therefore, the investigation of temperature and the progress of residual stress is of utmost important as these parameters collectively decide the fatigue life of a weld structure (Barsoum and Barsoum, 2009). The welding of dissimilar materials poses a major challenge due to discontinuity in the mechanical and metallurgical properties of the base materials (Çam, Javaheri and Heidarzadeh, 2023). This further creates the issues of determining optimum process parameters leading to the formation of different types of macroscopic defects and the formation of intermetallic compounds (Liu, Ren and Liu, 2014; Sahu *et al.*, 2016). Improper heat generation significantly affects the residual stress generation and distortion of the welded structure (Shi *et al.*, 2008; Yan *et al.*, 2011). Therefore, it is extremely important to investigate the parameters affecting heat evolution and its

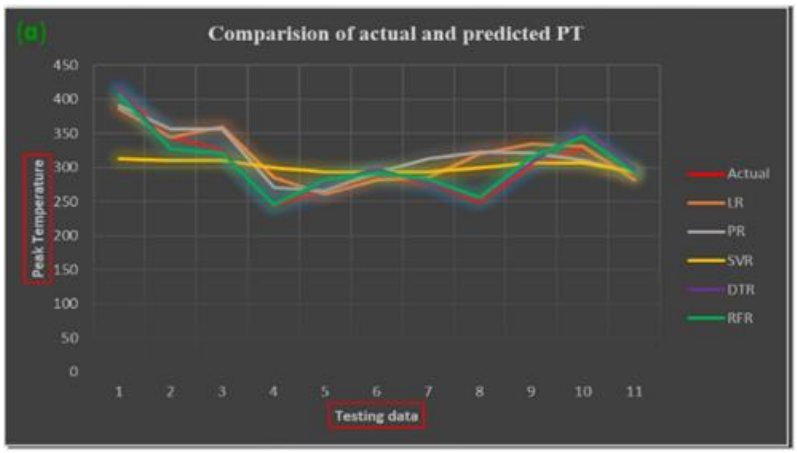

Fig. 2.43 Comparision between the actual and ML prediction peak temperature when performing FSW of AA7050 and AA2014A (Anandan and Manikandan, 2022).

effects on residual stress formation. The application of ML for the analysis of FSW opens an expeditious approach for the prediction of joint quality (Das, Pal and Bag, 2016a, 2017a).

Some of the key aspects that are investigated with the application of the ML in the FSW are the prediction of the mechanical properties of the joint, integration between the ML and the finite element models, real-time control of the FSW, and tool failure (Elsheikh, 2023; Guan *et al.*, 2023). Verma et al. (2022) applied Random Forest Regressor (RFR), M5P tree regression, and ANN to predict the tensile behavior of the welded joints. The RFR provided the best prediction with the least root mean square value of 6.72 MPa among the models. The joint strength of AA7475 and PPS polymer are also investigated with the help of ANN, support vector machine (SVM), and Gaussian process regression (GPR) to realize the ability of the SVM to perform the most effective prediction with an error limit of 5% (Sandeep and Natarajan, 2022). Anandan and Manikandan (Anandan and Manikandan, 2022) applied various ML algorithms, namely linear regression (LR), polynomial regression (PR), support vector regression (SVR), decision tree regression (DTR), and RFR to predict the peak temperature during similar and dissimilar FSW of AA 7050 and 2014A. The RFR is observed to have produced the best estimation for temperature evolution with an accuracy of about 90%. The temperature prediction by various ML algorithms is presented in Fig. 2.43.

Besides investigating mechanical strength and temperature evolution, ML algorithms are also applied to estimate tool failure and defective joints. Tool failure can be modelled and predicted with ~ 98% accuracy with the help of neural networks and DTR where the maximum shear and flow stresses are the most important causative factors for tool failure (Du *et al.*, 2020). The classification between sound and defective joints was performed with the help of ANN and a decision tree with an accuracy of ~ 95% (Ambrosio, Wagner, *et al.*, 2023). Figure 2.44 represents the classification of FSW joints where the ML model is capable of accurately predicting 44 cases of sound

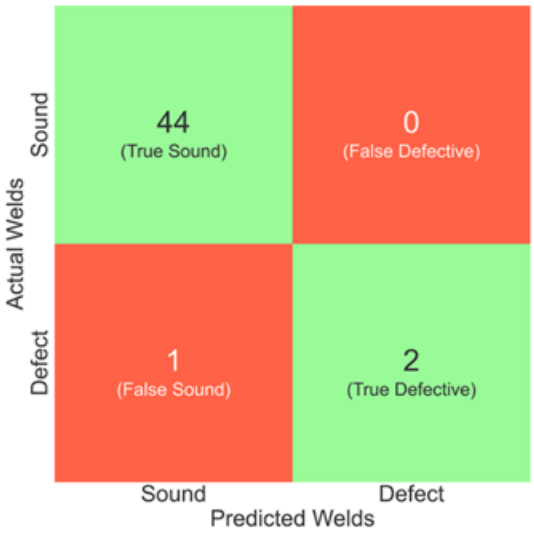

Fig. 2.44 The confusion matrix is used to classify between good and defective welding (Ambrosio, Wagner, *et al.*, 2023).

weld and 2 cases of defective weld, whereas in only one case the prediction gave a false positive result for a test case with 47 data points.

The residual stress is considered extremely deleterious for the weld quality. Various destructive and non-destructive techniques are utilized to measure the residual stress experimentally (Withers *et al.*, 2008). With the advent of numerical modelling strategies, the residual stresses can be evaluated for similar and dissimilar material combinations (Hattel, Sonne and Tutum, 2015). Further, different ML algorithms can also be used to model the residual stress, such as the M5 algorithm-based Model Trees Regression, RFR, SVR, Reduced Error Pruning Tree, Multi-layer perceptron, Instance-based k-nearest neighbor (KNN) algorithm (Das *et al.*, 2021). Mathew et al. (Mathew *et al.*, 2018) compared the ANN and adaptive neuro-fuzzy inference systems (ANFIS) for the prediction of residual stress in different welding methods to obtain superior prediction by the ANFIS model. The coupling of finite element based SPH technique with ANFIS can help to accurately predict the residual stress (Eivani *et al.*, 2021). The different ML algorithms can also be used in the additive manufacturing domain to accurately predict the residual stress and other defects associated with the process (Wu *et al.*, 2020; Du, Mukherjee and DebRoy, 2021). Multiple works are presented in the literature applying the different ML algorithms to predict weld quality. As the world is moving towards smart manufacturing and Industry 4.0, the application of ML for real-time process monitoring, prediction of thermo-mechanical responses, and defect prediction significantly increases the scope of FSW for real application (Mishra *et al.*, 2018, 2020).

2.10 Design and development of μ-FSW setup

The significant progress of the FSW process for the welding of different types of materials has led researchers to investigate the applicability of the FSW process for the welding of sheets with a thickness $\leq$1 mm. The researchers have already attempted the μ-FSW for the joining of sheets in various similar FSW of AA1060 (Zhang *et al.*, 2019), AA6061 (Liu, Fu and Chen, 2018), and dissimilar FSW of AA2024-AA6082 (Scialpi *et al.*, 2008), Al-Cu (Mao *et al.*, 2020). Although, the dissimilar μ-FSW is feasible; but in some case such as dissimilar μ-FSW of AZ31 and AA6061-T6 yields a relatively lower tensile strength of about 54% (Khalid, Shunmugasamy and Mansoor, 2022). Huang et al. (Huang *et al.*, 2017) observed that for the μ-FSW of AA6061 sheets of 0.5 mm thickness, 0.05 mm is the optimum plunge depth. The maximum strength of the joint was obtained to

be about 90%. Further, the taper triflat pin was used to obtain the highest strength of about 92% when welding 0.5 mm thick AA6061-T4 sheets (Huang *et al.*, 2019). The highest strength was obtained with the welding parameters of 6000 rpm and 1200 mm/min for 0.5 mm thick plate FSW of AA7075-T6 (Ni, Fu and Chen, 2019). The tensile strength of the welded joint increased with increasing the tool traverse speed between 300 mm/min and 1200 mm/min. The tool rotation speed to traverse speed ratio of 5 provides the highest tensile strength of about 90 %. The three-helix concave shoulder (THCS) provides the highest tensile strength compared to the concave shoulder (CS), and three-helix flat shoulder (THFS)) when μ-FSW of 0.8 mm AA6061-T6 (Liu *et al.*, 2020). The μ-FSW of 0.5 mm thick STS430M2 ferritic stainless stress reveals the suppression of the sigma phases that are responsible for the reduction in the toughness and ductility of the joint (Kim *et al.*, 2017). Although multiple research is performed in the domain of μ-FSW, the joining is performed majorly with the conventional FSW machines. The literature has not explored the design and fabrication of a dedicated μ-FSW setup.

A novel FSW setup has been disclosed in JP2005219092A (Ohashi *et al.*, 2004), in which the size of the setup can be miniaturized irrespective of the size of the workpiece to be welded. However, the aforementioned invention is focused on the welding of large plates while miniaturizing certain components of the setup. A portable type of FSW equipment is discussed in KR102033692B1 (Kang and Jung, 2018), which relates to FSW equipment, and more particularly, is installed inside a container that can be loaded on a truck, and can move quickly and conveniently to a work site, and work with large metal plates (such as wide plates) for FSW. This design cannot be used for thin sheet FSW. CN105665913A (Huihui *et al.*, 2014) exhibits a micro FSW setup for small-thickness components. The drawback of this equipment is the need for a high rotational speed between 5000 rpm and 27000 rpm of the tool spindle. As the rotational speed of the spindle is higher it would require a very sturdy and heavy body to absorb the reaction forces generated in the setup. This may hinder the portability of the equipment. Another portable FSW setup is disclosed in KR20140052807A (Kim, Kim and Joong-seok, 2013) that is easily portable in nature. However, the tool and the bed parts are integrated and therefore, a fault in either of the parts would cause the whole apparatus to be decommisioned.

2.11 Summary

There is a huge number of literature on FSW and allied processes discussing about a wide range of associated topics. The present work mainly targets the nature and type of different defect formations by means of experiments, and numerical modelling approaches, and different computational schemes. It is obvious that thermo-mechanical models with its own capability are available in the published literature to predict the different responses in the FSW process. A class of research work considers the tool-material interaction for modelling of FSW process. Hardly any model exclusively consider the free surface profile or lack of material flow to characterize different defect formation. The large deformation process considers either Eulerian or Lagrangian or some intermediate approach to model the thermo-mechanical behaviour of the FSW process by maintaining the energy balance equation. Hence various literature are reviewed to understand the approaches to be followed for a complete modelling of the FSW process.

The primary heat source in FSW is the frictional heating. The different frictional laws used to model the FSW process are Norton's law, modified Norton's law, Coulomb's law, modified Coulomb's law, Tresca's law, and combined Tresca's and Coulomb's laws. The Coulomb's law is the most utilised friction law in the literature. There are many instances where temperature independent Coulomb's coefficient of friction is considered. However, to improve the accuracy of the model many researchers have started utilising the temperature or slip rate dependent coefficient of friction. Furthermore, the utilization of the combination of laws such as Tresca's and Coulomb's law can help to improve the model accuracy further as the effect of both the normal and the shear stresses can be imported into the model simultaneously. The friction laws are used in combination with different material models to account for the flow of the material in the computational domain. The most commonly used material model is the Johnson-cook model due to its easy application and the accuracy in predicted results. The various other material models reported in the literature are the Norton-Hoff model, Sheppard-Wright model, Buffa law, Heurtier law, and Hansel-Spittel model. Numerous thermo-mechanical models following the CFD, ALE, CEL, and SPH approaches are disclosed in the literature. The numerical models can help develop a welding lobe with any combination of process parameters to achieve the desired results in a cost-effective manner. Further, these models are quite capable of predicting the various thermo-mechanical responses and material flow in the SZ. The understanding of the various responses and material flow can be further utilized to model the different surface and sub-surface defects in FSW.

The characterization of defects through numerical models is cumbersome until any specific computation scheme is followed. Hence the integration of the physical model with ML algorithms is a different approach where the physical model can be used to create huge discrete data points or convert it to a continuous profile. The physics-informed ML model is evolving for getting a quick prediction of defects in the FSW process. Few literature is directive to explore this area specific to the FSW process.

The conventional experiments on visualization of macro scale defect are well established where direct measurement of temperature and the shape and size of defects are usually used to validate the numerical simulation through calibration of the numerical model. However, with the reduction in sheet thickness, there develops several issues for a reduced scale FSW process. This problem needs to be addressed since very few works are reported in esteemed literature. An extensive literature review on the selected area is directive to define the scope of the present work.

2.12 Scope of Present Work

The literature survey highlights some key gaps through the investigation of FSW for Aluminium and Magnesium alloys. The scope of the present work is to predict through the classification of defective and non-defective welds for a set of process parameters by comprehensive process simulation. The elements of the present work are summarised as follows:

- There is a need of a thermo-mechanical model following the CEL approach to estimate the various temperature distribution and mechanical responses of the FSW process for a different set of process parameters and tool design. The validation of the numerical model through experiments where FSW of AA6061 is performed to evaluate the time-temperature history and the analysis of nugget shape and size.
- The utilization of a thermo-mechanical model to evaluate various surface and sub-surface defects occurred during the FSW of AA6061. The primary focus is to analyze the commonly occurring defects like tunnel defect, flash formation, partially failed joint, completely failed joint, and other surface irregularities. It is necessary to experimentally investigate the defects to ascertain the credibility of the model to predict the weld quality.
- The developed model is then utilised to classify the defective and non-defective welds that appeared during the FSW of AZ31B. The model is progressed to understand the variation in the time step increment and thus the total computational time for different

materials. This helps to gain an understanding of how the computational cost of the model will vary on the application of different materials.

- The mass scaling factor is utilised to reduce the total computational time with the CEL approach. The change in the evolution of various mechanical responses with the variation in the mass scaling factor is studied. Also, the determination of the mass scaling factors as a function of material properties is discussed in detail.
- The literature highlights the significance of dissimilar FSW of AA6061 and AZ31B. Therefore, the modelling approach is further improved to account for these dissimilar material combinations. The weld quality with varying process parameters, material mixing, and the effect of tool wear on the weld quality are numerically evaluated and experimentally estimated. The weld quality is estimated by investigating the presence and absence of various volumetric defects. The material mixing is investigated with the aid of FESEM-EDX analysis. The IMCs formation is determined with the assistance of XRD analysis and the tool wear is estimated both as a function of weight loss and change in the structural integrity of the tool.
- After an extensive literature survey and elaborate investigation into the developed numerical model, it is realised that the CEL based numerical model has several advantages, but it is limited to high computational time. Therefore, the numerical model is coupled with the ML algorithms to develop physics informed ML models to predict the various thermo-mechanical responses and defect formation in FSW. The utilization of the ML algorithms helps to rapidly and accurately predict the FSW responses.
- The survey of the μ-FSW process highlights that the process is still accomplished using the conventional FSW machine. These machines are bulky, have high energy requirements, and are not portable. Therefore, in the current scope of work, a portable μ-FSW setup is designed and developed.

Chapter 3

Experimental Investigations

3.1 General background

The FSW process is dominated by temperature generation and the material flow in the faying edges of the workpiece. The material mixing is more significant in the case of FSW due to the solid-state nature of the welding process. The experimental investigations are carried out in order to fundamentally generate a series of reliable data to perform a comprehensive validation of the computed results. The experiments are performed in a vertical milling machine with a maximum rotation speed of 1200 rpm. The Aluminium alloy AA 6061-T6 and Magnesium alloy AZ31B are used to perform similar and dissimilar FSW experiments. The said materials are selected due to their wide application in the automotive and aerospace industries due to their lightweight, good specific strength, and formability properties. A conventional FSW tool with either a cylindrical or conical pin is used for welding. The tool is made of H-13 tool steel due to its high strength and good wear resistance capabilities. In the present work, a numerical model is developed to estimate the formation of different surface and sub-surface defects. The developed numerical model is validated using a two-step approach. For the first step, the temperature evolution of the workpiece surface is measured, while for the second step, the residual stress in the welded joint is determined. The temperature measurement during the welding is performed with the help of an Infrared Gun of make TESTO 868. The residual stress measurement is performed using an XRD machine (make: Rigaku Technologies, model Smartlab). The main objective of the experimental investigation is to determine the formation of various

defects in a wide range of process parameters. The defects are experimentally analyzed to determine their spatial distribution and other geometric features. The geometric dimension of the defects is measured with the help of optical microscopes of make LEICA S6D and Nikon SMZ25. The FESEM (make: Sigma 300) and EDX (make: EDAX) are also used for compositional analysis of the material mixing of dissimilar AA6061-AZ31B FSW.

3.2 Materials

The FSW process comprises of the workpiece material and the tool material. The workpiece material is selected based on the expected application of the welded component. The tool material is selected in such a manner that it doesn't wear out quickly during FSW i.e. there are considerable differences in hardness values. Further, details regarding the selection of the workpiece and tool material are provided in subsequent sub-sections.

3.2.1 Substrate materials for FSW

The materials chosen for the current investigation are the AA6061 aluminium alloy, AZ31B magnesium alloy, AA1200 aluminium alloy, and H-13 tool steel. Among all the selected materials the AA6061 and the AZ31B are used to investigate similar and dissimilar FSW, whereas the AA1200 is used for the μ-FSW investigation. The major applications of the AA6061 and AZ31B are identified in truck bodies and frames, structural components, aircraft landing mats, and other lightweight applications. Further, the H-13 tool steel is used as the tool material for the FSW due to its high strength compared to the various aluminium and magnesium alloys (Singarapu, Adepu and Arumalle, 2015). Aircraft companies such as Boeing used magnesium for their aircraft (e.g., 737, 747, 757, and 767) to make thrust reversers (Hynes *et al.*, 2022). The AA6061-T6 and AZ31B in as received condition are used to perform FSW experiments. The dimensions chosen for the workpiece are $200 \times 80 \times 4\ mm^3$. The sample edges are prepared using emery sheets and acetone to achieve proper contact between the faying edges of both plates. The compositional analysis of both the materials in as-received condition is presented in Table 3.1. The AA6061 is heat treatable and precipitation hardened aluminium alloys with Mg and Si as its major alloying elements. The addition of the Mg and Si helps to improve the corrosion resisitance and prevents the formation of undesirable oxides on Al. The AZ31B are the magnesium alloys with good corrosion resistance. The Al and Zn are the major constituents of AZ31B at about 3% and 1%, respectively. The presence of about 3% of Al and 1% of Zn imparts the name

AZ31 to the alloy. The XRD pattern of the AA6061 and AZ31B is presented in Fig. 3.1. The measured XRD patterns are similar to what is observed in the published literature (Balakrishnan *et al.*, 2020; Mukunda *et al.*, 2023; Ye *et al.*, 2023). The AA6061 has a face-centered cubic (FCC) structure with the highest peak intensity at the (111) plane; whereas the AZ31B has a hexagonal close-packed (HCP) crystal structure with the highest intensity at (10 $\bar{1}$1) plane.

Table 3.1 Chemical composition (wt %) of AA6061-T6 and AZ31B.

Material	Si	Cu	Fe	Zn	Mn	Al	Mg
AA6061	0.89	0.37	0.13	-	-	95.59	2.21
AZ31B	-	-	-	0.71	0.15	3.07	94.76

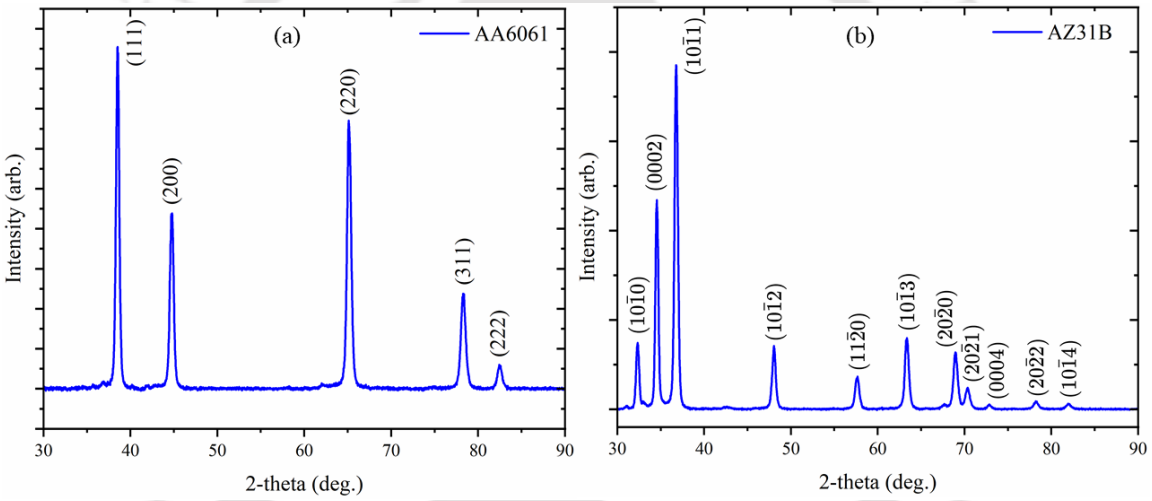

Fig. 3.1 XRD peak distribution for the as-received (a) AA6061 and (b) AZ31B

3.2.2 Tool materials and fabrication

The H-13 tool steel material is used to fabricate the FSW tools for all the experimental investigations. Based on the literature survey, the most commonly used material for the FSW of AA6061 and AZ31B is the H-13 tool steel (Woo *et al.*, 2008; Woo and Choo, 2011). The tool material is selected based on the condition that it has a higher hardness than the base material to be welded. The chemical composition of the material is provided in Table 3.2. The major alloying elements in the H-13 tool steel are Cr, W, Si, Mo, and Co. These elements jointly impart the properties of wear resistance, high toughness, and high temperature stability to the H-13 tool steel. These factors allow the wide application of the

H-13 tool steel in hot working conditions, such as FSW tool material. Multiple tools based on shoulder and pin designs are discussed in the published literature (Krasnowski, Hamilton and Dymek, 2015). The cylindrical and conical tool pins are commonly used to perform FSW with good-quality joints (Gratecap, Racineux and Marya, 2008; Hassanifard *et al.*, 2022). Due to the wide application of conventional cylindrical and conical tools and ease of fabrication compared to other complex designs, these tool pins are considered for the current investigation. Moreover, various shoulder designs are also disclosed in the literature (L. Zhang *et al.*, 2011). However, the conventional shoulder without any features is considered for the present investigation as they are the most widely used type of tool shoulder. The pin height of about 95% of the base plate thickness produces a good quality weld (Padmanaban and Balasubramanian, 2009). Further, the tool shoulder diameter of about three times the base plate thickness is more convenient to produce a good quality weld (Elangovan and Balasubramanian, 2008). Multiple FSW tools are fabricated based on tool shoulder dimension and tool pin design for the investigation of FSW and μ-FSW as shown in Figs. 3.2 and 3.3. As the thrust of the research work is the analysis of the defects, the tool dimensions are selected in such a manner that there are minor variations from the optimal design. Further, the other process parameters are also chosen such that it may produce different volumetric defects. The details of the tool used for the FSW of AA6061 and AZ31B and μ-FSW of AA1200 are provided in Table 3.3 and Table 3.4, respectively.

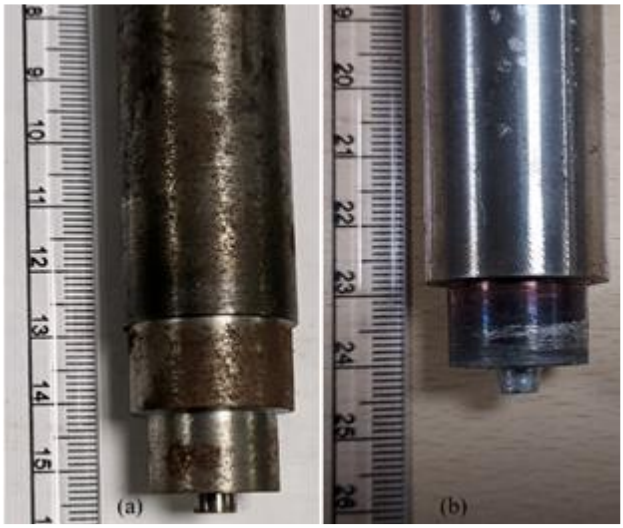

Fig. 3.2 Representation of various tools used for FSW with (a) cylindrical pin and (b) conical pin

Fig. 3.3 Representation of various tools used for FSW with varying shoulder and pin geometry

Table 3.2 Chemical composition (wt %) of H13 tool steel

Elements	Si	Mo	V	Cr	Mn	Co	W	Fe
(wt%)	1.89	1.81	0.60	4.72	0.62	1.03	1.98	87.35

Table 3.3 Geometric features of the tool used for the FSW of AA6061 and AZ31B

Features	Dimensions (mm)
Tool shoulder	18, 21, 24
Tool pin types	Cylindrical, conical
Tool pin diameter	4, 6
Tool Pin height	2.5, 3, 3.5

Table 3.4 Geometric features of the tool used for the μ-FSW of AA1200

Welding parameter	Dimensions (mm)
Tool shoulder diameter	6, 8, 10
Tool pin types	conical
Tool pin diameter (bigger)	3, 2
Tool pin diameter (smaller)	2, 1.5
Tool pin height	0.6, 0.7, 0.8

3.3 FSW and μ-FSW setup

A vertical milling machine is used for the different FSW experiments. The milling machine is commonly used in the experimental investigation of the FSW in the published literature (Arora *et al.*, 2010; Hynes *et al.*, 2022). The faying edges of the workpieces are properly ground and prepared before welding. The tool is placed with a 0 mm offset value, i.e., at the joint of the two workpieces. The workpieces are secured in the x and y-directions with the help of the clamps provided in the machine setup as indicated in Fig. 3.4. A backing plate with a thickness of about 20 mm is placed just below the workpiece. The welding machine used has nine different rotational speeds, i.e., 233, 342, 462, 360, 557, 750, 612, 900, and 1200 rpm. The traverse speed has 17 steps, i.e., 13, 20, 26, 30, 34, 40, 41, 60, 66, 68, 70, 82, 90, 132, 140, 180, and 300 mm/min. The spindle and feed motors have a power

of 20 HP and 3 HP, respectively. Multiple sets of experiments are performed by varying the different process parameters, the details of which are discussed in section 3.3.

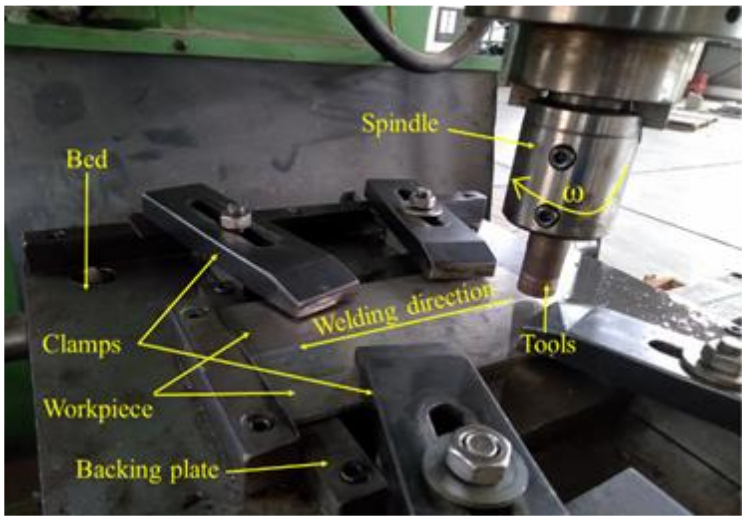

Fig. 3.4 FSW machine with different clamping and backing plate arrangements

The μ-FSW setup is designed and developed in-house. A mini bench drilling machine with the highest rotation speed of 2800 rpm is retro-fitted with the in-house developed CNC table. The movement of the welding table is controlled with the help of a microcontroller. The design and development of the μ-FSW will be detailed in the subsequent sections. Figure 3.5 depicts the complete experimental setup used for the μ-FSW.

3.4 Selection of process parameters

The FSW process is affected by a variety of process parameters, including the tool design and dimensions (Singh *et al.*, 2020). The process parameters for FSW include the tool rotation speed, traverse speed, tilt angle, plunge depth, plunge force, tool geometry, plate position, plate thickness, and tool offset (Padhy, Wu and Gao, 2018). In most cases, the process parameters are correlated with the mechanical strengths of the welded sample. However, the current investigation focuses on forming a certain type of volumetric defect for a given set of process parameters. The identification of a certain type of defect and its correlation to a set of process parameters will help to mitigate the identified

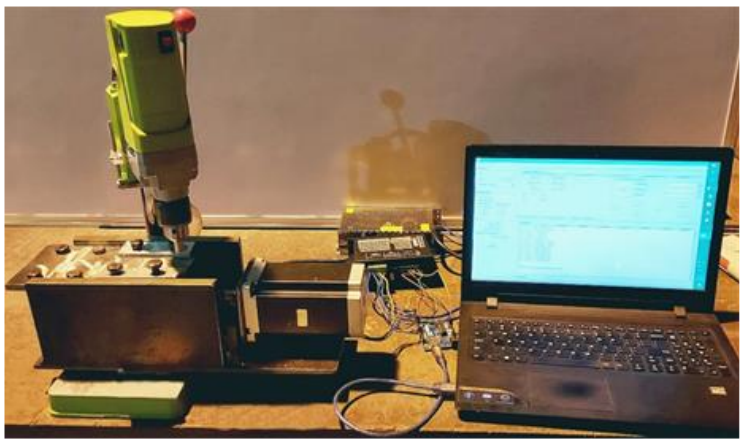

Fig. 3.5 Complete experimental setup developed for the μ-FSW

defect. The microscopic analysis of the surface and sub-surface cross-section of the welded sample helps identify the defect formation associated with a chosen set of process parameters. The microstructural analysis also helps to analyse the various metallographic zone associated with FSW. Further, the EDX and XRD analysis helps to identify the material mixing and IMC formation, respectively, during dissimilar FSW. However, from the literature survey, it is realized that all the process parameters are not affecting the weld equally. Further, it is also realised that a certain process parameter plays a more dominant role in the formation of a certain type of defect. For instance, the plunge depth plays a significant role in the formation of the flash formation defect. Therefore, it is more important to moderate this parameter for the mitigation of excessive material expulsion. As such, the process parameters for the current study are decided based on the defect that has to be analysed. The chosen range of process parameters for the complete duration of current investigation on FSW is provided in Table 3.5.

Table 3.5 Experimental conditions employed for FSW of AA6061 and AZ31B

Welding parameter	Values
Tool rotation speed (rpm)	360, 557, 750, 900, 1200
Tool traverse speed (mm/min)	13, 20, 26, 30, 60, 90, 120, 300
Tool plunge depth (mm)	0.1, 0.2, 0.3 0.5, 0.7, 0.84
Tool pin height (mm)	2.5, 3, 3.5, 3.7
Tool shoulder diameter (mm)	18, 21, 24
Tool pin diameter (mm)	4, 6
Tool tilt angle (°)	0
Tool offset (mm)	0

As the μ-FSW setup is designed and fabricated for the current work. It is of primary importance to investigate its ability to produce joints with a good accuracy level, which requires multiple experimental investigations. To study the feasibility of the developed process, multiple trial runs are performed initially. Once a certain level of confidence is achieved regarding the developed setup, further experimental runs are initiated to understand the mechanical prowess of the welded sample joined using the μ-FSW setup. A multi-factor, multi-level full factorial design of the experiment is used for both lap and butt welding configurations. The details of the experimental process parameters used for the μ-

FSW are provided in Table 3.6. Further, Table 3.7 highlights the various process parameters and their associated volumetric defects that are investigated in the current study.

Table 3.6 Details of variable and constant process parameters used for μ-FSW in lap configuration

Parameters (unit)	**Range**	**Levels**			
		1	**2**	**3**	**4**
Rotational Speed (rpm)	1400-2200	1400	1800	2300	
Shoulder diameter (mm)	6-12	6	8	10	12
Tool diameter (mm)	2-3	2	3	-	-
Constant parameters: Cylindrical pin					

Table 3.7 Summary of different process parameters investigated for various volumetic defects

Rotation speed (rpm)	**Traverse speed (mm/min)**	**Materials and defect**	**Associated defects**
1200	90	AA6061 (Tunnel defect)	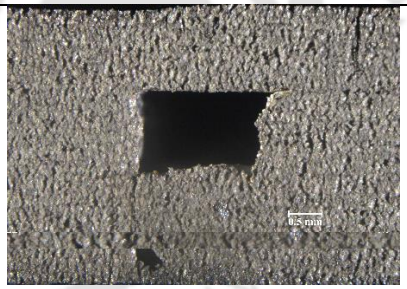
900	90	AZ31B (Flash formation)	
360	300	AA6061 (Partially welded joint)	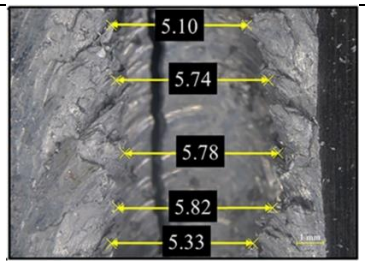

900	90	AA6061-AZ31B (Exit hole)	
900	30	AA6061-AZ31B (Micro-cracks)	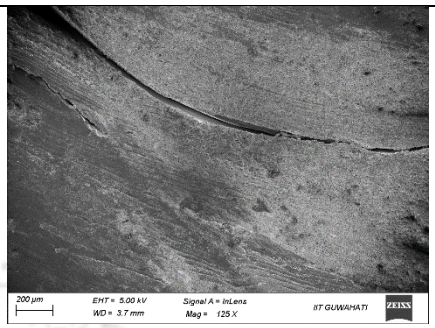
1200	30	AA6061-AZ31B (Surface defect)	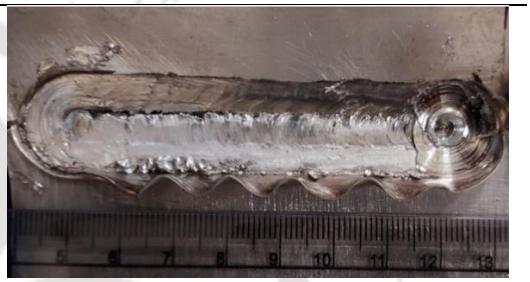

3.5 Measurement of Temperature

Temperature evolution is an important component of FSW. The temperature measurement is performed for the validation of the developed numerical model. An Infrared Gun (TESTO 868) is used to measure the temperature on the workpiece surface. The maximum permissible temperature that can be measured with the available infrared gun is $650°C$. As the maximum temperature in FSW of AA6061 remains below the permitted $650\ °C$ (Liu, Lan and Ni, 2015b), the infrared gun ca n provide temperature isotherms with reasonable accuracy. The white colour region around the tool indicates the temperature of the tool has risen above the permissible $650°C$, and therefore the temperature on the tool surface cannot be measured. The temperature range for experiments was set at $-30°C\ to\ 650°C$

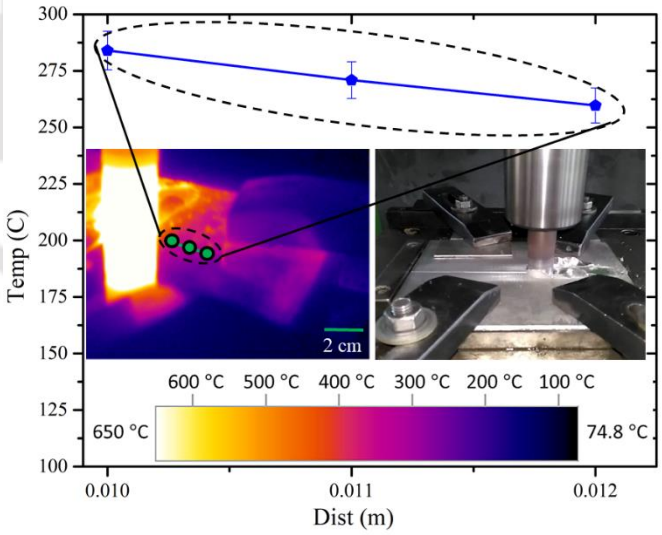

Fig. 3.6 Measurement of temperature evolution with Infrared gun during FSW at 1200 rpm and 90 mm/min

which has an accuracy of about ±2% (Testo.com). Initially, the IR Gun was calibrated by heating the workpieces to a defined temperature and adjusting the thermal emissivity accordingly, as discussed in the literature (Pankaj, Tiwari, Medhi, *et al.*, 2022). The obtained temperature isotherms are analyzed with the help of Testo IRsoft software to measure the temperature at different points on the workpiece surface. Pankaj et al. (2022) and Das and Narayanan (Das and Narayanan, 2023) followed a similar approach in independent literature for proper temperature measurements during FSW. The region indicated in Fig. 3.6 highlights the location for temperature measurement that is used for numerical model validation.

3.6 Measurement of defect

The process parameters of all the experiments are chosen individually, as demonstrated in Table 3.7, for the analysis of various volumetric defects. The samples are prepared for the defect analysis by following destructive techniques, primarily due to the sub-surface nature of most defects. On completion of the FSW, the samples for investigation are cut from the welded product using the wire electrical discharge machining (WEDM). This non-contact type process ensures precise cutting with negligible residual stresses and cutting forces into the cut sample. This helps to ensure that the dimensional integrity of the defects are not hampered and proper analysis can be performed. As the sample is isolated for investigation, it is cleaned with acetone if required. Then the samples are observed under a high magnification microscope to identify and analyze the defects. The optical microscopes of make LEICA S6D and Nikon SMZ25 are used to identify and measure the defects. The tunnel defect analysis is performed by cutting the sample in the transverse and longitudinal directions. This helps to realize both the cross-sectional area of the defect and the complete length of the presence of the defect. Similarly, the exit hole

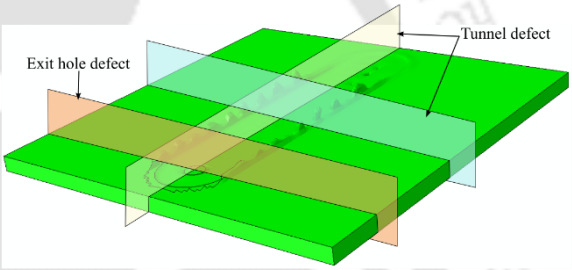

Fig. 3.7 Schematic of tunnel and exit hole defect directions in the welded workpiece

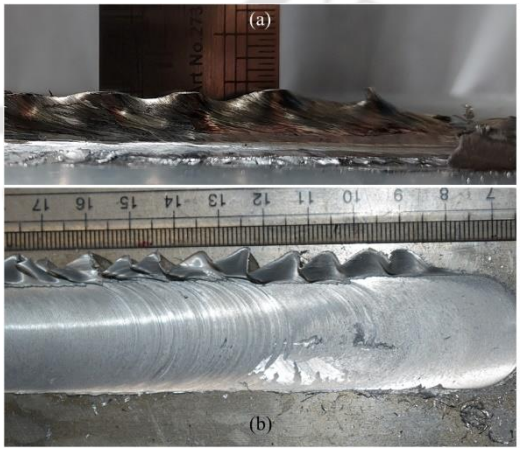

Fig. 3.8 Representation of the (a) side view and (b) top view of flash formation

defect is analyzed by sectioning the exit hole in the transverse direction to estimate the height of the defect. The schematic of the plane of cut for both the tunnel and exit hole defects is shown in Fig. 3.7. Alternatively, the flash formation is analyzed by taking both the top and the side view of the flash. As the material is expelled out of the workpiece, the flash can stand tall (Fig. 3.8a), or it can bend over along the transverse direction of the workpiece (Fig. 3.8b). The first case requires the height measurement from the side view, and the second case requires the measurement from the top view.

3.7 Residual stress measurement

The non-destructive XRD analysis was performed to estimate the residual stress in dissimilar AA6061-AZ31B FSW. The XRD investigation used a Rigaku X-ray diffractometer (model: Smart Lab) with CuKα radiation of $\lambda = 1.54$ Å. Initially, a full scan from $30 - 120°$ is performed for both of the base materials. However, on completion of the welding, the cut samples from the SZ produce various peaks indicating the formation of the IMCs. Further, the commonly accepted $d\ vs \sin^2\psi$ method with the XRD analysis is used to evaluate the residual stress in the welded sample. To perform the residual stress analysis, a sample was cut with a cross-section of $8\ mm \times 8\ mm$. Figure 3.9 shows the different locations of the measurement of the residual stresses. The 2θ value is initially fixed, and the XRD peaks are obtained for different ψ values to evaluate the change in the d spacing to

Table 3.8 Details of machine parameters used for residual stress measurement

Parameters	Details
Step (°)	0.01
Speed (°/min)	3
Psi (°)	0, 5, 10, 15, 20, 25, 30
Phi (°)	20
Mode	Theta-2 Theta

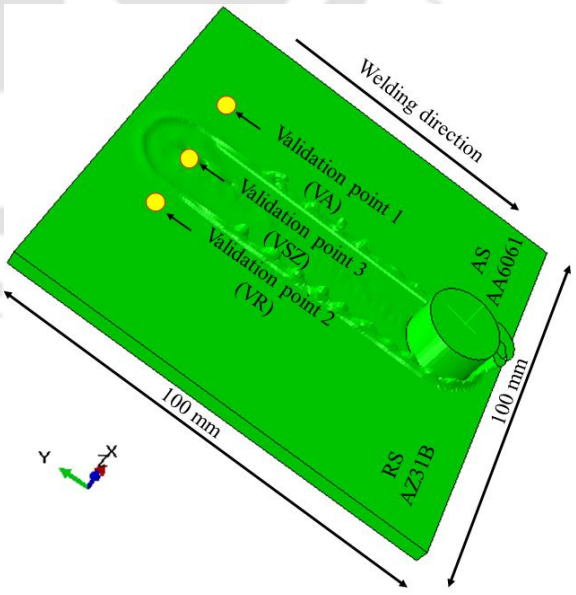

Fig. 3.9 Schematic of the various locations of residual stress measurement

determine the residual stress. The mathematical approach for determining the residual stress is provided elsewhere (Das and Joshi, 2020). Initially, a complete XRD scan was performed between $30° - 120°$ at a scanning speed of $0.05°s^{-1}$ to identify the various XRD peaks. The 2θ angle for AA6061 of 116.482°, for AZ31B of 99.665°, for the dissimilar SZ of AA6061-AZ321B of 99.7° is considered for the measurement of the residual stress as shown in Fig. 3.10. The higher angle 2θ value is considered for an easy and accurate measurement of the residual stress (Zapata, Toro and López, 2016). The details of the machine parameters used for the residual stress analysis is provided in Table 3.8.

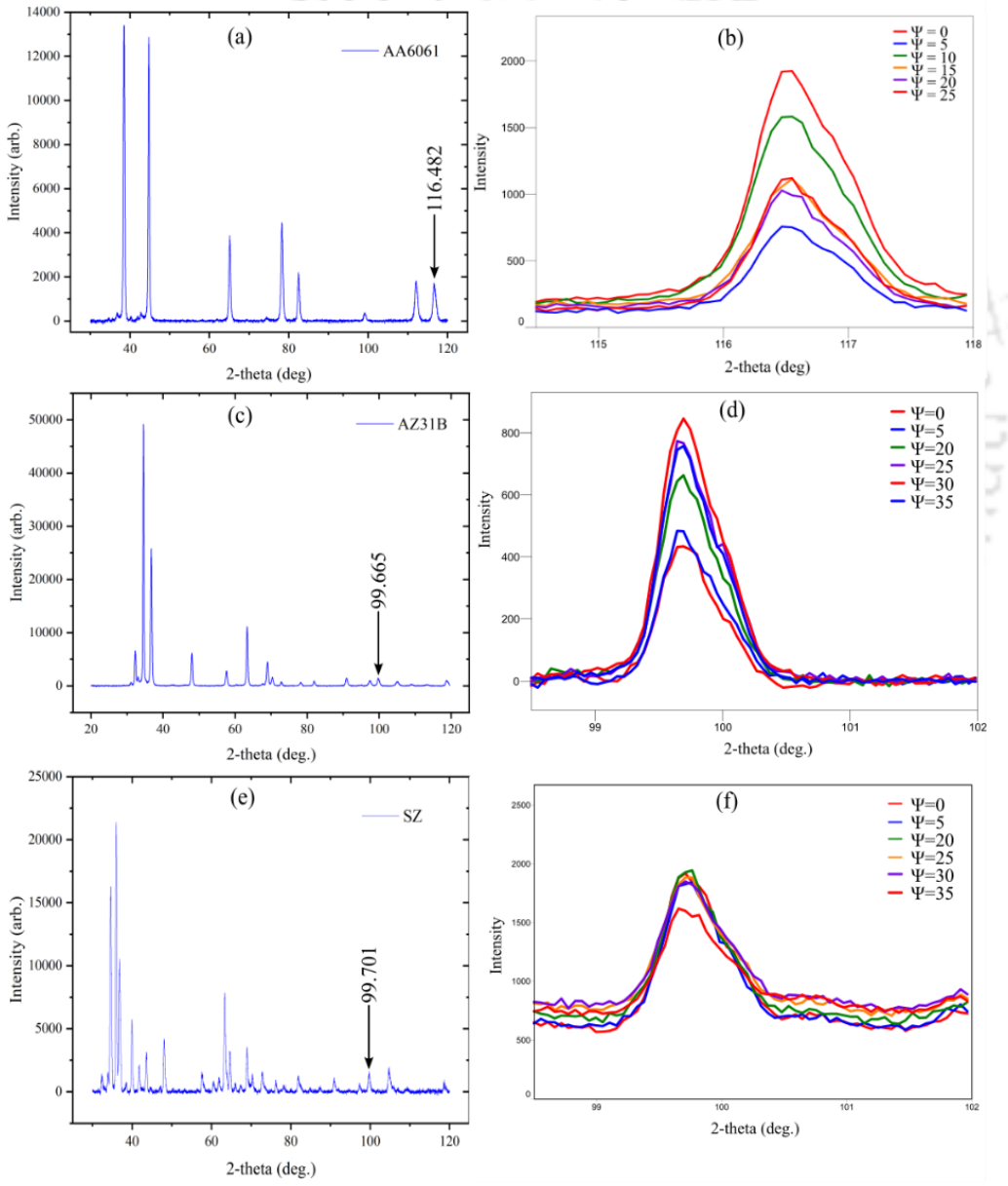

Fig. 3.10 Depiction of full scan XRD pattern for (a) AA6061, (c) AZ31B and (e) SZ; Intensity vs 2θ graph at different ψ for (b) AA6061 at $2\theta = 116.482°$, (d) AZ31B at $2\theta = 99.665°$, and (f) SZ at $2\theta = 99.701°$

3.8 EDX analysis

Energy Dispersive X-ray Spectroscopy (EDX) is generally used with the FESEM to simultaneously perform image and elemental analysis. The EDX is currently used to estimate the material mixing near the SZ of the dissimilar AA6061-AZ31B FSW. The sample to analyze is cut using the WEDM. The cut sample is then cleaned using a sonicator bath with acetone to remove any unwanted impurities from the WEDM process. The sample is then loaded into the FESEM-EDX machine using double-sided carbon tape. The sample is analyzed using an SE2 detector. The working distance is maintained between 7.5 and 8.5 mm. The EHT used is 20kV. Figure 3.11 shows the various locations for EDX analysis of the different base materials and the SZ during dissimilar AA6061-AZ31B FSW.

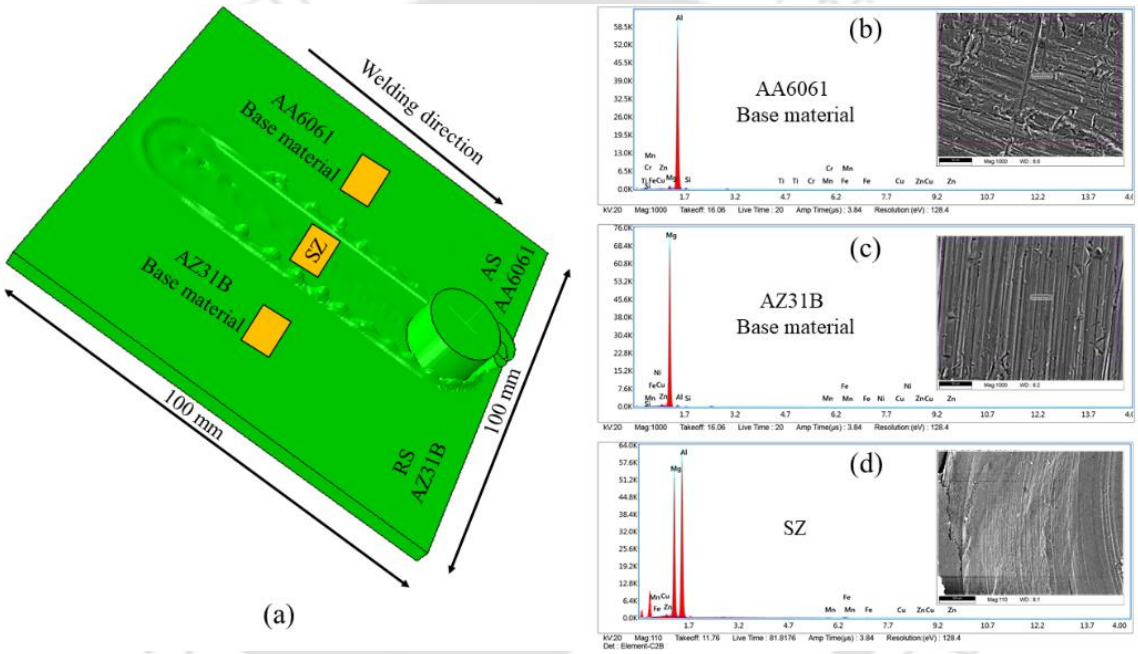

Fig. 3.11 (a) Schematic location for the EDX analysis of various regions during dissimilar FSW; EDX distribution of (b) AA6061 base material and (c) AZ31B

3.9 Tool wear estimation

The tool wear during FSW can occur either due to material erosion or due to geometric changes. The tool wear is experimentally investigated for dissimilar AA6061-AZ31B FSW. The various process parameters used for the investigation of the tool wear are highlighted in Table 3.9. A stereo microscope of make: Nikon, model: SMZ25 is used to capture and analyze the tool wear after each welding. The tool is observed to have a coating of base material on the tool shoulder and pin after every welding. The dimension of the tool is measured before and after removing the coating layer. The precise determination of the tool shape and size, more importantly, of the tool pin, is vital for a good quality weld.

Table 3.9 Details of experimental process parameters and plate positions

Weld No.	Plate positioning (AS-RS)	RPM	Traverse Speed (mm/min)
Weld-I1	Al-Mg	900	30
Weld-I2	Al-Mg	900	60
Weld-I3	Al-Mg	900	90
Weld-II1	Al-Mg	1200	30
Weld-II2	Al-Mg	1200	60
Weld-II3	Al-Mg	1200	90

3.10 Metallographic zones and lap-shear test

To identify the different zones arising due to the themo-mechanical effect during the FSW of AZ31B, the samples are initially cut from the welded joint using the WEDM. The cut sample is dipped in acetone and kept in the water bath for 30 minutes. The cut samples are then prepared firstly by polishing them in different grades of emery paper, sequentially from 1000, 1200, 1500, 1800, 2000, and 2500. Finally, it is polished using velvet cloth for a mirror-like finish. The polished surface is then etched using the picral etchant comprising 5 ml acetic acid, 5 g picric acid, 10 ml water, and 100 ml ethanol (Thakur, Sharma and Bhadauria, 2023). The etching is followed by water cleaning and air drying. The sample is etched for about 10 seconds before being washed in water, dried, and observed under a microscope for the desired result. This process is repeated until the desired metallographic zones are clearly visible. The location for the metallographic analysis is presented in Fig. 3.12.

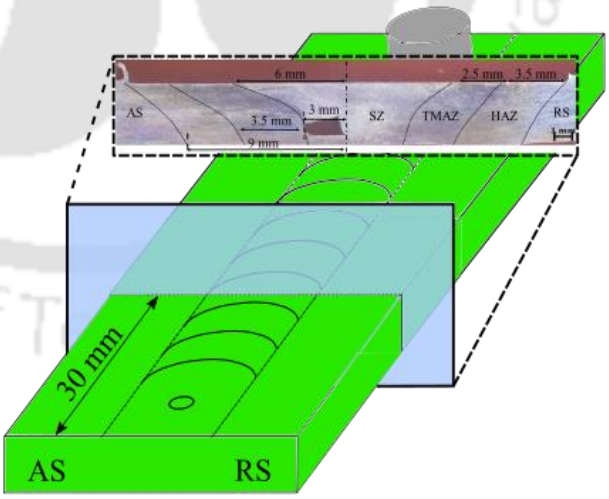

Fig. 3.12 Schematic of region of enquiry for the metallographic analysis

Multiple lap-shear tests are performed to ascertain the quality of the μ-FSW joints. The lap shear test measures the resistance to the shearing forces acting on the joint interface. A uniaxial force is applied to measure the maximum force required to cause failure in the welded product. A 5KN Electromechanical Universal Testing Machine (Make: ZwickRoell, and Model:

Z005TNProline) is used for the lap-shear tests. Each of the sheets is cut in a manner that they have a dimension of about $120\ mm \times 30\ mm$ as shown in Fig. 3.13 (Ferreira *et al.*, 2020). A detailed discussion of the lap-shear test is provided in Chapter 6.

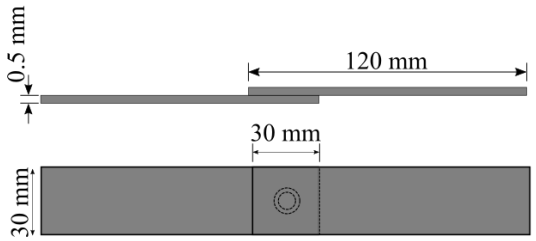

Fig. 3.13 Schematic of the μ-FSW specimen.

3.11 Design and Development of μ-FSW

The μ-FSW setup comprises of primarily three different components, i) welding bed to hold and move the workpiece, ii) clamp to constrain the workpiece in various axis, iii) welding tools, and iv) electronic circuit to control the motion of the bed. The welding bed is designed with two main objectives, i.e., the stability of the bed and the portability of the complete setup. It is realized that the welding bed would undertake the majority of the initial thrust of the tool. Therefore a sturdy build is essential for the bed. However, the bed has to be designed so that all the components required for the bed movement and completion of welding are incorporated into the bed setup simultaneously. Moreover, it also has to be of an optimum size such that the required welding can be performed and the total weight of the system remains in check so that the welding setup can be easily moved between different work locations. Multiple bed designs are considered and evaluated to achieve the stated objectives based on weight considerations and modal analysis.

3.11.1 Analysis of the μ-FSW setup

Over several trials for better stability of the model, the weight of the updated welding bed is estimated to be about 9 kg. This makes the current design the most portable setup. However, as the welding table is put in an overhung position (Fig. 3.14), the accuracy of the workpiece movement is hampered. This led to the development of another welding bed design, which has only one modification over the previous design. The final model has two guide rails to conduit the welding table and, thus, the workpiece through it. Fig. 3.15 (a and b) shows the final CAD model and the assembled welding bed, respectively. The guide rails are bolted to the base of the welding bed. A channel is built on the inside surface of both the support rails, and the welding table is supported in it. As the table passes through the channel, the vibration issue present in the previous model is significantly minimized in this design.

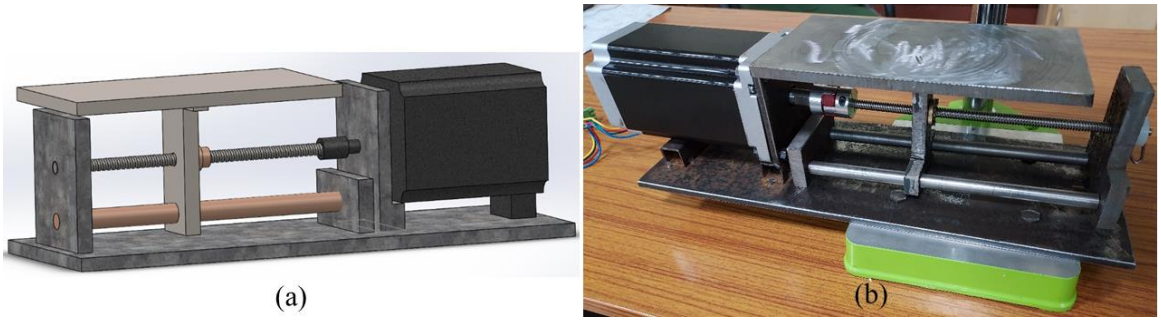

Fig 3.14 Depicts the (a) CAD model, and (b) photograph of initial welding bed assembly

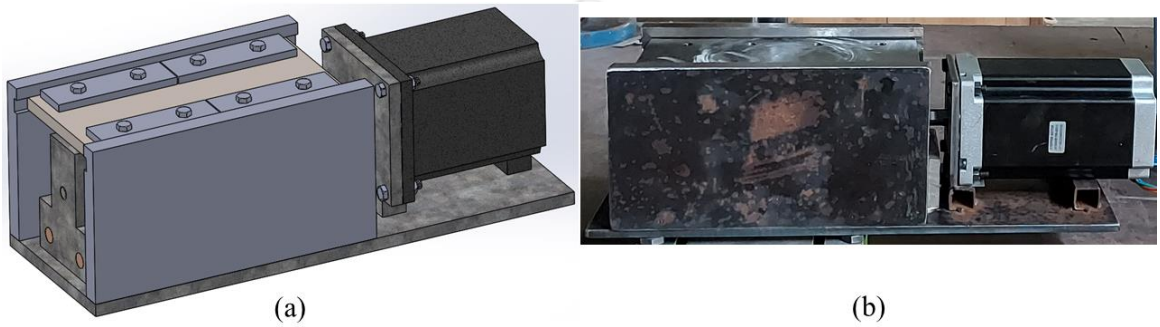

Fig. 3.15 Depicts the (a) CAD model and (b) final assembled welding bed

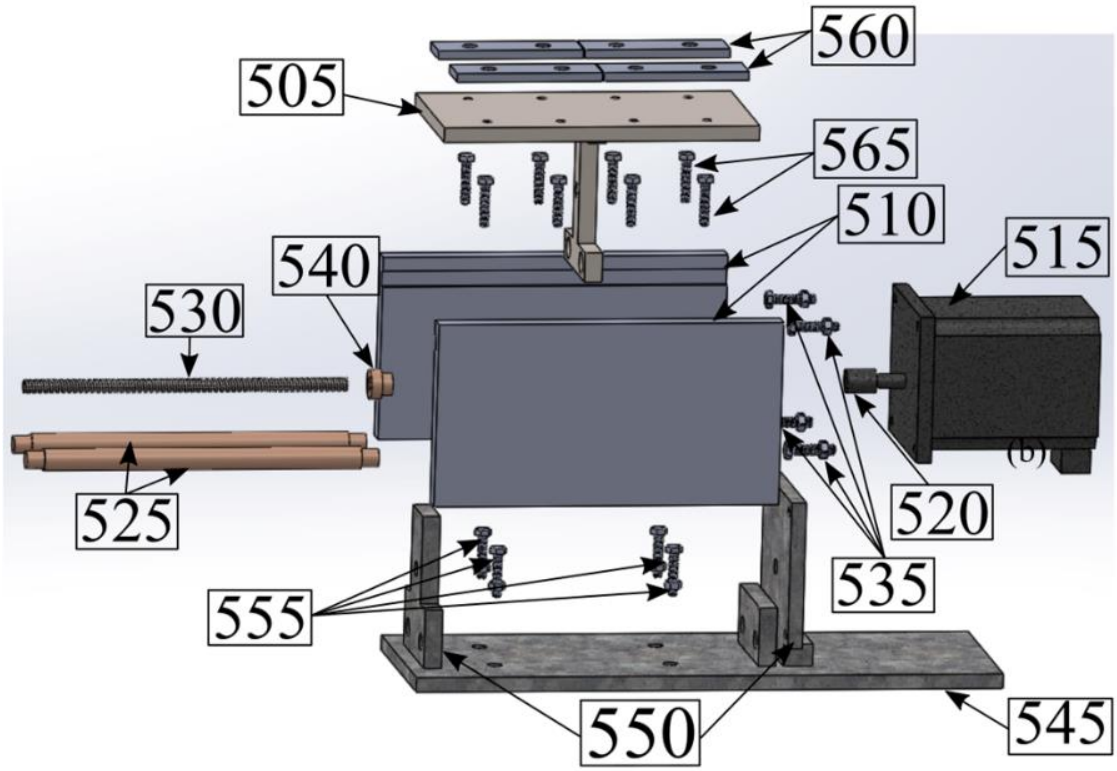

Fig. 3.16 Illustrates the exploded view of the developed welding bed comprising various components

Figure 3.16 shows the exploded view of the welding bed (500) with its various components. Any workpiece is secured on the welding table (505) with the help of z-clamps

(560). The z-clamps (560) are secured to the table with the help of threaded bolts (565), which behave as a y-clamp. The motor (515) is utilized to power the leadscrew (530). The leadscrew (530) is connected to the motor with the help of a coupling (520) and an attachment (540). The vertical support guides (510) are provided to allow the welding table (505) to run through the channel present in them. This allows to restrict any vibrations appearing on the table (505). The complete structure is supported on the bed base (545). Two vertical supports (550) are provided on either end to support the leadscrew (530) and support rails (525). These supports (550) also act as the mechanical stop to the welding table (505). Bolted joints (555) are used to secure the welding bed (500) to the tool spindle body (100). Simultaneously, the bolted joints (535) are used to secure the motor to the support (550) and maintain its alignment. As the complete welding bed is attached to the tool spindle with the help of bolted joints (555). These joints can easily assemble or disassemble the welding bed from the tool spindle to ease the portability of the complete system. Further, the weight of the complete setup is only about 20 kg. Therefore, both the objectives of being sturdy and portability are fulfilled by this design, which is utilized for further investigation. Figure 3.17 shows the various mode shapes associated with the welding bed design presented in Fig. 3.15. Table 3.10 highlights the various natural frequencies associated with the modal analysis. Figure 3.18 shows the complete assembly of the welding bed with the tooling spindle.

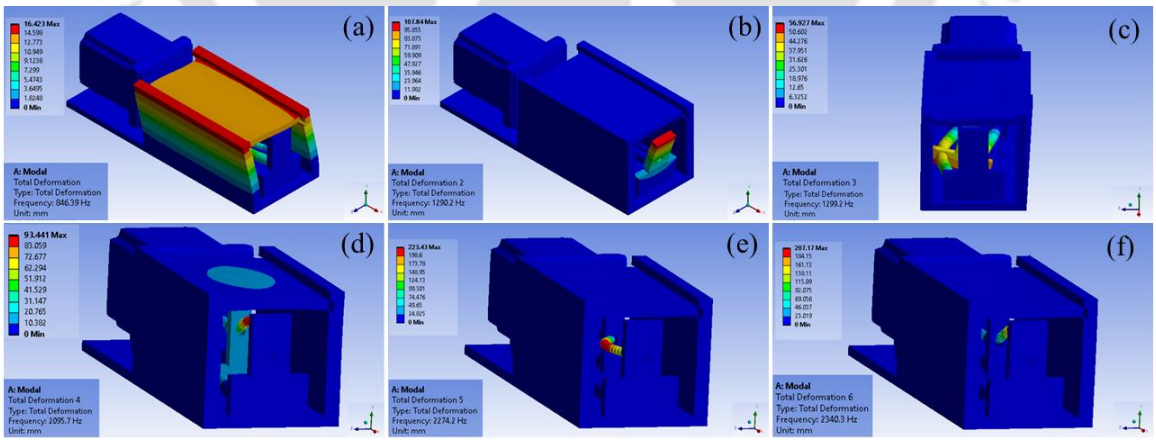

Fig 3.17 Various mode shapes associated with the modal analysis of the model.

Table 3.10 Natural frequencies of first six mode shapes for model

Mode	Frequency (Hz)
Mode – 1	852.52
Mode – 2	1292.2
Mode – 3	1303.6
Mode – 4	2099.9
Mode – 5	2242
Mode – 6	2292

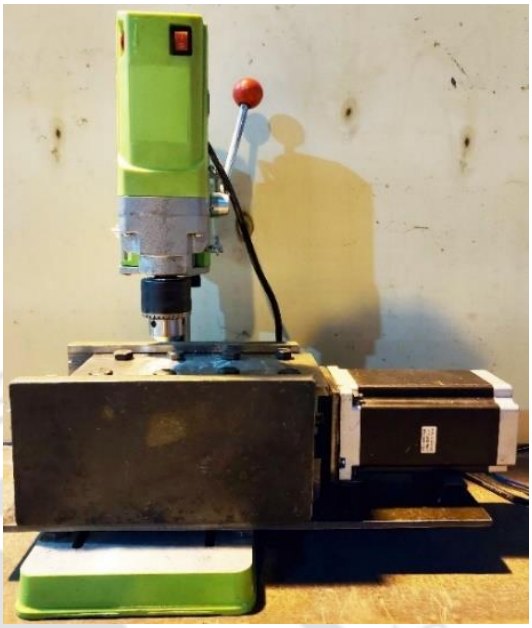

Fig. 3.18 Representation of the completed final setup

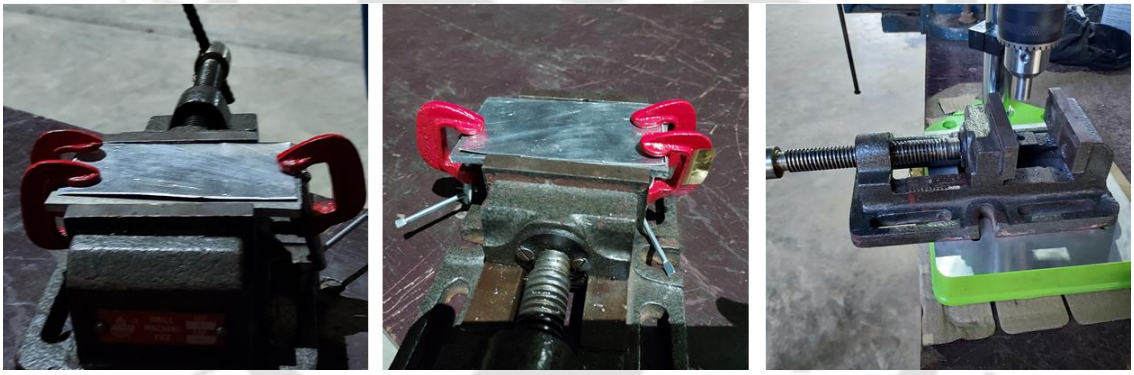

Fig. 3.19 Portable bench vice and 1-inch C-type clamping arrangement

The clamping of the workpiece is extremely important, as vibrations during welding can be detrimental to the weld quality. Figure 3.19 shows the application of a 1-inch, C-type clamp with a portable bench vice. The C-type clamp is used to secure the workpiece with the welding bed. The welding bed and the workpiece are placed on a portable bench vice. The bench vice is then placed on the base of the welding

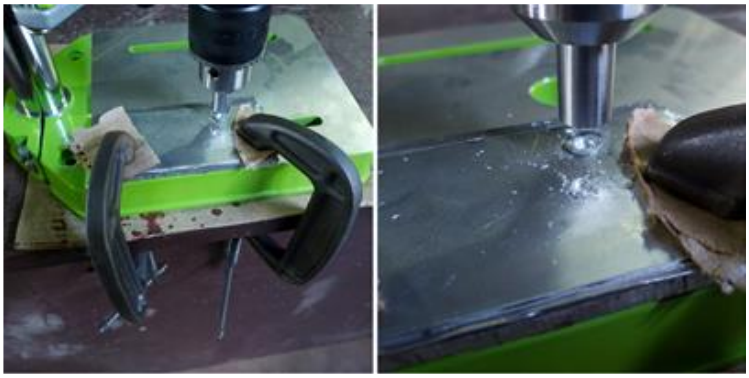

Fig. 3.20 3-inch C-type clamping arrangement used for μ-FSW.

setup. This setup is easy to assemble for welding and does not require much design or fabrication. However, the lack of a fixing mechanism between the bench vice and the base leads to vibration generation during welding. Due to this reason, the welding obtained in this case is of poor quality. Figure 3.20 shows the application of the bigger 3-inch C-type clamps. The bigger size of the clamps helps to eliminate the portable bench vice altogether. The workpiece is directly secured to a sturdy base. This helps to eliminate the vibration observed during welding in the previous case. The welding achieved in this case is of sound quality; however, moving the workpiece for linear welding or multiple spot welding cannot be fulfilled by simply using the C-type clamps. Therefore, using the designed welding bed from the previous section is paramount. However, the C-clamps can be employed if any additional securing is required.

The precise movement of the welding bed is important for successful linear μ-FSW or multi-spot μ-FSW. The electronic circuit used to program and control the movement of the welding bed is presented in Fig. 3.21. A switched mode power supply (SMPS) converts the AC to DC form and feeds it to the DC motor as a power source. The power supply is connected to the DC motor through a stepper driver. The stepper driver is connected to the microcontroller. The microcontroller and the IDE allow for any code to be written and input into the system with the help of a computer. This accurate regulation over the welding bed movement increases the versatility of the developed setup while performing different types and configurations of welding.

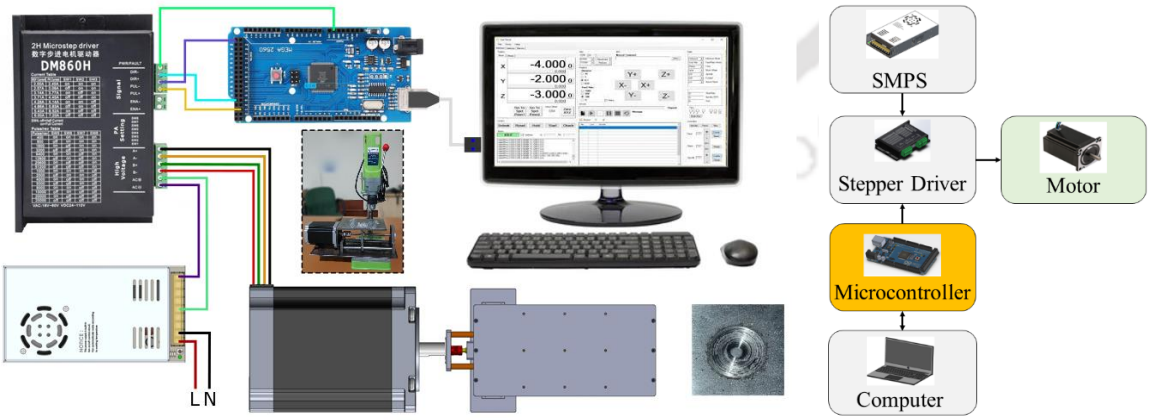

Fig. 3.21 Circuit diagram to control the welding bed movement.

3.11.2 Shear strength of μ-friction stir welded joints

The developed μ-FSW setup is used for spot welding of AA 1200 with a thickness of about 0.5 mm. Multiple experiments are performed according to the parameters presented in Table 3.6. A full factorial design of the experiment is used for the experimental investigation, and each experiment is repeated atleast twice. Figures 3.22 (a-c) show the results of the lap-shear test performed on the different μ-FSSW joints, whereas Fig. 3.22 (d) represents the experimental joint obtained while welding with a 2 mm pin diameter and 6 mm shoulder diameter. The lap-shear investigation for all the cases highlights that the best result is obtained when welding with 2200 rpm compared to 1400 rpm and 1800 rpm. The higher tool rotation speed generates more heat and provides better material plasticization, resulting in a good quality weld. The best three results are obtained when performing μ-FSSW with the tool of 2 mm pin diameter and 6 mm shoulder diameter, 2 mm pin diameter and 12 mm shoulder diameter, and 2 mm pin diameter and 10 mm shoulder diameter. Two different pin heights of 0.6 mm and 0.8 mm are used for the experimental investigation, but they are observed to have negligible effects on the weld quality. This happens due to an extremely small difference of 0.2 mm between the two pin heights. Therefore, the process parameter of pin height is ignored for this investigation. The smaller pin diameter of 2 mm produces better results due to the easy material movement around the tool. However, such definitive conclusions cannot be derived regarding the shoulder diameter from the current investigation. Alternatively, observing the results presented in Fig 3.22 under the lens of the shoulder diameter to pin diameter ratio, it is realized that the highest strength is achieved with a ratio of 3, and the strength reduces with an increase in the shoulder diameter to pin diameter ratio. A similar observation is made in the independent literature for conventional FSW with 5 mm plate thickness (Saravanan *et al.*, 2016). Therefore, it can be concluded that the shoulder diameter to pin diameter ratio of 3 will produce a good quality weld with the μ-FSW also.

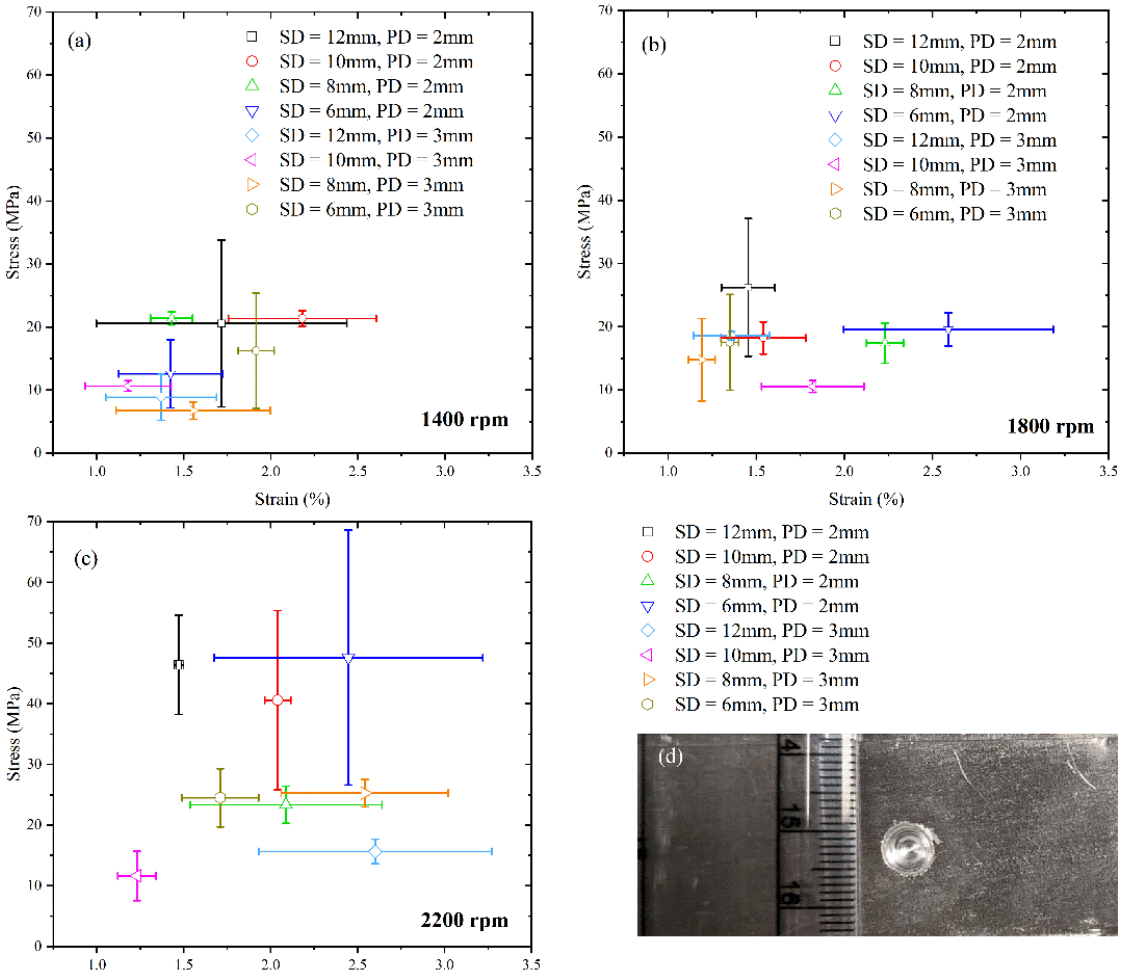

Fig. 3.22 Effect of the rotational speeds (a) 1400 rpm, (b) 1800 rpm, and (c) 2200 rpm on the shear strength of the μ-FSSW of AA1200

3.12 Summary

This chapter highlights the methodologies and analyses adopted for conducting the experimental investigation of the FSW process. The different materials utilized for similar and dissimilar FSW are presented here. The AA6061, AZ31B, and AA1200 are investigated in different process conditions to estimate the weld quality. The FSW is performed using the H-13 tool steel. Different types of tools with varying dimensions and process parameters are used for the FSW investigation. Various destructive and non-destructive analyses are performed to investigate the different surface and sub-surface defects occurring during FSW. The material mixing during dissimilar FSW is also experimentally investigated. The key non-destructive procedures utilized for the material mixing and defect analysis are the EDX and XRD analysis. The cut surface and sub-surface of the welded samples are observed under various microscopes for defect analysis. The macroscopic defects, such as the tunnel defect and partially or completely failed joints, can

be easily observed using an optical microscope. However, the micro-cracks, generally observed with dissimilar FSW, are observed under the high magnification FESEM. The optimal process parameters vary significantly between similar and dissimilar FSWs. The FSW of AA6061 with 1200 rpm and 90 mm/min produces a tunnel defect. However, the material deposition is proper on the top half and near the bottom surface of the workpiece. Alternatively, the FSW of AA6061-AZ31B with 1200 rpm produces a completely defective joint both near the top surface and within the weld volume. The plunge depth is a necessary evil that cannot be completely ignored and the use of plunge depth causes material loss. The plunge depth varying between 0.1 mm and 1 mm is investigated to estimate its effect on the defect formation. This chapter also details the fabrication and utilization of an in-house developed μ-FSW setup. The various parts of the developed setup, their selection, fabrication, modified clamping arrangements, and specially fabricated tools are discussed in this chapter. Experimental investigations are performed using the developed setup to realize the shear strength of the μ-FSSW of AA1200 of about 0.5 mm thickness. The lap-shear test highlights that the joint strength increases with the tool rotation speed. The pin height does not affect the weld quality significantly. The smaller pin diameter of 2 mm produces a good quality weld; however, the shoulder diameter does not show any definitive trend. It is also observed that a shoulder diameter to pin diameter ratio of 3 produces the best quality joint. All these experimental investigations are finally utilized to evaluate the prediction capability of a developed numerical model for similar and dissimilar materials joined by the FSW process.

Chapter 4

Numerical model

4.1 General background

The FSW process is a multifaceted manufacturing technique that involves the optimization of various process parameters, such as tool rotational speed, traverse speed, plunge depth, plunge velocity, and tool design (Das *et al.*, 2017a, 2017b). In many cases, achieving an optimal process window for producing a high-quality weld typically requires a trial-and-error approach, which can result in wasted materials and time. Researchers address this issue by developing mathematical tools and predictive models and optimizing the process parameters necessary to produce a defect-free weld (Das, Pal and Bag, 2016b, 2016c, 2016a). Mathematical models can take the form of analytical or numerical approaches. Analytical models usually account the heat transfer and are hard to include the plastic deformation. Therefore, the analytical models fail to capture the complete physical phenomena of the FSW process, especially the formation of any kind of defects (Das, Bag and Pal, 2017). Therefore, the use of numerical modeling has become a necessary approach for exploring the complex thermo-mechanical behavior of FSW, enabling the investigation of such systems that may otherwise be challenging to study using alternative analytical or experimental methods (Yaduwanshi, Bag and Pal, 2014, 2018). An accurate understanding of the FSW process requires consideration of both heat transfer and material flow physics. Neglecting either of these factors results in an incomplete investigation of FSW, as joint formation, microstructural changes, and defect formation are influenced by both of these factors. Therefore, incorporating both heat transfer and material flow physics along with

interface tracking is necessary for a comprehensive analysis of the FSW process. Numerous numerical techniques have been developed over time to investigate the heat conduction, mechanical responses, and material flow characteristics of the FSW process. The literature survey revealed that the CEL technique could substantially model the FSW process. The subsequent sections provide a comprehensive discussion on developing the CEL based model for FSW.

4.2 Model description

The CEL model comprises of three individual domains, i.e., the workpiece domain, the tool domain, and an artificial void domain, to accumulate the material coming out of the workpiece domain due to the tool and workpiece interaction. The tool and workpiece interact follows Coulomb's friction law causing the change in temperature of the body. The workpiece surface losses heat to the ambient by convection and radiation heat. The tool movement through the workpiece is responsible for the material movement modelled with the help of the Johnson-Cook (JC) material model.

4.2.1 Domains for CEL model

The CEL technique defines the bodies observing significant deformation as the Eulerian domain, while the bodies with negligible deformation are defined as the Lagrangian domain. The arrangements of the various domains for the FSW process are presented in Fig. 4.1. A non-Newtonian fluid is defined for the Eulerian (workpiece) domain, and a solid body is defined for the Lagrangian (tool) domain. The CEL-based computational model of the FSW process typically consists of an Eulerian (void) domain along with the workpiece domain [Fig. 4.1 (a)]. The workpiece domain is located beneath the void domain and has the exact dimensions of the actual workpiece, as shown in Fig. 4.1 (b). The top void domain allows the material movement from the workpiece during the process to flow through it. This allows visualization of the material movement that leads to the flash formation during welding. The length and width of the void domain can be similar to the workpiece dimensions; however, the height of the void domain depends on the amount of material expulsion and flash formation, which in turn depends on the various process parameters selected to execute the welding.

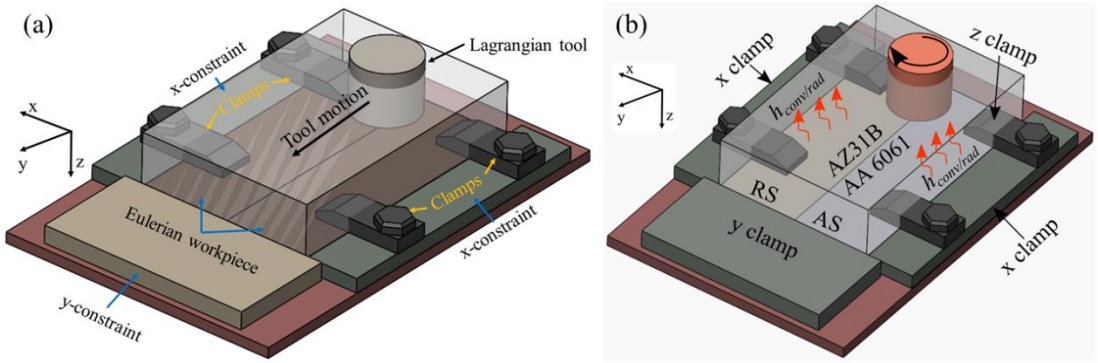

Fig. 4.1. Assembly of the Lagrangian tool and the Eulerian workpiece with the various mechanical and thermal constraints used for the computational domain for (a) similar FSW and (b) dissimilar FSW

4.2.2 Tool-workpiece interaction

The CEL approach is based on the fluid-structure interaction problem, where a Lagrangian domain interacts with an Eulerian domain. In the domain of an FSW system, the Eulerian workpiece is clamped in the x, y, and z-axes, and the rotational and translational boundary conditions are applied to the Lagrangian tool as shown in Fig. 4.1. The interaction between the Eulerian-Lagrangian domain is defined by Noh's method. Noh's method for the CEL approach can be divided into three phases, i.e., the Lagrangian step, the Eulerian step, and the coupling of the Lagrangian and Eulerian steps. The initial state of the material, i.e., density, energy, pressure, etc., at time t = 0 is known hitherto. The location of Eulerian mesh, which can be internal to, external to, or on the boundary with reference to the Lagrangian domain, is defined. The motion of the Lagrangian body at a finite time (say, t = 1) is determined by considering the initial state of the Lagrangian material (Noh, 1963). The pressure and normal velocities are continuous across the Eulerian-Lagrangian interface, considering the Rankine-Hugoniot jump condition (Fedkiw, 2002). The updated position of the Lagrangian domain is utilized to determine the position of the Eulerian domain in sequence. Similarly, the pressure value obtained by solving Eulerian equations acts on the boundary of the Lagrangian body (Brown, Burns and Christon, 2002). When the FSW tool interacts with the substrate, the material in the workpiece domain moves into an adjacent void domain. Accordingly, its Eulerian Volume Fraction (EVF) tracks the flow of the material by indexing one when the element is completely filled and considers the fraction as zero for the completely empty domain.

When ϕ is considered as an arbitrary variable, and $\boldsymbol{u}$ is material velocity, the relation between the material (Lagrangian domain) and spatial time derivative (Eulerian domain) is expressed as (Benson and Okazawa, 2004)

$$\frac{D\phi}{Dt} = \frac{\partial \phi}{\partial t} + \boldsymbol{u}.(\boldsymbol{\nabla}\phi) \tag{4.1}$$

where the term $\boldsymbol{u}.(\boldsymbol{\nabla}\phi)$ incorporates the convective effect of the system, $\frac{D\phi}{Dt}$ is the material time derivative, and $\frac{\partial \phi}{\partial t}$ is the spatial time derivative. The mass, momentum, and energy equations in the Lagrangian domain are converted into Eulerian conservative equation as (Jain, Pal and Singh, 2017)

$$\frac{\partial \rho}{\partial t} + \boldsymbol{\nabla} \cdot (\rho \mathbf{u}) = 0 \tag{4.2}$$

$$\frac{\partial (\rho \boldsymbol{u})}{\partial t} + \boldsymbol{\nabla} \cdot (\rho \boldsymbol{u} \otimes \boldsymbol{u}) = \boldsymbol{\nabla} \cdot \boldsymbol{\sigma} + \rho \boldsymbol{b} \tag{4.3}$$

$$\frac{\partial e}{\partial t} + \boldsymbol{\nabla} \cdot (e\boldsymbol{u}) = \boldsymbol{\sigma} : \boldsymbol{D} \tag{4.4}$$

where ρ is density, $\boldsymbol{\sigma}$ is Cauchy stress, $\boldsymbol{b}$ is the body force, e is the total energy per unit volume, and $\boldsymbol{D}$ is the velocity strain. The general form of the Eulerian equations is expressed as (Skrzat, 2012)

$$\frac{\partial \phi}{\partial t} + \boldsymbol{\nabla} \cdot \boldsymbol{\Phi} = \boldsymbol{S} \tag{4.5}$$

where $\boldsymbol{\Phi}$ is the flux and $\boldsymbol{S}$ is the source term. In the CEL approach, Eq. 4.5 is divided using a split operator and solved sequentially as (Ansari *et al.*, 2019)

$$\frac{\partial \phi}{\partial t} = \boldsymbol{S} \tag{4.6}$$

$$\frac{\partial \phi}{\partial t} + \boldsymbol{\nabla} \cdot \boldsymbol{\Phi} = 0 \tag{4.7}$$

It is noteworthy that the Lagrangian term consists of the source term (Eq. 4.6), whereas the convective term is included in the Eulerian equation (Eq. 4.7). The solution variables from the Lagrangian term are adjusted to accommodate the material flow by the transport algorithm (Benson, 1992, 1997).

4.2.3 Material model

The actual FSW process observes significant material straining and movement. The inclusion of a material model is necessary to accurately define the thermo-mechanical behaviour of the process. The most widely used material model confronted with the FSW in the published literature is the JC model. It is multiplicative in nature and is a function of strain, strain rate, and temperature. The JC model operates in the classic elastic-plastic framework, where an elastic constitutive model, a yield criterion, and a flow rule are utilized to model the elastic response, elastic-plastic boundary, and plastic flow, respectively (Gambirasio and Rizzi, 2014). Further, details of the JC model are provided in the literature (Gambirasio, 2013; Buzyurkin, Gladky and Kraus, 2015; Buchely *et al.*, 2019). The JC material model is expressed as (Al-Badour *et al.*, 2014)

$$\bar{\sigma}_s = [A + B\,\bar{\varepsilon}^n]\left[1 + C\,ln\left(\frac{\dot{\bar{\varepsilon}}}{\dot{\varepsilon}_0}\right)\right]\left[1 - \left(\frac{T - T_r}{T_m - T_r}\right)^m\right] \tag{4.8}$$

where m is the thermal softening coefficient, $\bar{\varepsilon}$ and $\dot{\bar{\varepsilon}}$ are effective plastic strain and strain rate respectively, $\dot{\varepsilon}_0$ is reference strain rate, A, B, C are material constants, n is the work-hardening exponent, T_r, and T_m are the reference room temperatures and melting temperatures, respectively. The majority of the literature ignores the inclusion of the JC damage model with the JC material model (Ambrosio, Tongne, *et al.*, 2023). The damage initiation or failure of elements is an important phenomenon to incorporate for the modelling of high distortion problems (Yu *et al.*, 2012). Ambrosio et al. (2023) investigated the improvement in the result proficiency during FSW with the inclusion of the JC damage model. They observed that without the use of the damage model, it is extremely difficult to fill the tunnel defect with the help of only the friction factor. Further, the use of the damage model reduces the maximum temperature observed at the tool-workpiece interface due to the failure of the workpiece material at the interaction zone and thus reduction in the frictional heating. This makes the prediction of the thermal results by the model more precise. The JC damage model is represented as (Johnson and Cook, 1985)

$$\Omega = \sum\left(\frac{\Delta\bar{\varepsilon}^{pl}}{\bar{\varepsilon}_f^{pl}}\right) \tag{4.9}$$

where $\Delta\bar{\varepsilon}^{pl}$is the increment in the effective plastic strain and $\bar{\varepsilon}_f^{pl}$ is the plastic strain in failure. The value of $\bar{\varepsilon}_f^{pl}$ is dependent on the material constants $d_1 - d_5$, stress ratio $\left(\frac{p}{q}\right)$ and temperature as given by

$$\bar{\varepsilon}_f^{pl} = \left[d_1 + d_2 exp\left(d_3 \frac{p}{q}\right)\right]\left[1 + d_4 ln\left(\frac{\dot{\bar{\varepsilon}}^{pl}}{\dot{\varepsilon_0}}\right)\right]\left[1 + d_5\left(\frac{T - T_r}{T_m - T_r}\right)\right] \quad (4.10)$$

where $d_1 - d_5$ are failure parameters measured at the material transition temperature, p and q are the pressure and von-Mises stress, respectively.

4.2.4 Thermal model

The frictional contact between the tool and the workpiece is the primary source of heat generation, whereas plastic heat generation aids in raising the temperature of the deforming material. The heat generation equation during FSW is given by:

$$\partial Q = \omega_v \partial M = \omega_v r \tau dA = \omega_v r^2 \tau d\theta dr \quad (4.11)$$

$$Q = \int_0^{2\pi} \int_{R_p}^{R_s} \omega_v r^2 \tau d\theta dr \quad (4.12)$$

where R_s is the radius of the shoulder, R_p is the radius of the pin, μ_f is coefficient of friction, τ is the contact stress, ω_v is the angular velocity in rad^{-1}. Further, the τ is evaluated according to Coulomb's law as follows:

$$\tau = \mu P \quad (4.13)$$

where P is the contact pressure. The plastic heat generated in the body is due to the plastic work done on the shear layer during the sticking phase and can be defined as

$$H_{plas} = \eta \sigma_d \dot{\varepsilon}_{plas} \quad (4.14)$$

where H_{plas} is the plastic heat generated, η is the thermal conversion efficiency, σ_d is the deviatoric stress and $\dot{\varepsilon}_{plas}$ is the plastic strain rate. The heat is conducted from the stir zone (SZ) to the rest of the workpiece in the form of conduction, while the workpiece losses heat to the ambient in the form of convection and radiation heat. The transient heat conduction equation is expressed as (Sahu and Bag, 2021)

$$\boldsymbol{\nabla} \cdot (k(T)\boldsymbol{\nabla} T) = \rho C_p \frac{\partial T}{\partial t} \tag{4.15}$$

while the convective and radiative heat losses are governed by (Prior, 1994; Harewood and McHugh, 2007)

$$q = h_{conv}(T - T_{amb}) + \omega\sigma_{sb}(T^4 - T^4{}_{amb}) \tag{4.16}$$

where k is thermal conductivity, C_p is specific heat capacity, h_{conv} is convective heat coefficient, ω is emissivity, σ_{sb} is Stefan-Boltzmann constant, T is temperature variable, T_{amb} is ambient temperature.

4.2.5 Mechanical model

The strain rate is calculated from the local velocity gradient (Arora *et al.*, 2009) as

$$\dot{\varepsilon}_{ij} = \frac{1}{2}\left(\frac{\partial u_i}{\partial x_j} + \frac{\partial u_j}{\partial x_i}\right) \tag{4.17}$$

where $\dot{\varepsilon}$ is the strain rate tensor, and $\frac{\partial u_i}{\partial x_j}$ is the velocity gradient. The strain is evaluated as

$$\varepsilon_{ij} = \int_0^t \dot{\varepsilon}_{ij} dt \tag{4.18}$$

The equivalent plastic strain ($\bar{\varepsilon}^{pl}$) is estimated as (Systèmes, 2007)

$$\bar{\varepsilon}^{pl} = \bar{\varepsilon}^{pl}|_0 + \int_0^t \dot{\bar{\varepsilon}}^{pl} dt \tag{4.19}$$

where $\bar{\varepsilon}^{pl}|_0$ is the initial equivalent plastic strain. $\dot{\bar{\varepsilon}}^{pl}$is the equivalent plastic strain rate and is calculated as per the material model adopted in the analysis. For the JC material model, the $\dot{\bar{\varepsilon}}^{pl}$ is defined as

$$\dot{\bar{\varepsilon}}^{pl} = \dot{\varepsilon}_0 \exp\left[\frac{1}{C}(R-1)\right] \qquad for\ \bar{\sigma}_s \geq \sigma^0 \tag{4.20}$$

where R is the yield stress ratio at a no-zero strain rate to the static yield stress, such that $R(\dot{\varepsilon}_0) = 1$. The von Mises equivalent stress (σ^{eq}) is defined as

$$\sigma^{eq} = \sqrt{\frac{3}{2}\boldsymbol{S}:\boldsymbol{S}} \tag{4.21}$$

where the deviatoric stress tensor $\boldsymbol{S}$ is defined as

$$\boldsymbol{S} = \boldsymbol{\sigma} + p\boldsymbol{I} \tag{4.22}$$

where $\boldsymbol{\sigma}$ is the stress, p is the pressure, and $\boldsymbol{I}$ is the unit matrix.

There are various actual and artificial energies associated with the CEL modelling of FSW. These are the elastic strain energy (SE), plastic strain energy (PD), and artificial strain energy (AE), and the kinetic energy (KE). The internal energy (IE) comprises of the SE, PD, and AE and is expressed as

$$IE = SE + PD + AE \tag{4.23}$$

The SE is negligible in the case of the FSW process. Moreover, the AE is the energy dissipated to control the artificial hour glassing effect, which does not have any physical significance (Systèmes, 2007). Thus, IE mainly accounts for the plastic deformation energy of the FSW system. Therefore, IE is approximated as

$$IE = \int_0^t \left(\int_v \sigma:\dot{\varepsilon} dV\right) dt \tag{4.24}$$

Since the plastic deformation path is highly nonlinear, the total strain is accounted for in an incremental mode. Therefore, the total strain rate is decomposed as

$$\dot{\varepsilon} = \dot{\varepsilon}^{el} + \dot{\varepsilon}^{pl} + \dot{\varepsilon}^{ae} \tag{4.25}$$

where $\dot{\varepsilon}^{el}, \dot{\varepsilon}^{pl}, \dot{\varepsilon}^{ae}$ are the elastic, plastic, and artificial components of the strain rate. Eq. 4.24 is thus modified to

$$IE = \int_0^t \left(\int_v \bar{\sigma}_s : \dot{\varepsilon}^{el}\, dV\right)dt + \int_0^t \left(\int_v \bar{\sigma}_s : \dot{\varepsilon}^{pl} dV\right)dt + \int_0^t \left(\int_v \bar{\sigma}_s : \dot{\varepsilon}^{ae} dV\right)dt \tag{4.26}$$

where $\bar{\sigma}_s$ is the stress derived from the JC constitutive equation. The KE of the system is calculated as

$$KE = \int_V \frac{1}{2}\rho \boldsymbol{v}.\boldsymbol{v} dV \tag{4.27}$$

where $\boldsymbol{v}$ is the velocity field vector. Further, the frictional heat generation is estimated as

$$FD = \eta\tau\frac{\Delta s}{\Delta t} \tag{4.28}$$

where Δs is the incremental slip, Δt is the incremental time.

4.2.6 Computational complexity

The explicit scheme is utilized for the current model due to its fast convergence to a solution while modeling complex contact problems (Harewood and McHugh, 2007). It is noteworthy that the time increment size for the explicit scheme is a function of element size and material properties only, unlike the implicit scheme (Prior, 1994). The explicit scheme follows a forward difference method to solve the heat transfer problem, thus allowing calculation from the current time step as (Systèmes, 2007)

$$\{T\}^{t+\Delta t} = \{T\}^t + \left\{\dot{T}\right\}^t \Delta t \tag{4.29}$$

where t is time, and $\{T\}^t$ is the temperature at time t. The values of $\left\{\dot{T}\right\}^t$ are computed as (Koric, Hibbeler and Thomas, 2009)

$$\left\{\dot{T}\right\}^t = [C]^{-1}\left(\int_{A_h}[N]^T h_{conv}(T - T_{amb})dA - \int_V [B]^T k[B]dV\{T\}^t\right) \tag{4.30}$$

where $[B]$ contains the spatial derivatives of the elemental shape function $[N]$, dA and dV are elemental surface area and volume, respectively, $[C]$ is the lumped capacitance matrix. Here, the solution is performed by inverted $[C]$, thus enabling an explicit solution for Eq. 4.30. The lumped capacitance matrix $[C]$ is given as

$$[C] = \int_V [N]^T \rho \left(\frac{dH}{dT}\right)^t [N] dV \tag{4.31}$$

where H is the enthalpy.

The mechanical analysis for FSW is performed by computing nodal acceleration terms that are explicitly advanced from the previous step without iteration. The dynamic equilibrium is solved at the beginning of each time step as (Cocchetti, Pagani and Perego, 2013)

$$\{\ddot{u}\} = [M]^{-1}\{f\} \tag{4.32}$$

where $[M]$ is the diagonal lumped nodal mass matrix, $\{\ddot{u}\}$ is the nodal acceleration at the beginning of the increment, $\{f\}$ represents the resultant force vector. The acceleration is assumed constant over a time step (Δt) and is integrated to calculate the change in velocity. Following the central difference scheme, the velocity in the current step is estimated as

$$\left\{\dot{u}^{t+\frac{\Delta t}{2}}\right\} = \left\{\dot{u}^{t-\frac{\Delta t}{2}}\right\} + \frac{(\Delta t^{t+\Delta t} + \Delta t^{t})}{2}\{\ddot{u}^t\} \tag{4.33}$$

Similarly, the displacement field at the end of the time step is calculated as

$$\{u^{t+\Delta t}\} = \{u^t\} + \Delta t^{t+\Delta t}\left\{\dot{u}^{t+\frac{\Delta t}{2}}\right\} \tag{4.34}$$

The explicit approach considers the contact variations as kinematic constraints. After each time increment, the displacement and velocity field engaged in contact are modified to maintain kinematical admissibility. In essence, this approach calculates nodal accelerations directly instead of using an iterative strategy or penalty method to establish contact equilibrium (Prior, 1994). Eqs. 4.29-4.34 signify the importance of the time step for the calculation of various output parameters for the thermo-mechanical analysis of the

FSW process. The explicit procedure starts with a small-time increment (Δt), and the total time (t) is divided into a large number of increments (n) as

$$n = \frac{t}{\Delta t} \tag{4.35}$$

An approximation for the result is performed at each time step by following central difference operators that are conditionally stable. The stability limit assuming no damping in the mechanical analysis is obtained by choosing (Systèmes, 2007)

$$\Delta t \leq \min\left(\frac{2}{\omega_{max}}, \frac{2}{\lambda_{max}}\right) \tag{4.36}$$

where ω_{max} and λ_{max} are the highest frequency (eigenvalue) in the system. The exact calculation of the highest frequency of the system is not always computationally feasible. Therefore, it is estimated as a function of the dilatational wave (v_w) in individual elements, which is mainly a function of the material properties. The time step increment for the mechanical analysis (Δt_{mech}) is given as (Olovsson et al., 2005)

$$\Delta t_{mech} \leq \frac{2}{\omega_{max}} \tag{4.37}$$

Further, the ω_{max} can be defined in terms of element length (L_e) and v_w as (Olovsson et al., 2004)

$$\omega_{max} = \frac{2v_w}{L_e} \tag{4.38}$$

$$\text{where} \quad v_w = \sqrt{\frac{\lambda_l + 2\mu_l}{\rho}} \tag{4.39}$$

where λ_l and μ_l are the Lame's constants. The Courant, Friedrichs, and Lewy (CFL) criterion for wave propagation indicates that the individual time step must be less than the time needed by v_w to pass through the smallest element (Cocchetti, Pagani and Perego, 2013). Thus, considering the smallest element in the domain with length (L_{min}), the time step from Eq. 4.37 can be calculated as

$$\Delta t_{mech} \leq \left(L_{min} \times \sqrt{\frac{\rho}{\lambda_l + 2\mu_l}} \right) \tag{4.40}$$

The numerical stability for the thermal analysis is expressed as (Koric, Hibbeler and Thomas, 2009)

$$\Delta t_{thermal} \leq \frac{\rho C_p L_{min}^2}{2k} \tag{4.41}$$

It is obvious that the mass scaling approach is associated with an artificial enhancement of elemental mass to increase the stable time increment in an explicit analysis. It is generally performed through the increase of material density. The increment in density is expressed as (Hammelmüller and Zehetner, 2015)

$$\rho^* = \kappa \times \rho \tag{4.42}$$

where κ is the mass scaling factor. Thus, Eq. 4.37 is modified as

$$\Delta t_{mech} \leq \left(L_{min} \times \sqrt{\frac{\rho^*}{\lambda_l + 2\mu_l}} \right) \tag{4.43}$$

such that, if the density is increased by a factor of 100, it would increase the stable time increment for mechanical analysis by a factor of 10 assuming that the minimum element size and other parameter remains same. It is obvious that the increment of density by a factor of κ should increase the time increment by a factor of $\sqrt{\kappa}$. The substitution of the density (ρ) by an artificial density (ρ^*) modifies the right-hand side of Eq. 4.15. This change is compensated by introducing an artificial specific capacity $(C_p' = \kappa^{-1} C_p)$ such that Eq. 4.15 is modified to

$$\nabla \cdot (k(T) \nabla T) = \rho^* C_p{}' \frac{\partial T}{\partial t} \tag{4.44}$$

Further, Eq. 4.41 is modified to

$$\Delta t_{thermal} \leq \frac{\rho^* C_p' L_{min}^2}{2k} \tag{4.45}$$

The value of κ is limited by the ratio of KE and IE of the system. The artificial mass increment also affects the momentum balance of the system. Thus, the artificial mass is chosen so that the rigid translational motion of the system is not affected. A detailed explanation to minimize the adverse effect of the artificial mass on the system is provided in the literature (Cocchetti, Pagani and Perego, 2013). This is ascertained by limiting the KE to IE ratio to a predefined 10% to maintain the quasi-static nature of the process (Zhang and Zhang, 2009).

4.2.7 Implementation in commercial software

Figure 4.2 shows the flow of the work using commercial software to model the FSW process. The designing of the different domains and associating them with the material properties are the initial steps for the numerical model. The interaction between the tool and the workpiece is defined by Coulomb's friction law. The boundary condition module is used to accommodate the convection and the radiation losses from the workpiece body. Further, the mechanical boundary conditions are also applied during this step. Although the convection and the radiation losses are applied to the top surface of the workpiece, the mechanical boundary conditions are not applied to ensure the free flow of the material from the workpiece domain. The workpiece and the tool are meshed separately while ensuring a finer mesh near the SZ. The load module is used to provide rotational and translational motion of the tool. The load is applied to one node of

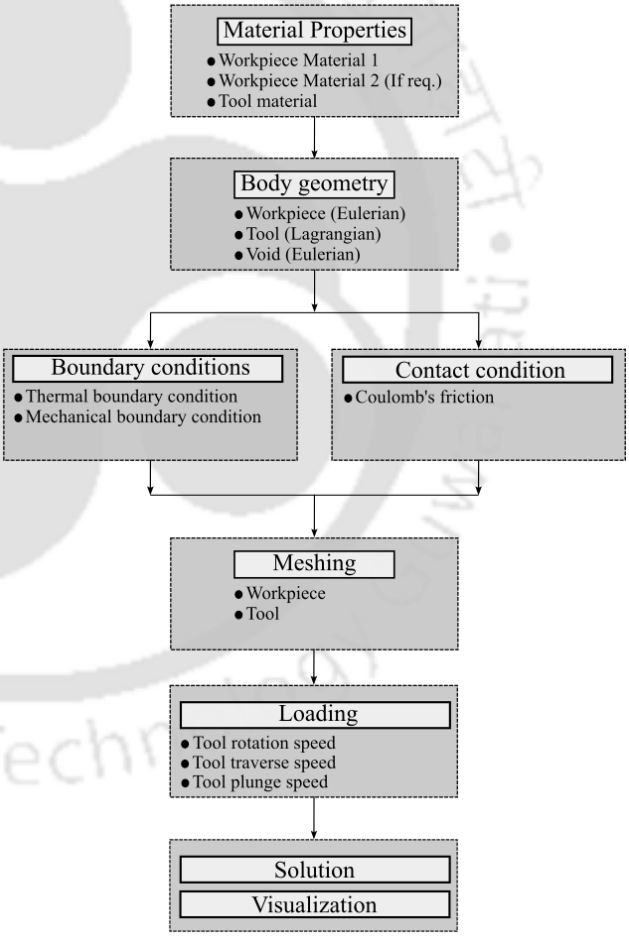

Fig. 4.2 Flow chart for the thermo-mechanical analysis of FSW

the tool, while all the other nodes are tied to the parent node. As the workpiece domain is an Eulerian domain, with a void domain on top of the actual workpiece domain, special care needs to be taken while filling each individual domain with material.

4.2.8 Solution domain and sensitivity analysis

The Eulerian workpiece domain used for the present work is $100\,mm \times 50\,mm \times 4\,mm$. The workpiece is discretized using an Eulerian brick element (EC3D8RT) and is divided into two regions (Fig. 4.3 (a)). The EC3D8RT is a 8 noded, thermally coupled brick element with reduced integration and hourglassing control (Systèmes, 2007). Region A signifies the stirred zone (SZ), thermo-mechanically affected zone (TMAZ), and heat-affected zone (HAZ). The mesh sensitivity analysis is performed by discretizing region A with a minimum mesh size of 0.6 mm to a maximum of 1.4 mm. Region A is bounded by a distance of 15 mm on both sides with reference to the weld centerline. Region B consists of base material (BM) where the coarse mesh (size of 5 mm) is considered. In total, eight elements are considered along the thickness direction uniformly. The nodes highlighted as points of interest (POI) in Fig. 4.3 (a) are used for mesh sensitivity analysis as the SZ observes the maximum in-process thermal and mechanical response variations. The mesh sensitivity analysis was performed by studying the thermal distribution as shown in Figs. 4.3 (b) and 4.3 (c). Figure 4.3 (b) shows the spatial temperature profile at different mesh sizes for AA6061. In a coarse mesh (size of 1.4 mm, 1.2 mm, and 1 mm), the temperature distribution shows a sudden increase or decrease unlike the 0.8 mm and 0.6 mm mesh sizes. Fig. 4.3 (c) shows the temperature variation with respect to time for both the 0.6 mm and 0.8 mm mesh sizes. The temperature differences are investigated at three different instances during the complete duration of welding. The highest difference in the predicted temperature between the 0.6 mm and 0.8 mm cases is within the 3% temperature range. Moreover, the model with 0.6 mm mesh takes about 22% more time than 0.8 mm mesh for the complete solution. Therefore, to keep a balance between the accuracy of the results and the total computational time, the 0.8 mm mesh size for the SZ is considered for the present investigation. Figure 4.4 shows the distribution of the final mesh sizes in the different regions of the workpiece used for the current work.

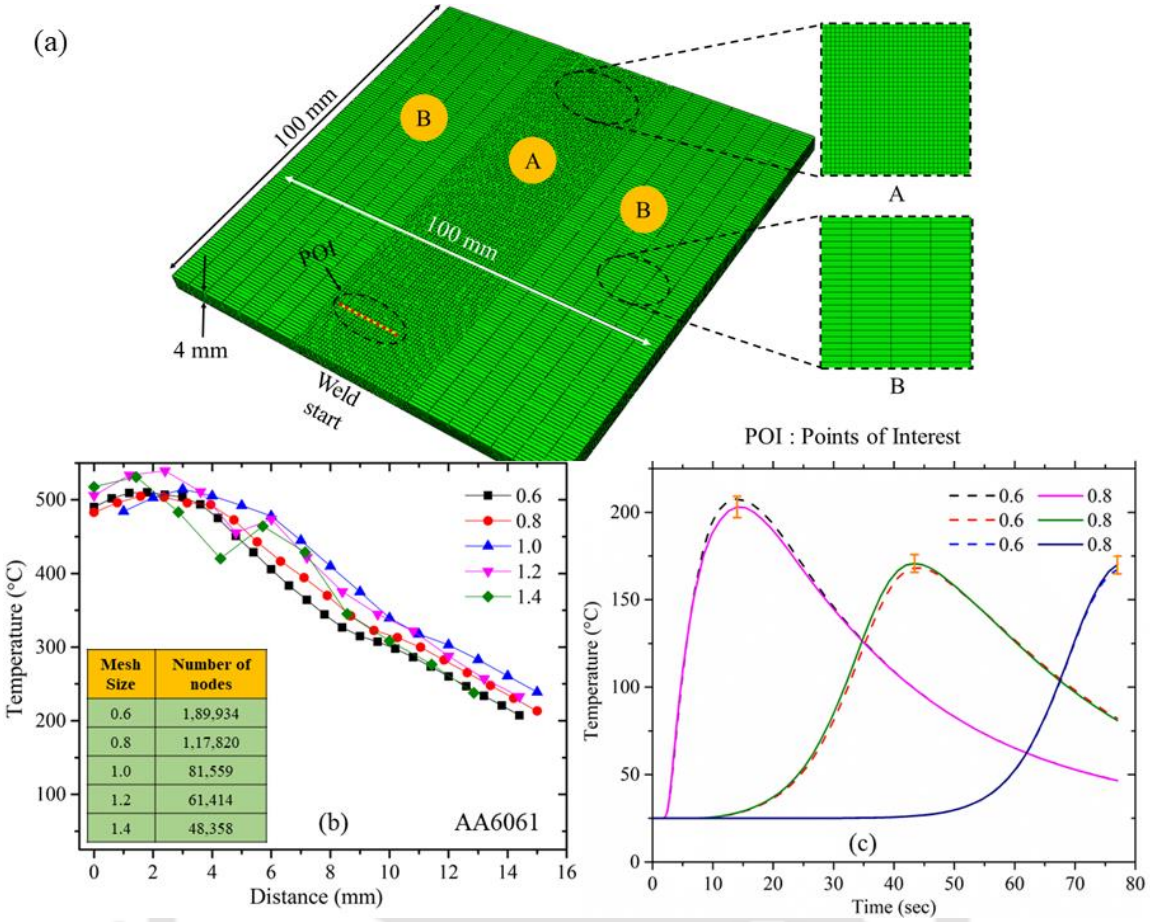

Fig. 4.3 (a) User-defined biased meshing scheme for workpiece domain; Mesh sensitivity analysis based on (b) temperature vs distance and (c) temperature vs time

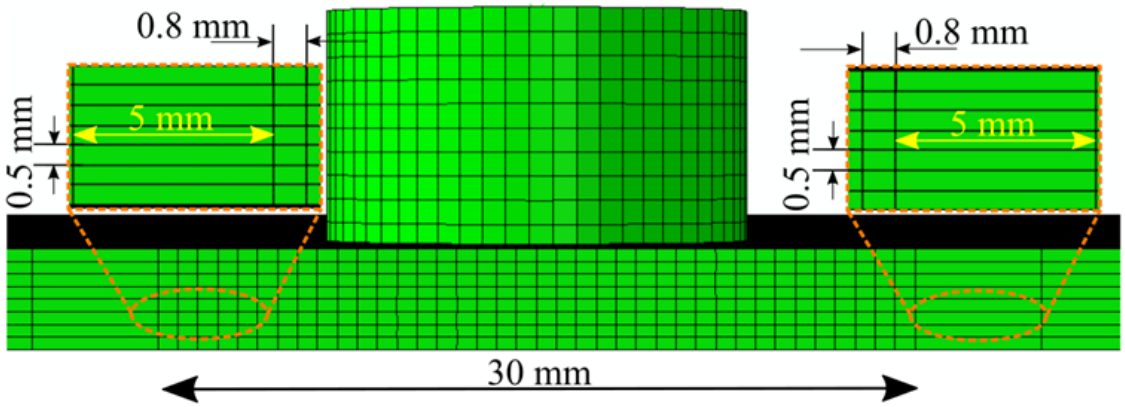

Fig. 4.4 User defined biased meshing of the computational domain for FSW modelling

Figure 4.5 shows both the cylindrical and conical tool used for the modelling of the FSW. The various tool geometries, such as the shoulder diameter, pin diameter, and pin height are considered as variables for the current work and it is modified accordingly. The tool is meshed using the unbiased meshing scheme. The tool is meshed with a uniform mesh size of 1 mm using the C3D8RT elements. These are 8 noded, thermally coupled brick elements with reduced integration and hourglass control. The main thrust of the current investigation is focussed on weld quality and defect prediction. Therefore, mesh sensitivity analysis for the tool domain is not performed. Moreover, the current study does not consider any wear or failure models for the tool.

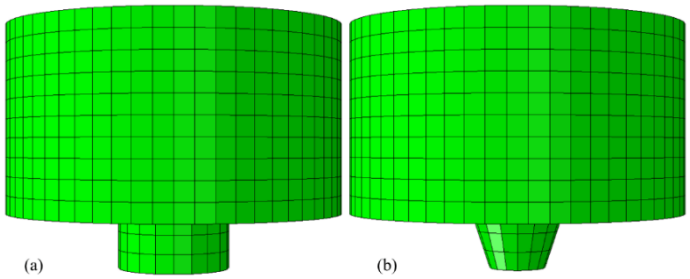

Fig. 4.5 Representation of the Lagrangian (tool) domain to model the (a) cylindrical and (b) conical tool

4.3 Material properties

This section details the various thermo-physical properties, thermo-mechanical properties, and other material constants used for the modelling of the FSW. The thermo-physical properties namely the thermal conductivity (k), density (ρ), and specific heat (C_p) are important for the evaluation of the thermal diffusivity. The thermo-mechanical properties including the modulus of elasticity (E), Poisson's ratio (ν), and coefficient of thermal expansion (α) are responsible for the various mechanical output responses by the numerical model. These thermo-physical and thermo-mechanical properties are material specific and vary with temperature. Other material properties such as the latent heat of fusion, and the melting temperature (T_m) are also incorporated into the model to correctly evaluate the temperature evolution and material flow within the body. These properties are temperature independent and are only material specific. Further, a constant coefficient of friction, i.e., 0.3, is used at the tool-workpiece interface. The various thermo-physical and thermo-mechanical properties of AA6061 and AZ31B are provided in Tables 4.1 and 4.2, respectively.

The determination of the material constants for the JC model is a herculean task and requires multiple experiments for torsion, tensile, and Hopkinson test data at various temperatures (Jain, Pal and Singh, 2017). Further, the five JC damage parameters

$(d_1, d_2, d_3, d_4, d_5)$ can be determined by the quasi-static uniaxial tensile tests of notched bar specimens (Cao *et al.*, 2020). Although the determination of the JC material and damage parameters as difficult; however, the JC model can be easily incorporated into various numerical techniques. The most important advantage of the JC model is its adaptability over a wide range of deformation and temperature values (Kuykendall, Nelson and Sorensen, 2013). Moreover, the JC model can incorporate the thermal softening effect of the material flow. Due to all these benefits, the JC model is incorporated with the CEL approach for the current investigation. The material specific constants for the JC material and damage models used for the AA6061 and AZ31B are provided in Tables 4.3- 4.6.

Table 4.1. Thermo-physical and thermo-mechanical properties of AA6061 (Al-Badour *et al.*, 2013)

$\boldsymbol{T}$ **(°C)**	**25**	**100**	**149**	**201**	**260**	**316**	**371**	**427**	**482**
$\boldsymbol{E}$ **(GPa)**	66.94	63.21	61.32	56.80	51.15	47.17	43.51	28.77	20.20
$\boldsymbol{\nu}$	0.33	0.334	0.335	0.336	0.338	0.36	0.40	0.41	0.42
$\boldsymbol{C_p}$**(Jkg^{-1}°C^{-1})**	945	978	1000	1030	1052	1080	1100	1130	1276
$\boldsymbol{\rho}$**(kgm^{-3})**	2690	2690	2670	2660	2660	2630	2630	2600	-
$\boldsymbol{\alpha}$**(µmm^{-1}°C^{-1})**	23.5	24.6	25.7	26.6	27.6	28.5	29.6	30.7	-
$\boldsymbol{k}$ **(Wm^{-1}°C^{-1})**	162	177	184	192	201	207	217	229	-

Table 4.2. Thermo-physical and thermo-mechanical properties of AZ31B (Hou *et al.*, 2018)

$\boldsymbol{T(°C)}$	**20**	**75**	**100**	**125**	**150**	**200**	**250**
$\boldsymbol{E\ (GPa)}$	40.2	37.3	34.3	30.9	30.4	29.4	27.5
$\boldsymbol{T(°C)}$	**25**	**100**	**200**	**300**	**350**	-	-
$\boldsymbol{k(Wm^{-1}°C^{-1})}$	96.4	101	105	109	113	-	-
$\boldsymbol{T(°C)}$	**20**	**100**	**200**	**300**	**350**	-	-
$\boldsymbol{C_p(Jkg^{-1}°C^{-1})}$	1050	1130	1170	1210	1260	-	-
$\boldsymbol{T(°C)}$	**100**	**200**	**300**	-	-	-	-
$\boldsymbol{\alpha(\mu mm^{-1}°C^{-1})}$	26.4	27.0	27.9	-	-	-	-

Table 4.3. Johnson-Cook material constant for AA6061 (Al-Badour *et al.*, 2014)

A (MPa)	B (MPa)	C	m	n	T_r (°C)	T_m(°C)
324	114	0.002	1.34	0.42	24	583

Table 4.4. Johnson-cook damage parameters for AA6061 (Hou *et al.*, 2018)

Materials	d_1	d_2	d_3	d_4	d_5
AA6061	0.071	1.248	1.142	0.147	0

Table 4.5. Johnson-Cook material constant for AZ31B (Hou *et al.*, 2018)

A (MPa)	B (MPa)	C	m	n	T_r (°C)	T_m(°C)
279.827	159	0.013	1.573	0.327	22	605

Table 4.6. Johnson-cook damage parameters for AZ31B (Abbassi *et al.*, 2016)

Materials	d_1	d_2	d_3	d_4	d_5
AZ31B	-0.35	0.6025	-0.4537	0.206	7.2

4.4 Summary

The current chapter summarizes the numerical modelling of the FSW process using the CEL approach. The FSW process observes maximum material straining and mixing in the workpiece SZ. Alternatively, negligible material movement is observed in the tool. Therefore, the workpiece is defined as an Eulerian domain, such that the material flows through the fixed nodes of the domain. This ensures any adverse issues with excessive mesh deformation do not arise within the computational domain. Alternatively, the tool is defined as a solid Lagrangian body such that the geometric integrity of the body is retained during the welding process. The tool-workpiece interaction is defined such that the frictional contact between the tool and workpiece causes temperature generation. The convection and the radiation coefficients are also modelled on the different workpiece surfaces to account for the heat losses. The Coulomb's friction law is used to model the contact between the tool and the workpiece. The JC material and damage models are included to account for the flow stresses and material movement during the welding process. The material movement helps to investigate the material mixing and deposition behind the traversing tool. The tracking of the material movement following the EVF technique helps to predict

the various subsurface defects associated with FSW. The material movement causes some elements in the computational domain to be completely filled, partially filled or completely empty. Tracking such elements with the EVF techniques helps predict the formation of tunnel defect, void defect, weld quality with partially or completely failed joints, and exit holes. The CEL techniques profess to utilize a third void domain on top of the workpiece domain. The sole responsibility of the void domain is to collect the material coming out of the workpiece domain during the plunging and further interactions of the tool with the workpiece. The application of this third domain provides the flash formation numerically.

Chapter 5

Result and Discussions

5.1 General Background

Although the FSW process is a commonly used joining process for low melting point materials, it is not completely free from deleterious surface and sub-surface defects. The prediction of defects such as tunnel defects, flash formation, voids, failed joints, and inhomogenous material mixing brings the opportunity to produce the feasible range of parameters for a defect-free weld. The numerical modelling approach is realized to predict the defects and the weld quality to reduce material wastage. The current work follows the finite element modelling of defects using the CEL approach from the perspective of a high-strain rate FSW process. Effectively, the model predicts the thermo-mechanical responses and weld quality for similar (AA6061 and AZ31B) and dissimilar (AA6061-AZ31B) joining. A wide range of process parameters are considered by varying the tool rotation speed, traverse speed, plunge depth, and tool geometry to evaluate any defect formation in FSW of different types of material combinations. The results include the temperature evolution on the workpiece and its comparison with the experimental data to validate the model. The model is further validated using the residual stress data. The temperature distribution is shown on both the advancing and the retreating sides of the workpiece due to the non-uniform nature of heat distribution on the workpiece. The literature highlighted the high computational cost as one of the key drawbacks of the CEL approach. The mass scaling approach is used to reduce the associated high computational cost with the numerical model. A discussion is provided regarding mass scaling and its effect on the total computational time, weld quality, and thermo-mechanical responses, for different types of

materials. The effect of varying process parameters on mass scaling is also analyzed to encounter the high computational time. After the successful development and implementation of the model, it is used to predict the surface morphology and sub-surface defects appearing during the FSW process. The numerically predicted results, such as chip height and chip width, the geometric dimensions of various defects, and residual stresses are supplemented with experimental results. The material flow in similar FSW and material mixing in dissimilar FSW provide key insight into the formation of defects. The influence of tool wear on defect formation is also investigated in dissimilar FSW process. The effect of tool wear and plate position is considered for determining the weld quality. In general, this section demonstrates the results in terms of temperature distribution, material flow and identification of defects, the influence of process parameters on defect formation, and surface morphologies at different process conditions.

5.2 Temperature evolution and validation

Different materials are used for the current investigation, i.e., the AA6061 and AZ31B. As the material properties are different in both cases, the numerically predicted temperature results are validated with the experimental results for both AA6061 (Figs. 5.1 and 5.2) and AZ31B (Fig. 5.3), individually. The experimental and simulated temperatures for the AA6061 are compared in Fig. 5.1. The temperature measurement is performed using an Infrared camera. A 3% error bar is considered on the experimental data. The difference between both results lies within the 3% range. The small difference may be due to the constant convection and radiation losses considered for the numerical model, and material properties used in the model. Moreover, slight errors can also creep in during the experimental temperature measurement, affecting the accuracy of the results. Three discrete points are considered to validate the result, as shown in Fig. 5.1. The points beyond these three points are not considered due to the presence of the clamps, which hinders the

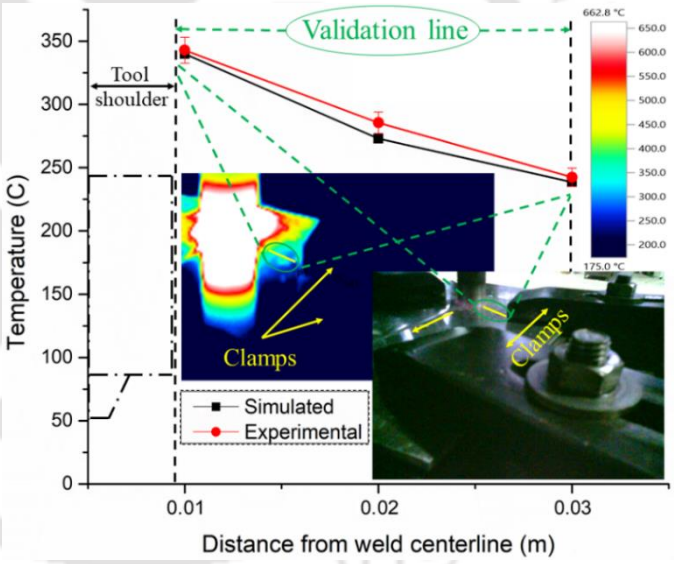

Fig. 5.8.1 Comparison between the simulated and the experimental temperature data for FSW at 1200 rpm and 90 mm/min

temperature measurement on the surface of the workpiece. Fig. 5.2 shows the predicted temperature data on both the AS and RS of the weld centreline. It is observed that the peak temperature on the AS is slightly higher than the RS. The temperature difference at the same distance on both sides of the weld centreline is about 5˚C to 10˚C. Hamilton et al. (Hamilton *et al.*, 2013) made a similar observation in independent literature.

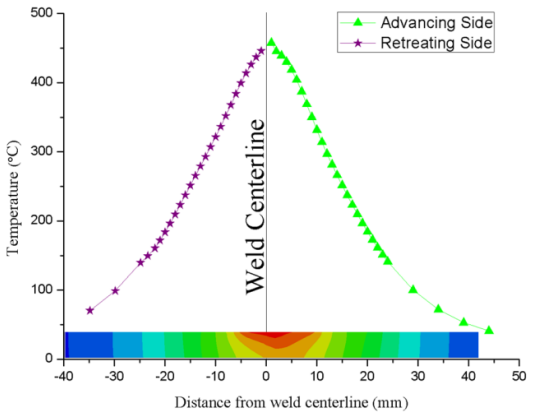

Fig. 5.2 Temperature change in the workpiece on advancing and retreating sides

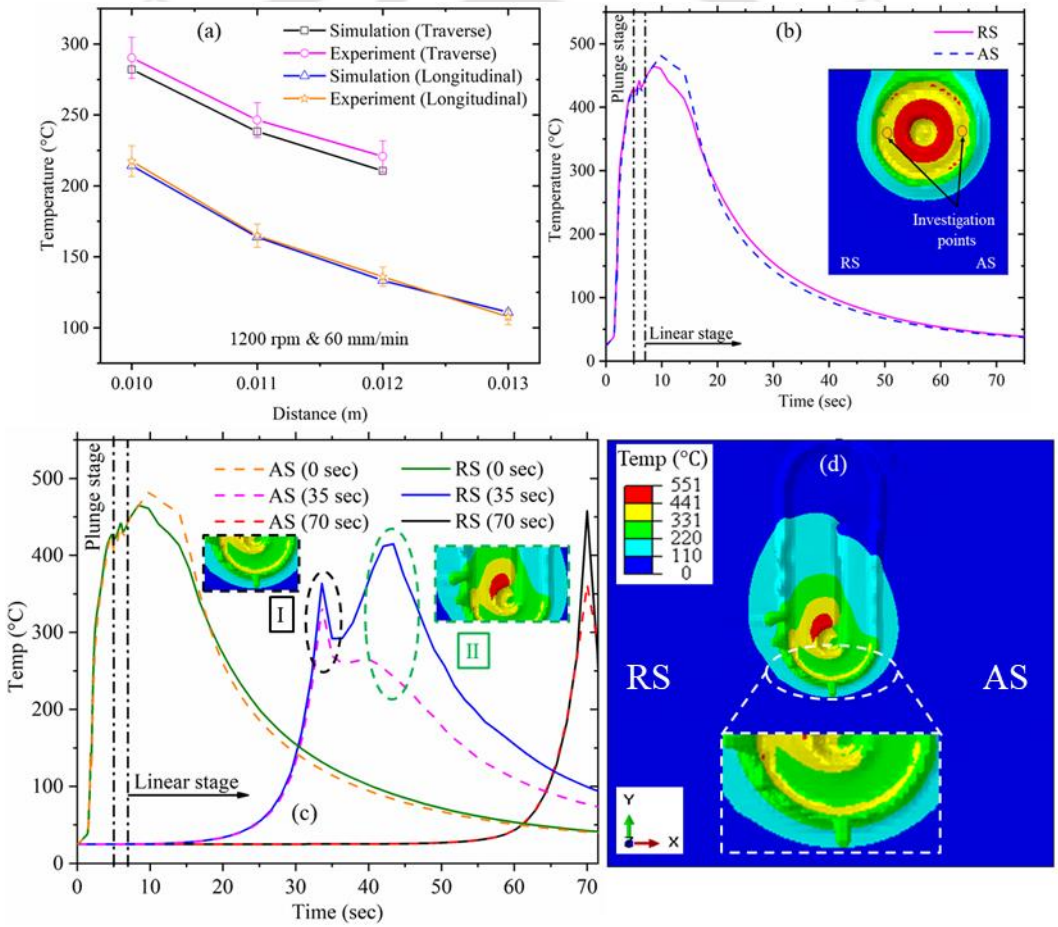

Fig. 5.3 (a) Experimental and numerically predicted temperature profile for AZ31B at 1200 rpm and 60 mm/min, (b) temperature vs time progression towards the AS and RS at weld start, (c) temperature vs time progression towards the AS and RS at weld start, middle and weld end, (d) temperature profile at tool shoulder interaction

Figure 5.3 (a) shows the validation of results with experiments for 0.8 mm mesh. The temperature validation is performed both in the traverse and the longitudinal directions, i.e.,

away from the weld centerline and in the direction of the tool travel, respectively. The temperature prediction is within a reasonable ~ 5% range. Henceforth, the mesh size of 0.8 mm is used for the current work. The temperature measurement near the tool shoulder is performed using an IR camera. The presence of workpiece clamps limits the further measurement points of the temperature. The limited discrepancy between the experimental and numerically computed temperature ascertains the accuracy of the model. Fig. 5.3 (b) shows the temperature distribution on the AS and RS after 10 seconds of welding. The AS shows a relatively higher temperature as the tool passes the region. However, with the passage of time, the temperature on both sides of the weld centerline becomes comparable. Figure 5.3 (c) shows the comparison between the temperature evolution on the AS and the RS as the welding progresses. As the tool is near half of the total weld length, two separate peaks (denoted by I and II) are observed instead of the conventional one peak. The peak I appear due to the higher temperature at the tool shoulder periphery where the material is being actually pushed in the forward direction. As the tool periphery passes the regions, there is a drop in temperature, and the highest temperature is observed when the tool shoulder passes the region. A significant temperature difference is observed between the AS and RS temperatures around half of the welding length. The RS temperature is observed to be significantly higher than the AS. This temperature difference appears due to the presence of the surface tunnel defect. As the material is removed out of the AS, the temperature rise on AS is limited (Fig. 5.3 (d)) and remains below the RS temperature.

5.3 Mass scaling factor in CEL approach

The instrumentation of computational time largely depends on the mass scaling factor in the CEL approach. An artificial increase of the mass of the system upto a certain extent judiciously reduces the computational time without affecting the solution quality. Hence, the mass scaling factor is an important parameter for computationally intensive CEL model, specifically for large deformation FSW problem. This mass scaling factor is sensitive to the density of the material and hence to the type of materials. This section demonstrates the effect of the mass scaling factor for similar and dissimilar materials' joining by the FSW process.

5.3.1 Effect of process parameters on mass scaling for FSW of AA6061

The analysis of the mass scaling factor starts with the different energy calculations associated with the welding system. Figure 5.4 shows the KE to IE ratio during the welding process. Two different plunge depth values, i.e. 0.1 mm and 0.5 mm are used to investigate

the effectiveness of mass scaling in this model. These plunge depth values are chosen since good quality welds can be obtained with plunge depth ranging between 0 and 0.5 mm (Q. Zheng *et al.*, 2017). The tool rotation speed is used as 1200 rpm, and the traverse speed is 90 mm/min. The highest percentage of 0.41% is observed for the KE to IE ratio in the case of 0.1 mm plunge depth, while 0.3% is the highest value observed with 0.5 mm plunge depth. A value of less than 10% ensures that the process remains quasi-static in nature and thus ensures the mass scaling factor is not adversely affecting the predicted results (Zhang and Zhang, 2009; Riahi and Nazari, 2011). A mass scaling factor of 10^7 is used in this study. In both cases, the highest value of the ratio is observed just before the end of the plunge step when there is a significant change in the energy estimation (Fig. 5.4) as the tool shoulder starts interacting with the workpiece. The highest KE to IE ratio remains below 1% for both cases. A similar trend is also obtained in the published literature (Riahi and Nazari, 2011). The sudden increase in the KE of the system, as seen from Fig. 5.5, is responsible for the increase in the KE to IE ratio. As the FSW progresses to the dwell and linear stages of welding, the KE of the system reduces from the highest value and becomes practically constant. A similar trend is observed in the KE to IE ratio also. After the completion of the plunge stage, the KE to IE percentage observes a decline and becomes almost negligible. The IE is the summation of the elastic strain energy (ALLSE), plastic strain energy (ALLPD), and artificial strain energy (ALLAE). The ALLAE is the energy dissipated primarily to control the non-physical hourglassing deformation (Systèmes, 2007). The variation of various components of IE is provided in Fig. 5.6. During the plunge stage, the ALLSE, the ALLPD, and the ALLAE are relatively less, which observes a significant increase when approaching the dwell stage. In the final two stages of the welding, there is a linear increase in the energy values till the completion of the linear stage. Fig. 5.6 also clearly highlights the fact that the heat generation due to plastic deformation is significantly larger than the heat generation due to elastic deformation. Another important form of energy encountered during FSW is frictional energy. This energy is majorly responsible for the generation of heat responsible for the joining of the plates. The frictional heat generation is almost 90% of the total heat generated in the body (Aziz *et al.*, 2018). The total frictional energy change with the increase in the welding time is shown in Fig. 5.7. The frictional energy during the plunge stage is practically negligible compared to the rest of the stages. This limited frictional energy is due to the very limited contact area of the tool and the workpiece. On the completion of the plunge stage, as the tool shoulder interacts with the workpiece, an instantaneous rise in the frictional energy is observed. The

total frictional energy at the end of dwell stage for P_d~0.1 mm is 35633.5 J, while the total frictional energy at the end of dwell stage for P_d~0.5 mm is 49362.4 J. This slightly higher frictional energy trend for the P_d~0.5 mm case than the P_d~0.1 mm case holds until the completion of welding. This difference in the total frictional energy can be due to more contact area between the tool and the workpiece for the P_d~0.5 mm. A similar range of frictional energy dissipation is obtained in the published literature (Ansari and Behnagh, 2019).

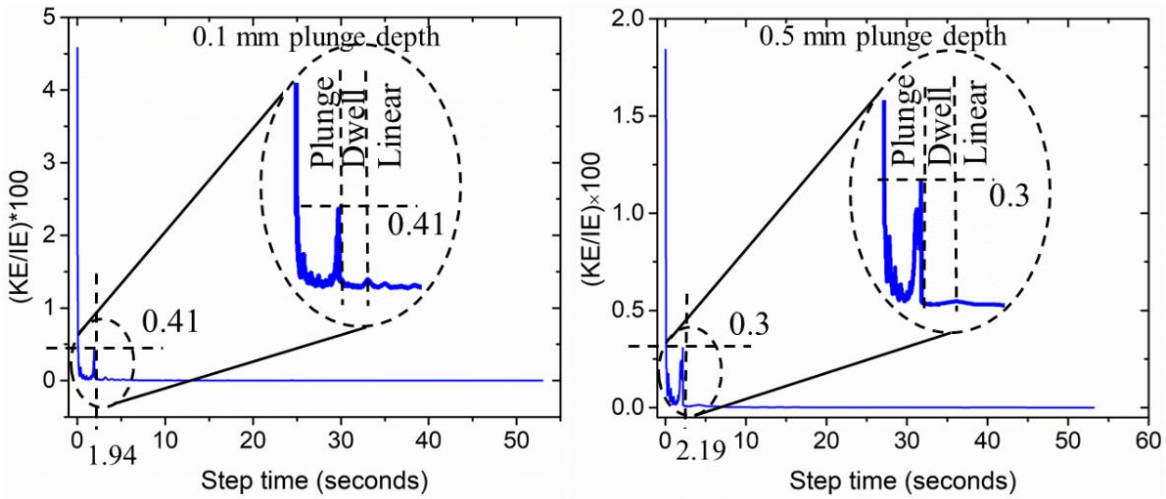

Fig. 5.4 Effect of different plunge depths (a) 0.1 mm and (b) 0.5 mm on the ratio of kinematic to internal energies (KE to IE) originating at different stages of FSW process.

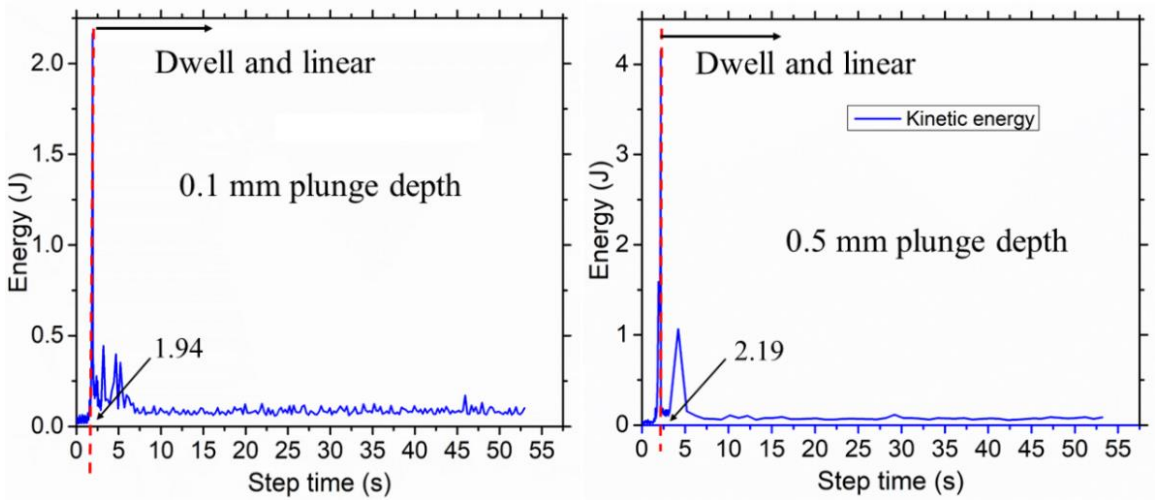

Fig. 5.5 Influence of varying plunge depths (a) 0.1 mm and (b) 0.5 mm on the generation of the KE for different stages of FSW occurring at 1200 rpm and 90 mm/min

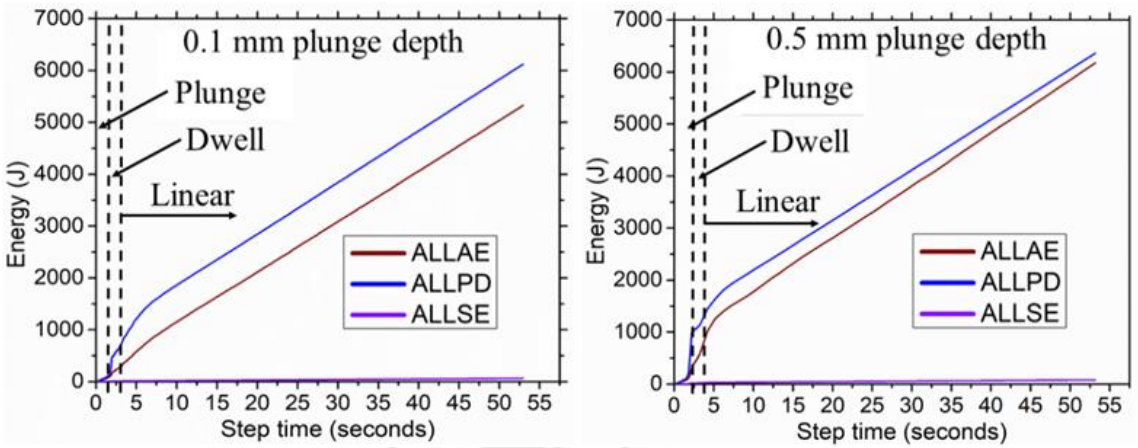

Fig. 5.6 Illustration of the generation of IE in the solution domain at different stages of FSW performed at 1200 rpm and 90 mm/min for varying plunge depths of (a) 0.1 mm and (b) 0.5 mm

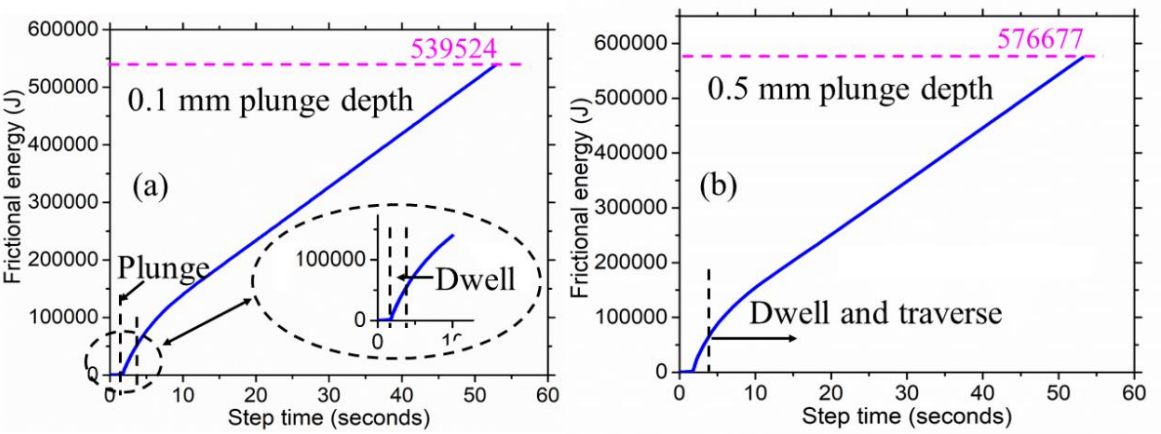

Fig. 5.7 Graphical representation of the variation in the frictional energy due to different plunge depths of (a) 0.1 mm and (b) 0.5 mm when the tool is moving at 1200 rpm and 90 mm/min

5.3.2 Effect of mass scaling on weld quality for dissimilar FSW of AA6061-AZ31B

The mass scaling factor (κ) of 10^7 is used to model of FSW process for both AA6061 and AZ31B alloys. In both cases (Figs. 5.8 and 5.9), the highest KE to IE ratio remains below the critical value of the 10% mark. The experimental validation of the results is shown in Figs. 5.8 and 5.9 are presented in Figs. 5.29 and 5.42, respectively. At the end of the plunging stage, there is a sharp rise in both the KE and IE of the system. As the welding progresses to the dwelling stage, the KE to IE ratio becomes negligible (Fig. 5.9). A similar trend is observed for the AZ31B till the completion of the dwell stages, as seen in Fig. 5.8 (a). As the tool progresses for the linear stage, the ratio remains minimal for the welding of AA6061 (Fig. 5.9), whereas two different peaks are observed in the KE for the welding of AZ31B. At the same time, a slight rise in the KE to IE ratio is observed. It is noteworthy that even with a sudden peak in KE, the ratio remains well within the acceptable limit. When the tool moves from a region of proper weld to improper weld, a sudden increase in the KE of the system (Fig. 5.8 (a)) is observed. Fig. 5.8 (b) shows the change in the surface profile during welding of AZ31B alloy. Multiple surface defects are observed at time 21 s (marked by I) and at time 55 s (marked by II). The jump in the KE is observed only when the tool moves from a proper weld region to a defective weld. Alternatively, such KE variations are absent in the case of either completely defective (Fig. 5.9 (a)) or proper welding occurs (Fig. 5.9 (b)). The continuous rise in the IE of the system (Figs. 5.8 and 5.9) is due to a similar increase in its constituent energies as observed in Figs. 5.10 (a) and (b).

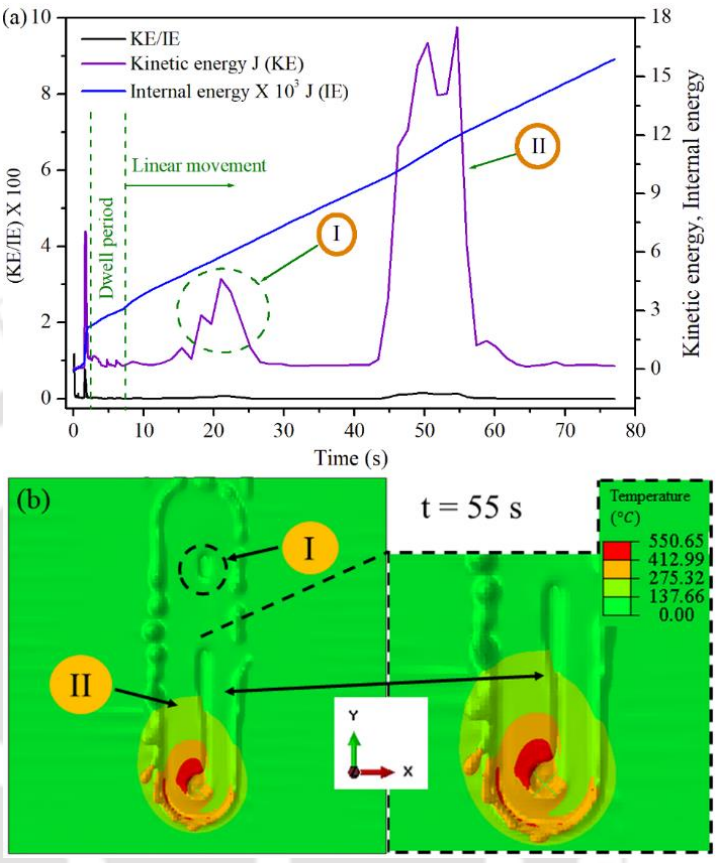

Fig. 5.8 (a) KE/IE ratio and (b) variation in the surface profile with the progress of welding for AZ31B at 1200 rpm, 60 mm/min, and 0.2 plunge depth

FD shows a minimum value during the plunge stage as the surface contact area between the tool, and the workpiece is low. As the welding progresses towards the dwell and linear stages, the FD increases with an increase in the tool-workpiece contact area. A similar increase in the PD and AE energies is observed with the progress of welding. The PD is significantly less than the FD, thus highlighting the well-known fact that the primary mode of heat generation in FSW is frictional contact. The SE during the FSW is marginal and is significantly lower than the PD, as observed in Fig. 5.10. Figures 5.8 and 5.9 show the energy variations when the weld defects are encountered. However, these energy variations cannot be used as distinct indicators to determine weld quality. The energy changes other than KE are minimal. Moreover, the KE changes indicate the change in the state of motion of the tool without giving a clear idea about the nature of the weld (Figs. 5.8 (a) and (b)). Material flow can be treated as a primary indicator for defect prediction, whereas the energy changes are the secondary indicators. Here, the analysis of different energy variations is helpful only to determine the proper application of the mass scaling for the CEL approach. From this analysis, it can be realised that the κ of 10^7 produces an acceptable result for both similar and dissimilar FSW with AA6061 and AZ31B. The said κ also helps to reduce the total computational time drastically as explained in the subsequent sections.

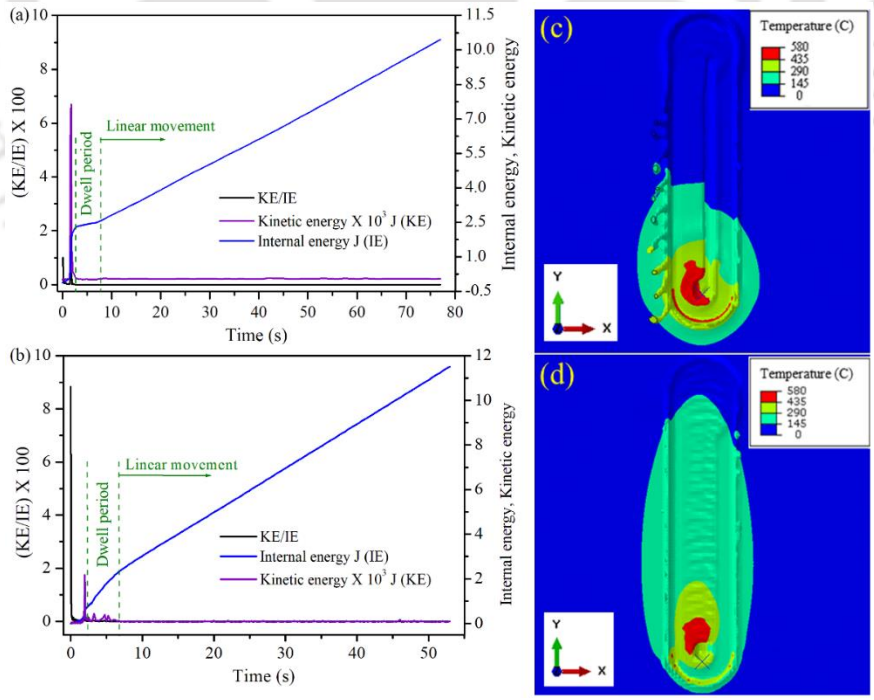

Fig. 5.9 (a) KE/IE ratio and (c) surface profile variation at 1200 rpm, 60 mm/min and 0.2-plunge depth; (b) KE/IE ratio and (d) surface profile variation at 1200 rpm, 90 mm/min and 0.1 plunge depth for AA6061

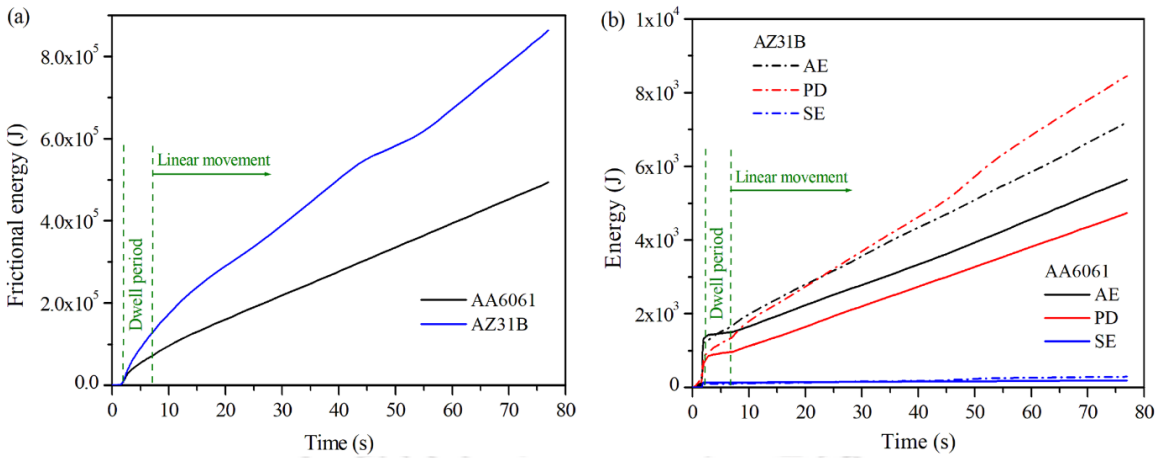

Fig. 5.10 Variation of the (a) frictional energy (FD); (b) artificial energy (AE), plastic energy (PD), and elastic strain energy (SE) for AA6061 and AZ31B alloys.

5.3.3 Limiting computational cost

Figure 5.11 illustrates the total computational time required to model the welding process with various mass scaling factors. Five different mass scaling factors are compared, as shown in Fig. 5.11. On increasing the mass scaling factor from 10^3 to 10^7, the total computational time is reduced by almost 100 times. A i-7 processor, with 8 GB RAM was used for the current investigation. The total computational time required for various mass scaling factors such as 10^3, 10^4 and 10^5 cases are significantly high and it is not feasible to simulate such cases. Therefore, the simulation for such cases is performed for the initial plunge stage only, and the total time required is linearly extrapolated. Since the mesh size and number of variables remain constant throughout the welding process, it can be stated with confidence the total time required to complete the simulation can be predicted by the linear extrapolation of the first step.

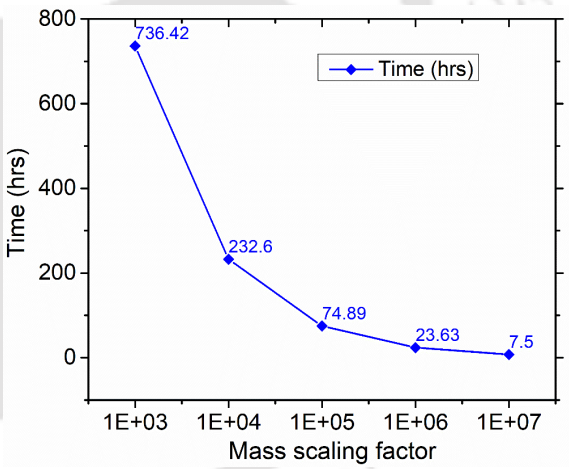

Fig. 5.11 Illustration of the change in total computational time with varying mass scaling factor

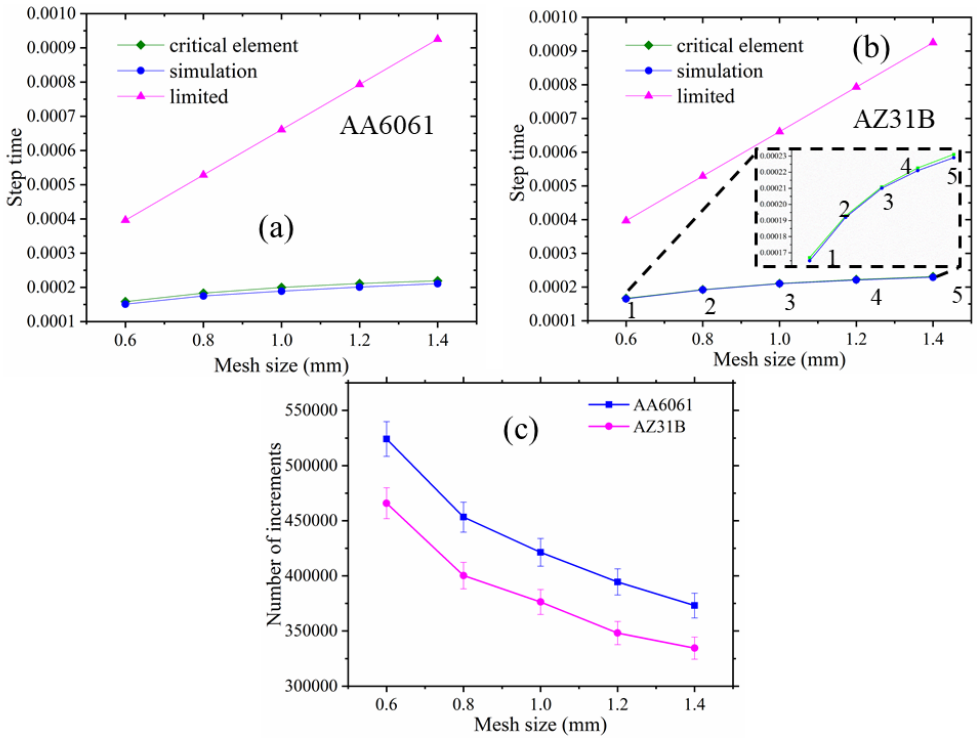

Fig. 5.12 Comparison between the limited (calculated by Eq. 28), simulation and critical time increment (a) AA6061, (b) AZ31B, and (c) the number of increments required for both (a) and (b)

Figure 5.12 shows the step time increment for different mesh sizes and different metal alloys. A comparison is drawn between the limited time increment calculated from Eq. 4.43, the time increment used in the simulation, and the time step for the most critical element in the solution domain. As observed from Eq. 4.43, the time increment depends not only on the density of the material but also on the critical length of the elements. Some researchers have proposed that the simulation time increment for a system will lie between the range of $1/\sqrt{3}$ to 1 time of the actual step time for a 3D computational domain (Schmidt and Hattel, 2005). The reason for proposing this range is a more precise calculation of step time using Eq. 4.43 for 2D cases than for 3D cases. Although the mass scaling can increase each step time increment, the presence of the critical element limits this increment. The step time increment for the complete solution domain is controlled by the dilatational waves to pass through the smallest element in the domain, i.e., the critical element. Thus, the step time increment used in the simulation is always less than the critical time in all the cases considered (Fig. 5.12). A simple yet efficient method to further improve the increment time is to identify the critical elements and increase the size of the particular elements without affecting the resulting output. It is evident from Figs. 5.12 (a) and (b) that the step increment time for AZ31B is marginally higher than the AA6061 welding. Therefore, the total number

of increments required for AZ31B is less than the aluminum alloy. Figure 5.12 (c) shows the number of increments required in the case of AA 6061 and AZ31B alloys. In this study, more significance is given to the number of increments than the total computational time, as the total computational time is dependent on the available computational facility. Moreover, the condition of the computational facility can vary over time.

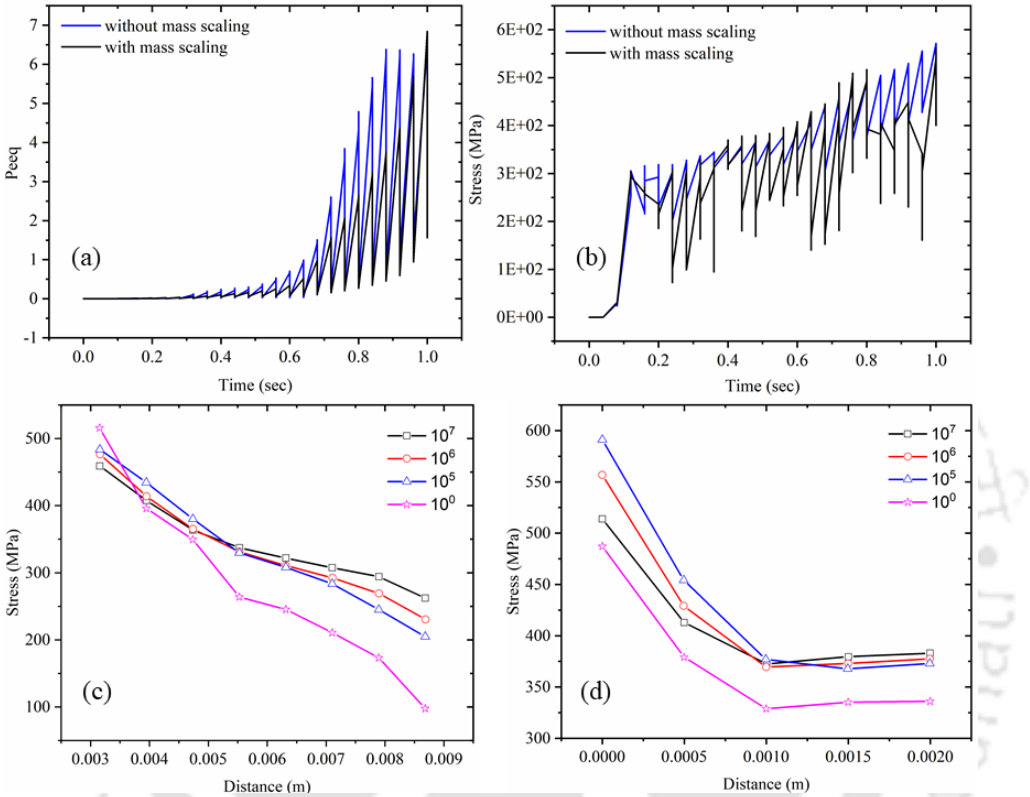

Fig. 5.13 Numerical prediction of (a) Equivalent plastic strain ($\bar{\varepsilon}^{pl}$) and (b) Stress (σ^{eq}) in the workpiece (AZ31B) with and without mass scaling; variation of stress distribution for different values of κ along the (c) traverse and (d) depth direction

Figures 5.13 (a) and (b) show the numerically predicted equivalent strain and stress on the workpiece surface in contact with the tool pin bottom surface at two different values of κ. The current analysis is restricted to the initial 1 second of the plunging stage as it takes huge computational time to perform the analysis without any mass scaling effect. A detailed description of the computational time dependence of κ is provided in the published literature (Hammelmüller and Zehetner, 2015). There is a time lag of about 0.3 seconds between the highest value of $\bar{\varepsilon}^{pl}$ for $k = 10^7$ and $\kappa = 1$. Simultaneously, there is a slight difference in the stress distribution between the two cases. Figures 5.13 (c) and (d) show the variation in the stress distribution along the traverse and the depth direction for $\kappa = 10^7, 10^6, 10^5, 10^0$. The stress variation is similar near the SZ between the $k = 10^0$ and

$\kappa = 10^7$ cases. However, the difference in the stress distribution increases as one moves away from the weld centerline (Fig. 5.13 (c)). Moreover, there is an over-prediction of stress in the depth direction between the $\kappa = 0$ and $\kappa = 10^7$ cases (Fig. 5.13 (d)). The significant difference between the total time required to model the FSW process using $k = 1$ and $\kappa = 10^7$ varies between about 168 hours and 5 minutes, respectively, using the computing facility of an i7 Intel processor and 16 GB RAM for the initial 1 seconds of plunging. This difference in the computational time between the two cases highlights the advantage of using κ in the FSW model to make it computationally feasible. Alternatively, there is not much difference in the predicted results between the $10^7, 10^6, 10^5$ cases, and therefore, the $\kappa = 10^7$ is used for the current work due to the least total computational time required.

5.3.4 Effect of mass scaling on mechanical reponses

Currently, the literature lacks a comprehensive study to determine the correlation between different MSFs, quality of result, and computational time. An attempt to remedy the same is deployed in Fig. 5.14 at different MSFs (κ values). Figure 5.14 shows the variation of the stress, strain rate, material flow velocity, and computational time for the initial 1s period of the FSW process when the tool is rotating at 1200 rpm and the workpiece material is AZ31B. The mechanical responses such as the strain rate and stress depend on the material flow velocity. As the κ increases, the mass of the material increases, thus reducing the velocity and affecting the other mechanical responses. The case with $\kappa = 1$ is without any MSF and takes about 1 week to simulate the initial 1 s of welding using the computing facility of an i7 Intel processor and 16 GB RAM, whereas the same can be simulated in about 300 s using $\kappa = 10^7$. The $\kappa = 10^8$ can further reduce this simulation time to about 70 s, but an arbitrary increase in the κ value can adversely affect the material flow responses and the prediction

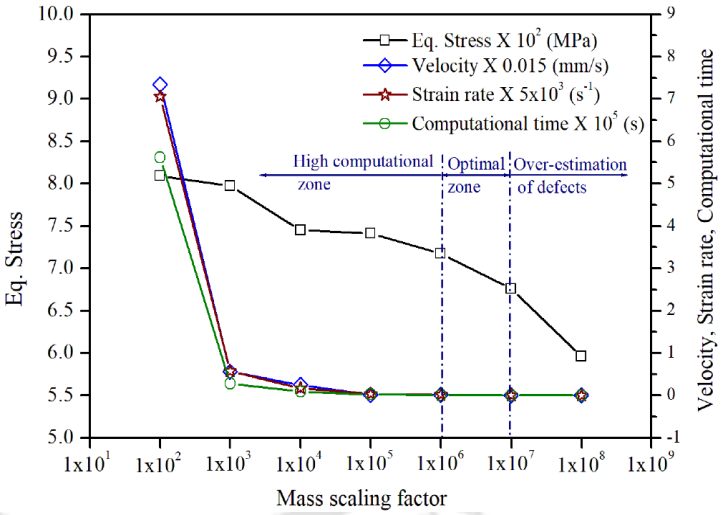

Fig. 5.14 Mass scaling factor window for efficient modelling of FSW using CEL

of defects. Thus, an optimum range between 10^6 and 10^7 can successfully model the FSW process for low strength materials like aluminum and magnesium alloys. There is a marginal change in strain rate and velocity between these values of MSFs. Although, the equivalent stress changes ~40 MPa with this variation of MSFs, it does not affect the defect prediction with sufficient accuracy and ensures minimum computational time. Further increment of MSF alters the solution quality.

Figure 5.15 shows the FSW results of AZ31B at 1200 rpm and 60 mm/min with $\kappa = 10^8$. The temperature and stress distribution on the workpiece and a partially defective joint are predicted (Fig. 5.15 (b) and (c)). Here, the KE/IE ratio is within acceptable limits of 5%. However, the predicted results in Fig. 5.15 are incorrect as the longitudinal defects are absent when compared with the experiments (depicted in Figs. 5.28 and 5.29). The reduction in the material flow velocity and the strain rate with an increase in the MSF can be a possible reason for the same (Fig. 5.14). Therefore, the over prediction of defects (Figs. 5.15 (b) and (c)) occurs due to adverse effects of inertia related to the improper choice of MSF. The unaccountable increase in the mass of the system mainly leads to low material velocity. It has been realized the MSF is a necessary evil that must be utilized judiciously to model the thermo-mechanical responses while predicting the surface and subsurface morphology. Therefore, to successfully perform the thermo-mechanical modelling and defect prediction, a window of optimal κ needs to be determined for

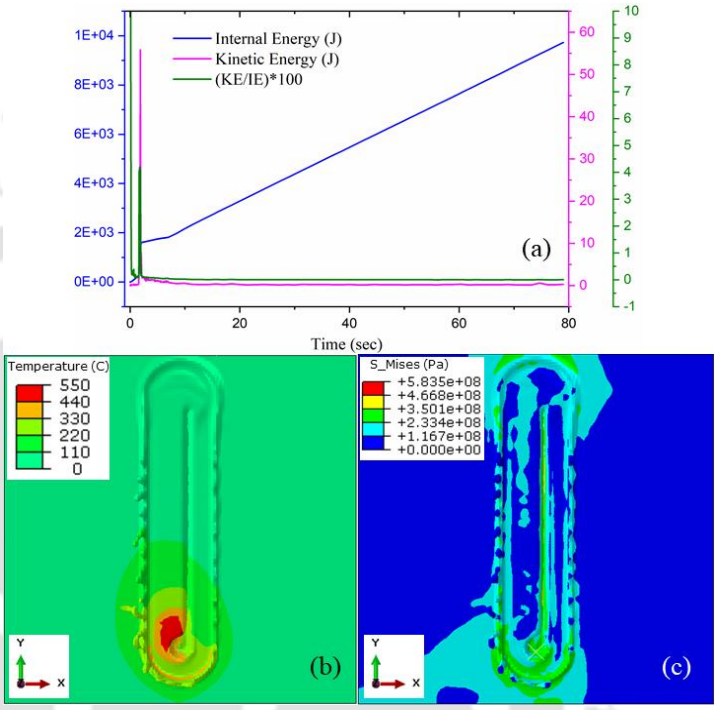

Fig. 5.15 (a) IE, KE and KE/IE ratio, (b) temperature and (c) stress distribution for the complete duration of welding for $\kappa = 10^8$ and AZ31B workpiece

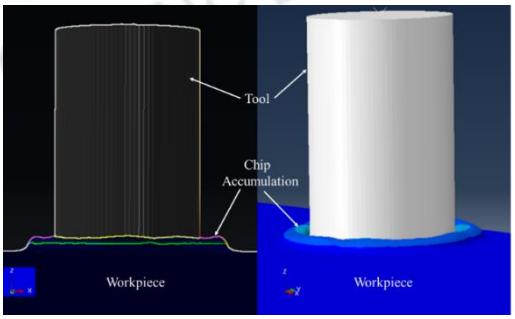

Fig. 5.16 Representation of the chip accumulation around the tool periphery by pushing out of material from the workpiece occurred at the plunge and the dwell stages

various materials. The potentiality of the mass scaling technique to improve the computational cost is a function of the mesh size, as the time increment is dependent on the smallest element in the solution domain Eq. (11). Although the solution quality improves with a fine mesh, the step time increment lessens with the reduction in mesh size, thus increasing the total computational time. Therefore, even with the application of mass scaling, there must be a tradeoff between the quality of the result and computational cost. In general, the mass scaling technique can be applied to the model irrespective of the quality of welding (Fig. 5.9) and the type of material. As a rule of thumb, the time increment calculated for the thermal analysis Eq. (4.45) is greater than the time increment for the mechanical analysis Eq. (4.43). Therefore, the computational time required for mechanical analysis is more critical in a coupled thermo-mechanical analysis, as it dictates the time step increment.

5.4 Material flow

As the tool plunges into the workpiece, the material is pushed out, and it accumulates around the tool. This flash accumulation around the tool is shown in Fig. 5.16. When the tool shoulder is in proper contact with the workpiece towards the end of the plunge stage, the material is rotating along with the tool with a velocity of upto 22 mm/s (Fig 5.17). The region closer to the tool pin observes a higher velocity than the rest of the region, where the maximum velocity is 11 mm/s. The material flow around the flash is shown in Fig. 5.18. An upward flow direction of the material is observed at the root of the flash. This upward direction movement is responsible for the flow of material out of the workpiece and the flash formation.

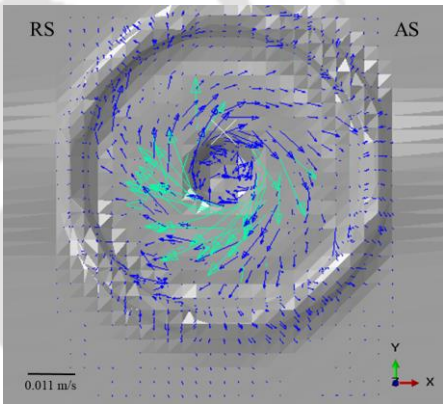

Fig. 5.17 Velocity profile (m/s) on the workpiece top surface about the trailing end of the plunge stage with a tool speed of 1200 rpm and 90 mm/min

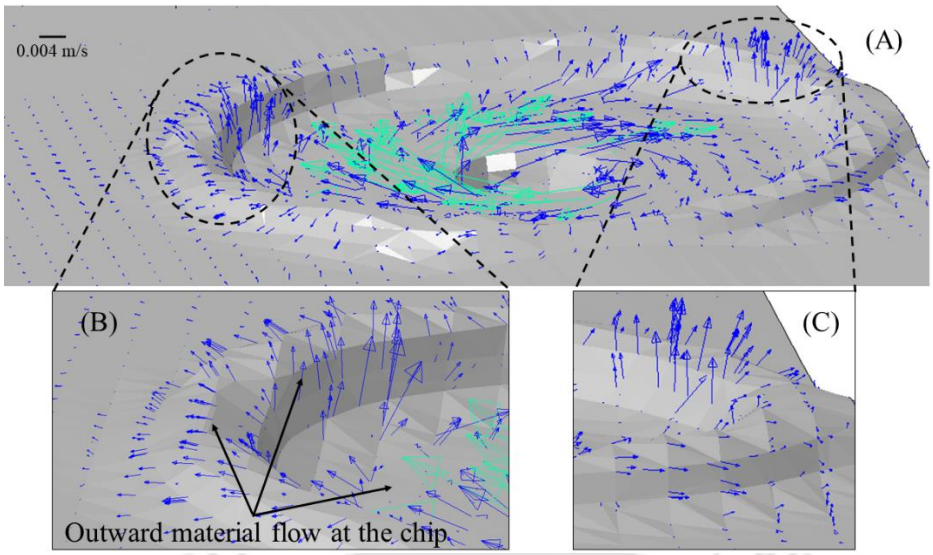

Fig. 5.18 Illustration of the direction and the velocity (m/s) of the material flow at the tool-workpiece interface towards the end of the plunge stage with tool rotation at 1200 rpm and traversing at 90 mm/min

Fig. 5.19 shows the initiation in the splitting of the flash, thus dividing the circular flash formed around the tool (Fig. 5.17) into separate flash formed on the AS and the RS. This split in the flash occurs due to the linear movement of the tool with the progress of FSW. Here, in addition to the velocity of the material, the direction of the flow is also important. The material flow direction can be grouped into three categories, i.e., the AS direction, the RS direction, and towards the direction of the tool movement. Shortly before the splitting of the chips, the material flows at constant velocity in the outward direction (Fig. 5.19 (a) and (b)). It is noticed that the concentrated velocity lines are pointing towards the tool motion direction as the tool movement pushes them. Fig. 5.19 (c) shows the side view of the flash split. Location II shows more material deposition than location I, resulting in a more significant and continuous flash on the RS after FSW. In contrast, the material deposited on the AS is sporadic. Figure 5.20 shows the flow of the material towards the finishing stages of FSW. The significant material

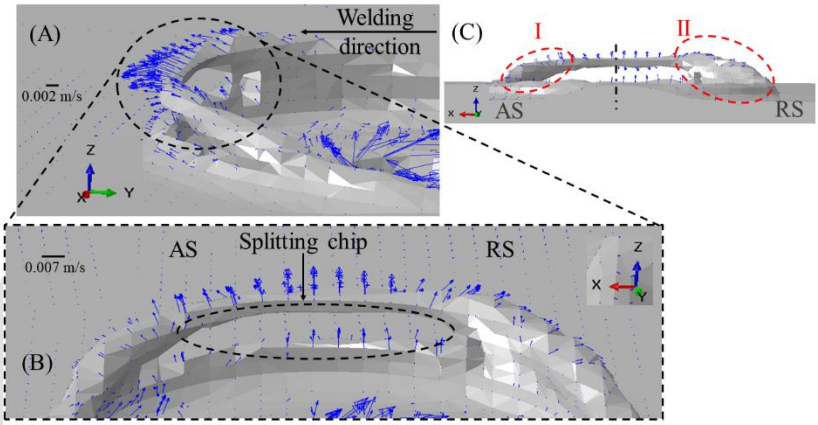

Fig. 5.19 Illustration of the flow direction of the expelled material resulting in the initiation of splitting in the chip on the advancing and the retreating sides of the workpiece, (a) front view, (b) bird-eye view, and (c) side view

movement is concentrated primarily in two locations on the workpiece, i.e., around the tool pin and the flash (Fig. 5.20 (a) and (b)). Interestingly, in both cases, the material flow is concentrated and directed towards the RS. The flow velocity is about 123 mm/s when the tool is traversing at 90 mm/min (Fig. 5.20 (a)), whereas the maximum velocity remains 83 mm/min when the tool travel velocity is doubled to 180 mm/min (Fig. 5.20 (b)). This reduction in the flow velocity in the second case is due to a reduction in the heat input per unit area due to the faster tool travel speed. As the temperature rise is less in the 180 mm/min traverse speed case, the ease of expulsion of material will also be reduced.

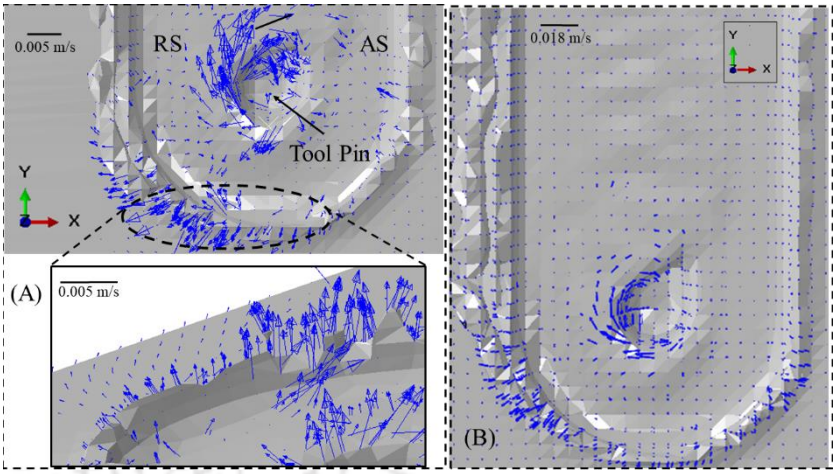

Fig. 5.20 Material flow around the tool pin and the chip at the concluding stages of the welding with rotational speed of 1200 rpm and transverse speed of (a) 90 mm/min and (b) 180 mm/min

Figure 5.21 shows the distribution of velocity lines on the top surface and along the depth of the workpiece. The top of the workpiece observes an even distribution of the velocity lines due to the constant rotation of the tool without any traverse velocity at the initial stages of welding, as shown in Fig. 5.21 (a). The material flow is more evident around the tool pin as the material is gripped by the pin and rotated around it. Similar material flow lines are observed around the shoulder periphery also (Fig. 5.21 (a)). This suggests that the majority of the area under the tool and workpiece contact is responsible for the frictional

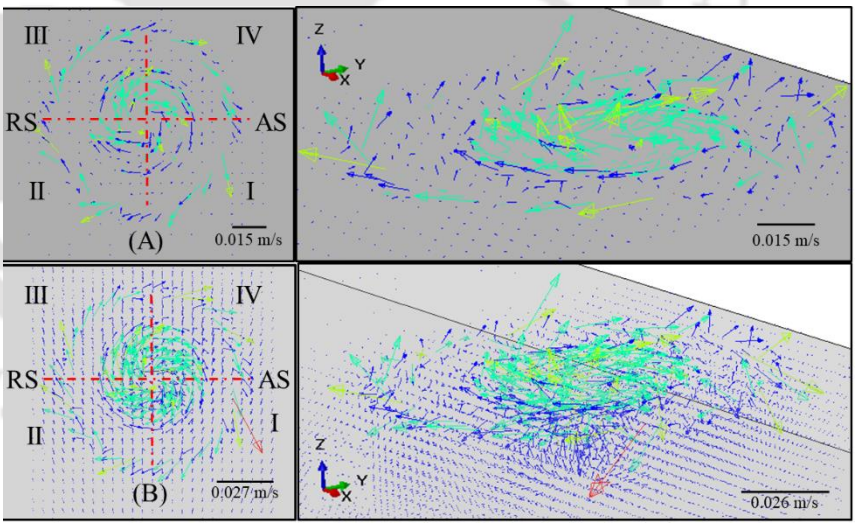

Fig. 5.21 Flow of the material on the (a) top surface and (b) subsurface of the workpiece at the initiation of the welding due to the tool and workpiece interaction at 1200 rpm. A higher velocity of the material at the advancing side is observed

heat generation during FSW. Simultaneously, the pin and the shoulder boundary are the regions that observe the major material movement. The highest velocity of about 30 mm/s is observed at a depth of about 0.1 mm in the workpiece on the advancing side (Fig. 5.21 (b)). The literature survey indicates that the workpiece material on the AS is rotated and is deposited to the RS with the complete rotation of the tool during FSW. Assuming that the material movement starts in quadrant IV (Fig. 5.21 (b)), it cannot achieve the highest velocity in this quadrant. The highest velocity by the material is achieved as the material flows into quadrant I. Thus in Fig. 5.21 (b), we observe the highest material velocity to be directed outwards along the AS. As the material flows to the II and III quadrants, the velocity of the material decreases moderately due to the opposing sense of tool rotation and tool traverse in the RS.

5.5 Surface morphology

The CEL approach allows to capture of surface morphologies at the void domain. Figure 5.22 shows the formation of the chip on the RS with the progress of the tool. At t = 0 s i.e., at the end of the dwell stage, the flash is evenly distributed around the tool (Fig. 5.22 (a)). Figure 5.22 (b) shows the chip formation after ~ 10 s. A small depression similar to the shape of the tool shoulder is also observed along with the thickness of the workpiece. This depression originates due to the plunging of the tool into the workpiece. A gradual increase in the size of the flash can be observed near the weld start location. Such a gradual increase in the flash height appears due to the availability of less material for expulsion at the initial stages of welding. As the flash is being continuously pressed towards the weld direction by the traversing tool, the flash is split and get deposited on either the AS or the RS, as seen from the bird-eye view of Fig. 5.22 (b). Fig. 5.22 (c), shows the progress of welding and flash formation. Fig. 5.22 (e) shows the complete stretch of the flash formed when welding with the process parameters of 1200 rpm and 90 mm/min. Overall, Fig. 5.22 highlights various flash morphologies observed during FSW, such as the forming of a small depression in the workpiece due to the plunging of the tool, the initiation of chip formation, splitting of the chips between both the AS and RS.

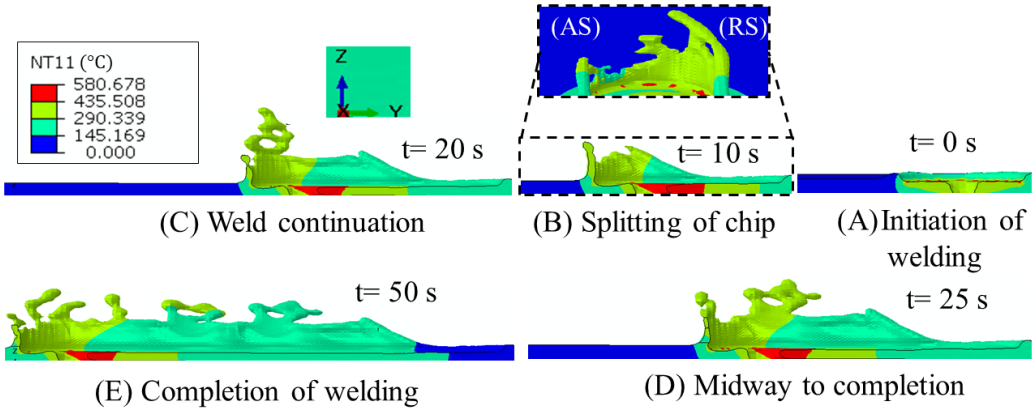

Fig. 5.22 Visualization of the surface morphology with temperature profile ($°C$) in the complete solution domain at different time intervals with process parameters of 1200 rpm and 90 mm/min for AA6061 with a conical tool

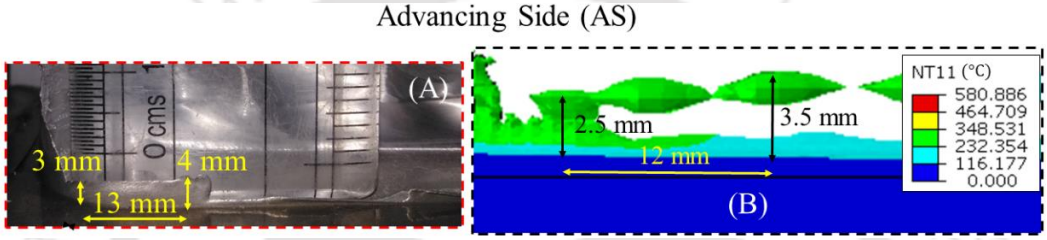

Fig. 5.23 Illustration of the flash formation on the AS for AA6061 with a conical tool at 1200 rpm and 90 mm/min: (a) experimental view and (b) numerically predicted chip

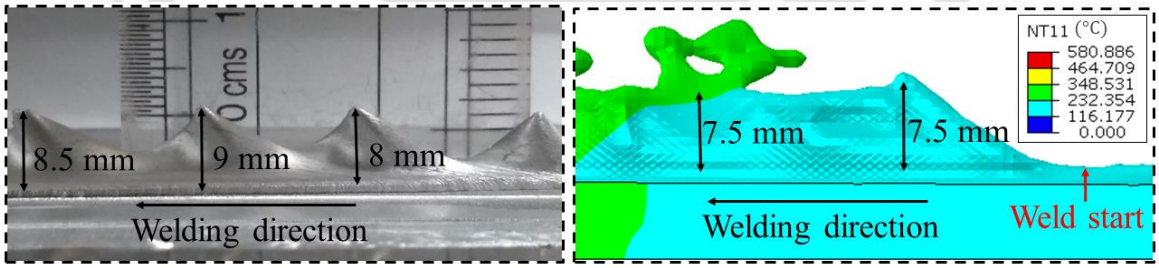

Fig. 5.24 Comparison of the (a) experimental and (b) simulated flash formation on the RS for AA6061 with a conical tool at 1200 rpm and 90 mm/min

Figure 5.23 shows the comparison between experimentally and numerically predicted flash obtained on the AS of the workpiece when plunge depth is maintained at ~ 0.7 mm. The numerical model clearly predicts a sporadic and small size flash on the AS. The average size of the flash is measured as 3.5 mm, while the predicted size of the chip is 3 mm. Fig. 5.24 shows the comparison of the chip formed on the RS when the plunge depth is maintained at ~ 0.45 mm. Different plunge depths are used for both cases (Fig. 5.23 and 5.24) to understand the surface morphology since less value of plunge depth produces negligible flash on the AS, and thus a proper measurement of the same is challenging. The average size of the flash measured throughout the weld length is about 8.5 mm, while the average size of the predicted flash is about 7.5 mm (Fig. 5.24). The size of the flash

predicted on both the AS and RS is similar to the experimental measurement (Figs. 5.23 and 5.24). However, the shape of the flash is not predicted very accurately in some locations of the weld. This discrepancy between the numerical and the experimental results occurs due to the mesh size considered in the analysis. The CEL technique employed for this analysis traces the amount of material present in each element by computing the EVF of the element (Systèmes, 2007). The EVF value ranges between 0 and 1, where 0 signifies empty, and 1 signifies a filled domain. Considering smaller size elements can ensure easy filling of material in each element that, in turn, can affect the shape of the flash predicted by the numerical model. The mesh size considered in this case is $1 \times 1 \times 0.5\ mm^3$. Further reduction in the mesh size will increase the computational time significantly. Thus, the prediction of chip shape is a trade-off between the accuracy of the prediction and the computational time.

It is obvious from Fig. 5.25 that the total length of the welding can be divided into three stages, i.e., the weld start (Fig. 5.25), length of the welding (Fig. 5.24), and the weld end (Fig. 5.26). The numerical model can predict the flash size formed both at the initial and final stages of FSW, which is in close proximity to the experimental result (Fig. 5.25). The model can also locate minute surface discontinuities observed in the flash profile, as shown in Fig. 5.25 (b). The initial stages of the FSW observe a gradual increase in the flash height that is properly predicted by the numerical model. Similarly, the model can also predict the flash formation towards the end of the welding. However, the shape of the flash can be further improved by the optimization of the mesh size and computational time involved in the solution process. Figure 5.26 shows the material accumulation in front of the tool at the end of its traversing motion. A significant change in the flash height is observed as one moves from the RS to the AS. Figure 5.26 shows comparison of the experimental and numerically predicted flash height at different locations on the RS when a relatively higher plunge depth of 0.7 mm is used. The predicted results are found to be in close acceptance of the experimental result.

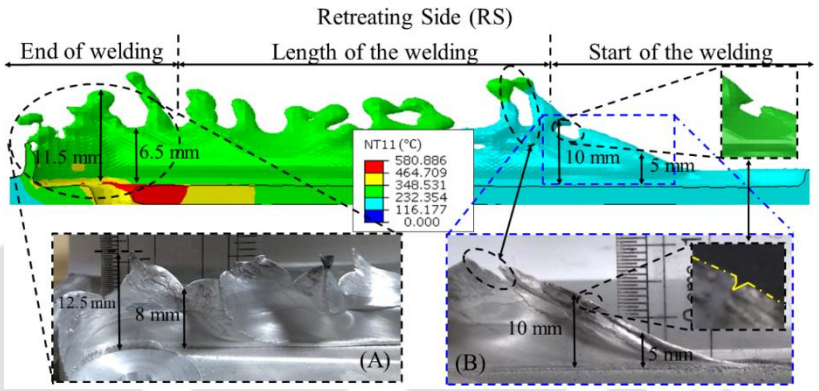

Fig. 5.25 Comparative analysis of the experimental and numerically predicted flash formation around the tool periphery for AA6061 with a conical tool at the (a) finishing and (b) initial

It can also be observed from Figs. 5.24 and 5.25 that the temperature of the flash near the tool is about $349°C$, which is almost 60% of the maximum temperature observed in the workpiece. This temperature keeps on reducing as one moves towards the weld start point. This reduction of temperature is due to the thermal losses occurring during the welding.

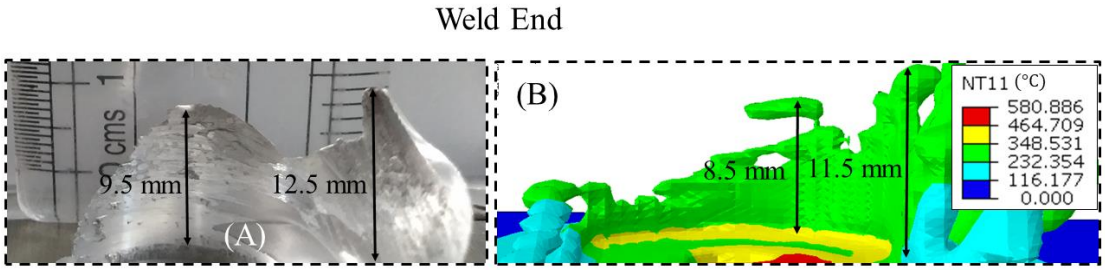

Fig. 5.26 Bird-eye view of the flash formation along the stirred zone at the weld end for AA6061 with a conical tool: (a) experimental and (b) numerically calculated at 1200 rpm, 90 mm/min, and $P_d \sim 0.7$ mm

Figure 5.27 shows the comparison of flash thickness at plunge depth of 0.7 mm. The average thickness of the chip is ~ 1 mm (Fig. 5.27 (a)) while the numerical model predicts it to be about 1.3 mm. The measurement of flash thickness is an approximate approach as the flash profile keeps changing shape and size very frequently throughout the length of the welding. This makes it difficult to ascertain a plane parallel to the flash width to measure the flash width or thickness correctly. Therefore, certain variations are observed between the experimentally observed and the numerically predicted results.

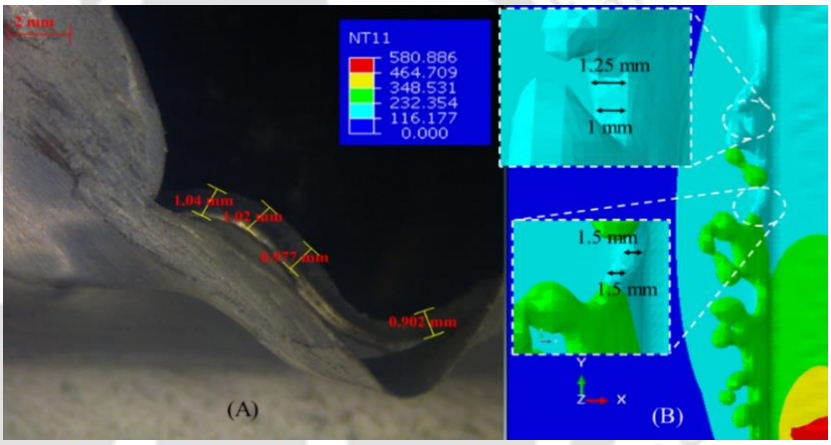

Fig. 5.27 Illustration of the flash thickness formed on the RS for AA6061 with a conical tool: (a) macrograph and (b) numerically predicted at $P_d \sim 0.7$ mm

5.6 Thermal and mehcanical responses

The temperature evolution gives rise to the different metallographic zones, namely the stir zone (SZ), thermo-mechanically heat affected zone (TMAZ), heat affected zone (HAZ) and the unaffected base material (BM). The current section investigates the temperature, stress, strain, strain rate, and velocity distribution within the workpiece surface.

5.6.1 Isotherm prediction

Figure 5.28 shows the location of the various cross-sectional planes used for the temperature profile in the workpiece cross-section (Fig. 5.28 (a)), plastic strain and strain rate distribution (Fig. 5.28 (b)), and progress of the tunnel defect (Fig. 5.28 (c)).

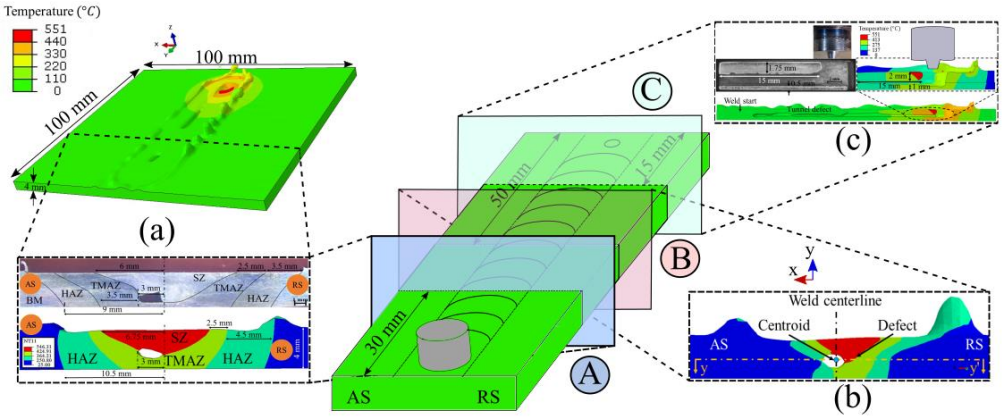

Fig. 5.28 (a) Illustration of the cross-sectional planes in the solution domain for the tunnel defect (Fig. 5.29); (b) Plastic strain and strain rate analysis (Fig. 5.30) and (c) Comparison of the tunnel defect progression (Fig. 5.36)

Figure 5.29 (b) shows the macrograph of the welded sample comprising of SZ, TMAZ, HAZ, and the BM. The predicted size of the different zones at the top and bottom surfaces is in close agreement with the experimental results. The predicted width of the SZ (top surface) and HAZ (bottom surface) on the AS is 6 mm and 10 mm, respectively, as shown in Fig. 5.29 (b). The experimental results at a similar location are 6 mm and 9 mm, respectively. The predicted width of the TMAZ (top surface) and HAZ (top surface) on the RS is 2.5 mm and 4 mm, respectively. In comparison, the experimental results at the same position are 2.5 mm and 3.5 mm, respectively. Although the size of the various zones is predicted accurately, there is a discrepancy in the shape of these zones. The experimental measurement shows the transition zone is like a concave surface, while the numerical result is convex in nature. These differences may appear due to the consideration of isotropic material properties and, accordingly, the effect on the material model considered in the numerical model. This model can also predict sub-surface tunnel defects in the FSW process with more close proximity to experimental results. The measured width of the tunnel defect is about 3 mm, whereas the numerical model predicts 2.5 mm.

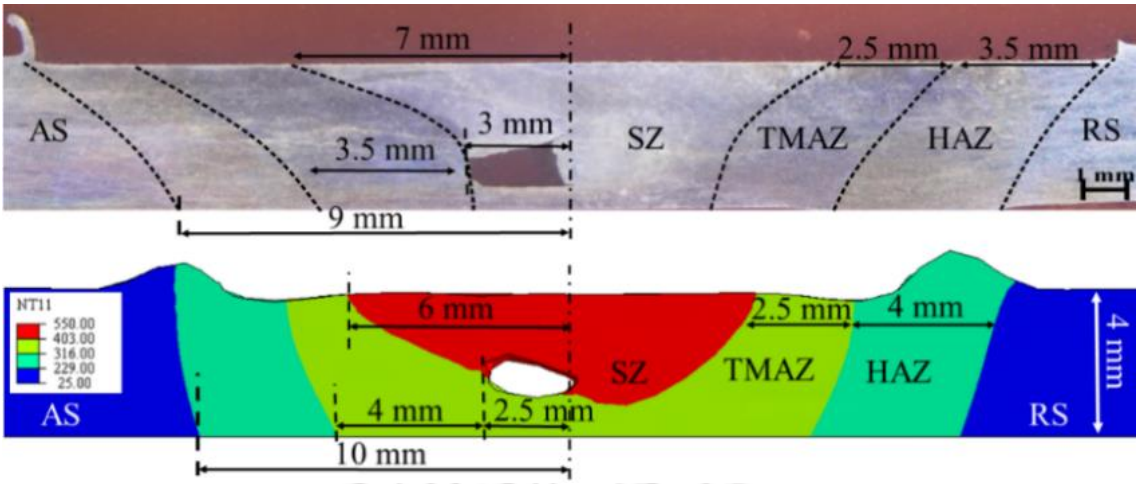

Fig. 5.29 Comparative analysis of experimental (top) and predicted (bottom) temperature distribution on workpiece cross-section

5.6.2 Thermo-mechanical response

The internal voids or tunnel defect in the FSW process arises due to the lack of material flow behind the moving tool. The appearance of these defects is relevant to the proper selection of process parameters and the type of materials used. In Fig. 5.30 (a), the equivalent plastic strain ($\bar{\varepsilon}^{pl}$) value greater than 0 indicates yielding in the material (Systèmes, 2007). The highest $\bar{\varepsilon}^{pl}$ of about 14 is observed in the SZ, and it reduces towards the BM, indicating the highest mixing of material in the SZ, while BM observes no yielding. The lack of material on the AS (Fig. 5.30 (a)) represents the tunnel defect. The absence of material arises due to the material moving out of this region. Figures 5.33 (b) and 5.33 (c) show the strain and strain rate variations on the cross-section of the weld along the y-y' plane of Fig. 5.33 (a). Figures 5.33 (d) and 5.33 (e) show the strain and strain rate distribution at the centroid (Fig. 5.33 (a)) of the workpiece for the complete duration of welding formed at 1200 rpm and 60 mm/min. The plastic strain (ε) is the highest near the weld centerline, as seen in Fig. 5.30 (b). The strain value is cumulative in nature, the strain at any given point is the summation of the strain of all the initial points encountered by the traversing tool (Arora *et al.*, 2009). The strain value reduces away from the SZ due to the resistance offered by the undeformed solid material present beyond the TMAZ (Fig. 5.30 (b)). In the tool pin region, as the material is pushed in the y-direction with the tool movement, the ε_{22}^{pl} is compressive in nature. Similarly, compressive ε_{33}^{pl} is low in magnitude, thus indicating less material movement in the z-direction. Conversely, a positive value of the plastic strain in the x-direction indicates a tensile nature, i.e., the material is being elongated due to the tool rotation. Towards the TMAZ, the ε_{11}^{pl} becomes

compressive, indicating the material is being pushed in the TMAZ with the rotation of the tool. The positive ε_{22}^{pl} indicates the material is being elongated in the y-direction due to the dragging action of the forward motion of the tool. The plastic strain value becomes negligible as one moves toward the HAZ, thus indicating an undeformed region of the workpiece. Figure 5.30 (d) shows the plastic strain distribution at the centroid of the workpiece when the tool is moving along the y-direction. When the tool is closer to the centroid (Fig. 5.30 (a)), a positive ε_{11}^{pl} and a negative ε_{22}^{pl} indicate the material in front of the tool is being compressed due to the undeformed material in front of the tool. In contrast, the material is pulled and elongated in the x-axis to rotate it around the tool. Figure 5.33 (c) shows the strain rate distribution along the y-y' plane. A negative $\dot{\varepsilon}_{11}$ value is observed for the RS, indicating a decrease in the material velocity gradient $\left(\frac{\partial u_1}{\partial x}\right)$ due to compression of material towards the non-plasticized HAZ, while a slightly positive $\dot{\varepsilon}_{22}$ value indicates an increase in the $\left(\frac{\partial u_2}{\partial y}\right)$ due to the rotation and the traverse action of the tool. A similar trend is also observed for the plastic strain distribution in Fig. 5.33 (b). Conversely, $\dot{\varepsilon}_{11}$ and $\dot{\varepsilon}_{22}$ have a marginal positive magnitude on the AS. The reduced strain rate in the SZ and TMAZ on the AS indicates less material deposition on the AS. The significant difference in the strain rate between the RS and AS is due to the tunnel defect on the AS. Figure 5.33 (e) shows the strain rate distribution for the complete duration of the welding. As the tool moves along the weld line, the $\left(\frac{\partial u_2}{\partial y}\right)$ velocity component first increases due to the action of the tool and then decreases as the material is dragged from the front and deposited to the back of the tool. Consequently, the $\dot{\varepsilon}_{22}$ changes from positive to negative. During the welding process, significantly less movement of the material occurs in the z-direction. The $\dot{\varepsilon}_{33}$ is negative as the tool passes the centroid, thus indicating a decrease in velocity gradient in the z-direction. The $\dot{\varepsilon}_{11}$ value remains primarily positive, indicating an increase in the $\left(\frac{\partial u_1}{\partial x}\right)$ component of the velocity. The increase in the $\left(\frac{\partial u_1}{\partial x}\right)$ velocity component indicates a flow of the material from the weld centerline towards the transverse direction. The first spike in the strain rate is due to the action of the tool pin's forward surface, while the second spike is due to the rear end of the tool pin. As the tool moves away from the centroid, the change in the strain rates is marginal as the material is already deposited behind the tool. In general, the mass scaling approach is a preferred methodology to improve the computational efficiency of a model while performing quasi-static analysis. The mass of

the solution domain is artificially increased to reduce the solution time without affecting the output results. However, it is not required to reduce the mass of the domain from its physical value after mass scaling (Systèmes, 2007). Moreover, it is not possible to arbitrarily increase the mass of the system without increasing the adverse inertia effects. Thus, the extent of the mass scaling factor depends on the material properties and the resulting changes to the inertia forces.

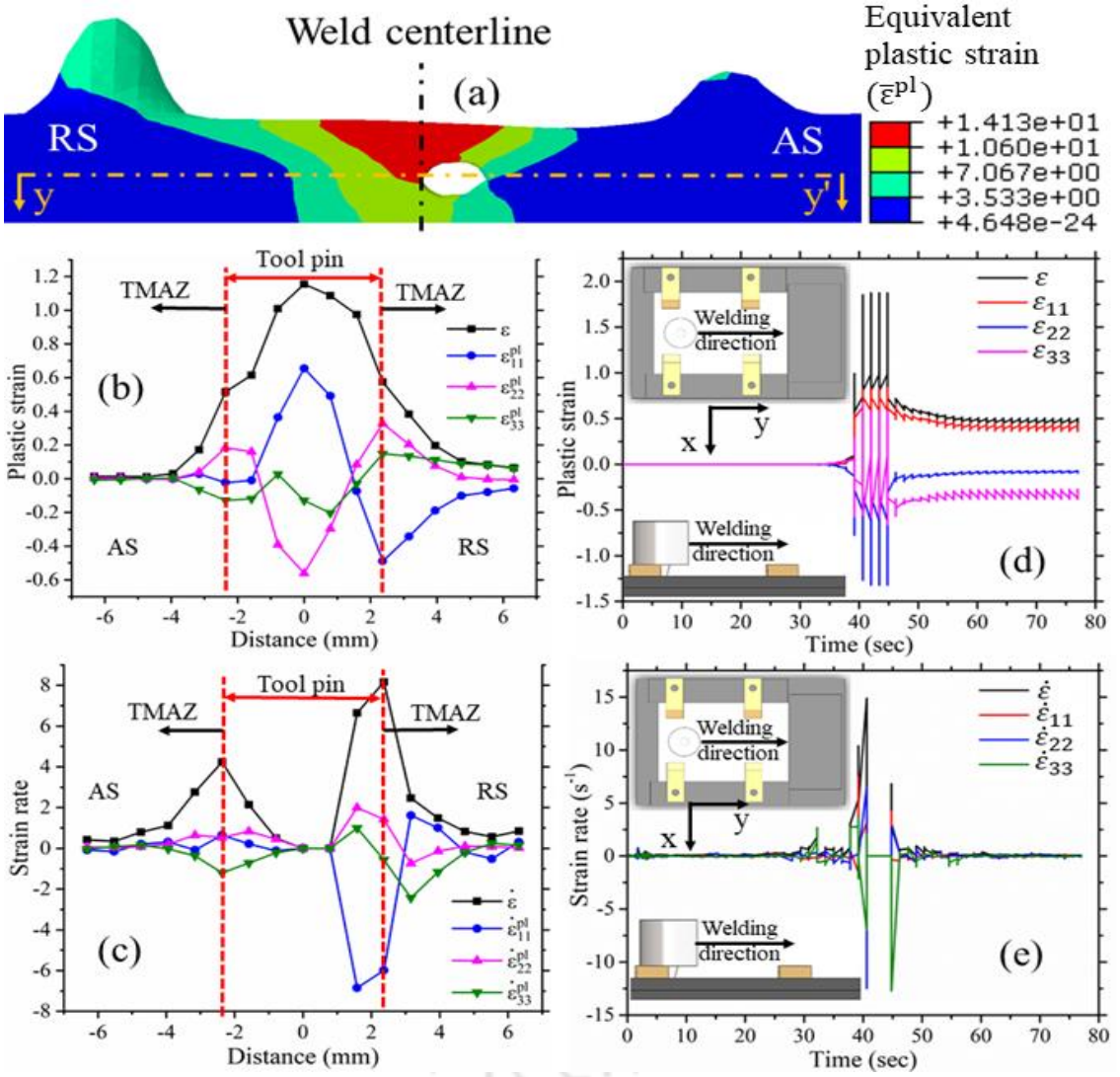

Fig. 5.30 (a) Equivalent plastic strain ($\bar{\varepsilon}_{pl}$) distribution in the workpiece cross-section; (b) plastic strain (ε) and (c) strain rate ($\dot{\varepsilon}$) distribution along the y-y' plane as seen in (a); and (d) plastic strain and (e) strain rate (s^{-1}) at the centroid of AZ31B for the complete duration of welding.

5.7 Material mixing

The FSW produces a sound quality weld due to proper mechanical and metallurgical aspects and material mixing and bonding. The material mixing of AA6061 and AZ31B is predicted in Fig. 5.31 at the end of the dwell stage. The EVF approach tracks the presence

of material inside each Eulerian domain. Figs. 5.31 (a-b) tracks the material mixing at the top surface of the workpiece, and Figs. 5.31 (c-d) tracks the material mixing at the cross-section after the dwelling stage. In each case the material flow from either the AS or RS is modelled to estimate the material flow between both AS and RS. An EVF value of 0.5 can indicate the presence of both materials of dissimilar welding in a single element. The material on the RS side pushes into the AS side with the rotation of the tool, while a similar proportion of the material from the AS is also pushed into the RS. Figures 5.31 (c) and (d) show the cross-sectional view of the material flow at the end of the dwell stage. Figure 5.31 (c) indicates the presence of some AZ31B on the AS. In contrast, the presence of AA6061 on the RS is marginal in Fig. 5.31 (d). This indicates easy plasticization and better flow of material from RS to AS than AS to RS at the end of the dwell stage. As the modulus of elasticity of AZ31B is lower than that of the AA6061, it is easily plasticized, rotated, and deposited around the dwelling tool.

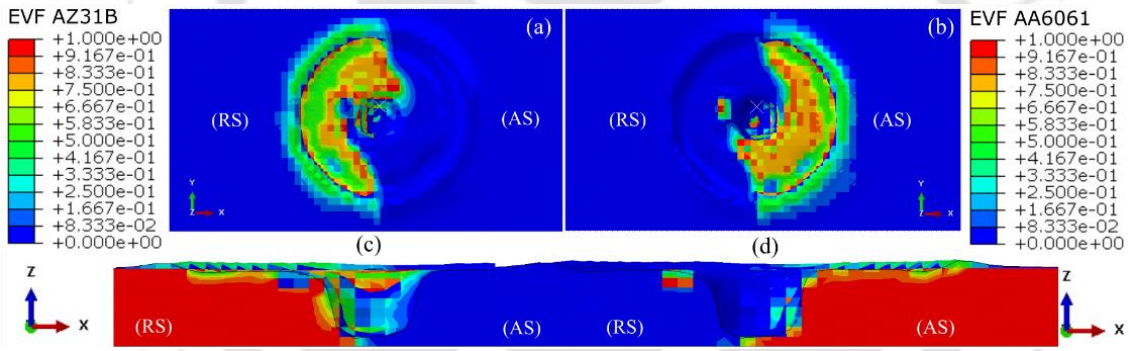

Fig. 5.31 Numerical modelling of the material flow on the top surface of the SZ (a) RS, (b) AS; and cross-section (c) RS, and (d) AS at the end of the dwell stage at 900 rpm

Figure 5.32 shows the numerical prediction and experimental investigation using FESEM-EDS analysis of the material mixing and flow at the end of welding. The FESEM-EDS analysis is used to perform the line scan and area mapping. Figure 5.32 (a) and (b) show a significant amount of material mixing at the beginning of the weld length, i.e., at the end of the dwell stage. However, such material mixing is not evident for the remaining weld length. The higher concentration of the AZ31B is predicted near the weld centerline on the RS side. Simultaneously, a minor amount of AA6061 is predicated on the RS adjacent to the weld centreline. The small amount of AA6061 on the RS indicates the transfer of material from AS with the rotation of the tool. Figure 5.32 (d) shows the FESEM-EDS line scan on the RS of the welded sample. The higher AZ31B peaks indicate a higher presence of AZ31B on the RS. As one moves toward the weld centreline, the

elemental presence of the AZ31B reduces to be similar to that of the AA6061, as predicted in Figure 5.32 (b). Furthermore, the presence of AA6061 is higher away from the weld centreline on the AS and reduces to be similar to that of AZ31B on moving towards the weld centreline. At the centre of the weld, the elemental composition of the AZ31B and AA6061 is almost similar, as also indicated by Figure 5.32 (f). Figures 4.32 (g) and (h) show the FESEM-EDS area mapping on the RS and AS, respectively. The uniform distribution of the material within the SZ is evident. However, the presence of dark patches in Figure 5.32 (h) indicates the intermittent presence of the Mg within the SZ. The same is responsible for the sudden spike in the Mg presence in Figure 5.32 (e).

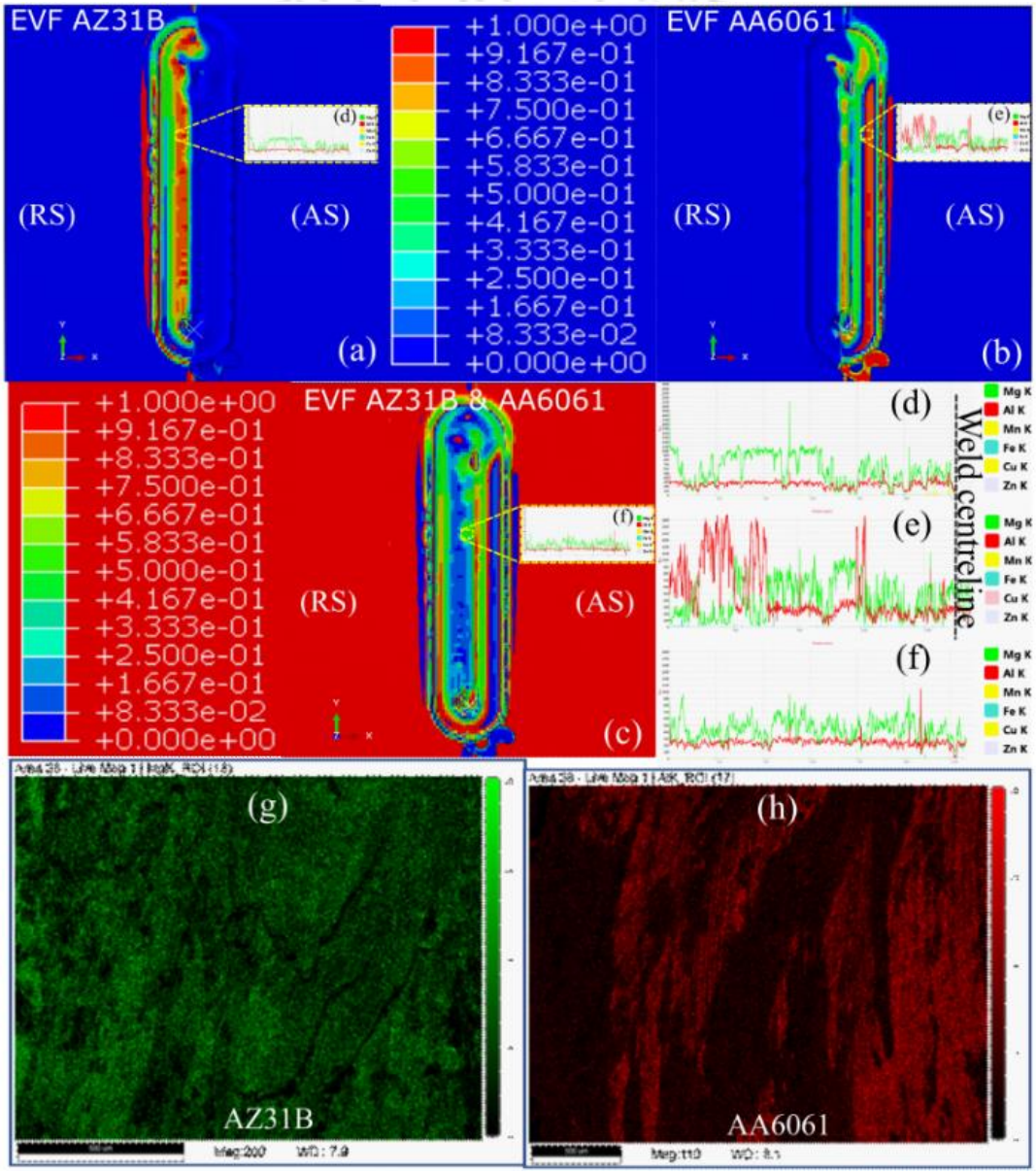

Fig. 5.32 Numerical modelling of the material mixing on the (a) RS, (b) AS, (c) SZ; EDS line scan on the (d) RS, (e) AS, (f) SZ; elemental mapping on the (g) RS, and (h) AS with 900 rpm and 30 mm/min

The material mixing pattern and the location of the interface line are predicted in Fig. 5.33. Figure 5.33 (a) shows the experimental cross-section of the AA6061-AZ31B weld. The interface line between the materials is visible on the cross-section. Figures 5.33 (b) and (c) predict the presence of AA6061 and AZ31B, respectively. The interface line between both materials is predicted on the RS. Material mixing is observed primarily in the location denoted by I and II in Figs. 5.33 (b) and (c). The tunnel defect is responsible for insufficient material mixing in the void region. The presence of the tunnel defect and improper material mixing will lead to the weakening of the joint. The material mixing pattern in Fig. 5.33 also indicates that more material flows from the AS to the RS side due to the presence of the interface line on the RS.

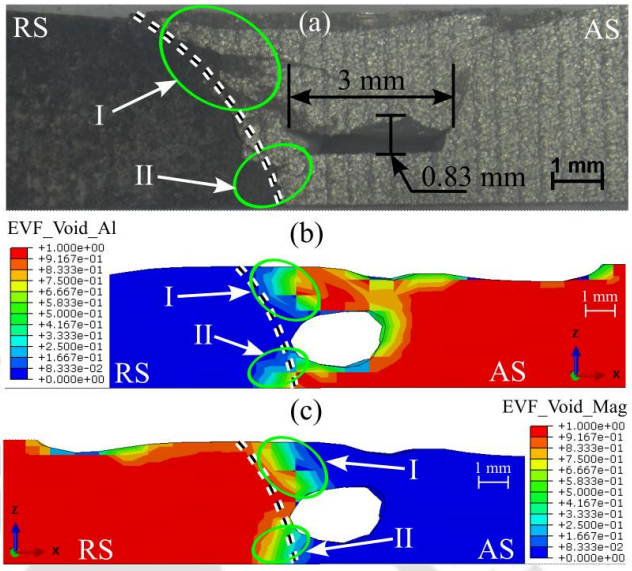

Fig. 5.33 Visualization of the material mixing and prediction of the interface line in AA6061-AZ31B dissimilar FSW, (a) experimental, (b) AA6061, and (c) AZ31B when welding at 900 rpm and 30 mm/min

5.8 Prediction of various defects

The accurate estimation of the heat generation and temperature evolution on the workpiece surface, material flow, and material mixing should collectively be able to dictate the weld quality. The improper heat flow or material movement can lead to the generation of any volumetric defect within the workpiece. The developed numerical model is used to estimate the different defect formations for the varying process parameters. The defect estimation is performed for three cases, i.e., the similar AA6061 FSW, similar AZ31B FSW, and dissimilar AA6061-AZ31B FSW.

5.8.1 Tunnel defect

The tunnel defect signifies a region of unfilled material within the stirred zone. Sometimes, it can also be referred to as a wormhole defect. The identification of this defect is challenging as it develops within the material volume, and thus without performing a

post-processing operation, it is not visible to the naked eye. Therefore, developing a model to predict the subsurface tunnel defect is always insightful.

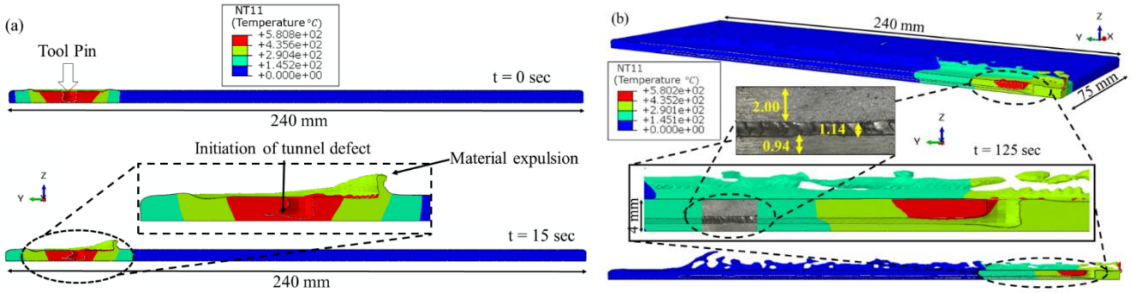

Fig. 5.34 Illustration of the initiation and progress of tunnel defect in 3D solution domain with temperature distribution ($°C$) in the workpiece at: (a) initial stage (0 s, 15 s), and on the (b) verge of completion (125 s) along with the comparison of the numerically modelled and experimentally observed tunnel defect

Figure 5.34 shows the simulation (at 1200 rpm and 90 mm/min) of a typical tunnel defect observed during the FSW of AA6061. The top half of the workpiece achieves a temperature of about 580 $°C$ (Fig. 5.34 (a)), which is approximately 90% of the melting point of Aluminium. At the time, t = 0 s, the temperature propagates properly along the depth of the workpiece. The dwell time is mainly responsible for the proper heating of the workpiece. No defect is observed until 15 s after the initiation of the welding. At the time, t =15 s, with the onset of material expulsion, the initiation of the tunnel defect starts (Fig. 5.34 (a)). This expulsion of material in the form of flash causes a shortage of material for deposition in the stirred zone, which leads to the development of the tunnel defect. Fast rotation of the tool with low traverse speed leads to higher than optimal heat generation per rotation of the tool. This softens the workpiece material and eases its expulsion from the workpiece (Nandan, DebRoy and Bhadeshia, 2008). The temperature difference between the upper and lower halves of the plate is quite negligible at the beginning of the weld, but this difference becomes significant towards the end of the

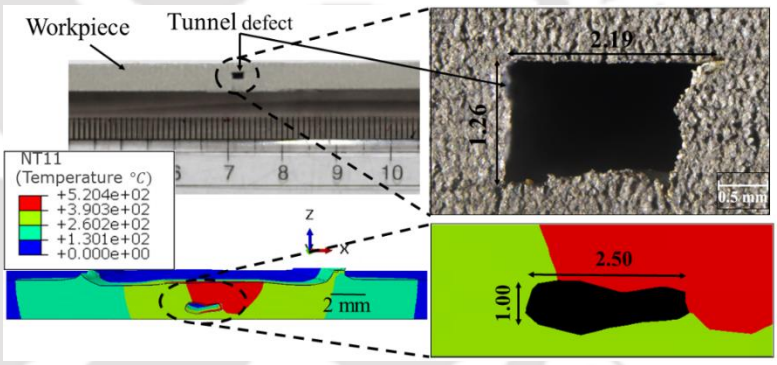

Fig. 5.35 A comparative analysis of experimental and numerically predicted cross-section of tunnel defect generated with a process parameters of 1200 rpm and 90 mm/min

weld (Fig. 5.34 (b)). The temperature difference along the thickness of the plate is of the order of $150\,°C$. Due to this lack of proper temperature generation throughout the plate and expulsion of material in the form of flash, the defect that originated at the beginning of the weld continues until the end. Figure 5.35 shows the comparison between the numerically calculated and experimentally observed tunnel defect. The dimension of the experimentally observed defect is 2.19 mm × 1.26 mm, while the numerically predicted defect is 2.5 mm × 1 mm. A minor difference is present in the size of the predicted and experimental defects. Many factors can be responsible for this difference, such as the constant coefficient of friction, and the mesh size. Optimum temperature generation and proper tool design with threaded pin help in the easy rotation of material about the tool and eliminate the tunnel defect (Dialami, Cervera and Chiumenti, 2020).

Figure 5.36 (a) compares the position and progress of the tunnel defect in the AS for the AZ31B along the welding direction at 1200 rpm and 60 mm/min. The tunnel defect is experimentally observed at a depth of about 1.75 mm from the top surface, while a 0.5 mm thick stirred material is present near the bottom surface. The tunnel defect is investigated for a length of 15 mm towards the end of the welding for a 4 mm thick AZ31B plate. The numerical result at a similar location predicts 2 mm of material near the top surface and 1 mm of material at the bottom surface. The difference in the height of the experimentally obtained and numerically predicted tunnel defect is about 0.75 mm. The difference can be due to the mesh size considerations. Moreover, a small amount of material loss can also occur during the post-processing of the sample. Fig. 5.36 (b) shows the through-hole tunnel defect. The backlight effect is used to observe the continuous nature of the tunnel defect. The presence of a similar continuous type of tunnel defect is predicted in Fig. 5.36 (c).

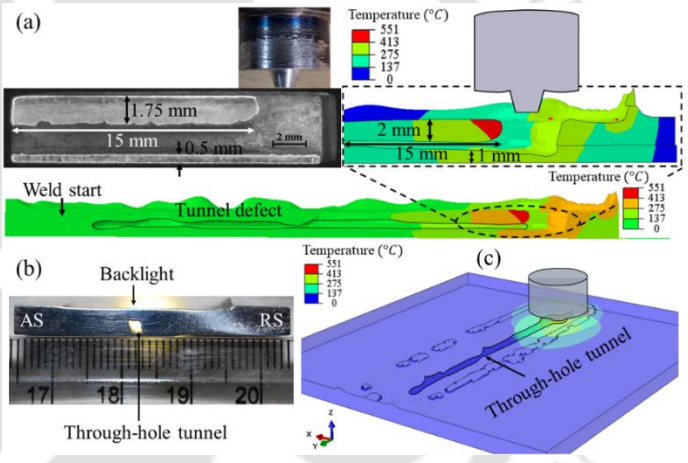

Fig. 5.36 (a) Comparison of tunnel defect in the AS for AZ31B; (b) Experimentally observed through-hole tunnel defect; (c) Numerically predicted subsurface continuous length tunnel defect

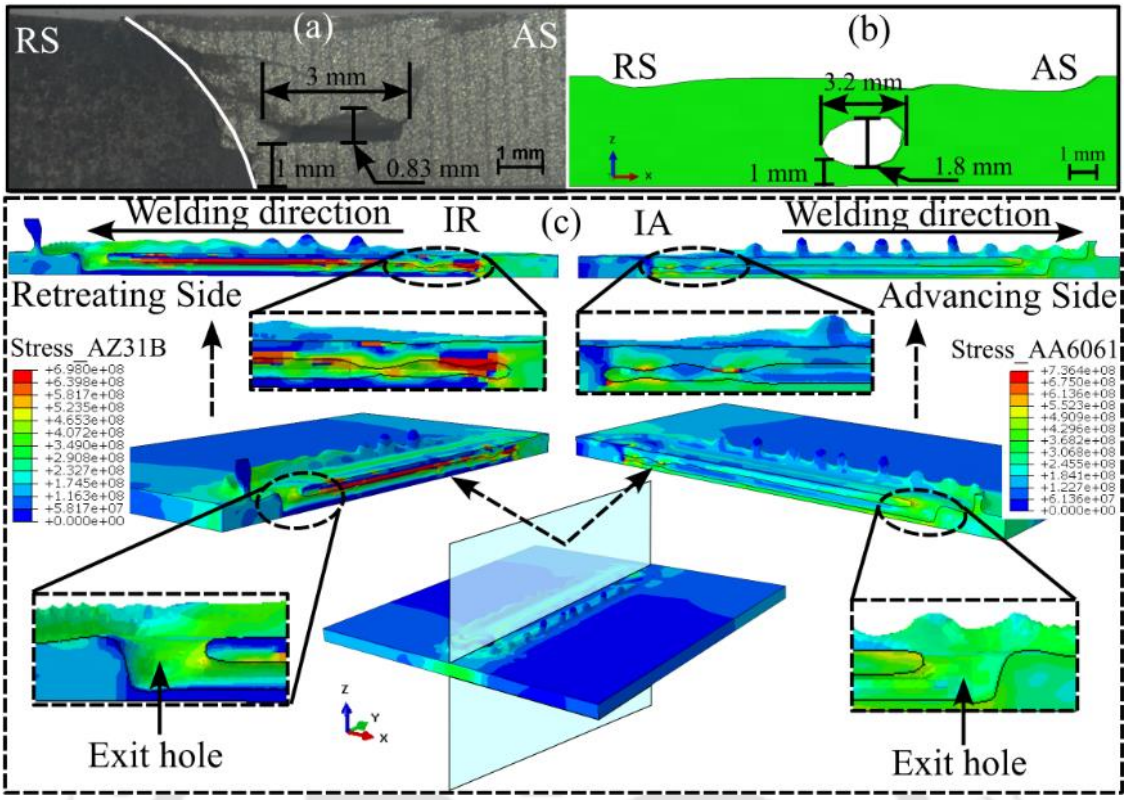

Fig. 5.37 Illustration of the cross-sectional subsurface tunnel defect (a) experimental, (b) numerically modelled, and (c) progress of subsurface tunnel defect and stress distribution within the workpiece

Figure 5.37 illustrates the subsurface tunnel defect appearing during dissimilar AA6061-AZ31B FSW. Figure 5.37 (a) shows the experimentally observed tunnel defect, while Fig. 5.37 (b) shows the numerically predicted result. The location and the width of the tunnel defect are closely predicted. The height of the tunnel defect is over-predicted numerically. The possible reasons for the same can be the mesh size considerations and isotropic material properties used for the modelling. The workpiece is split longitudinally and shown in Fig. 5.37 (c) to observe the progress of the tunnel defect and stress distribution around the defect. The weld initiation site on the AS and RS, as denoted by IA and IR, respectively, observes a varying depth tunnel defect; however, the defect depth becomes almost uniform thereafter. The generation of sufficient heat during the dwell stage can be responsible for lesser defect depth at the weld initiation. A slightly higher stress value is observed on the AS than on the RS; however, the higher stress concentration on the AS is localized to certain regions in SZ. The stress is evenly distributed in the remainder of the plate on the AS. Alternatively, the higher stress is concentrated near the top surface of the workpiece on the RS, whereas the stress near the bottom surface on the RS is almost negligible. This shows that most of the material is deposited around the top surface, and

very less material movement is observed around the bottom surface. This is a very potent reason for the generation of the tunnel defect. Further, using the conical pin can be a possible reason for improper material movement near the bottom surface.

Figure 5.38a indicates the formation of the tunnel defect with the progress of the tool. The material flow within the workpiece indicates a significant flow towards the RS in front of the tool than the AS in front of the tool. Further, the flow velocity on AS in front of the tool increases from about $10\ mm/s$ to $15\ mm/s$ towards the RS in front of the tool (Fig. 5.38b). The highest flow velocity is observed towards the RS behind the tool of about $20\ mm/s$. However, as the material is directed toward the AS behind the tool, the flow drops significantly and becomes marginal. This marginal flow of material towards the AS behind the tool results in the improper filling of the void left behind by the traversing tool and leads to the formation of the tunnel defect.

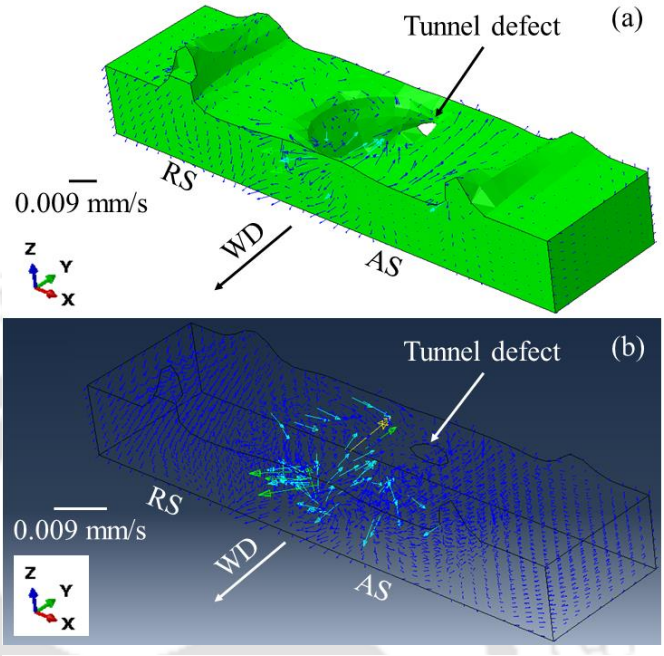

Fig. 5.38 Representation of the formation of the (a) tunnel defect; and (b) sub-surface material flow for AZ31B at 1200 rpm and 60 mm/min

Figure 5.39 shows the material flow at about half the workpiece thickness, i.e., at the mid-plane. The material flow at this location is due to the interaction of the tool pin with the workpiece material. Figure 5.39a shows a uniform distribution of material around the tool pin. The highest speed of $25\ mm/s$ is observed around the tool pin on the RS in front of the tool; however, all the other directions collect a uniform

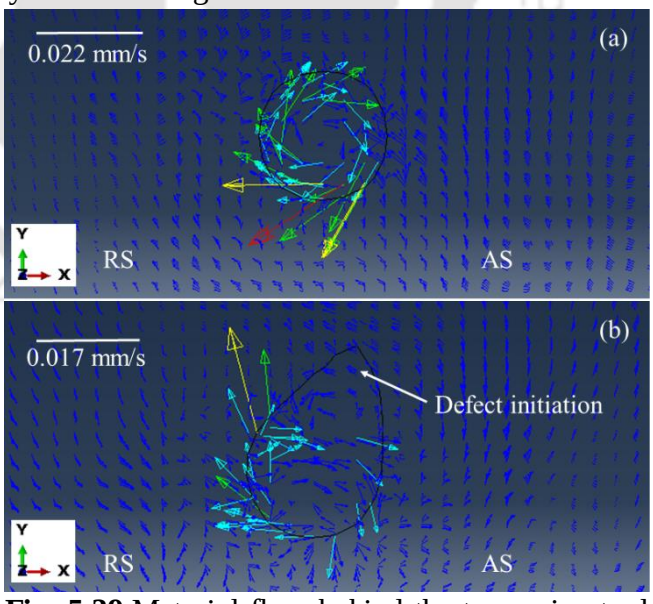

Fig. 5.39 Material flow behind the traversing tool on the mid-plane indicating (a) uniform distribution; and (b) non-uniform distribution for AZ31B at 1200 rpm and 60 mm/min

distribution of material. As the tool progresses in the welding direction (WD), a non-uniform material deposition is observed around the pin, leading to the initiation of the tunnel defect. With the initiation of tunnel defect, the highest speed is observed towards the RS behind the tool, whereas the AS behind the tool is collecting marginal material flow (Fig. 5.39). A difference in the flow velocity of about $10\ mm/s$ is observed between AS and RS. This significant discrepancy in the material flow aids the formation of tunnel defects.

5.8.2 Insufficient or failed joint between plates

The insufficient joint between plates or lack of fusion is a defect that appears due to two improperly joined workpieces. This defect is observed at process parameters of 360 rpm and 300 mm/min. Multiple cases with varying pin geometry are considered as the pin geometry plays an important role in material movement and joint formation. The Johnson-Cook damage model is factored into the model to observe the failure in the joint formation. Failure is assumed to occur when the Ω value exceeds 1 in Eq. 4.9. The Ω is dependent on strain at failure $\bar{\varepsilon}_f^{pl}$, which is, in turn, dependent on the temperature as observed in Eq. 4.10. The elements in the Eulerian (workpiece) domain are deleted with the progress of the tool if the limiting criteria of the failure model are reached. Thus, the formation of the failed joints can be captured in Fig. 5.40 with the progress of tool movement. High traverse speed, along with low tool rotation speed leads to poor heat generation. The heat generated per rotation and per unit length of the workpiece is relatively much lower with this set of process parameters. Moreover, the dwell time, which is responsible for the preheating of the material, is as low as 2 s for low heat diffusion. The highest temperature observed in the workpiece in Fig. 5.40 is about 65% of the melting point of Aluminium. The

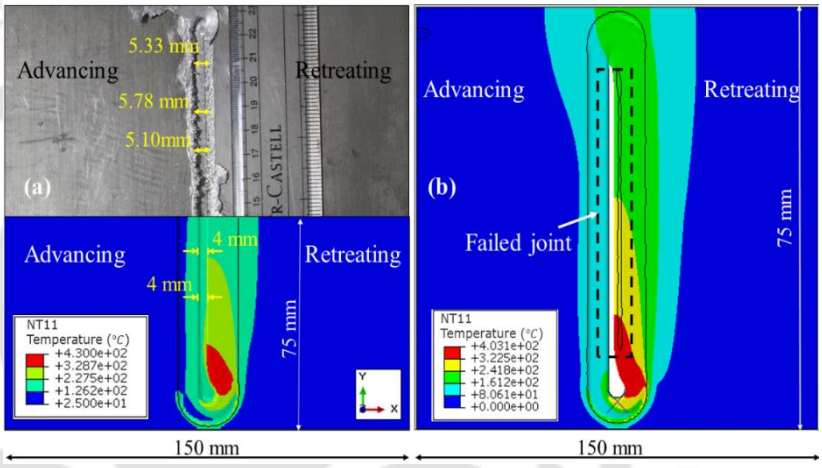

Fig. 5.40 Influence of P_h on weld joint a) experimental and numerically observed partial joint with P_h ~2.5 mm; b) failed joint with P_h ~3.5 mm at rotation speed of 360 rpm and traverse speed of 300 mm/min

temperature range is not sufficient to obtain a good weld joint. The region of the highest temperature is just below the tool shoulder on one side of the workpiece. Due to improper deposition of material just below the tool shoulder throughout the tool radius, the heat is concentrated in only one region of the workpiece. In Fig 5.40 (a), the pin length is much smaller than the thickness of the workpiece, therefore a thin section of the workpiece is partially joined underneath the region where the tool pin passed. With an increase in pin height (Fig. 5.40 (b)), the material is totally displaced from the joint region, and a see-through region is created. Due to the rapid movement of the tool, the inadequately plasticized material is forged out of the stirred zone in a direction away from the tool pin. This creates a region of void or no-fill in the stirred zone, resulting in the formation of failed joints.

5.8.3 Excessive flash formation

Flash formation is one of the most commonly occurring phenomena during FSW. The loss of material from the stirred zone in the form of a flash reduces the plate thickness and thus affects the structural integrity of the body. The void domain here captures the material expelling out of the workpiece and thus enables the study of flash formation. Any material moving out of the defined computational domains would be lost for the solution. The rotation and traverse speed used for the simulation is 1200 rpm and 90 mm/min, respectively

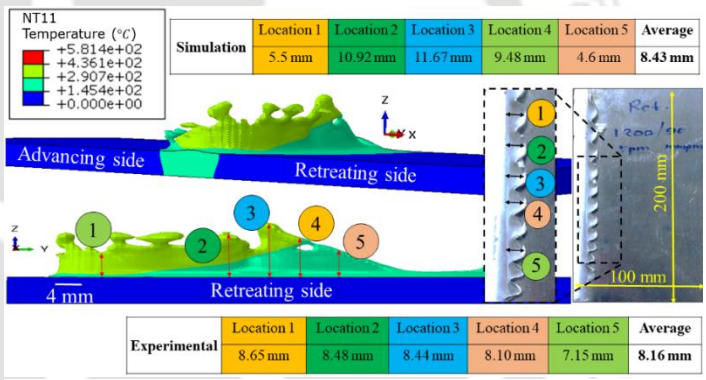

Fig. 5.41 Comparison of the experimental and numerical chip height formed at 1200 rpm, 90 mm/min, and 0.84 mm plunge depth. The chip size near the weld start is small and keeps on increasing initially. Once it reaches the maximum height, the chip size becomes constant

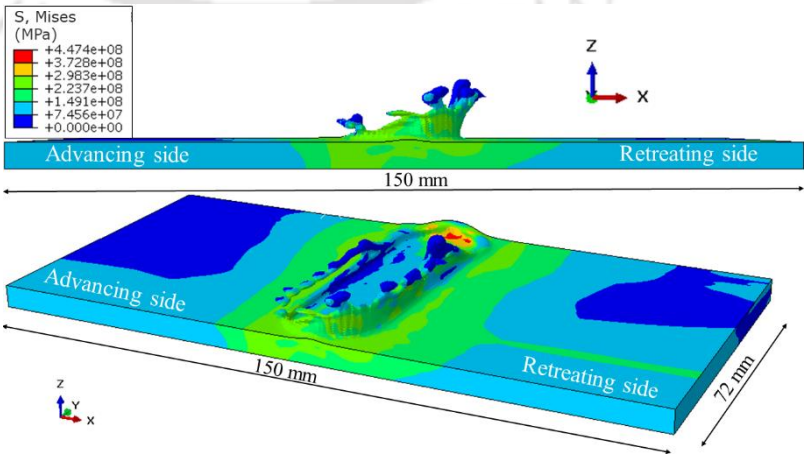

Fig. 5.42 Von-Mises stress distribution on full solution domain at 1200 rpm, 90 mm/min, and 0.84 mm plunge depth

and a high plunge depth of 0.84 mm is chosen. The size and shape morphology of the flash formation during similar AA6061 is described in Fig. 5.41. The chip size is measured at five different locations, and the average size of chip formation is determined. The average chip size observed from the simulation is 8.43 mm, while the average chip size observed experimentally is 8.16 mm. During tool rotation, the material from the AS is rotated around the tool pin and is pushed into the RS. This results in the formation of a more continuous and prominent chip on the RS as compared to the AS (Figs. 5.41 and 5.42). The temperature of the chip ranges from about 350˚C to 170˚C. This high temperature of the chip helps it to flow easily out of the workpiece. If the temperature generated during the welding is over the optimum limit, the workpiece material undergoes severe plastic deformation at hot processing conditions. This excessive heat generated and plasticization of the material pushes it out of the stirred zone in the form of a chip. This expulsion of the material can also lead to insufficient filling of the stirred zone which can lead to tunnel defect formation. The material being expelled out is under significant pressure because of the force applied on them due to the tool motion. Figure 5.42 shows the stress variation observed in the workpiece. The stress generated in the flash and the flash root is higher than the stress observed in the rest of the workpiece. The highest stress value is observed at the beginning of the weld when the tool shoulder makes sudden contact with the workpiece at the end of the plunge step. The stress generated in the rest of the workpiece is fairly uniform, where it varies between 150 – 300 MPa. This stress distribution is similar in nature to the observations made by Sun et al. (Sun *et al.*, 2017) while working with AA2219. The stress generated in the flash is much higher, breaching 300 MPa at some locations. This shows that the flash is formed under extreme pressure and is pushed out of the workpiece due to the tool action.

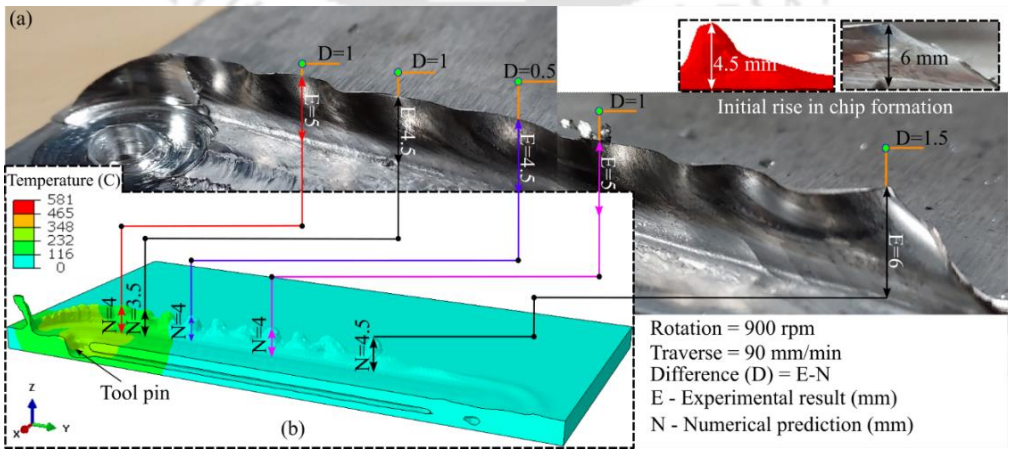

Fig. 5.43 (a) Experimental investigation and (b) Numerical modelling of the flash formation on the retreating side with 900 rpm and 90 mm/min

Figure 5.43 shows the prediction of the surface flash defect during dissimilar FSW of AA6061-AZ31B. As more material is deposited on the RS resulting in more flash formation (Fig. 5.43 (a)), the RS, i.e., the side consisting of AZ31B, is considered for our analysis. The predicted flash is compared to the experimental investigation for the complete length of the welding. The maximum difference in pin height prediction is about 1.5 mm, observed at the beginning of the flash formation. The average difference in flash size prediction is about 1 mm compared to the experimental result. The difference in the result can be due to the mesh size considerations and human error during experimental measurements.

5.8.4 Surface defects

Apart from flash formation, other surface defects such as voids, cracks, and grooves are also observed in friction stir welded samples (Ranjan *et al.*, 2016). These defects can also be termed as discontinuities. A significant difference between the flash and other surface defects is the sporadic nature as opposed to the continuous nature of the flash. Figure 5.44 (a) shows a numerically predicted and greyscale image of the similar AA6061 FSW having process variables of 1200 rpm and 90 mm/min. A distinct shoulder and pin profiles at the weld start and weld ends are visible. As the welding progresses, multiple surface discontinuities arise at the stirred zone of the weld. Initially, these discontinuities are no bigger than small spots or dots. These spots, as seen in Fig. 5.44 (a) are considered as voids on the surface. These defects can have variable sizes and can be oriented in any direction. As the tool approaches the end of the welding, the small size of these voids increases to take the shape of small curves. Figure 5.44 (b) describes the voids that are observed experimentally with the same process parameters as used in the FE model. Improper heat generation, improper material plasticization, and improper contact between the tool and the workpiece are mainly responsible for the generation of these surface defects. The void defect is predicted when the material is absent in one or more of the surrounding elements. Sufficiently small mesh size ($1 \times 1 \times 0.5\, mm^3$) is used to capture these surface irregularities. A smaller element

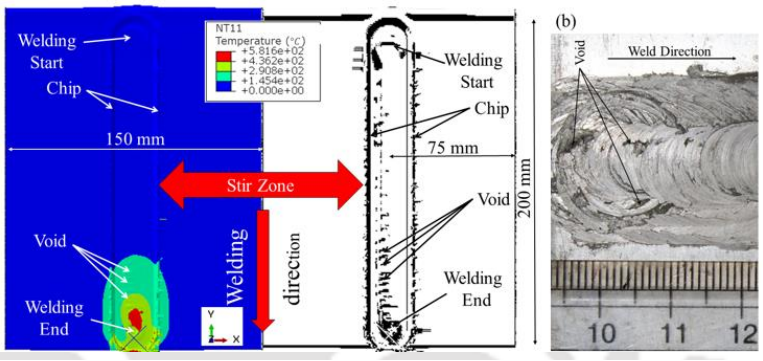

Fig. 5.44 Void on surface obtained at rotational speed of 1200 rpm and traverse speed of 90 mm/min: (a) FE model, and (b) Experimental observation

domain can be used to capture smaller defects or discontinuities, but that would make the process computationally expensive. Fig. 5.45 shows a schematic and numerically predicted form of another type of surface defect where the traversing tool shoulder leaves behind a trace of semi-circular shape. It is formed due to the rotation and deposition of material around the tool shoulder. Although this surface non-uniformity can be present throughout the weld, but at the weld end, a clear semi-circle is visible due to the presence of the end-dwell step. The pin-hole surface defect is also visualized at the end of the weld in both Figs. 5.44 and 5.45. This defect generates due to the unfilled region left by the tool pin on plunging out of the workpiece at the end of the welding. This defect can be eliminated by using a consumable pin.

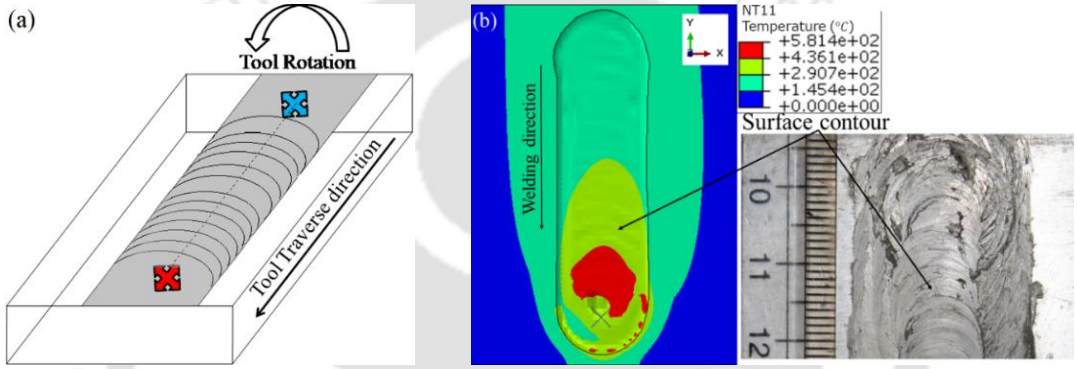

Fig. 5.45 Illustration of surface contours on stirred zone: (a) schematic diagram, (b) 2D contour with experimental observation at 1200 rpm and 90 mm/min. Surface contours are observed practically throughout the length of the stir zone

The tunnel defect is one of the most common forms of the defect in FSW. The defect is generally present below the workpiece's top surface. However, improper process parameter selection can also lead to tunnel defects on the surface. An instance of the surface tunnel is depicted for dissimilar AA6061-AZ31B FSW in Fig. 5.46. The improper process parameters lead to insufficient heat generation and reduce material plasticization at the SZ. The maximum temperature under the tool shoulder and around the tool pin is about 400 °C. Thus, the maximum temperature is about 60% of the melting point temperature of the base materials; thus, it is not sufficient to properly plasticize the material. Moreover, the sense of the tool rotation and traverse are similar on the AS. Therefore, the tool, thus leaving behind the surface tunnel defect, forcibly pushes out the material. Alternatively, as the material is deposited behind the tool with each rotation, such defect is not observed on the RS. A continuous length surface tunnel on the AS is predicted numerically, and a similar

surface tunnel is also observed experimentally (Fig. 5.46). The width of the experimental surface tunnel is about 1 mm throughout, whereas the numerically predicted result is about 0.8 mm. However, at a unique location at the beginning of the defect, the width of the defect is about 2 mm. The minor deviation between the predicted and experimental results can be due to machine and human errors.

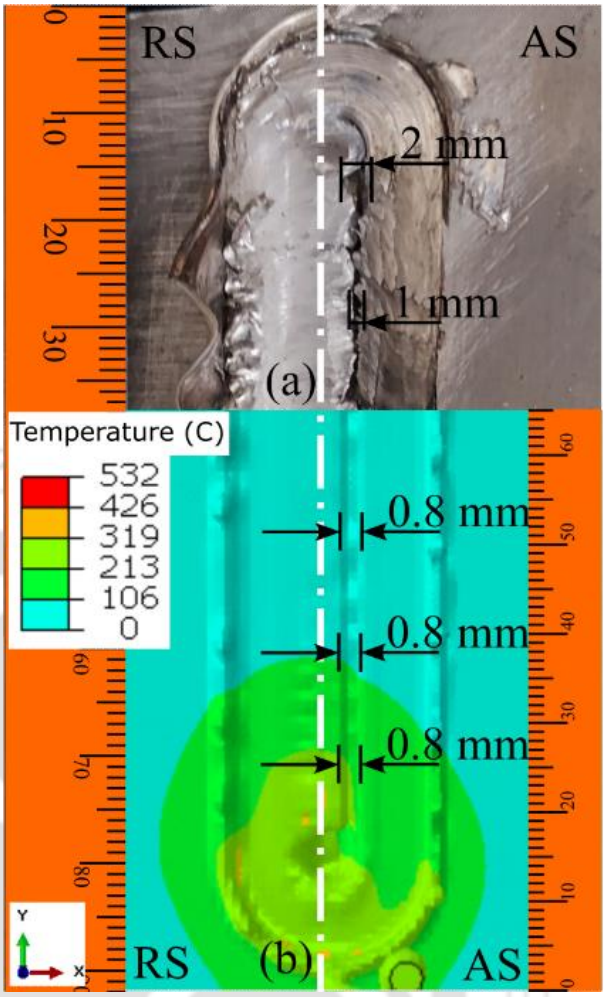

Fig. 5.46 (a) Experimental and (b) numerical investigation of the surface tunnel generating on the SZ during dissimilar AA6061-AZ31B FSW with 1200 rpm and 30 mm/min

Figure 5.47 indicates the material flow around the tool at about 7 seconds of the initiation of welding. Figure 5.47a depicts the material flow for the complete workpiece domain, whereas Fig. 5.47b indicates the deformed weld zone from the top. The majority of the material flow occurs at the tool pin root. The material completely rotates around the tool, and uniform distribution of the material is observed in all directions. This phenomenon leads to good weld quality, as observed in Fig. 5.47b. The highest flow velocity is observed in the RS behind the tool and within the workpiece domain, which is about 20 mm/s (Fig. 5.47a). As the tool further progresses in the welding stage, the deposition of the material around the tool pin becomes significantly non-uniform (Fig. 5.48a). The flow velocity increases to ~ 25 mm/s. However, unlike the previous case, the material is deposited primarily towards the RS in front of the tool. This causes a lack of material flow towards the AS behind the tool. It means the material is not properly plasticized and rotated around the tool. This improper material flow and deposition drive to the initiation of defective welding near the AS behind the tool. The non-uniform deposition, as depicted in Fig. 5.48b, may lead to the formation of sporadic voids on the top surface, or it can be present for a significant length where the defect is referred to as the surface tunnel defect.

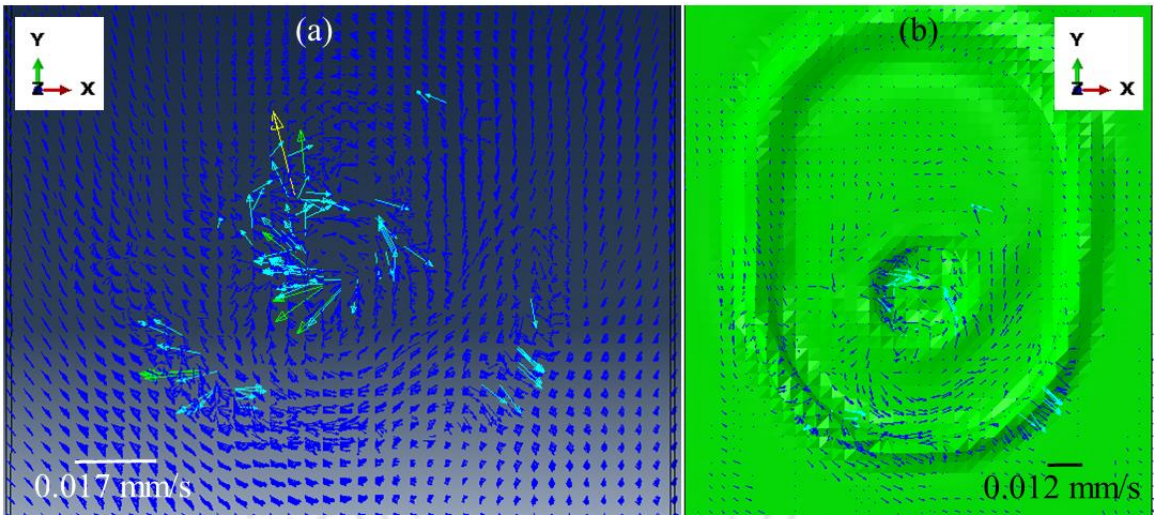

Fig. 5.47 Prediction of surface (a) material flow; and (b) weld quality to indicate proper material deposition behind the traversing tool for AZ31B at 1200 rpm and 60 mm/min

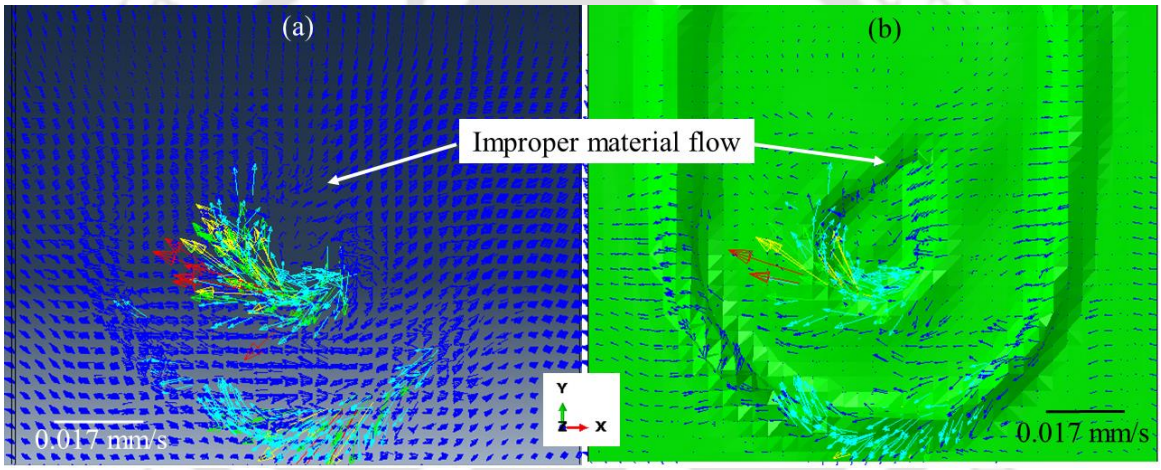

Fig. 5.48 Prediction of surface (a) material flow; and (b) weld quality to indicate improper material deposition behind the traversing tool for AZ31B at 1200 rpm and 60 mm/min

5.8.5 Exit hole defect

Figure 5.49 presents the unavoidable exit hole in FSW. The experimentally observed exit hole is shown in Fig. 5.49 (a), whereas the height and the cross-sectional width of the defect are presented in Figs. 5.49 (b) and (c), respectively. The height of the defect is predicted with substantial accuracy. The difference between the experimental and the numerical result is marginal at about 0.2 mm. The exit hole diameters near the top and bottom surface of the workpiece have a minor deviation of about 0.4 mm and 0.1 mm, respectively. The refilling technique can repair the exit hole in a similar FSW. However, the refilling technique can be a difficult approach due to the dissimilar nature of the weld zone (Mehta *et al.*, 2021).

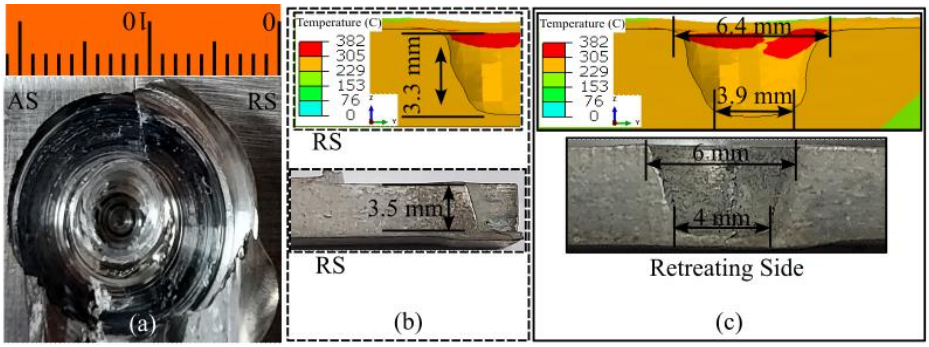

Fig. 5.49 Experimental and numerical investigation of exit hole (a) experimental, (b) height, and (c) cross-sectional variations in the solution domain

5.8.6 Effect of tool wear on weld quality

The FSW is performed with AA6061 on the AS and AZ31B on the RS. The tool profile change after welding with 900 rpm and 1200 rpm is presented in Figs. 5.50 and 5.51, respectively. The tool profiles depicted in these figures are analyzed after removing the adhered base material coating on the tool surface, i.e., the tool profile shown in Figs. 5.50 and 5.51 are actual tool profiles after welding. Figure 5.50 (a) shows the initial tool condition, and Fig. 5.50 (d) shows the tool condition after the completion of the welding at 900 rpm and 90 mm/min. The major pin diameter (d_1), minor diameter (d_2), and pin length (h) change by 0.47%, 18.06%, and -12.19%, respectively, between the initial and final tool conditions (Fig. 5.50). There is a minor change in the volume of the pin, i.e., 82.114 mm^3 and 82.773 mm^3 between Figs. 5.50 (a) and (d). The slight difference in the volume can be due to the small quantity of workpiece material on the tool and human error during experimental measurements. The d_2 observes a more significant change in dimension due to its smaller diameter and initial and constant contact with the workpiece during the plunge stage. The same is responsible for reducing the height of the tool pin also, which can lead to root defect due to improper tool pin penetration. The change in the d_1, d_2, and h between Figs. 5.51 (a) and (d), i.e., the initial and the final tool conditions, are 2.56 %, 28.32%, and -10.23%, respectively. Furthermore, the volume of the tool pin (Fig. 5.51 (d)) is 82.639 mm^3 and has a minimal difference of 0.134 mm^3 from the tool pin shown in Fig. 5.50 (d). The similar volume of the tool pin after equal numbers of weld runs, irrespective of the process parameters, indicates marginal material loss from the tool pin. In contrast, the tool pin shape changes drastically after each weld run (Figs. 5.50 and 5.51). Thus, it can be concluded that during dissimilar AA6061-AZ31B FSW, the primary concern for tool wear is diminishing dimensional integrity rather than the material loss from the tool surface.

Table 5.1 summarizes the changes in the d_1, d_2, and h values after each weld run when welding at 900 rpm and 1200 rpm.

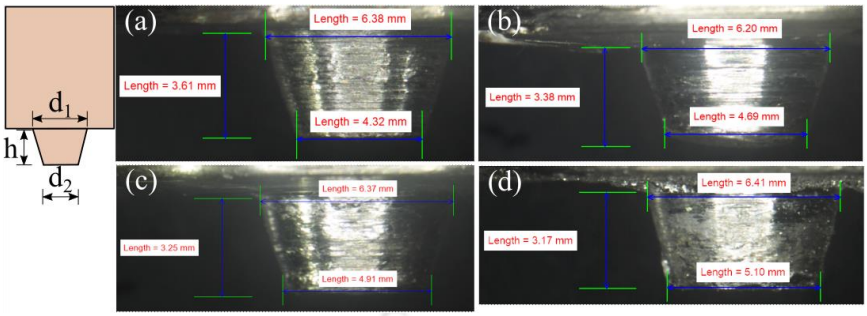

Fig. 5.50 Progressive variation in the tool pin geometry when welding at 900 rpm and traverse speed of (a) initial tool under no weld condition, (b) 30 mm/min, (c) 60 mm/min, and (d) 90 mm/min

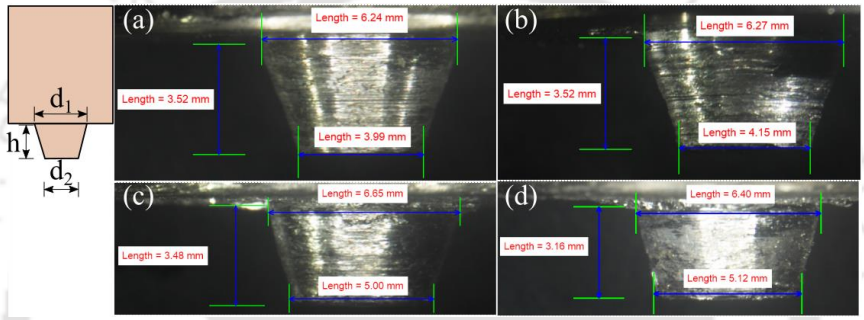

Fig. 5.51 Progressive variation in the tool pin geometry when welding at 1200 rpm and traverse speed of (a) initial tool under no weld condition, (b) 30 mm/min, (c) 60 mm/min, and (d) 90 mm/min

Table 5.1. Alterations in the pin length, major and minor diameters of the conical pin with successive weld runs

Weld No.	Pin Length (h) (mm)	Pin length change (%)	Pin major diameter (d_1) (mm)	Pin major diameter (d_1) change (%)	Pin minor diameter (d_2) (mm)	Pin minor diameter (d_2) change (%)
Tool-I	3.61	-	6.38	-	4.32	-
Weld-I1	3.38	-6.37	6.20	-2.82	4.69	8.56
Weld-I2	3.25	-9.97	6.37	-0.16	4.91	13.66
Weld-I3	3.17	-12.19	6.41	0.47	5.10	18.06
Tool-II	3.52	-	6.24	-	3.99	-
Weld-II1	3.52	0.00	6.27	0.48	4.15	4.01
Weld-II2	3.48	-1.14	6.65	6.57	5.00	25.31

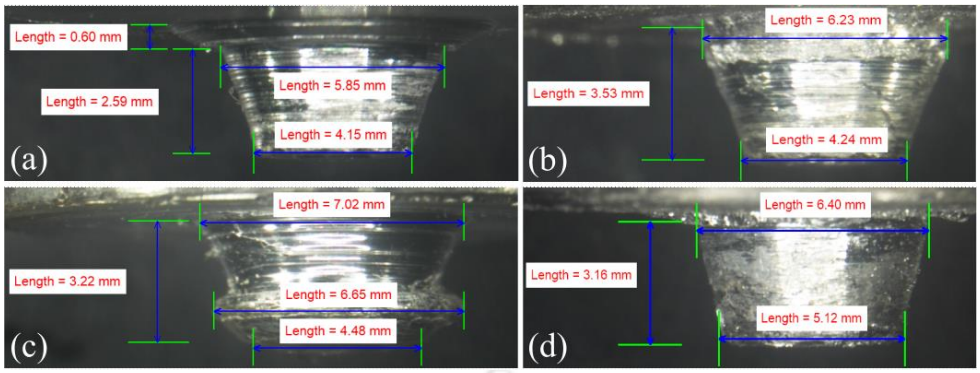

Fig. 5.52 Variation in the tool pin geometry when welding at 1200 rpm (a) weld material is adhered to the tool surface and (b) the weld material is removed from the tool surface when the tool traverse speed is 60 mm/min, and (c) weld material is adhered to the tool surface and (d) the weld material is removed from the tool surface when the tool traverse speed is 90 mm/min

Figure 5.52 shows the difference in the actual tool pin profile due to the adhesion of the workpiece material on the tool pin. Figure 5.52 (a) and (c) show the material adhesion after FSW at 60 mm/min and 90 mm/min, respectively; and the tool rotation speed is 1200 rpm. The original pin shape after removal of the adhered material is shown in Figs. 5.52 (b) and (d). The presence of foreign material on the tool is easily visible at the root of the tool pin (Fig. 5.52 (a)). The pin height reduces by about 0.6 mm due to the adhered material, while the d_1, and d_2, endure a change of -6.09% and -2.12%, respectively. Moreover, in Fig. 5.52 (c), the original conical shape of the tool pin changes into a mushroom shape due to the adhesion of the workpiece material (Majeed, Mehta and Siddiquee, 2021). This leads to a significant change in the original tool dimension of d_1, and d_2, i.e., 9.69% and -12.5%, respectively. The adhered material to the tool pin was analyzed using a FESEM-EDS analysis, as shown in Fig. 5.53. Figure 5.53 (a) indicates the uniform distribution of Mg, Al, and Fe, i.e., the main constituents of the AA6061, AZ31B, and H-13 tool steel, respectively, on the material adhered to the tool surface. Figs. 5.53 (b)-(d) shows the distribution of the Mg, Al, and Fe on the surface of the adhered material. The FESEM-EDS analysis indicates the uniform distribution of the Mg and Al on the top surface of the SZ, while a meagre presence of Fe is detected in the mixed material. Although the FSW was performed using a 0 mm tool offset, the material on the tool surface shows a higher percentage of AA6061, i.e., 58.86%, compared to AZ31B, having 40.97% (Fig. 5.53 (e)). The numerical modelling of the material mixing also indicates higher material movement from the AS to the RS (Fig. 5.33). The Fe concentration is marginal (0.16%). It thus further stipulates that the tool material is not being eroded during welding.

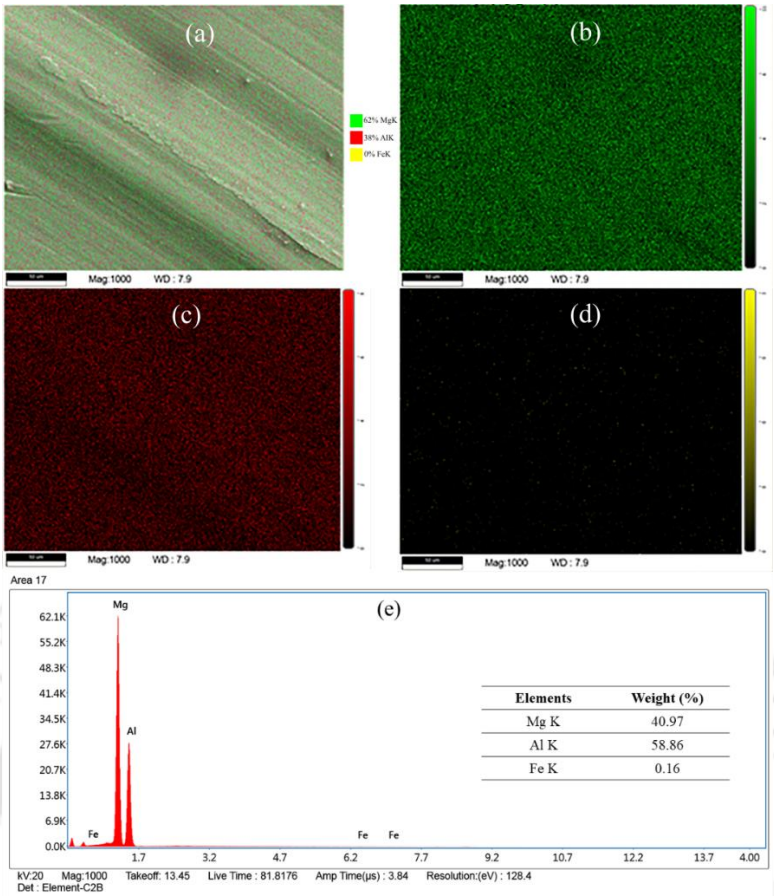

Fig. 5.53 Scanning electron microscopy- EDS mapping of the (a) workpiece material adhered to the tool during welding showing the presence of (b) Magnesium (Mg), (c) Aluminium (Al), (d) Iron (Fe), and (e) intensity peak of the constituent materials

Figure 5.54 shows the difference in the weld quality when modelling the initial 300 mm welding with the tool in different wear-out conditions, as provided in Table 5.1. Figure 5.54 (a) is modelled with the initial unvarying tool condition, and the result predicts a sub-surface tunnel defect, whereas the surface tunnel is avoided. However, Fig. 5.54 (b) is modelled with the actual condition tool observed during experimentation (Fig. 5.51 (c)). The critical modelling with the actual

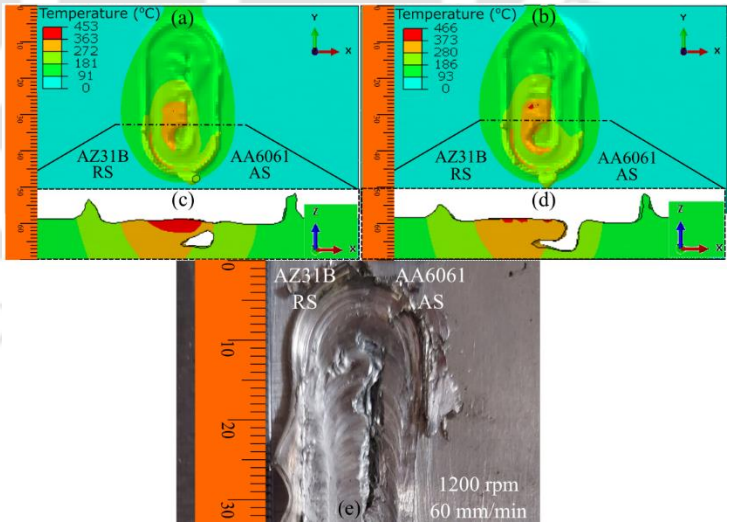

Fig. 5.54 Comparative illustration of the progress of FSW at 1200 rpm and 60 mm/min with (a) tool as shown in Fig. 5.51 (a), (b) tool as shown in Fig. 5.51 (c), (c) cross-section view of the defect in Fig. 5.54 (a), and (d) cross-sectional view of the defect in Fig. 5.54 (b) and (e) experiments on FSW

condition tool generates a combination of defects, i.e., the surface tunnel and the sub-surface tunnel defect (Figs. 5.54 (b) and (d)). The surface tunnel defect is also observed when welding at 1200 rpm and 60 mm/min using the moderately worn-out tool, as shown in Fig. 5.54 (e). Therefore, it can be postulated that the quality and condition of the tool are very important to numerically predict the weld quality. Figure 5.54 (c) is void of any surface defect due to the initial pin dimension, which allows for a moderately easy flow of material around it. Alternatively, as the dimension of the tool is modified due to tool wear after multiple uses in Fig. 5.54 (d), the surface tunnel defect also appears because the tool is no longer capable of sufficient plasticization and mixing of material around the tool pin.

5.8.7 Effect of plate position on weld quality

Figure 5.55 presents the prediction of the surface defects during FSW at different process parameters when the position of the plates was interchanged between the AS and RS. The FSW with AA6061 on the AS produces a more uniform weld than the welding with AZ31B on the AS. The higher heat generation and better tear drop-shaped heat zone in Figs. 5.55 (a) and (b) are responsible for better welding. However, the heat flow pattern is improper when AZ31B is placed on the AS, leading to the formation of a surface tunnel in both cases (Figs. 5.55 (c) and (d)). The cross-sectional investigation near the weld completion for all four cases also indicates the presence of a surface tunnel with a depth of more than half of the

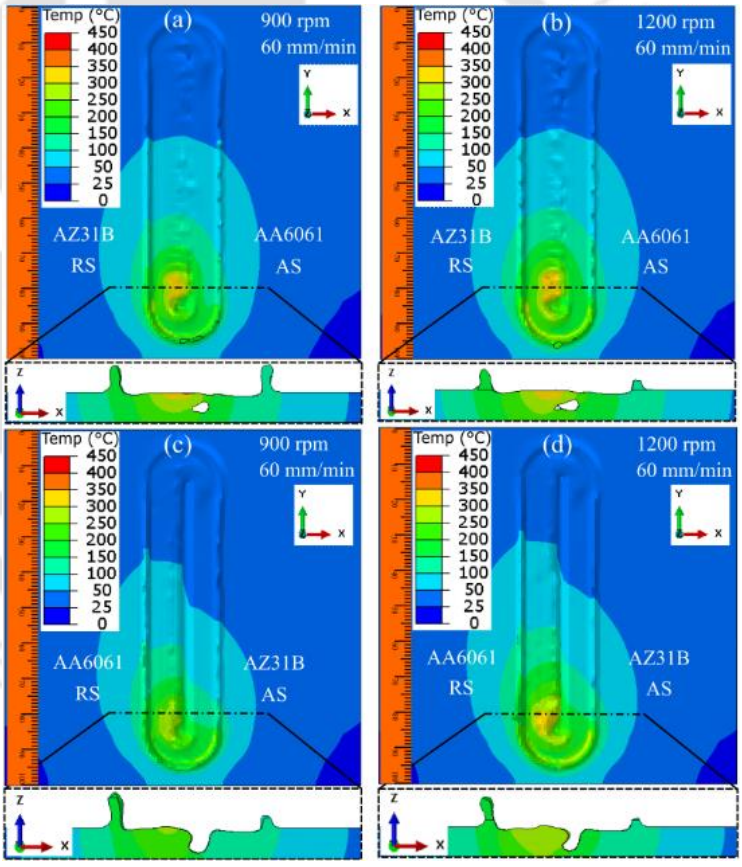

Fig. 5.55 Numerical modelling of the surface non-uniformity evolution during AA6061-AZ31B dissimilar FSW when the position of the base material is interchanged, (a) AA6061-AZ31B at 900 rpm and 60 mm/min, (b) AA6061-AZ31B at 1200 rpm and 60 mm/min, (c) AZ31B-AA6061 at 900 rpm and 60 mm/min and (d) AZ31B-AA6061 at 1200 rpm and 60 mm/min

workpiece thickness when AZ31B is used on the AS (Figs. 5.55 (c) and (d)). Alternatively, no surface defects are observed when AA6061 is used on the AS. Multiple researchers have recommended placing the aluminium alloy on the AS and magnesium alloy on RS (Somasekharan and Murr, 2004; Chang *et al.*, 2011; Zhao *et al.*, 2016). The absence of the surface tunnel defect in Figs. 5.55 (a) and (b) indicate a better weld than the FSW with AZ31B on AS, but the quality of the weld can be further improved. Multiple factors are responsible for defect generation in FSW. The change in base material position helped eliminate the surface defects. Subsequently, proper heat generation and material flow can eliminate the sub-surface tunnel defect. These can be achieved by proper tool shape and size investigations. As the material flow improves with better tool design, the sub-surface tunnel defect will be eliminated, thereby improving the weld quality.

5.9 Prediction of residual stress using physics-informed ML models

The residual stress is the stress remaining in the body on removing any external loads. The effective stress is found to have the highest magnitude and is tensile in nature. As the tensile stresses are more detrimental to the product life than the compressive stresses, the effective stress is considered for further investigations. The current investigation focuses on both the residual stress at room temperature and stress evolution during the FSW. When the maximum stress exceeds the yield strength of the material, the plastic deformation is to be retained by the body leading to weld distortion (Kong, Ma and Kovacevic, 2011). As such, the ML algorithms are applied to predict both the temperature and stress evolution as the output variable in the body during the welding and cooling stages. The tool rotational speeds considered are 600, 700, and 800 rpm, whereas the traverse speed varies between 60 and 150 mm/min with an increment of 10 mm/min. For each case, 306 data points are generated. Therefore, the total data points generated for training and testing of the ML algorithms are $3 \times 9 \times 306$. The initial datapoints are generated using the CEL based numerical model. The 600 rpm and 60 mm/min dataset is not used for training the model, and it is separately used to determine the accuracy of the predicted results by the ML model. From the total datasets, 80% of the data points are used for training, while the remaining are used for testing. The robustness of the numerical model relies on the validation of residual stress both for AS and RS. The two-way validation is significant due to the different mixing of materials on both the AS and the RS. The generated dataset for the temperature and residual stress is employed for training and prediction by the ML models.

The data feed to the ML models is generated from the numerical model, thus, the reliability of the ML results significantly depends on the accuracy of the thermo-mechanical results obtained by the numerical model. Therefore, the temperature and stress data of the numerical model are meticulously validated with experimental investigation. As it is very tricky to accurately determine the residual stress value using the non-destructive XRD method, a range for the residual stress value is determined and compared with the numerical result (Figs. 5.56 (a) and (b)). The predicted residual stress by the numerical model is within the limits of the experimentally calculated stress value.

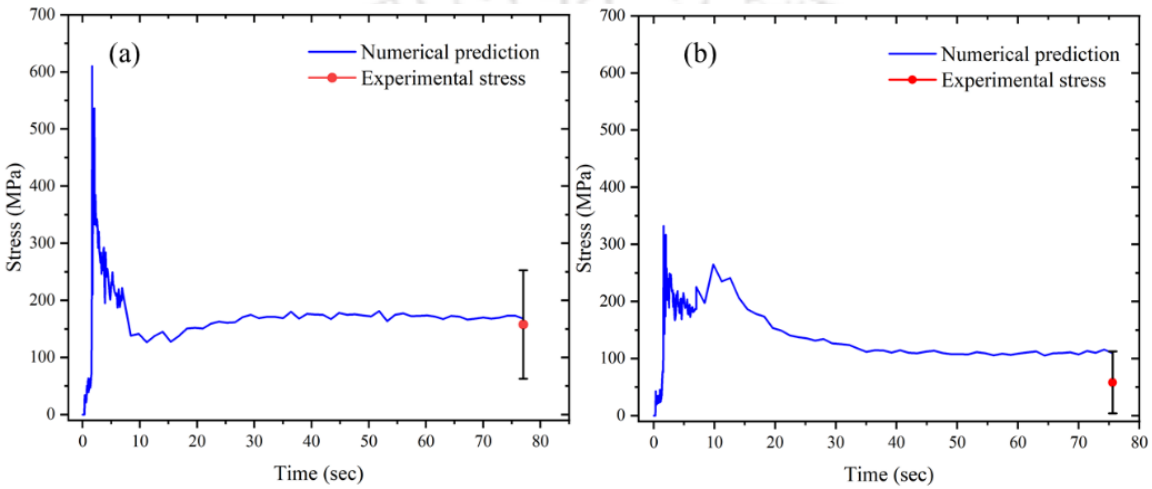

Fig. 5.56 Comparison of the predicted and residual stress value during dissimilar FSW of AA6061-AZ31B on the (a) AS and (b) RS at 1200 rpm and 60 mm/min

For the current work, various ML models are compared to determine their accuracy in predicting temperature and residual stress. The R^2 value and the mean squared error (MSE) for the testing dataset is used to rank the different ML algorithms as shown in Fig. 5.57 (Wang *et al.*, 2023). The R^2 value is calculated until the fourth decimal to nullify any rounding off error. The best three ML algorithms namely the ETR, XGB, and RFR performed well for the current work and are used for further analysis.

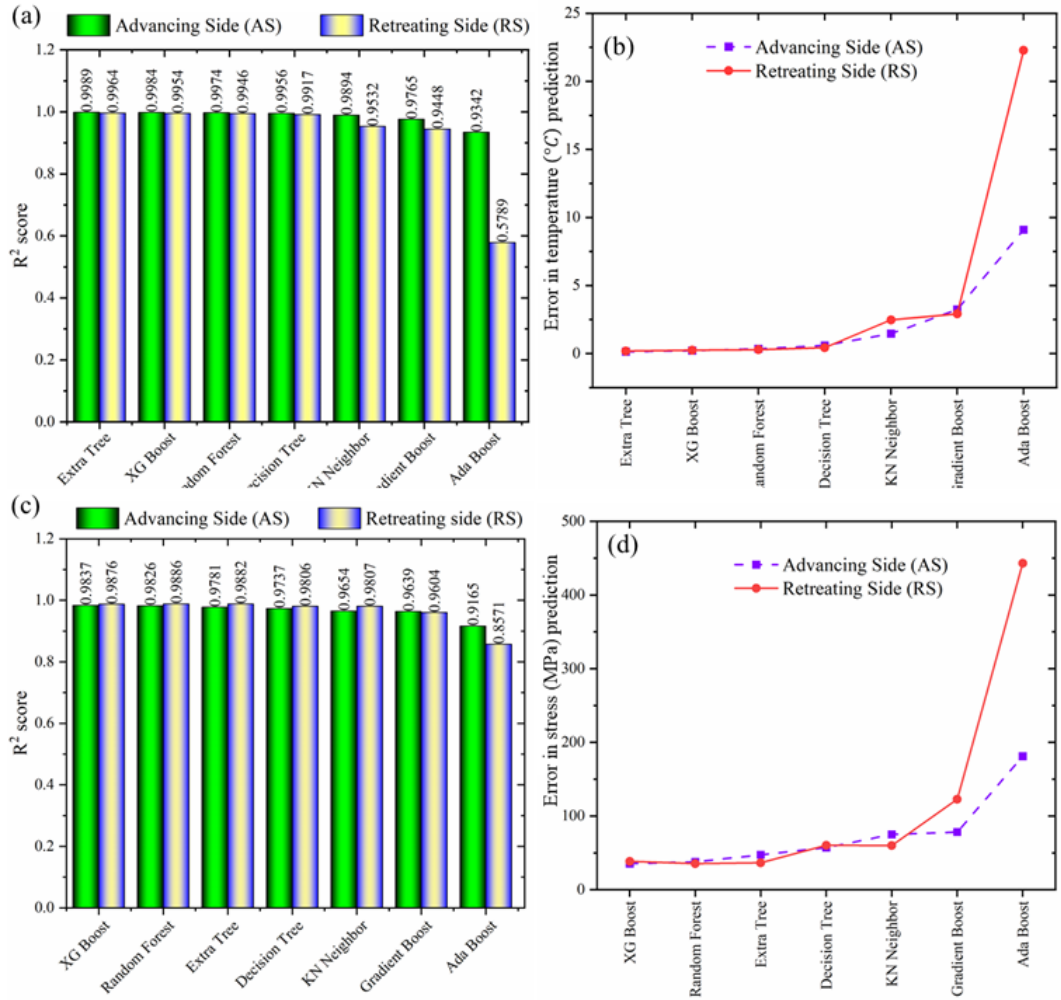

Fig. 5.57 Comparative analysis of the various ML models applied to the AS and RS for the temperature evolution based on (a) R^2 score, and (b) MSE; Residual stress propagation based on (c) R^2 score, and (d) MSE

Figures 5.58 and 5.59 present the relationship between the different process parameters and their effect on the temperature and residual stress, respectively. The temperature shows an increasing trend with the increase in the tool rotational speed on the AS and RS. However, the effect of tool rotational speed is more prominent on the AS than the RS. An increase in the traverse speed to 125 mm/min significantly reduces the temperature on the AS, beyond which it becomes constant. The traverse speed has a marginal effect on the temperature of the RS. The increase in the tool rotational speed to traverse speed ratio enhances the temperature of the AS and has a limited effect in varying the temperature of the RS. A higher temperature is observed on the RS compared to AS. The higher thermal conductivity and diffusivity of AA6061 placed on the AS could be responsible for the same. The increase in the tool rotational speed to traverse speed ratio affects the residual stresses differently on the AS and RS. As the tool rotational speed increases, the stress on the AS

increases while it reduces marginally on the RS. The traverse speed has a more prominent effect on the stress progression of the AS than the RS. After welding, the residual stress on the RS spreads over a wide range compared to the AS at the end of the welding. The force with which the material is deposited to the RS varies due to the formation of the various volumetric defects and is responsible for the distribution of residual stress on the RS.

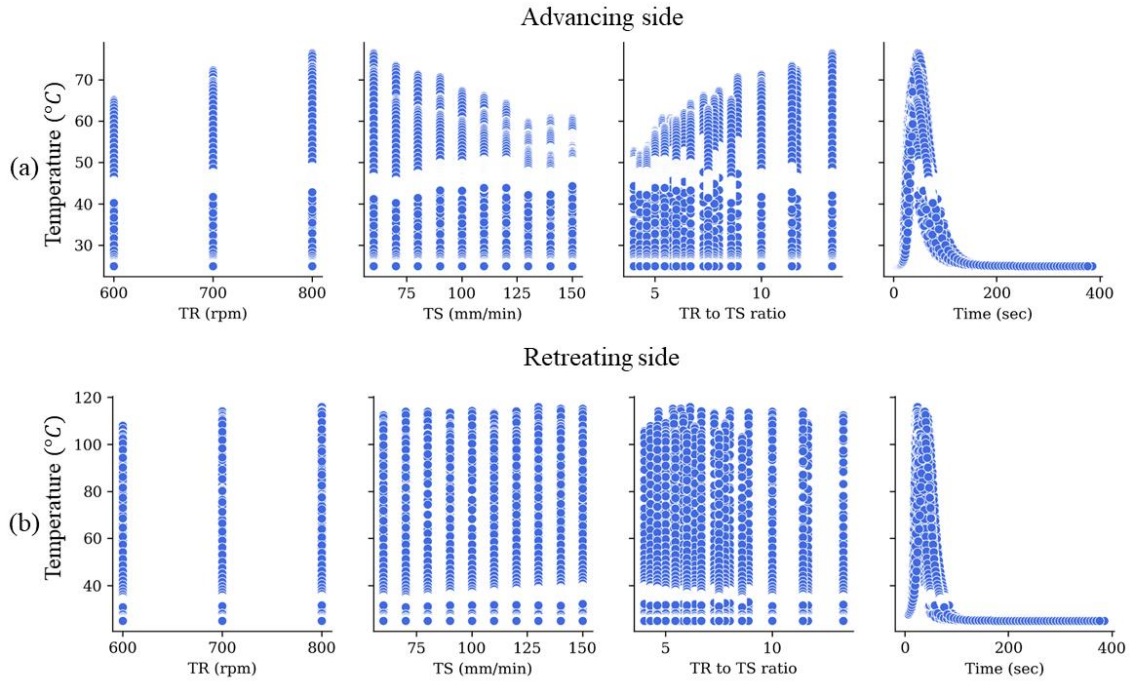

Fig. 5.58 Correlation and dependence of different process parameters on the predicted temperature on the (a) AS and (b) RS

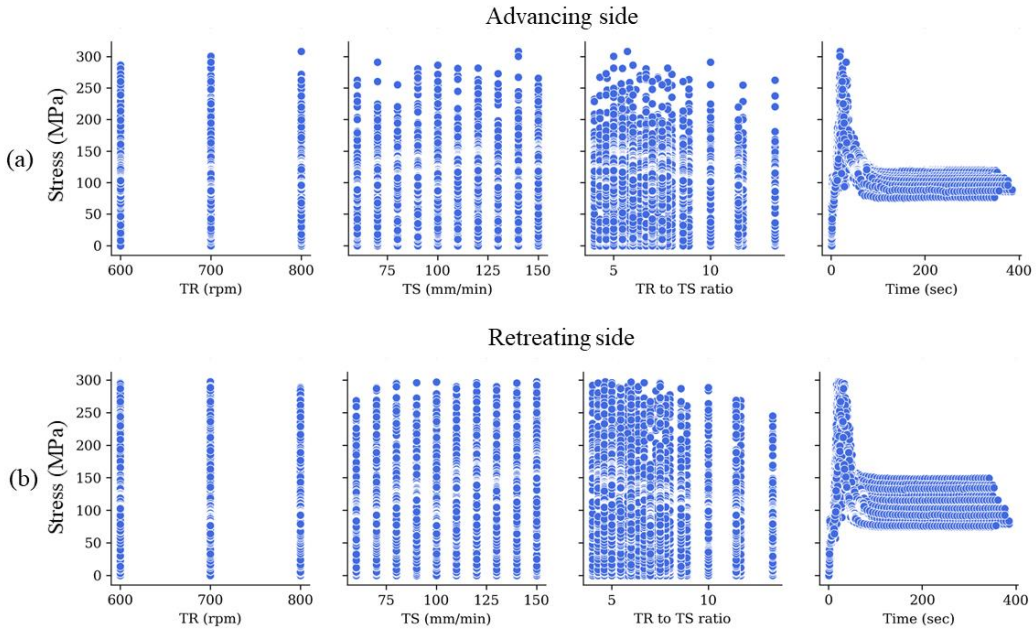

Fig. 5.59 Correlation and dependence of different process parameters on the predicted residual stress on the (a) AS and (b) RS

Figure 5.60 compares the temperature evolution during dissimilar FSW at 600 rpm and 60 mm/min with the ML model predictions about 15 mm away from the weld centerline. The predictions are mostly within the acceptable range, but the maximum temperature predicted by ETR is discreetly less than the maximum temperature. However, the other models predict temperature evolution with reasonable accuracy. The heating, cooling, and constant trends of the temperature evolution during different phases of FSW are predicted in close acceptance to the temperature changes. The average error in prediction for the temperature evolution with the ETR, XGB, and RFR are 7.75%, 4.31%, and 6.50%, respectively.

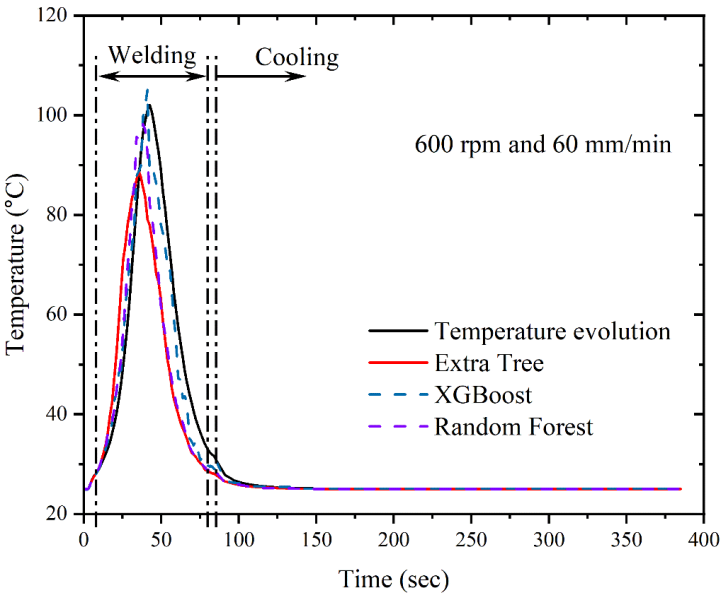

Fig. 5.60 Prediction of the temperature progress for 600 rpm and 60 mm/min on the RS for dissimilar AA6061-AZ31B

Figure 5.61 compares the ML predicted residual stress to the stress evolution at 600 rpm and 60 mm/min with the ML model predictions about 15 mm away from the weld centerline. ML algorithms can accurately predict the stress evolution for the initiation of welding, cooling stages, and the other essential stages of welding until the workpiece cools to room temperature. Alternatively, there is a discrepancy in the prediction of the highest stress value as the tool passes and presses the

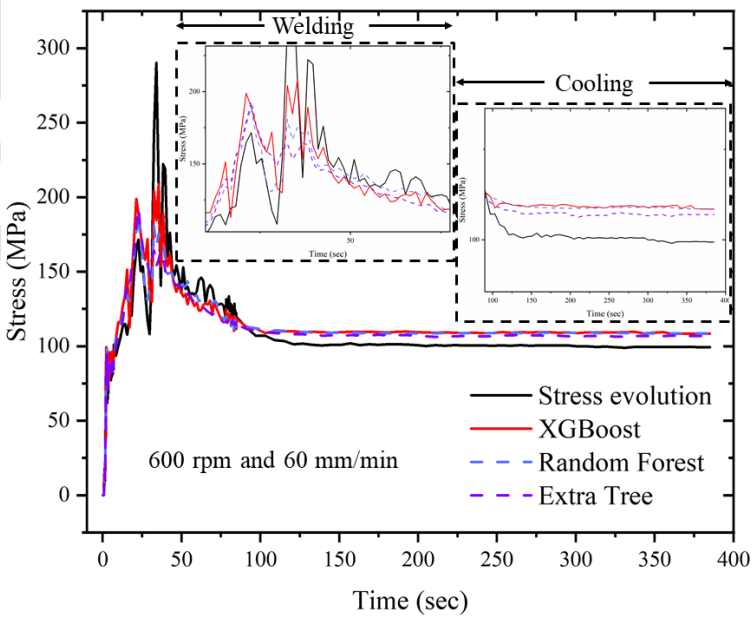

Fig. 5.61 Prediction of the stress at 600 rpm and 60 mm/min on the AS for welding of dissimilar AA6061-AZ31B

material around it. However, at the end of the cooling stage, it can be claimed that the ML model predictions are well within the acceptable range. The prediction accuracy of the different models for temperature evolution is moderately better than the residual stress prediction. Simultaneously, the R^2 score for the temperature prediction is also marginally better than the stress prediction (Fig. 5.57). The reason for such an observation is the smooth profile for temperature progress where only one peak is observed. However, there are multiple abrupt peaks and valleys for stress evolution when the tool passes the point of investigation. This sudden change in stress affects the prediction accuracy marginally. The average difference in the XGB, RFR, and ETR prediction at the end of welding for the residual stress is 10.24%, 8.82%, and 9.30% (Fig. 5.61). The difference in the stress prediction can be further improved by considering other parameters such as tool tilt angle and tool geometry. Accurately predicting the maximum stress encountered during welding is very important as it can be used to predict weld distortion. This can be incorporated into the model to classify the parameters responsible for distortion defects during FSW.

5.10 Summary

The current investigation focuses on the development of a novel numerical model following the CEL approach for the similar AA6061, AZ31B, and dissimilar AA6061-AZ31B welding and their validation through experiments. The selection of inappropriate process parameters and tool design can lead to the generation of defective joints. The defects can be present on the surface or within the workpiece. The shape, size, and location of these defects are predicted using the developed FE model accustomed to the material flow with the application of the JC plasticity and failure models. The mass scaling technique is utilized to reduce the computational time associated with the CEL approach. A KE-to-IE ratio is determined to keep the possible adverse effects of the mass scaling factor in check. Any change in the KE relates to the sudden encounter of the defect by the tool (case of AZ31B). Alternatively, if the defect is present continuously or the defect is absent completely (AA6061 case) there is no sudden spike in the KE. On increasing the mass scaling factor from 1 to 10^7, the total computational time is reduced from 168 hours to 6 mins for modelling the initial 1s of FSW. Hence, a mass scaling factor of 10^7 is recommended for both the AA6061 and AZ31B. The model predicts the isotherms of different zones of FSW within 1 mm dimensional accuracy as compared to experimental measurement. The variation in flash formation is accustomed to the plunge depths. There

is an increase of about 4 mm in flash height on the RS, as the plunge depth is increased from 0.45 mm to 0.7 mm. The variation in the process parameters affects the intensity of material flow, however, the material still flows towards the RS. Alternatively, the sub-surface workpiece observed higher material flow towards the AS, having the highest velocity of 30 mm/s for AA6061 FSW at 1200 rpm due to the same sense of tool rotation and translation.

The maximum deviations in flash height, exit hole diameter, surface tunnel width, and subsurface tunnel height prediction were 1, 0.4, 1.2, and 1 mm, respectively for dissimilar AA6061-AZ31B. The 360 rpm and 300 mm/min produced severely defective joints due to extremely low heat generation. The maximum temperature just below the tool shoulder could reach about 65% of the melting point temperature of AA6061. A continuous surface tunnel is predicted with an average width of 0.8 mm for dissimilar AA6061-AZ31B FSW due to improper heat dissipation. The material (plastic strain) is observed to compress along the weld direction and depth direction, whereas it is stretched along the traverse direction. The highest strain rate on the RS is about $8\,s^{-1}$ which is significantly more than the strain rate of $4\,s^{-1}$ on the AS indicating less material flow and tunnel defect formation on the AS. The material mixing in dissimilar AA6061-AZ31B FSW is observed from the AS to the RS and the weld interface is also observed on the RS. The FSW process also observes tool wear due to continuous contact between the tool and the workpiece. The developed numerical model could predict the difference in weld quality and defect formation when the condition of the tool was modified due to tool wear. The tool shape also varies due to the material adhering to the tool from the workpiece. A surface tunnel with a height of more than 50% of the plate thickness is predicted when AZ31B is placed on the AS and AAA6061 on the RS. The surface tunnel defect was eliminated when the plate positions were interchanged.

The ML algorithms are combined with the CEL based model to accurately predict the thermal and residual stress evolution for different stages of dissimilar AA6061-AZ31B FSW. The ML algorithms predict that the temperature increases with the tool rotational speed and decreases with the traverse speed. The residual stress decreases with the increase in tool rotational speed to traverse speed ratio. The residual stress on the RS varies over a wider range than the AS for the defined range of tool rotation and traverse speeds. For a known range of process parameters, the Extra Tree Regressor and XGBoost exhibit the least deviation from the actual result for predicting temperature and residual stress, respectively. However, for an independent set of process parameters, the accuracy was best

for XGBoost to predict temperature change with an average prediction error of 4.31 % and the Random Forest Regressor to predict the residual stress with an average prediction error of 8.82 %. The present investigation recommends the XGBoost for temperature prediction and the Random Forest Regressor for residual stress prediction.

Chapter 6

Conclusions and Future scope of work

6.1 Introduction

The FSW process is a widely utilised and investigated solid-state welding process. The AA6061 and AZ31B alloys are preferred to be welded by the FSW process. They have significant applications in the aerospace, automobile, and maritime industries due to their low weight-to-strength ratio. However, the comprehensive investigation of the FSW process is full of challenges as the sub-surface material flow, weld quality, and defect formation cannot be easily investigated by experimental means alone. To remedy this the current work is focussed on developing a CEL based 3D model for the investigation and estimation of the FSW process. The mass scaling feature is given special importance to reduce the total computational time for the process. Moreover, the developed model is also linked with various ML algorithms to further improve the prediction cost. The materials and the prediction strategies investigated in the current work are selected in such a manner that their scope of application is not only limited to FSW but can also be applied to other domains of manufacturing.

6.2 General background

The present investigation deals with the FSW of AA6061 and AZ31B at similar and dissimilar combinations of materials. The main thrust of the current work lies in developing a three-dimensional numerical model based on the CEL approach capable of predicting the various surface and sub-surface defects in FSW of similar and dissimilar materials. The FSW is performed on the 4 mm thick AA6061 and AZ31B plates. The various volumetric

defects are experimentally investigated and numerically predicted for both the similar and dissimilar AA6061 and AZ31B FSW. The application of the CEL technique is associated with high computational time. The mass scaling factor is optimized to reduce the computational time without the loss of computational accuracy of the results. A comprehensive investigation is performed into applying the mass scaling for AA6061 and AZ31B FSW. The developed numerical model considers the effect of the tool rotation speed, tool traverse speed, plunge depth, pin height, tool wear, plate position, tool shoulder, and pin dimensions to estimate their individual or combined effect on the defect formation. The residual stress investigation and tool wear studies are also performed for dissimilar FSW. The inhomogeneous material properties during dissimilar FSW lead to a difference in residual stress and temperature evolution on AS and RS. On completion of welding, the undesirable residual stresses play spoilsport to destabilize the welded structure. The developed model is used to predict the residual stresses arising in the body and validated with experimental results. The ML algorithms are jointly used with the numerical model to predict the residual stress and temperature evolution in the body. The advantage of ML prediction over the CEL model is the significant reduction in prediction time. The major findings and conclusion of the current investigation are summarised subsequently.

6.3 Conclusions

The FSW of AA6061 and AZ31B are investigated in similar and dissimilar combinations. The temperature evolution, mechanical responses, material flow, and defect formation, are some of the key attributes investigated during the course of the current work. Numerical investigations and experimental validation are performed with an emphasis on a 3D thermo-mechanical model with volumetric defect prediction capabilities and a physics-informed ML model for thermo-mechanical response estimations. The summary and conclusions of the current investigation are:

❖ The literature review presented numerical models for predicting temperature and mechanical responses in FSW. While the Johnson-Cook material model is commonly used for flow stress in FSW. This study introduces a numerical model that integrates both the Johnson-Cook material and failure models to accurately predict thermo-mechanical responses and volumetric defects. Unlike some literature, our model extends both surface and volumetric defect prediction to both similar and dissimilar FSW.

❖ The CEL approach predicts discontinuities in large deformation processes like FSW using Eulerian volume fraction, applicable to both similar and dissimilar welding.

However, the CEL process is computationally expensive until the mass scaling factor is properly optimized. CEL uses an explicit scheme with a stable time increment as a function of the smallest element and material density. The mass scaling factor of 10^7 is found to provide an accurate result for AA6061, and AZ31B FSW. An increase in mass scaling factor from 1 to 10^7 reduces the computational time requirement by 1680 times for AZ31B; whereas an increase in mass scaling factor from 10^3 to 10^7 reduces the computational time by 100 times for AA6061.

❖ The KE to IE energy ratio is the detrimental factor to keep the adverse effect of artificial mass scaling within limits. The KE to IE ratio is maintained below 10% to ensure efficient mass scaling of the system. However, the variations in the KE, IE, or KE to IE ratio cannot be considered as an explicit indicator to predict defect formation. Sudden spikes occur only during the transition from a sound weld to a defective weld, with no spikes observed in fully sound or defective welds.

❖ The model accurately predicts temperature isotherms and metallurgical zones in FSW. The temperature evolution and the material movement is accounted to predict the metallurgical zones. The model exhibits strong agreement with experimental results within 1 mm accuracy.

❖ The flash formation is continuous towards the RS and sporadic towards the AS due to the material rotation and deposition by the tool towards the RS. A high plunge depth of 0.7 mm leads to excessive material expulsion at various locations, where the flash height exceeds 10 mm. A reduction in plunge depth from 0.7 mm to 0.45 mm reduced the flash height by about 4 mm towards RS, and minimal flash formation was observed towards AS.

❖ The AS observes the highest velocity of 30 mm/s for AA6061 FSW at 1200 rpm. Any discrepancy in the material flow and deposition between the AS and RS leads to the formation of various sub-surface defects. The EVF technique allows tracking the domains that remain partially or completely void of material after welding. Determining the void domains allows to predict the formation of sub-surface defects such as tunnel defect, exit hole, and failed joints.

❖ The maximum deviations in exit hole diameter, surface tunnel width, flash height, and subsurface tunnel height prediction are about 0.4, 1.2, 1.5, and 1 mm for dissimilar AA6061-AZ31B. The surface tunnel defect formed at 1200 rpm and 30 mm/min whereas the subsurface tunnel defect formed at 900 rpm and 90 mm/min. The rotation speed to traverse speed ratio of 40 leads to overheating the workpiece, easy material plasticization,

and excessive material removal and expulsion. When the rpm to traverse speed ratio is only 10 and sufficient material plasticization does not occur, sub-surface tunnel defect formation is observed. Volumetric tunnel defect is observed with AA6061 FSW at 1200 rpm and 90 mm/min. FSW of AA6061 with 360 rpm and 300 mm/min leads to completely failed joints due to extremely low heat generation and material plasticization.

❖ The workpiece material is compressed along the weld and depth directions, whereas it is stretched along the traverse direction with the rotation and translation of the tool. The RS observes almost double the strain rate than the AS, indicating less material flow and thus the tunnel defect most favorably occurs towards the AS.

❖ The tool wear in FSW is observed due to dimensional changes and material adhesion to the tool surface. The maximum tool dimension variation is observed for the minor pin diameter between 18% - 28% and the pin height between 10% - 12%. The major pin diameter observes a minimal dimensional change between 0.5% - 2.5%. The analysis of adhered workpiece material on the tool surface indicates the presence of more material from AS than RS. The material adhered to the tool surface is analysed using the FESEM-EDS area mapping to detect about 59% of Al from the AS and about 41% of Mg from the RS. The presence of Fe is marginal and proves that the tool material is not eroding during FSW.

❖ The EVF tracking is used to track the presence of the AA6061 or AZ31B within an element to estimate the material mixing and distribution. Almost equal presence of AA6061 and AZ31B is estimated near the weld centerline. As one moves towards the AS or RS, the presence of AA6061 or AZ31B increases, respectively. The FESEM-EDS analysis of the samples also confirms the predicted results.

❖ The numerical model predicted a tunnel defect towards the AS whereas the material interface is predicted towards the RS for FSW of AA6061-AZ31B. The experimental investigation also highlights a tunnel defect of about $3\ mm \times 0.83\ mm$ stretching from the weld center to the AS, whereas the weld interface is located about $1\ mm$ from the weld center towards the RS.

❖ It has been realized that the relative position of the workpiece with respect to weld direction severely affects the weld quality in dissimilar FSW. The placement of AA6061 produced a sound weld without any surface defect, whereas the placement of AZ31B on the AS produced a surface defect that is present for more than half of the workpiece thickness.

❖ A portable μ-FSW setup is developed to weld sheets of thickness less than 1 mm. The tool spindle is coupled with a welding bed which is designed and fabricated in-house after performing modal analysis. The welding bed is attached to a CNC controller to provide precise motion to the workpiece. Multiple spot welds are performed using the developed setup and analysed using the lap shear test. The tool rotation speeds of 1400 rpm, 1800 rpm, and 2200 rpm are used for experimental investigation to observe that the welding with 2200 rpm produced the best results.

❖ The ML algorithms coupled with the CEL model improve prediction time for temperature and stress evolution in dissimilar AA6061-AZ31B FSW. XGBoost and Random Forest Regressor yield the best results, with average prediction errors of 4.31% for temperature and 8.82% for residual stress. The accuracy for stress evolution predictions is marginally less due to variations in maximum stress prediction, whereas the lower stress values are in close acceptance. Therefore, using the current model for weld distortion is unadvisable, and further investigations are required to perform weld distortion predictions.

6.4 Scope for future investigations

In the current investigation, experimental and numerical modelling is performed for similar and dissimilar FSW. Several insights are made into the efficient and accurate modelling of the FSW process to estimate the weld quality and defect formation. The present findings further open up various new and interesting areas of investigation. Some of the potential expansions of the current work can be summarised as follows:

❖ In the present investigation, different process parameters are considered to estimate their effect on the defect formation, such as the tool rotation speed, tool traverse speed, plunge depth, pin design, tool quality, and plate position. However, various other parameters can be considered to make the model more wholesome such as the tool tilt angle, use of complicated tool geometries, plunge force, and plunge speed.

❖ The different metallurgical zones of the FSW observe different microstructural changes. The predicted thermo-mechanical responses can be used as a precursor to predict the microstructural changes in similar and dissimilar FSW. The modelling of the microstructural changes appearing in the FSW process will help to improve the final weld quality estimation and joint properties.

❖ Various metallurgical defects, such as the formation of the IMCs and the associated micro-cracks, are currently ignored. The inclusion of microstructural modelling will help to accurately predict these defects.

❖ The developed numerical model can be complemented with solid-state phase transformation modelling. This will allow for predicting the metallurgical changes, residual stress in the body, joint properties, and mechanical and microstructural defect formation. The coupling of the numerical model with the solid-state phase transformation effect drives to develop a digital twin for the FSW process.

❖ Incorporating the real-time tool responses, such as the tool force and tool condition, can help develop the current numerical model as a complete FSW simulation package for industrial purposes. The numerical model can be used to determine the maximum shear stress observed by the tool. The material properties along with the estimated shear stress can be used to determine the tool durability factor. The tool durability factor is a measure of the FSW tool life longevity. The coupling of the ML algorithms with the numerical model will help to predict the temperature on tool surface and stresses for any given set of process parameters. The use of the tool life information with the developed numerical model in the current work will help to develop a complete simulator for the FSW process.

❖ The current investigation focuses on the butt welding of different low melting point materials; however, other materials such as steel, Inconel, and Titanium alloys are increasingly used with the FSW process. The current model can be furthered to incorporate the different materials in different weld configurations.

❖ The residual stresses and the distortion significantly affect the service life and structural integrity of a product. An attempt is made in the current work to estimate the residual stress using a physics-informed ML model. However, the distortion arising in the body is ignored and can be further explored. Moreover, the physics informed ML model can be used for the prediction of thermo-mechanical responses and classification of process parameters based on weld quality.

References

Abbassi, F. *et al.* (2016) 'Experimental and numerical analyses of magnesium alloy hot workability', *Journal of Magnesium and Alloys*, 4(4), pp. 295–301. doi: 10.1016/j.jma.2016.10.004.

Abdollahzadeh, A. *et al.* (2018) 'The effect of changing chemical composition in dissimilar Mg/Al friction stir welded butt joints using zinc interlayer', *Journal of Manufacturing Processes*, 34(May), pp. 18–30. doi: 10.1016/j.jmapro.2018.05.029.

Abdullah, A. B. *et al.* (2013) 'Numerical investigation of geometrical defect in cold forging of an AUV blade pin head', *Journal of Manufacturing Processes*, 15(1), pp. 141–150. doi: 10.1016/j.jmapro.2012.11.003.

Abhilash, J., Apeksha and Acharjee, B. (2018) 'Simulation of friction stir welding using thermo-mechanical coupled finite element method', in *IOP Conference Series: Materials Science and Engineering*, pp. 0–8. doi: 10.1088/1757-899X/455/1/012113.

Ahmad, B., Galloway, A. and Toumpis, A. (2018) 'Advanced numerical modelling of friction stir welded low alloy steel', *Journal of Manufacturing Processes*, 34, pp. 625–636. doi: 10.1016/j.jmapro.2018.07.003.

Ahmad, B., Galloway, A. and Toumpis, A. (2019) 'Numerical optimisation of laser assisted friction stir welding of structural steel', *Science and Technology of Welding and Joining*, 24(6), pp. 548–558. doi: 10.1080/13621718.2019.1570682.

Ahmed, M. M. Z. *et al.* (2021) 'Dissimilar Friction Stir Welding of AA2024 and AISI 1018: Microstructure and Mechanical Properties', *Metals*, 11(2), p. 330. doi: 10.1016/b978-0-12-804782-8.00004-5.

Ahmed, S. and Saha, P. (2018) 'Development and testing of fixtures for friction stir welding of thin aluminium sheets', *Journal of Materials Processing Technology*, 252(May 2017), pp. 242–248. doi: 10.1016/j.jmatprotec.2017.09.034.

Ahmed, S. and Saha, P. (2020) 'Selection of optimal process parameters and assessment of its effect in micro-friction stir welding of AA6061-T6 sheets', *International Journal of Advanced Manufacturing Technology*, 106(7–8), pp. 3045–3061. doi: 10.1007/s00170-019-04840-6.

Ahmed, S., Verma, M. and Saha, P. (2021) 'Process responses during μFSW of AA6061-T6 under the influence of triple-spiral micro-grooves on shoulder end-surface', *Journal of Materials Processing Technology*, 290(May 2020), p. 116984. doi: 10.1016/j.jmatprotec.2020.116984.

Ajri, A. and Shin, Y. C. (2017) 'Investigation on the Effects of Process Parameters on Defect Formation in Friction Stir Welded Samples Via Predictive Numerical Modeling and Experiments', *Journal of Manufacturing Science and Engineering, Transactions of the ASME*, 139(11), pp. 1–10. doi: 10.1115/1.4037240.

Al-Badour, F. *et al.* (2013) 'Coupled Eulerian Lagrangian finite element modeling of friction stir welding processes', *Journal of Materials Processing Technology*, 213(8), pp. 1433–1439. doi: 10.1016/j.jmatprotec.2013.02.014.

Al-Badour, F. *et al.* (2014) 'Thermo-mechanical finite element model of friction stir welding of dissimilar alloys', *The International Journal of Advanced Manufacturing Technology*, 72(5–8), pp. 607–617.

Al-moussawi, M. *et al.* (2017) 'Modelling of friction stir welding of DH36 steel', *International Journal of Advanced Manufacturing Technology*, 92(1–4), pp. 341–360. doi: 10.1007/s00170-017-0147-y.

Al-Moussawi, M. and Smith, A. J. (2018) 'Defects in Friction Stir Welding of Steel', *Metallography, Microstructure, and Analysis*, 7(2), pp. 194–202. doi: 10.1007/s13632-018-0438-1.

Alfaro, I. *et al.* (2009) 'Numerical simulation of friction stir welding by natural element methods', *International Journal of Material Forming*, 2(4), pp. 225–234. doi: 10.1007/s12289-009-0406-z.

Aliha, M. R. M. *et al.* (2016) 'Mechanical and metallurgical properties of dissimilar AA6061-T6 and AA7277-T6 joint made by FSW technique', *International Journal of Advanced Manufacturing Technology*, 86(9–12), pp. 2551–2565. doi: 10.1007/s00170-016-8341-x.

Álvarez, A. I. *et al.* (2014) 'Evaluation of an induction-assisted friction stir welding technique for super duplex stainless steels', *Surface and Interface Analysis*, 46(10–11), pp. 892–896. doi: 10.1002/sia.5442.

Ambrosio, D., Wagner, V., *et al.* (2023) 'Machine learning tools for flow-related defects detection in friction stir welding', *Journal of Manufacturing Science and Engineering*, pp. 1–23. doi: 10.1115/1.4062457.

Ambrosio, D., Tongne, A., *et al.* (2023) 'Towards material flow prediction in friction stir welding accounting for mechanisms governing chip formation in orthogonal cutting', *Journal of Manufacturing Processes*, 85(November 2022), pp. 450–465. doi: 10.1016/j.jmapro.2022.11.047.

Anandan, B. and Manikandan, M. (2022) 'Machine learning approach for predicting the peak temperature of dissimilar AA7050-AA2014A friction stir welding butt joint using various regression models',

Materials Letters, 325, p. 132879. doi: 10.1016/j.matlet.2022.132879.

Ansari, M. A. *et al.* (2019) 'An efficient coupled Eulerian-Lagrangian finite element model for friction stir processing', *The International Journal of Advanced Manufacturing Technology*, 101(5–8), pp. 1495–1508. doi: 10.1007/s00170-018-3000-z.

Ansari, M. A. and Behnagh, R. A. (2019) 'Numerical study of friction stir welding plunging phase using smoothed particle hydrodynamics', Modelling and Simulation in Materials Science and Engineering, 27(5). doi: 10.1088/1361-651X/ab1ca7.

Ansys (2005) 'ANSYS Workbench Documentation', *ANSYS Workbench Release 10.0*. Available at: http://kashanu.ac.ir/Files/Content/ANSYS Workbench.pdf.

Arbegast, W. J. (2008) 'A flow-partitioned deformation zone model for defect formation during friction stir welding', *Scripta Materialia*, 58(5), pp. 372–376. doi: 10.1016/j.scriptamat.2007.10.031.

Arora, A. *et al.* (2009) 'Strains and strain rates during friction stir welding', *Scripta Materialia*, 61(9), pp. 863–866. doi: 10.1016/j.scriptamat.2009.07.015.

Arora, K. S. *et al.* (2010) 'Effect of process parameters on friction stir welding of aluminum alloy 2219-T87', *International Journal of Advanced Manufacturing Technology*, 50(9–12), pp. 941–952. doi: 10.1007/s00170-010-2560-3.

Asadi, P., Mahdavinejad, R. A. and Tutunchilar, S. (2011) 'Simulation and experimental investigation of FSP of AZ91 magnesium alloy', *Materials Science and Engineering A*, 528(21), pp. 6469–6477. doi: 10.1016/j.msea.2011.05.035.

Askour, O., Mesmoudi, S. and Braikat, B. (2020) 'On the use of Radial Point Interpolation Method (RPIM) in a high order continuation for the resolution of the geometrically nonlinear elasticity problems', *Engineering Analysis with Boundary Elements*, 110(September 2019), pp. 69–79. doi: 10.1016/j.enganabound.2019.09.015.

Assidi, M. *et al.* (2010) 'Friction model for friction stir welding process simulation: Calibrations from welding experiments', *International Journal of Machine Tools and Manufacture*, 50(2), pp. 143–155. doi: 10.1016/j.ijmachtools.2009.11.008.

Assidi, M. and Fourment, L. (2009) 'Accurate 3D Friction Stir Welding simulation tool based on friction model calibration', *International Journal of Material Forming*, 2(SUPPL. 1), pp. 327–330. doi: 10.1007/s12289-009-0541-6.

Aval, H. J., Serajzadeh, S. and Kokabi, A. H. (2012) 'Experimental and theoretical evaluations of thermal histories and residual stresses in dissimilar friction stir welding of AA5086-AA6061', *International Journal of Advanced Manufacturing Technology*, 61(1–4), pp. 149–160. doi: 10.1007/s00170-011-3713-8.

Aydin, I. *et al.* (2000) 'Physical and numerical modelling of ram extrusion of paste materials: Conical die entry case', *Computational Materials Science*, 18(2), pp. 141–155. doi: 10.1016/S0927-0256(00)00098-7.

Aziz, S. B. *et al.* (2016) 'Impact of Friction Stir Welding (FSW) process parameters on thermal modeling and heat generation of aluminum alloy joints', *Acta Metallurgica Sinica (English Letters)*, 29(9), pp. 869–883. doi: 10.1007/s40195-016-0466-2.

Aziz, S. B. *et al.* (2018) 'A fully coupled thermomechanical model of friction stir welding (FSW) and numerical studies on process parameters of lightweight aluminum alloy joints', *Acta Metallurgica Sinica (English letters)*, 31(1), pp. 1–18.

Bachmann, M. *et al.* (2017) 'Numerical simulation of thermally induced residual stresses in friction stir welding of aluminum alloy 2024-T3 at different welding speeds', *International Journal of Advanced Manufacturing Technology*, 91(1–4), pp. 1443–1452. doi: 10.1007/s00170-016-9793-8.

Bakroon, M. *et al.* (2019) 'Multi-material arbitrary Lagrangian-Eulerian and coupled Eulerian-Lagrangian methods for large deformation geotechnical problems', in *Numerical Methods in Geotechnical Engineering IX*, pp. 673–681. doi: 10.1201/9781351003629-84.

Balakrishnan, M. *et al.* (2020) 'Friction stir processing of Al3Ni intermetallic particulate reinforced cast aluminum matrix composites: Microstructure and tensile properties', *Journal of Materials Research and Technology*, 9(3), pp. 4356–4367. doi: 10.1016/j.jmrt.2020.02.060.

Balasundar, I. and Raghu, T. (2010) 'Investigations on the extrusion defect - Axial hole or funnel', *Materials and Design*, 31(6), pp. 2994–3001. doi: 10.1016/j.matdes.2010.01.027.

Bang, Han Sur *et al.* (2013) 'Joint properties of dissimilar Al6061-T6 aluminum alloy/Ti-6%Al-4%V titanium alloy by gas tungsten arc welding assisted hybrid friction stir welding', *Materials and Design*, 51, pp. 544–551. doi: 10.1016/j.matdes.2013.04.057.

Bang, Hee Seon *et al.* (2020) 'A prediction of Fe-Al IMC layer thickness in TIG-assisted hybrid friction stir welded Al/steel dissimilar joints by numerical analysis', *International Journal of Advanced Manufacturing Technology*, 106(1–2), pp. 765–778. doi: 10.1007/s00170-019-04560-x.

Bang, Hee Seon *et al.* (2021) 'Study on the Weldability and Mechanical Characteristics of Dissimilar Materials (Al5052-DP590) by TIG Assisted Hybrid Friction Stir Welding', *Metals and Materials*

International, 27(5), pp. 1193–1204. doi: 10.1007/s12540-019-00461-6.

Barsoum, Z. and Barsoum, I. (2009) 'Residual stress effects on fatigue life of welded structures using LEFM', *Engineering Failure Analysis*, 16(1), pp. 449–467. doi: 10.1016/j.engfailanal.2008.06.017.

Bastier, A. *et al.* (2006) 'Steady state thermomechanical modelling of friction stir welding', *Science and Technology of Welding and Joining*, 11(3), pp. 278–288. doi: 10.1179/174329306X102093.

Behmand, S. A. *et al.* (2015) 'Filling exit holes of friction stir welding lap joints using consumable pin tools', *Science and Technology of Welding and Joining*, 20(4), pp. 330–336. doi: 10.1179/1362171815Y.0000000018.

Benson, D. J. (1992) 'Computational methods in Lagrangian and Eulerian hydrocodes', *Computer Methods in Applied Mechanics and Engineering*, 99(2–3), pp. 235–394. doi: 10.1016/0045-7825(92)90042-I.

Benson, D. J. (1997) 'A mixture theory for contact in multi-material Eulerian formulations', *Computer Methods in Applied Mechanics and Engineering*, 140(1–2), pp. 59–86. doi: 10.1016/S0045-7825(96)01050-X.

Benson, D. J. and Okazawa, S. (2004) 'Contact in a multi-material Eulerian finite element formulation', *Computer Methods in Applied Mechanics and Engineering*, 193(39-41 SPEC. ISS.), pp. 4277–4298. doi: 10.1016/j.cma.2003.12.061.

Beygi, R. *et al.* (2021) 'Design of friction stir welding for butt joining of aluminum to steel of dissimilar thickness: heat treatment and fracture behavior', *International Journal of Advanced Manufacturing Technology*, 112(7–8), pp. 1951–1964. doi: 10.1007/s00170-020-06406-3.

Bhat, N. N. *et al.* (2015) 'Friction stir weld classification by applying wavelet analysis and support vector machine on weld surface images', *Journal of Manufacturing Processes*, 20, pp. 274–281. doi: 10.1016/j.jmapro.2015.07.002.

Bonnet, C., Pottier, T. and Landon, Y. (2021) 'Development of a multi-scale and coupled cutting model for the drilling of Ti-6Al-4V', *CIRP Journal of Manufacturing Science and Technology*, 35, pp. 526–540. doi: 10.1016/j.cirpj.2021.08.007.

Brown, K. H., Burns, S. P. and Christon, M. a (2002) 'Coupled Eulerian-Lagrangian Methods for Earth Penetrating Weapon Applications', *SAND2002-1014, Sandia National Laboratories, Albuquerque, NM*, (May). doi: 10.2172/808588.

Buchely, M. F. *et al.* (2019) 'The Use of Genetic Algorithms to Calibrate Johnson-Cook Strength and Failure Parameters of AISI/SAE 1018 Steel', *Journal of Engineering Materials and Technology, Transactions of the ASME*, 141(2), pp. 1–12. doi: 10.1115/1.4042382.

Buchibabu, V., Reddy, G. M. and De, A. (2017) 'Probing torque, traverse force and tool durability in friction stir welding of aluminum alloys', *Journal of Materials Processing Technology*, 241, pp. 86–92. doi: 10.1016/j.jmatprotec.2016.11.008.

Buffa, G. *et al.* (2020) 'Surface and mechanical characterization of stationary shoulder friction stir welded lap joints: experimental and numerical approach', *International Journal of Material Forming*, 13(5), pp. 725–736. doi: 10.1007/s12289-020-01574-9.

Buffa, G., Fratini, L. and Shivpuri, R. (2008) 'Finite element studies on friction stir welding processes of tailored blanks', *Computers and Structures*, 86(1–2), pp. 181–189. doi: 10.1016/j.compstruc.2007.04.007.

Buzyurkin, A. E., Gladky, I. L. and Kraus, E. I. (2015) 'Determination and verification of Johnson-Cook model parameters at high-speed deformation of titanium alloys', *Aerospace Science and Technology*, 45, pp. 121–127. doi: 10.1016/j.ast.2015.05.001.

Çam, G., Javaheri, V. and Heidarzadeh, A. (2023) 'Advances in FSW and FSSW of dissimilar Al-alloy plates', *Journal of Adhesion Science and Technology*, 37(2), pp. 162–194. doi: 10.1080/01694243.2022.2028073.

Camilleri, D., Micallef, D. and Mollicone, P. (2015) 'Thermal stresses and distortion developed in mild steel DH36 friction stir-welded plates: An experimental and numerical assessment', *Journal of Thermal Stresses*, 38(5), pp. 485–508. doi: 10.1080/01495739.2015.1015856.

Cao, F. *et al.* (2022) 'Inhomogeneous microstructure and properties along the thickness of stir zone in friction stir welded SAF 2507 super duplex stainless steel joint', *Journal of Manufacturing Processes*, 73(November 2021), pp. 611–623. doi: 10.1016/j.jmapro.2021.11.043.

Cao, J. Y. *et al.* (2017) 'Numerical modeling and experimental investigation of material flow in friction spot welding of Al 6061-T6', *International Journal of Advanced Manufacturing Technology*, 89(5–8), pp. 2129–2139. doi: 10.1007/s00170-016-9247-3.

Cao, Y. *et al.* (2020) 'Determination of Johnson–Cook parameters and evaluation of Charpy impact test performance for X80 pipeline steel', *International Journal of Mechanical Sciences*, 179(February), p. 105627. doi: 10.1016/j.ijmecsci.2020.105627.

Carlone, P. and Palazzo, G. S. (2015) 'Characterization of TIG and FSW weldings in cast ZE41A

magnesium alloy', *Journal of Materials Processing Technology*, 215, pp. 87–94. doi: 10.1016/j.jmatprotec.2014.07.026.

Chadha, K. (2018) 'An Approach to Develop Hansel–Spittel Constitutive Equation during Ingot Breakdown Operation of Low Alloy Steels', in *Frontiers in Materials Processing, Applications, Research and Technology*. doi: 10.1007/978-981-10-4819-7.

Chalurkar, C. and Shukla, D. K. (2022) 'Temperature Analysis of Friction Stir Welding (AA6061-T6) with Coupled Eulerian-Lagrangian Approach', in *International Conference on Materials Science and Engineering (ICMSE 2022)*. doi: 10.1088/1757-899X/1248/1/012035.

Chang, W. S. *et al.* (2011) 'Microstructure and Mechanical Properties of Hybrid Laser-Friction Stir Welding between AA6061-T6 Al Alloy and AZ31 Mg Alloy', *Journal of Materials Science and Technology*, 27(3), pp. 199–204. doi: 10.1016/S1005-0302(11)60049-2.

Chao, Y. J., Qi, X. and Tang, W. (2003) 'Heat transfer in friction stir welding - Experimental and numerical studies', *Journal of Manufacturing Science and Engineering*, 125(1), pp. 138–145. doi: 10.1115/1.1537741.

Chauhan, P. *et al.* (2018) 'Modeling of defects in friction stir welding using coupled Eulerian and Lagrangian method', *Journal of Manufacturing Processes*, 34(November 2017), pp. 158–166. doi: 10.1016/j.jmapro.2018.05.022.

Chen, D. C. *et al.* (2007) 'Investigation into cold extrusion of aluminum billets using three-dimensional finite element method', *Journal of Materials Processing Technology*, 192–193, pp. 188–193. doi: 10.1016/j.jmatprotec.2007.04.067.

Chen, G. *et al.* (2018) 'Effects of pin thread on the in-process material flow behavior during friction stir welding: A computational fluid dynamics study', *International Journal of Machine Tools and Manufacture*, 124(September 2017), pp. 12–21. doi: 10.1016/j.ijmachtools.2017.09.002.

Chen, G. *et al.* (2019) 'Three-dimensional thermal-mechanical analysis of retractable pin tool friction stir welding process', *Journal of Manufacturing Processes*, 41(March), pp. 1–9. doi: 10.1016/j.jmapro.2019.03.022.

Chen, S. *et al.* (2013) 'Microstructural characteristics of a stainless steel/copper dissimilar joint made by laser welding', *Metallurgical and Materials Transactions A: Physical Metallurgy and Materials Science*, 44(8), pp. 3690–3696. doi: 10.1007/s11661-013-1693-z.

Chen, S. *et al.* (2019) 'Effect of a Zinc Interlayer on a Cu/Al Lap Joint in Ultrasound-Assisted Friction Stir Welding', *Journal of Materials Engineering and Performance*, 28(8), pp. 5245–5254. doi: 10.1007/s11665-019-04244-3.

Chen, W. *et al.* (2021) 'Improvement in tensile strength of Mg/Al alloy dissimilar friction stir welding joints by reducing intermetallic compounds', *Journal of Alloys and Compounds*, 861, p. 157942. doi: 10.1016/j.jallcom.2020.157942.

Chen, Y. *et al.* (2017) 'Microstructural and Mechanical Characterization of a Dissimilar Friction Stir-Welded AA5083-AA7B04 Butt Joint', *Journal of Materials Engineering and Performance*, 26(2), pp. 530–539. doi: 10.1007/s11665-016-2482-9.

Chen, Y. *et al.* (2019) 'Effects of microstructural inhomogeneities and micro-defects on tensile and very high cycle fatigue behaviors of the friction stir welded ZK60 magnesium alloy joint', *International Journal of Fatigue*, 122(January), pp. 218–227. doi: 10.1016/j.ijfatigue.2019.01.016.

Chiumenti, M. *et al.* (2013) 'Numerical modeling of friction stir welding processes', *Computer Methods in Applied Mechanics and Engineering*, 254, pp. 353–369. doi: 10.1016/j.cma.2012.09.013.

Chiuzuli, F. R. *et al.* (2021) 'Effect of the gap width in AZ31 magnesium alloy joints obtained by friction stir welding', *Journal of Materials Research and Technology*, 15, pp. 5297–5306. doi: 10.1016/j.jmrt.2021.10.115.

Choudhary, A. K. and Jain, R. (2022) 'Numerical prediction of various defects and their formation mechanism during friction stir welding using coupled Eulerian-Lagrangian technique', *Mechanics of Advanced Materials and Structures*, 0(0), pp. 1–14. doi: 10.1080/15376494.2022.2053911.

Chu, Q. *et al.* (2018) 'Numerical analysis of material flow in the probeless friction stir spot welding based on Coupled Eulerian-Lagrangian approach', *Journal of Manufacturing Processes*, 36(July), pp. 181–187. doi: 10.1016/j.jmapro.2018.10.013.

Chu, Q. *et al.* (2021) 'In-depth understanding of material flow behavior and refinement mechanism during bobbin tool friction stir welding', *International Journal of Machine Tools and Manufacture*, 171(October). doi: 10.1016/j.ijmachtools.2021.103816.

Cocchetti, G., Pagani, M. and Perego, U. (2013) 'Selective mass scaling and critical time-step estimate for explicit dynamics analyses with solid-shell elements', *Computers & Structures*, 127, pp. 39–52.

Constantin, M. A., Nițu, E. L. and Bădulescu, C. (2019) 'Numerical simulation of friction stir welding of pure copper plates', *IOP Conference Series: Materials Science and Engineering*, 564(1). doi: 10.1088/1757-899X/564/1/012031.

Das, B., Bag, S. and Pal, S. (2017) 'Probing weld quality monitoring in friction stir welding through characterization of signals by fractal theory', *Journal of Mechanical Science and Technology*, 31(5), pp. 2459–2465. doi: 10.1007/s12206-017-0444-2.

Das, B., Pal, S. and Bag, S. (2016a) 'A combined wavelet packet and Hilbert-Huang transform for defect detection and modelling of weld strength in friction stir welding process', *Journal of Manufacturing Processes*, 22, pp. 260–268. doi: 10.1016/j.jmapro.2016.04.002.

Das, B., Pal, S. and Bag, S. (2016b) 'Defect detection in friction stir welding process through characterization of signals by fractal dimension', *Manufacturing Letters*, 7, pp. 6–10. doi: 10.1016/j.mfglet.2015.11.006.

Das, B., Pal, S. and Bag, S. (2016c) 'Monitoring of friction stir welding process using weld image information', *Science and Technology of Welding and Joining*, 21(4), pp. 317–324. doi: 10.1080/13621718.2015.1109805.

Das, B., Pal, S. and Bag, S. (2017a) 'Torque based defect detection and weld quality modelling in friction stir welding process', *Journal of Manufacturing Processes*, 27, pp. 8–17. doi: 10.1016/j.jmapro.2017.03.012.

Das, B., Pal, S. and Bag, S. (2017b) 'Weld quality prediction in friction stir welding using wavelet analysis', *International Journal of Advanced Manufacturing Technology*, 89(1–4), pp. 711–725. doi: 10.1007/s00170-016-9140-0.

Das, B., Pal, S. and Bag, S. (2018) 'Monitoring of Friction Stir Welding Process using Main Spindle Motor Current', *Journal of The Institution of Engineers (India): Series C*, 99(6), pp. 711–716. doi: 10.1007/s40032-017-0371-0.

Das, D. *et al.* (2021) 'Prediction of residual stress in electron beam welding of stainless steel from process parameters and natural frequency of vibrations using machine-learning algorithms', *Proceedings of the Institution of Mechanical Engineers, Part C: Journal of Mechanical Engineering Science*, 235(11), pp. 2008–2021. doi: 10.1177/0954406220950343.

Das, S. and Joshi, S. N. (2020) 'Estimation of wire strength based on residual stresses induced during wire electric discharge machining', *Journal of Manufacturing Processes*, 53(January), pp. 406–419. doi: 10.1016/j.jmapro.2020.03.015.

Das, S. and Narayanan, R. G. (2023) 'Friction stir spot welding of aluminum and steel sheets using a consumable sheet', *International Journal of Advanced Manufacturing Technology*, (0123456789). doi: 10.1007/s00170-023-11863-7.

De, A., Bhadeshia, H. K. D. H. and Debroy, T. (2014) 'Friction stir welding of mild steel: Tool durability and steel microstructure', *Materials Science and Technology (United Kingdom)*, 30(9), pp. 1050–1056. doi: 10.1179/1743284714Y.0000000534.

Dehghani, M., Amadeh, A. and Akbari Mousavi, S. A. A. (2013) 'Investigations on the effects of friction stir welding parameters on intermetallic and defect formation in joining aluminum alloy to mild steel', *Materials and Design*, 49, pp. 433–441. doi: 10.1016/j.matdes.2013.01.013.

Dewan, M. W. *et al.* (2016) 'Prediction of tensile strength of friction stir weld joints with adaptive neuro-fuzzy inference system (ANFIS) and neural network', *Materials and Design*, 92, pp. 288–299. doi: 10.1016/j.matdes.2015.12.005.

Dialami, N., Cervera, M., *et al.* (2017) 'A fast and accurate two-stage strategy to evaluate the effect of the pin tool profile on metal flow, torque and forces in friction stir welding', *International Journal of Mechanical Sciences*, 122(January), pp. 215–227. doi: 10.1016/j.ijmecsci.2016.12.016.

Dialami, N., Chiumenti, M., *et al.* (2017) 'Enhanced friction model for Friction Stir Welding (FSW) analysis: Simulation and experimental validation', *International Journal of Mechanical Sciences*, 133, pp. 555–567. doi: 10.1016/j.ijmecsci.2017.09.022.

Dialami, Narges *et al.* (2017) 'Experimental validation of an FSW model with an enhanced friction law: Application to a threaded cylindrical pin tool', *Metals*, 7(11). doi: 10.3390/met7110491.

Dialami, N. *et al.* (2019) 'Prediction of joint line remnant defect in friction stir welding', *International Journal of Mechanical Sciences*, 151(September 2018), pp. 61–69. doi: 10.1016/j.ijmecsci.2018.11.012.

Dialami, N., Cervera, M. and Chiumenti, M. (2018) 'Numerical modelling of microstructure evolution in friction stir welding (FSW)', *Metals*, 8(3), pp. 1–15. doi: 10.3390/met8030183.

Dialami, N., Cervera, M. and Chiumenti, M. (2019) 'Effect of the tool tilt angle on the heat generation and the material flow in friction stir welding', *Metals*, 9(1). doi: 10.3390/met9010028.

Dialami, N., Cervera, M. and Chiumenti, M. (2020) 'Defect formation and material flow in Friction Stir Welding', *European Journal of Mechanics, A/Solids*, 80(May 2019), p. 103912. doi: 10.1016/j.euromechsol.2019.103912.

Ditchburn, R. J., Burke, S. K. and Scala, C. M. (1996) 'NDT of welds: State of the art', *NDT and E International*, 29(2), pp. 111–117. doi: 10.1016/0963-8695(96)00010-2.

Dohda, K. *et al.* (2021) 'Galling phenomena in metal forming', *Friction*, 9(4), pp. 665–685. doi: 10.1007/s40544-020-0430-z.

Du, Y. *et al.* (2020) 'Machine learning based hierarchy of causative variables for tool failure in friction stir welding', *Acta Materialia*, 192, pp. 67–77. doi: 10.1016/j.actamat.2020.03.047.

Du, Y., Mukherjee, T. and DebRoy, T. (2019) 'Conditions for void formation in friction stir welding from machine learning', *npj Computational Materials*, 5(1), pp. 1–8. doi: 10.1038/s41524-019-0207-y.

Du, Y., Mukherjee, T. and DebRoy, T. (2021) 'Physics-informed machine learning and mechanistic modeling of additive manufacturing to reduce defects', *Applied Materials Today*, 24. doi: 10.1016/j.apmt.2021.101123.

Dubourg, L., Merati, A. and Jahazi, M. (2010) 'Process optimisation and mechanical properties of friction stir lap welds of 7075-T6 stringers on 2024-T3 skin', *Materials and Design*, 31(7), pp. 3324–3330. doi: 10.1016/j.matdes.2010.02.002.

Durdanović, M. B. *et al.* (2009) 'Heat generation during friction stir welding process', *Tribology in Industry*, 31(1–2), pp. 8–14.

Eckerson, K., Liechty, B. and Sorensen, C. D. (2008) 'Thermomechanical similarity between Van Aken plasticine and metalS in hot-forming processes', *Journal of Strain Analysis for Engineering Design*, 43(5), pp. 383–394. doi: 10.1243/03093247JSA364.

Eivani, A. R. *et al.* (2021) 'A novel approach to determine residual stress field during FSW of AZ91 Mg alloy using combined smoothed particle hydrodynamics/neuro-fuzzy computations and ultrasonic testing', *Journal of Magnesium and Alloys*, 9(4), pp. 1304–1328. doi: 10.1016/j.jma.2020.11.018.

Elangovan, K. and Balasubramanian, V. (2008) 'Influences of tool pin profile and tool shoulder diameter on the formation of friction stir processing zone in AA6061 aluminium alloy', *Materials and Design*, 29(2), pp. 362–373. doi: 10.1016/j.matdes.2007.01.030.

Elsheikh, A. H. (2023) 'Applications of machine learning in friction stir welding: Prediction of joint properties, real-time control and tool failure diagnosis', *Engineering Applications of Artificial Intelligence*, 121(November 2022), p. 105961. doi: 10.1016/j.engappai.2023.105961.

Emamian, S. S. *et al.* (2020) 'Improving the friction stir welding tool life for joining the metal matrix composites', *International Journal of Advanced Manufacturing Technology*, 106(7–8), pp. 3217–3227. doi: 10.1007/s00170-019-04837-1.

Eslami, S. *et al.* (2015) 'Shoulder design developments for FSW lap joints of dissimilar polymers', *Journal of Manufacturing Processes*, 20, pp. 15–23. doi: 10.1016/j.jmapro.2015.09.013.

Esmaeilzadeh, P. *et al.* (2020) 'Phase-field modeling of fracture and crack growth in friction stir processed pure copper', *International Journal of Advanced Manufacturing Technology*, 109(9–12), pp. 2377–2392. doi: 10.1007/s00170-020-05488-3.

Fall, A. *et al.* (2016) 'Tool wear characteristics and effect on microstructure in Ti-6Al-4V friction stir welded joints', *Metals*, 6(11). doi: 10.3390/met6110275.

Fande, A. W., Taiwade, R. V. and Raut, L. (2022) 'Development of activated tungsten inert gas welding and its current status: A review', *Materials and Manufacturing Processes*, 37(8), pp. 841–876. doi: 10.1080/10426914.2022.2039695.

Fanelli, P., Vivio, F. and Vullo, V. (2012) 'Experimental and numerical characterization of Friction Stir Spot Welded joints', *Engineering Fracture Mechanics*, 81, pp. 17–25. doi: 10.1016/j.engfracmech.2011.07.009.

Fedkiw, R. P. (2002) 'Coupling an Eulerian fluid calculation to a Lagrangian solid calculation with the ghost fluid method', *Journal of Computational Physics*, 175(1), pp. 200–224. doi: 10.1006/jcph.2001.6935.

Fei, X. *et al.* (2016) 'Effect of pre-hole offset on the property of the joint during laser-assisted friction stir welding of dissimilar metals steel and aluminum alloys', *Materials Science and Engineering A*, 653, pp. 43–52. doi: 10.1016/j.msea.2015.11.101.

Feng, Z. *et al.* (2007) 'Modelling of residual stresses and property distributions in friction stir welds of aluminium alloy 6061-T6', *Science and Technology of Welding and Joining*, 12(4), pp. 348–356. doi: 10.1179/174329307X197610.

Ferreira, A. C. *et al.* (2020) 'Investigation of internal defects and premature fracture of dissimilar refill friction stir spot welds of AA5754 and AA6061', *International Journal of Advanced Manufacturing Technology*, 106(7–8), pp. 3523–3531. doi: 10.1007/s00170-019-04819-3.

Forcellese, A. and Gabrielli, F. (2000) 'Warm forging of aluminum alloys: A new approach for time compression of the forging sequence', *International Journal of Machine Tools and Manufacture*, 40(9), pp. 1285–1297. doi: 10.1016/S0890-6955(99)00127-3.

Fourment, L. and Guerdoux, S. (2008) '3D numerical simulation of the three stages of Friction Stir Welding based on friction parameters calibration', *International Journal of Material Forming*, 1(SUPPL. 1), pp. 1287–1290. doi: 10.1007/s12289-008-0138-5.

Fraser, K. A. (2014) 'Numerical Simulation of Bobbin Tool Friction Stir Welding', in *Proceedings of the 10th International Friction Stir Welding Symposium*.

Fraser, K., Kiss, L. I. and St-Georges, L. (2016) 'Adaptive Thermal Boundary Conditions for Smoothed Particle Hydrodynamics', *14th International LS-DYNA Users Conference*, (June), pp. 1–18.

Fratini, L., Macaluso, G. and Pasta, S. (2009) 'Residual stresses and FCP prediction in FSW through a continuous FE model', *Journal of Materials Processing Technology*, 209(15–16), pp. 5465–5474. doi: 10.1016/j.jmatprotec.2009.05.001.

Gambirasio, L. (2013) *HIGH STRAIN RATE PHENOMENA IN PERFORATING GUN DEVICES BY LAGRANGIAN / EULERIAN FEM SIMULATIONS*. UNIVERSITY OF TRENTO.

Gambirasio, L. and Rizzi, E. (2014) 'On the calibration strategies of the Johnson-Cook strength model: Discussion and applications to experimental data', *Materials Science and Engineering A*, 610, pp. 370–413. doi: 10.1016/j.msea.2014.05.006.

Gao, P. F. *et al.* (2019) 'Prediction of the folding defect in die forging: A versatile approach for three typical types of folding defects', *Journal of Manufacturing Processes*, 39(September 2018), pp. 181–191. doi: 10.1016/j.jmapro.2019.02.027.

Geng, P. *et al.* (2022) 'Prediction of residual stresses within dissimilar Al/steel friction stir lap welds using an Eulerian-based modeling approach', *Journal of Manufacturing Processes*, 79(May), pp. 340–355. doi: 10.1016/j.jmapro.2022.05.001.

Ghetiya, N. D. and Patel, K. M. (2018) 'Numerical simulation on an effect of backing plates on joint temperature and weld quality in air and immersed FSW of AA2014-T6', *International Journal of Advanced Manufacturing Technology*, 99(5–8), pp. 1937–1951. doi: 10.1007/s00170-018-2632-3.

Gibson, B. T. *et al.* (2014) 'Friction stir welding: Process, automation, and control', *Journal of Manufacturing Processes*, 16(1), pp. 56–73. doi: 10.1016/j.jmapro.2013.04.002.

de Giorgi, M. *et al.* (2009) 'Effect of shoulder geometry on residual stress and fatigue properties of AA6082 FSW joints', *Journal of Mechanical Science and Technology*, 23(1), pp. 26–35. doi: 10.1007/s12206-008-1006-4.

Gratecap, F. *et al.* (2012) 'Exploring material flow in friction stir welding: Tool eccentricity and formation of banded structures', *International Journal of Material Forming*, 5(2), pp. 99–107. doi: 10.1007/s12289-010-1008-5.

Gratecap, F., Racineux, G. and Marya, S. (2008) 'A simple methodology to define conical tool geometry and welding parameters in friction stir welding', *International Journal of Material Forming*, 1(3), pp. 143–158. doi: 10.1007/s12289-008-0370-z.

Grujicic, M. *et al.* (2010) 'Modeling of AA5083 material-microstructure evolution during butt friction-stir welding', *Journal of Materials Engineering and Performance*, 19(5), pp. 672–684. doi: 10.1007/s11665-009-9536-1.

Grujicic, M. *et al.* (2011) 'Computational investigation of hardness evolution during friction-stir welding of AA5083 and AA2139 aluminum alloys', *Journal of Materials Engineering and Performance*, 20(7), pp. 1097–1108. doi: 10.1007/s11665-010-9741-y.

Grujicic, M. *et al.* (2012) 'Modifications in the AA5083 Johnson-Cook material model for use in friction stir welding computational analyses', *Journal of Materials Engineering and Performance*, 21(11), pp. 2207–2217. doi: 10.1007/s11665-011-0118-7.

Grujicic, M. *et al.* (2019) 'Computational analysis of the intermetallic formation during the dissimilar metal aluminum-to-steel friction stir welding process', *Proceedings of the Institution of Mechanical Engineers, Part L: Journal of Materials: Design and Applications*, 233(6), pp. 1080–1100. doi: 10.1177/1464420716673670.

Guan, W. *et al.* (2021) 'Detection of tunnel defects in friction stir welded aluminum alloy joints based on the in-situ force signal', *Journal of Manufacturing Processes*, 71(July), pp. 1–11. doi: 10.1016/j.jmapro.2021.09.014.

Guan, W. *et al.* (2022) 'Force data-driven machine learning for defects in friction stir welding', *Scripta Materialia*, 217(February), p. 114765. doi: 10.1016/j.scriptamat.2022.114765.

Guan, W. *et al.* (2023) 'The response of force characteristic to weld-forming process in friction stir welding assisted by machine learning', *International Journal of Mechanical Sciences*, 253(April), p. 108409. doi: 10.1016/j.ijmecsci.2023.108409.

Guerdoux, S. (2008) *Numerical simulation of the friction stir welding process*. Mines Paris ParisTech.

Guerdoux, S. and Fourment, L. (2009) 'A 3D numerical simulation of different phases of friction stir welding', *Modelling and Simulation in Materials Science and Engineering*, 17(7), p. 075001. doi: 10.1088/0965-0393/17/7/075001.

Gupta, S., Abotula, S. and Shukla, A. (2014) 'Determination of johnson-cook parameters for cast aluminum alloys', *Journal of Engineering Materials and Technology*, 136(3), pp. 1–4. doi:

10.1115/1.4027793.

Hamade, R. F. and Baydoun, A. M. R. (2019) 'Nondestructive detection of defects in friction stir welded lap joints using computed tomography', *Materials and Design*, 162, pp. 10–23. doi: 10.1016/j.matdes.2018.11.034.

Hamilton, C. *et al.* (2013) 'A coupled thermal/material flow model of friction stir welding applied to Sc-modified aluminum alloys', *Metallurgical and Materials Transactions A*, 44(4), pp. 1730–1740. doi: 10.1007/s11661-012-1512-y.

Hammelmüller, F. and Zehetner, C. (2015) 'Increasing numerical efficiency in coupled Eulerian-Lagrangian metal forming simulations', in *COMPLAS XIII: proceedings of the XIII International Conference on Computational Plasticity: fundamentals and applications*, pp. 727–733.

Harewood, F. J. and McHugh, P. E. (2007) 'Comparison of the implicit and explicit finite element methods using crystal plasticity', *Computational Materials Science*, 39(2), pp. 481–494. doi: 10.1016/j.commatsci.2006.08.002.

Hartl, R. *et al.* (2021) 'Process monitoring in friction stir welding using convolutional neural networks', *Metals*, 11(4). doi: 10.3390/met11040535.

Hasan, A. F. *et al.* (2017) 'A numerical methodology for predicting tool wear in Friction Stir Welding', *Journal of Materials Processing Technology*, 241, pp. 129–140. doi: 10.1016/j.jmatprotec.2016.11.009.

Hasan, A. F., Bennett, C. J. and Shipway, P. H. (2015) 'A numerical comparison of the flow behaviour in Friction Stir Welding (FSW) using unworn and worn tool geometries', *Materials and Design*, 87, pp. 1037–1046. doi: 10.1016/j.matdes.2015.08.016.

Hassanifard, S. *et al.* (2022) 'The effect of the friction stir welding tool shape on tensile properties of welded Al 6061-T6 joints', *Materials Today Communications*, 31(November 2021), p. 103457. doi: 10.1016/j.mtcomm.2022.103457.

Hattel, J. H., Sonne, M. R. and Tutum, C. C. (2015) 'Modelling residual stresses in friction stir welding of Al alloys—a review of possibilities and future trends', *International Journal of Advanced Manufacturing Technology*, 76(9–12), pp. 1793–1805. doi: 10.1007/s00170-014-6394-2.

Hawryluk, M. and Jakubik, J. (2016) 'Analysis of forging defects for selected industrial die forging processes', *Engineering Failure Analysis*, 59, pp. 396–409. doi: 10.1016/j.engfailanal.2015.11.008.

He, Y., Dawson, P. R. and Boyce, D. E. (2008) 'Modeling damage evolution in friction stir welding process', *Journal of Engineering Materials and Technology*, 130(2), pp. 0210061–02100610. doi: 10.1115/1.2840963.

Heidarzadeh, A. *et al.* (2020) 'Friction stir welding/processing of metals and alloys: A comprehensive review on microstructural evolution', *Progress in Materials Science*, 117(March 2019), p. 100752. doi: 10.1016/j.pmatsci.2020.100752.

Heurtier, P. *et al.* (2006) 'Mechanical and thermal modelling of Friction Stir Welding', *Journal of Materials Processing Technology*, 171(3), pp. 348–357. doi: 10.1016/j.jmatprotec.2005.07.014.

Hou, Z. *et al.* (2018) 'Residual Stresses in Dissimilar Friction Stir Welding of AA2024 and AZ31: Experimental and Numerical Study', *Journal of Manufacturing Science and Engineering, Transactions of the ASME*, 140(5), pp. 1–10. doi: 10.1115/1.4039074.

Huang, Y. *et al.* (2017) 'Micro friction stir welding of ultra-thin Al-6061 sheets', *Journal of Materials Processing Technology*, 250(July), pp. 313–319. doi: 10.1016/j.jmatprotec.2017.07.031.

Huang, Y. *et al.* (2018) 'Numerical design of high depth-to-width ratio friction stir welding', *Journal of Materials Processing Technology*, 252(August 2017), pp. 233–241. doi: 10.1016/j.jmatprotec.2017.09.029.

Huang, Y. *et al.* (2019) 'Microstructures and mechanical properties of micro friction stir welding (μFSW) of 6061-T4 aluminum alloy', *Journal of Materials Research and Technology*, 8(1), pp. 1084–1091. doi: 10.1016/j.jmrt.2017.10.010.

Huggett, D. J. *et al.* (2017) 'Phased Array Ultrasonic Testing for Post-Weld and OnLine Detection of Friction Stir Welding Defects', *Research in Nondestructive Evaluation*, 28(4), pp. 187–210. doi: 10.1080/09349847.2016.1157660.

Huihui, Z. *et al.* (2014) 'Micro friction stir welding method for small-thickness component and stir shaft shoulder of micro friction stir welding method'. China.

Hussein, S. A., Tahir, A. S. M. and Hadzley, A. B. (2015) 'Characteristics of aluminum-to-steel joint made by friction stir welding: A review', *Materials Today Communications*, 5, pp. 32–49. doi: 10.1016/j.mtcomm.2015.09.004.

Hynes, N. R. J. *et al.* (2022) 'An experimental insight of friction stir welding of dissimilar AA 6061/Mg AZ 31 B joints', *Proceedings of the Institution of Mechanical Engineers, Part B: Journal of Engineering Manufacture*, 236(6–7), pp. 787–797. doi: 10.1177/09544054211043474.

Infante, V. *et al.* (2016) 'Study of the fatigue behaviour of dissimilar aluminium joints produced by

friction stir welding', *International Journal of Fatigue*, 82, pp. 310–316. doi: 10.1016/j.ijfatigue.2015.06.020.

Iordache, M. D. *et al.* (2021) 'A numerical strategy to identify the FSW process optimal parameters of a butt-welded joint of quasi-pure copper plates: modeling and experimental validation', *International Journal of Advanced Manufacturing Technology*, 115(7–8), pp. 2505–2520. doi: 10.1007/s00170-021-07296-9.

Iqbal, M. P. *et al.* (2020) 'Numerical modelling of microstructure in friction stir welding of aluminium alloys', *International Journal of Mechanical Sciences*, 185(May). doi: 10.1016/j.ijmecsci.2020.105882.

Iqbal, M. P. *et al.* (2022) 'Numerical modelling of friction stir welding of pipes: Effect of tool shoulder on mechanical property and metallurgical characterization', *Journal of Manufacturing Processes*, 79(May), pp. 326–339. doi: 10.1016/j.jmapro.2022.04.028.

Jabraeili, R. *et al.* (2021) 'Effect of FSW process parameters on microstructure and mechanical properties of the dissimilar AA2024 Al alloy and 304 stainless steel joints', *Materials Science and Engineering A*, 814(December 2020), p. 140981. doi: 10.1016/j.msea.2021.140981.

Jacquin, D. *et al.* (2011) 'A simple Eulerian thermomechanical modeling of friction stacir welding', *Journal of Materials Processing Technology*, 211(1), pp. 57–65. doi: 10.1016/j.jmatprotec.2010.08.016.

Jacquin, D., Desrayaud, C. and Montheillet, F. (2007) 'A Thermo-Fluid Analysis of the Friction Stir Welding Process', *Materials Science Forum*, 539–543, pp. 3832–3837. doi: 10.4028/www.scientific.net/msf.539-543.3832.

Jain, R. *et al.* (2015) 'Friction Stir Welding: Scope and Recent Development', in Davim, J. P. (ed.) *Modern Manufacturing Engineering, Materials Forming, Machining and Tribology*,. Springer International Publishing Switzerland 2015, pp. 179–229. doi: 10.1007/978-3-319-20152-8.

Jain, R., Pal, S. K. and Singh, S. B. (2017) 'Numerical modeling methodologies for friction stir welding process', in *Computational Methods and Production Engineering*. Elsevier, pp. 125–169. doi: 10.1016/B978-0-85709-481-0.00005-7.

Jain, R., Pal, S. K. and Singh, S. B. (2018) 'Finite element simulation of pin shape influence on material flow, forces in friction stir welding', *International Journal of Advanced Manufacturing Technology*, 94(5–8), pp. 1781–1797. doi: 10.1007/s00170-017-0215-3.

Jain, R., Pal, S. K. and Singh, S. B. (2019) 'Investigation on effect of pin shapes on temperature, material flow and forces during friction stir welding: A simulation study', *Proceedings of the Institution of Mechanical Engineers, Part B: Journal of Engineering Manufacture*, 233(9), pp. 1980–1992. doi: 10.1177/0954405418805615.

Jamshidi Aval, H. *et al.* (2011) 'Effect of tool geometry on mechanical and microstructural behaviours in dissimilar friction stir welding of AA 5086-AA 6061', *Science and Technology of Welding and Joining*, 16(7), pp. 597–604. doi: 10.1179/1362171811Y.0000000044.

Jamshidi Aval, H., Serajzadeh, S. and Kokabi, A. H. (2011) 'Evolution of microstructures and mechanical properties in similar and dissimilar friction stir welding of AA5086 and AA6061', *Materials Science and Engineering A*, 528(28), pp. 8071–8083. doi: 10.1016/j.msea.2011.07.056.

Jana, S. and Hovanski, Y. (2012) 'Fatigue behaviour of magnesium to steel dissimilar friction stir lap joints', *Science and Technology of Welding and Joining*, 17(2), pp. 141–145. doi: 10.1179/1362171811Y.0000000083.

Ji, S. *et al.* (2013) 'Design of friction stir welding tool for avoiding root flaws', *Materials*, 6(12), pp. 5870–5877. doi: 10.3390/ma6125870.

Ji, S. D. *et al.* (2012) 'Numerical simulation of material flow behavior of friction stir welding influenced by rotational tool geometry', *Computational Materials Science*, 63, pp. 218–226. doi: 10.1016/j.commatsci.2012.06.001.

Jia, H., Wu, K. and Sun, Y. (2022) 'Numerical and experimental study on the thermal process, material flowand welding defects during high-speed friction stir welding', *Materials Today Communications*, 31(August 2021), p. 103526. doi: 10.1016/j.mtcomm.2022.103526.

Jian, H. *et al.* (2021) 'Microstructure and fatigue crack growth behavior in welding joint of Al-Mg alloy', *Engineering Failure Analysis*, 120(June 2020), p. 105034. doi: 10.1016/j.engfailanal.2020.105034.

Jiang, T., Wu, C. S. and Shi, L. (2022) 'Effects of tool pin thread on temperature field and material mixing in friction stir welding of dissimilar Al/Mg alloys', *Journal of Manufacturing Processes*, 74(November 2021), pp. 112–122. doi: 10.1016/j.jmapro.2021.12.008.

Jiang, T., Wu, C. S. and Su, H. (2022) 'Determination of self-adaptive slip rate at tool/workpiece interface in numerical model of friction stir welding', *Materials Today Communications*, 33(August), p. 104428. doi: 10.1016/j.mtcomm.2022.104428.

Johnson, G. R. and Cook, W. H. (1985) 'Fracture characteristics of three metals subjected to various strains, strain rates, temperatures and pressures', *Engineering Fracture Mechanics*, 21(1), pp. 31–48. doi: 10.1016/0013-7944(85)90052-9.

Le Jolu, T. *et al.* (2014) 'Microstructural Characterization of Internal Welding Defects and Their Effect on the Tensile Behavior of FSW Joints of AA2198 Al-Cu-Li Alloy', *Metallurgical and Materials Transactions A: Physical Metallurgy and Materials Science*, 45(12), pp. 5531–5544. doi: 10.1007/s11661-014-2537-1.

Joo, S. (2013) 'Joining of dissimilar AZ31B magnesium alloy and SS400 mild steel by hybrid gas tungsten arc friction stir welding', *Metals and Materials International*, 19(6), pp. 1251–1257. doi: 10.1007/s12540-013-6016-9.

Joshi, G. R. and Badheka, V. J. (2017) 'Microstructures and Properties of Copper to Stainless Steel Joints by Hybrid FSW', *Metallography, Microstructure, and Analysis*, 6(6), pp. 470–480. doi: 10.1007/s13632-017-0398-x.

K Elangovan, K. and Balasubramanian (2007) 'Influences of pin profile and rotational speed of the tool on the formation of friction stir processing zone in AA2219 aluminium alloy', *Materials Science and Engineering A*, 459(1–2), pp. 7–18. doi: 10.1016/j.msea.2006.12.124.

Kang, S. and Jung, Y. (2018) 'Friction stir welding equipment of container-type that is easy to be transported'. South Korea.

Karrar, G. *et al.* (2022) 'Prediction and validation of intermetallic compound formation during friction stir welding of AA6061 to commercially pure copper', *Science and Technology of Welding and Joining*, 27(5), pp. 374–387. doi: 10.1080/13621718.2022.2055289.

Kasai, H., Morisada, Y. and Fujii, H. (2015) 'Dissimilar FSW of immiscible materials: Steel/magnesium', *Materials Science and Engineering A*, 624, pp. 250–255. doi: 10.1016/j.msea.2014.11.060.

Kaushik, P. and Dwivedi, D. K. (2021) 'Effect of tool geometry in dissimilar Al-Steel Friction Stir Welding', *Journal of Manufacturing Processes*, 68(PB), pp. 198–208. doi: 10.1016/j.jmapro.2020.08.007.

Kaushik, P. and Kumar Dwivedi, D. (2021) 'Induction preheating in FSW of Al-Steel combination', *Materials Today: Proceedings*, 46, pp. 1091–1095. doi: 10.1016/j.matpr.2021.01.438.

Khalid, E., Shunmugasamy, V. C. and Mansoor, B. (2022) 'Dissimilar micro friction stir welding of ultra-thin Mg AZ31 to Al 6061 sheets', *Journal of Materials Research and Technology*, 21, pp. 1528–1533. doi: 10.1016/j.jmrt.2022.09.098.

Khan, A. *et al.* (2016) 'An alternative explanation of forming force reduction for forming process submitted to vibration: Influence of the waveform in the viscoplastic domain', *Journal of Materials Processing Technology*, 230, pp. 288–299. doi: 10.1016/j.jmatprotec.2015.11.019.

Khan, N. Z. *et al.* (2015) 'Investigations on tunneling and kissing bond defects in FSW joints for dissimilar aluminum alloys', *Journal of Alloys and Compounds*, 648, pp. 360–367. doi: 10.1016/j.jallcom.2015.06.246.

Khodaverdizadeh, H., Heidarzadeh, A. and Saeid, T. (2013) 'Effect of tool pin profile on microstructure and mechanical properties of friction stir welded pure copper joints', *Materials and Design*, 45, pp. 265–270. doi: 10.1016/j.matdes.2012.09.010.

Kim, J., Kim, S. and Joong-seok, N. (2013) 'Portable type friction stir welding apparatus'. South Korea.

Kim, K. H. *et al.* (2017) 'Joint properties of ultra thin 430M2 ferritic stainless steel sheets by friction stir welding using pinless tool', *Journal of Materials Processing Technology*, 243, pp. 381–386. doi: 10.1016/j.jmatprotec.2016.12.018.

Kim, Y. G. *et al.* (2006) 'Three defect types in friction stir welding of aluminum die casting alloy', *Materials Science and Engineering A*, 415(1–2), pp. 250–254. doi: 10.1016/j.msea.2005.09.072.

Ko, D. C. and Kim, B. M. (2000) 'Prediction of central burst defects in extrusion and wire drawing', *Journal of Materials Processing Technology*, 102(1), pp. 19–24. doi: 10.1016/S0924-0136(99)00461-6.

Kobayashi, H. and Onoue, H. (1943) 'Brittle Fracture of Liberty Ships', *Failure Knowledge Database*, 100(April), p. 67. doi: http://www.sozogaku.com/fkd/en/hfen/HB1011020.pdf.

Kong, F., Ma, J. and Kovacevic, R. (2011) 'Numerical and experimental study of thermally induced residual stress in the hybrid laser-GMA welding process', *Journal of Materials Processing Technology*, 211(6), pp. 1102–1111. doi: 10.1016/j.jmatprotec.2011.01.012.

Koric, S., Hibbeler, L. C. and Thomas, B. G. (2009) 'Explicit coupled thermo-mechanical finite element model of steel solidification', *International Journal for Numerical Methods in Engineering*, 78, pp. 1–31.

Krasnowski, K., Hamilton, C. and Dymek, S. (2015) 'Influence of the tool shape and weld configuration on microstructure and mechanical properties of the Al 6082 alloy FSW joints', *Archives of Civil and Mechanical Engineering*. doi: 10.1016/j.acme.2014.02.001.

Krawezik, G. P. and Poole, G. (2009) 'Accelerating the ANSYS Direct Sparse Solver with GPUs', *Symposium on Application Accelerators in High Performance Computing*, (June), pp. 7–10. Available at: http://saahpc.ncsa.illinois.edu/09/papers/Krawezik_paper.pdf.

Krutzlinger, M. *et al.* (2019) 'Gaussian process regression to predict the morphology of friction-stir-welded aluminum/copper lap joints', *International Journal of Advanced Manufacturing Technology*, 102(5–8), pp. 1839–1852. doi: 10.1007/s00170-018-03229-1.

Kumar, K. and Kailas, S. V. (2008) 'The role of friction stir welding tool on material flow and weld formation', *Materials Science and Engineering A*, 485(1–2), pp. 367–374. doi: 10.1016/j.msea.2007.08.013.

Kumar, R. *et al.* (2021) 'Experimental and computational analyses of material flow characteristics in friction stir welding', *International Journal of Advanced Manufacturing Technology*, 115(9–10), pp. 3011–3020. doi: 10.1007/s00170-021-07345-3.

Kumar, S. and Wu, C. (2021) 'Eliminating intermetallic compounds via Ni interlayer during friction stir welding of dissimilar Mg/Al alloys', *Journal of Materials Research and Technology*, 15, pp. 4353–4369. doi: 10.1016/j.jmrt.2021.10.065.

Kunnathur Periyasamy, Y., Perumal, A. V. and Kunnathur Periyasamy, B. (2019) 'Influence of Tool Shoulder Concave Angle and Pin Profile on Mechanical Properties and Microstructural Behaviour of Friction Stir Welded AA7075-T651 and AA6061 Dissimilar Joint', *Transactions of the Indian Institute of Metals*, 72(4), pp. 1087–1109. doi: 10.1007/s12666-019-01584-5.

Kuykendall, K., Nelson, T. and Sorensen, C. (2013) 'On the selection of constitutive laws used in modeling friction stir welding', *International Journal of Machine Tools and Manufacture*, 74, pp. 74–85. doi: 10.1016/j.ijmachtools.2013.07.004.

Kwan, C. T. (2003) 'An analysis of the eccentric nosing process of metal tubes', *Journal of Materials Processing Technology*, 140(1-3 SPEC.), pp. 530–534. doi: 10.1016/S0924-0136(03)00781-7.

Lacki, P. *et al.* (2020) 'Evaluation of usefulness of AlCrN coatings for increased life of tools used in friction stir welding (FSW) of sheet aluminum alloy', *Materials*, 13(18). doi: 10.3390/ma13184124.

Lader, S. K., Baruah, M. and Ballav, R. (2023) 'Improvement in the weldability and mechanical properties of CuZn40 and AA1100-O dissimilar joints by underwater friction stir welding', *Journal of Manufacturing Processes*, 85(November 2022), pp. 1154–1172. doi: 10.1016/j.jmapro.2022.12.033.

Lakshminarayanan, A. K., Malarvizhi, S. and Balasubramanian, V. (2011) 'Developing friction stir welding window for AA2219 aluminium alloy', *Transactions of Nonferrous Metals Society of China (English Edition)*, 21(11), pp. 2339–2347. doi: 10.1016/S1003-6326(11)61018-2.

Lee, W. B., Yeon, Y. M. and Jung, S. B. (2003) 'The joint properties of dissimilar formed Al alloys by friction stir welding according to the fixed location of materials', *Scripta Materialia*, 49(5), pp. 423–428. doi: 10.1016/S1359-6462(03)00301-4.

Li, B., Shen, Y. and Hu, W. (2011) 'The study on defects in aluminum 2219-T6 thick butt friction stir welds with the application of multiple non-destructive testing methods', *Materials and Design*, 32(4), pp. 2073–2084. doi: 10.1016/j.matdes.2010.11.054.

Li, H. Y. *et al.* (2015) 'Nonlinear dynamic analysis efficiency by using a GPU parallelization', *Engineering Letters*, 23(4), pp. 232–238.

Li, J. *et al.* (2020) 'Friction stir welding of Ti-6Al-4V alloy: Friction tool, microstructure, and mechanical properties', *Journal of Manufacturing Processes*, 58(July), pp. 344–354. doi: 10.1016/j.jmapro.2020.08.025.

Li, K. *et al.* (2022) 'Residual stress distribution of aluminium-lithium alloy in hybrid process of friction stir welding and laser peening', *Optics and Laser Technology*, 152(December 2021). doi: 10.1016/j.optlastec.2022.108149.

Li, W. *et al.* (2014) 'Improving mechanical properties of pinless friction stir spot welded joints by eliminating hook defect', *Materials and Design*, 62, pp. 247–254. doi: 10.1016/j.matdes.2014.05.028.

Liang, Q. *et al.* (2020) 'Development and application of high-temperature constitutive model of hni55-7-4-2 alloy', *Metals*, 10(9), pp. 1–19. doi: 10.3390/met10091250.

Liang, Z. *et al.* (2013) 'Effect of tool offset and tool rotational speed on enhancing mechanical property of Al/Mg dissimilar FSW joints', *Metallurgical and Materials Transactions A: Physical Metallurgy and Materials Science*, 44(8), pp. 3721–3731. doi: 10.1007/s11661-013-1700-4.

Liechty, B. C. and Webb, B. W. (2008) 'Modeling the frictional boundary condition in friction stir welding', *International Journal of Machine Tools and Manufacture*, 48(12–13), pp. 1474–1485. doi: 10.1016/j.ijmachtools.2008.04.005.

Lin, S. B. *et al.* (2011) 'Modeling of friction stir welding process for tools design', *Frontiers of Materials Science*, 5(2), pp. 236–245. doi: 10.1007/s11706-011-0128-2.

Liu, F. C. *et al.* (2018) 'A review of friction stir welding of steels: Tool, material flow, microstructure, and properties', *Journal of Materials Science and Technology*, 34(1), pp. 39–57. doi: 10.1016/j.jmst.2017.10.024.

Liu, F., Fu, L. and Chen, H. (2018) 'High speed friction stir welding of ultra-thin AA6061-T6 sheets using different backing plates', *Journal of Manufacturing Processes*, 33(March), pp. 219–227. doi: 10.1016/j.jmapro.2018.05.020.

Liu, F. J. *et al.* (2020) 'Effect of shoulder geometry and clamping on microstructure evolution and mechanical properties of ultra-thin friction stir-welded Al6061-T6 plates', *International Journal of Advanced Manufacturing Technology*, 106(3–4), pp. 1465–1476. doi: 10.1007/s00170-019-04795-8.

Liu, H. J. *et al.* (2003) 'Tensile properties and fracture locations of friction-stir-welded joints of 2017-T351 aluminum alloy', *Journal of Materials Processing Technology*, 142(3), pp. 692–696. doi: 10.1016/S0924-0136(03)00806-9.

Liu, L. M. and Wang, H. Y. (2009) 'The effect of the adhesive on the microcracks in the laser welded bonding Mg to Al joint', *Materials Science and Engineering A*, 507(1–2), pp. 22–28. doi: 10.1016/j.msea.2008.11.061.

Liu, L., Ren, D. and Liu, F. (2014) 'A review of dissimilar welding techniques for magnesium alloys to aluminum alloys', *Materials*, 7(5), pp. 3735–3757. doi: 10.3390/ma7053735.

Liu, X. C. and Wu, C. S. (2016) 'Elimination of tunnel defect in ultrasonic vibration enhanced friction stir welding', *Materials and Design*, 90, pp. 350–358. doi: 10.1016/j.matdes.2015.10.131.

Liu, X., Lan, S. and Ni, J. (2015a) 'Electrically assisted friction stir welding for joining Al 6061 to TRIP 780 steel', *Journal of Materials Processing Technology*, 219, pp. 112–123. doi: 10.1016/j.jmatprotec.2014.12.002.

Liu, X., Lan, S. and Ni, J. (2015b) 'Thermal mechanical modeling of the plunge stage during friction-stir welding of dissimilar Al 6061 to TRIP 780 steel', *Journal of Manufacturing Science and Engineering, Transactions of the ASME*, 137(5), pp. 1–9. doi: 10.1115/1.4031188.

Liu, Z., Ji, S. and Meng, X. (2018a) 'Improving Joint Formation and Tensile Properties of Dissimilar Friction Stir Welding of Aluminum and Magnesium Alloys by Solving the Pin Adhesion Problem', *Journal of Materials Engineering and Performance*, 27(3), pp. 1404–1413. doi: 10.1007/s11665-018-3216-y.

Liu, Z., Ji, S. and Meng, X. (2018b) 'Joining of magnesium and aluminum alloys via ultrasonic assisted friction stir welding at low temperature', *International Journal of Advanced Manufacturing Technology*, 97(9–12), pp. 4127–4136. doi: 10.1007/s00170-018-2255-8.

Lohwasser, D.; Chen, Z. . (ed.) (2009) *Friction stir welding: From basics to applications*. Woodhead publising Ltd. and CRC press LLC.

Maekawa, K., Kubo, A. and Childs, T. H. C. (2001) 'A friction model for free-machining steels and its applicability to machinability analysis', *Key Engineering Materials*, 196, pp. 79–90. doi: 10.4028/www.scientific.net/kem.196.79.

Mahto, R. P., Kumar, R. and Pal, S. K. (2020) 'Characterizations of weld defects, intermetallic compounds and mechanical properties of friction stir lap welded dissimilar alloys', *Materials Characterization*, 160(August 2019), p. 110115. doi: 10.1016/j.matchar.2019.110115.

Majeed, T., Mehta, Y. and Siddiquee, A. N. (2021) 'Analysis of tool wear and deformation in friction stir welding of unequal thickness dissimilar Al alloys', *Proceedings of the Institution of Mechanical Engineers, Part L: Journal of Materials: Design and Applications*, 235(3), pp. 501–512. doi: 10.1177/1464420720971769.

Malarvel, M. and Singh, H. (2021) 'An autonomous technique for weld defects detection and classification using multi-class support vector machine in X-radiography image', *Optik*, 231(November 2020), p. 166342. doi: 10.1016/j.ijleo.2021.166342.

Malik, V. *et al.* (2014) 'Finite element simulation of exit hole filling for friction stir spot welding - A modified technique to apply practically', *Procedia Engineering*, 97, pp. 1265–1273. doi: 10.1016/j.proeng.2014.12.405.

Malik, V. and Kailas, S. V. (2021) 'Understanding the effect of tool geometrical aspects on intensity of mixing and void formation in friction stir process', *Proceedings of the Institution of Mechanical Engineers, Part C: Journal of Mechanical Engineering Science*, 235(4), pp. 744–757. doi: 10.1177/0954406220938410.

Mandache, C. *et al.* (2012) 'Non-destructive detection of lack of penetration defects in friction stir welds', *Science and Technology of Welding and Joining*, 17(4), pp. 295–303. doi: 10.1179/1362171812Y.0000000007.

Mandal, S., Rice, J. and Elmustafa, A. A. (2008) 'Experimental and numerical investigation of the plunge stage in friction stir welding', *Journal of Materials Processing Technology*, 203(1–3), pp. 411–419. doi: 10.1016/j.jmatprotec.2007.10.067.

manuel, A. (2004) 'ANSYS Low-Frequency Electromagnetic Analysis Guide', *Analysis*, (November).

Mao, Y. *et al.* (2018) 'Inhomogeneity of microstructure and mechanical properties in the nugget of friction stir welded thick 7075 aluminum alloy joints', *Journal of Materials Science and Technology*, 34(1), pp. 228–236. doi: 10.1016/j.jmst.2017.11.039.

Mao, Y. *et al.* (2020) 'Microstructural characterization and mechanical properties of micro friction stir welded dissimilar Al/Cu ultra-thin sheets', *Journal of Manufacturing Processes*, 60(November), pp. 356–365. doi: 10.1016/j.jmapro.2020.10.064.

Mao, Z., Liu, G. R. and Dong, X. (2017) 'A comprehensive study on the parameters setting in smoothed particle hydrodynamics (SPH) method applied to hydrodynamics problems', *Computers and Geotechnics*, 92, pp. 77–95. doi: 10.1016/j.compgeo.2017.07.024.

Markov, K. and Matsui, T. (2014) 'Music genre and emotion recognition using Gaussian processes', *IEEE Access*, 2(July), pp. 688–697. doi: 10.1109/ACCESS.2014.2333095.

Martínez, H. V., Coupard, D. and Girot, F. (2006) 'Constitutive model of the alloy 2117-T4 at low strain rates and temperatures', *Journal of Materials Processing Technology*, 173(3), pp. 252–259. doi: 10.1016/j.jmatprotec.2005.05.056.

Masoumi Khalilabad, M. *et al.* (2018) 'Effect of tool geometry and welding speed on mechanical properties of dissimilar AA2198–AA2024 FSWed joint', *Journal of Manufacturing Processes*, 34(June), pp. 86–95. doi: 10.1016/j.jmapro.2018.05.030.

Mathew, J. *et al.* (2018) 'Prediction of welding residual stresses using machine learning: Comparison between neural networks and neuro-fuzzy systems', *Applied Soft Computing Journal*, 70, pp. 131–146. doi: 10.1016/j.asoc.2018.05.017.

Mehta, K. *et al.* (2021) 'Investigation of exit-hole repairing on dissimilar aluminum-copper friction stir welded joints', *Journal of Materials Research and Technology*, 13, pp. 2180–2193. doi: 10.1016/j.jmrt.2021.06.019.

Mehta, K. P. *et al.* (2020) 'Repairing of exit-hole in dissimilar Al-Mg friction stir welding: Process and microstructural pattern', *Manufacturing Letters*, 23, pp. 67–70. doi: 10.1016/j.mfglet.2020.01.002.

Mehta, K. P. and Badheka, V. J. (2016) 'A review on dissimilar friction stir welding of copper to aluminum: Process, properties, and variants', *Materials and Manufacturing Processes*, 31(3), pp. 233–254. doi: 10.1080/10426914.2015.1025971.

Mehta, K. P. and Badheka, V. J. (2017) 'Hybrid approaches of assisted heating and cooling for friction stir welding of copper to aluminum joints', *Journal of Materials Processing Technology*, 239, pp. 336–345. doi: 10.1016/j.jmatprotec.2016.08.037.

Meng, X. *et al.* (2018) 'Improving friction stir weldability of Al/Mg alloys via ultrasonically diminishing pin adhesion', *Journal of Materials Science and Technology*, 34(10), pp. 1817–1822. doi: 10.1016/j.jmst.2018.02.022.

Meyghani, B., Awang, M. and Wu, C. S. (2020) 'Finite element modeling of friction stir welding (FSW) on a complex curved plate', *Journal of Advanced Joining Processes*, 1, p. 100007. doi: 10.1016/j.jajp.2020.100007.

Meyghani, B. and Wu, C. (2020) 'Progress in Thermomechanical Analysis of Friction Stir Welding', *Chinese Journal of Mechanical Engineering (English Edition)*, 33(1). doi: 10.1186/s10033-020-0434-7.

Mishra, D. *et al.* (2018) 'A review on sensor based monitoring and control of friction stir welding process and a roadmap to Industry 4.0', *Journal of Manufacturing Processes*. Elsevier, pp. 373–397. doi: 10.1016/j.jmapro.2018.10.016.

Mishra, D. *et al.* (2020) 'Real time monitoring and control of friction stir welding process using multiple sensors', *CIRP Journal of Manufacturing Science and Technology*, 30, pp. 1–11. doi: 10.1016/j.cirpj.2020.03.004.

Mishra, R. S., De, P. S. and Kumar, N. (2014) *Friction stir welding and processing: Science and engineering*, *Friction Stir Welding and Processing: Science and Engineering*. doi: 10.1007/978-3-319-07043-8.

Mishra, R. S. and Ma, Z. Y. (2005) 'Friction stir welding and processing', *Materials Science and Engineering R: Reports*, 50(1–2), pp. 1–78. doi: 10.1016/j.mser.2005.07.001.

Mohan, R., Jayadeep, U. B. and Manu, R. (2021) 'CFD modelling of ultra-high rotational speed micro friction stir welding', *Journal of Manufacturing Processes*, 64(March), pp. 1377–1386. doi: 10.1016/j.jmapro.2021.02.060.

Momeni, F. and Ni, J. (2020) 'A new model for predicting the thickness of intermetallic compounds in friction stir welding', *Journal of Manufacturing Processes*, 56(February), pp. 1331–1339. doi: 10.1016/j.jmapro.2020.04.028.

Moreira, P. M. G. P. *et al.* (2009) 'Mechanical and metallurgical characterization of friction stir welding joints of AA6061-T6 with AA6082-T6', *Materials and Design*, 30(1), pp. 180–187. doi: 10.1016/j.matdes.2008.04.042.

Morisada, Y., Imaizumi, T. and Fujii, H. (2015) 'Clarification of material flow and defect formation during friction stir welding', *Science and Technology of Welding and Joining*, 20(2), pp. 130–137. doi: 10.1179/1362171814Y.0000000266.

Morsi, K., McShane, H. B. and McLean, M. (2000) 'Processing defects in hot extrusion reaction synthesis', *Materials Science and Engineering A*, 290(1), pp. 39–45. doi: 10.1016/S0921-5093(00)00932-1.

Moura, A. E. *et al.* (2015) 'Non-destructive evaluation of weld discontinuity in steel tubes by gamma ray CT', *Nuclear Instruments and Methods in Physics Research, Section B: Beam Interactions with Materials*

and Atoms, 349, pp. 155–162. doi: 10.1016/j.nimb.2015.02.024.

Muhammad, N. A. *et al.* (2023) 'Unravelling the ultrasonic effect on residual stress and microstructure in dissimilar ultrasonic-assisted friction stir welding of Al/Mg alloys', *International Journal of Machine Tools and Manufacture*, 186(November 2022), p. 104004. doi: 10.1016/j.ijmachtools.2023.104004.

Mukunda, S. G. *et al.* (2023) 'Wear Performance Prediction of MWCNT-Reinforced AZ31 Composite Using Machine Learning Technique', *Journal of Bio- and Tribo-Corrosion*, 9(2), pp. 1–13. doi: 10.1007/s40735-023-00745-w.

Murillo-Marrodán, A., García, E. and Cortés, F. (2017) 'Friction modelling of a hot rolling process by means of the finite element method', *Lecture Notes in Engineering and Computer Science*, 2230, pp. 965–969.

Muthu, M. F. X. and Jayabalan, V. (2015) 'Tool travel speed effects on the microstructure of friction stir welded aluminum-copper joints', *Journal of Materials Processing Technology*, 217, pp. 105–113. doi: 10.1016/j.jmatprotec.2014.11.007.

Nandan, R. *et al.* (2006) 'Numerical modelling of 3D plastic flow and heat transfer during friction stir welding of stainless steel', *Science and Technology of Welding and Joining*, 11(5), pp. 526–537. doi: 10.1179/174329306X107692.

Nandan, R. *et al.* (2007) 'Three-dimensional heat and material flow during friction stir welding of mild steel', *Acta Materialia*, 55(3), pp. 883–895. doi: 10.1016/j.actamat.2006.09.009.

Nandan, R., DebRoy, T. and Bhadeshia, H. K. D. H. (2008) 'Recent advances in friction-stir welding - Process, weldment structure and properties', *Progress in Materials Science*, 53(6), pp. 980–1023. doi: 10.1016/j.pmatsci.2008.05.001.

Ni, Y., Fu, L. and Chen, H. Y. (2019) 'Effects of travel speed on mechanical properties of AA7075-T6 ultra-thin sheet joints fabricated by high rotational speed micro pinless friction stir welding', *Journal of Materials Processing Technology*, 265(June 2018), pp. 63–70. doi: 10.1016/j.jmatprotec.2018.10.006.

Nicholson, D. W. (2008) *Finite element analysis: Thermomechanics of solids*. CRC press.

Nie, L., Wu, Y. X. and Gong, H. (2020) 'Prediction of temperature and residual stress distributions in friction stir welding of aluminum alloy', *International Journal of Advanced Manufacturing Technology*, 106(7–8), pp. 3301–3310. doi: 10.1007/s00170-019-04826-4.

Nishi, T. *et al.* (2003) 'Evaluation of the heat leakage in the thermal diffusivity measurement of molten metals by a laser flash method', *International Journal of Thermophysics*, 24(6), pp. 1735–1751. doi: 10.1023/B:IJOT.0000004102.55688.c7.

Nishi, Tsuyoshi *et al.* (2003) 'Thermal conductivities of molten iron, cobalt, and nickel by laser flash method', *Metallurgical and Materials Transactions A: Physical Metallurgy and Materials Science*, 34(12), pp. 2801–2807. doi: 10.1007/s11661-003-0181-2.

Noh, W. F. (1963) *CEL: A time-dependent, two-space-dimensional, coupled Eulerian-Lagrange code*.

Noreika, A. and Tarvydas, P. (2007) 'Analysis of finite element method equation solvers', in *Proceedings of the International Conference on Information Technology Interfaces, ITI*, pp. 633–638. doi: 10.1109/ITI.2007.4283845.

Ogawa, D. *et al.* (2019) 'Residual stress measurement of Al/steel dissimilar friction stir weld', *Science and Technology of Welding and Joining*, 24(8), pp. 685–694. doi: 10.1080/13621718.2019.1588521.

Ohashi, R. *et al.* (2004) 'Friction stir welding apparatus'. Japan.

Olovsson, L., Simonsson, K. and Unosson, M. (2005) 'Selective mass scaling for explicit finite element analyses', *International Journal for Numerical Methods in Engineering*, 63(10), pp. 1436–1445.

Olovsson, L., Unosson, M. and Simonsson, K. (2004) 'Selective mass scaling for thin walled structures modeled with tri-linear solid elements', *Computational Mechanics*, 34(2), pp. 134–136. doi: 10.1007/s00466-004-0560-6.

Oosterkamp, A., Oosterkamp, L. D. and Nordeide, A. (2004) '"Kissing bond" phenomena in solid-state welds of aluminum alloys', *Welding Journal (Miami, Fla)*, 83(8), pp. 225-S.

Ouyang, J., Yarrapareddy, E. and Kovacevic, R. (2006) 'Microstructural evolution in the friction stir welded 6061 aluminum alloy (T6-temper condition) to copper', *Journal of Materials Processing Technology*, 172(1), pp. 110–122. doi: 10.1016/j.jmatprotec.2005.09.013.

Padhy, G. K., Wu, C. S. and Gao, S. (2018) 'Friction stir based welding and processing technologies - processes, parameters, microstructures and applications: A review', *Journal of Materials Science and Technology*, 34(1), pp. 1–38. doi: 10.1016/j.jmst.2017.11.029.

Padmanaban, G. and Balasubramanian, V. (2009) 'Selection of FSW tool pin profile, shoulder diameter and material for joining AZ31B magnesium alloy - An experimental approach', *Materials and Design*, 30(7), pp. 2647–2656. doi: 10.1016/j.matdes.2008.10.021.

Pankaj, P., Tiwari, A., Medhi, T., *et al.* (2022) 'Multi-species transport CFD simulation and

experimental verification for material flow properties in dissimilar friction stir welding', *Materials Today Communications*, 33(September), p. 104959. doi: 10.1016/j.mtcomm.2022.104959.

Pankaj, P., Tiwari, A., Dhara, L. N., *et al.* (2022) 'Multiphase CFD simulation and experimental investigation of friction stir welded high strength shipbuilding steel and aluminum alloy', *CIRP Journal of Manufacturing Science and Technology*, 39, pp. 37–69. doi: 10.1016/j.cirpj.2022.07.001.

Pantalé, O. (2005) 'Parallelization of an object-oriented FEM dynamics code: Influence of the strategies on the Speedup', *Advances in Engineering Software*, 36(6), pp. 361–373. doi: 10.1016/j.advengsoft.2005.01.003.

Park, S., Joo, Y. and Kang, M. (2020) 'Effect of backing plate materials in micro-friction stir butt welding of dissimilar aa6061-t6 and aa5052-h32 aluminum alloys', *Metals*, 10(7), pp. 1–9. doi: 10.3390/met10070933.

Pashazadeh, H. and Teimournezhad, J. (2014) 'Numerical investigation on the mechanical, thermal, metallurgical and material flow characteristics in friction stir welding of copper sheets with experimental verification', *Materials and Design*, 55, pp. 619–632. doi: 10.1016/j.matdes.2013.09.028.

Paulo, R. M. F. *et al.* (2017) 'Prediction of friction stir welding effects on AA2024-T3 plates and stiffened panels using a shell-based finite element model', *Thin-Walled Structures*, 120(August), pp. 297–306. doi: 10.1016/j.tws.2017.09.009.

Pei, X. and Dong, P. (2017) 'A selectively-coupled shear localization model for friction stir welding process window estimation', *International Journal of Machine Tools and Manufacture*, 123(August), pp. 89–104. doi: 10.1016/j.ijmachtools.2017.08.003.

Petit, C. *et al.* (2017) 'Two-scale study of the fracture of an aluminum foam by X-ray tomography and finite element modeling', *Materials and Design*, 120, pp. 117–127. doi: 10.1016/j.matdes.2017.02.009.

Du Plessis, A. and Rossouw, P. (2015) 'X-ray computed tomography of a titanium aerospace investment casting', *Case Studies in Nondestructive Testing and Evaluation*, 3, pp. 21–26. doi: 10.1016/j.csndt.2015.03.001.

Pourali, M. *et al.* (2017) 'Influence of welding parameters on intermetallic compounds formation in dissimilar steel/aluminum friction stir welds', *Journal of Alloys and Compounds*, 715, pp. 1–8. doi: 10.1016/j.jallcom.2017.04.272.

Prasanna, P., Rao, B. S. and Rao, G. K. M. (2010) 'Finite element modeling for maximum temperature in friction stir welding and its validation', *International Journal of Advanced Manufacturing Technology*, 51(9–12), pp. 925–933. doi: 10.1007/s00170-010-2693-4.

Prater, T. (2011) 'Solid-state joining of metal matrix composites: A survey of challenges and potential solutions', *Materials and Manufacturing Processes*, 26(4), pp. 636–648. doi: 10.1080/10426914.2010.492055.

Prior, A. M. (1994) 'Applications of implicit and explicit finite element techniques to metal forming', *Journal of Materials Processing Technology*, 45(1–4), pp. 649–656. doi: 10.1016/0924-0136(94)90413-8.

Ragab, M. *et al.* (2021) 'Friction stir welding of 1cr11ni2w2mov martensitic stainless steel: Numerical simulation based on coupled eulerian lagrangian approach supported with experimentalwork', *Applied Sciences (Switzerland)*, 11(7), pp. 1–18. doi: 10.3390/app11073049.

Ragu Nathan, S. *et al.* (2016) 'An investigation on metallurgical characteristics of tungsten based tool materials used in friction stir welding of naval grade high strength low alloy steels', *International Journal of Refractory Metals and Hard Materials*, 56, pp. 18–26. doi: 10.1016/j.ijrmhm.2015.12.005.

Raguvarun, K. *et al.* (2015) 'A study of internal structure in components made by additive manufacturing process using 3 D X-ray tomography', *AIP Conference Proceedings*, 1650, pp. 146–155. doi: 10.1063/1.4914604.

Rai, R. *et al.* (2011) 'Review: Friction stir welding tools', *Science and Technology of Welding and Joining*, 16(4), pp. 325–342. doi: 10.1179/1362171811Y.0000000023.

Rajesh, S. and Badheka, V. (2018) 'Influence of heat input/multiple passes and post weld heat treatment on strength/electrochemical characteristics of friction stir weld joint', *Materials and Manufacturing Processes*, 33(2), pp. 156–164. doi: 10.1080/10426914.2017.1279310.

Rajesh, S. and Badheka, V. J. (2018) 'Process parameters/material location affecting hooking in friction stir lap welding: Dissimilar aluminum alloys', *Materials and Manufacturing Processes*, 33(3), pp. 323–332. doi: 10.1080/10426914.2017.1317798.

Rana, P. K., Narayanan, R. G. and Kailas, S. V. (2021) 'Assessing the dwell time effect during friction stir spot welding of aluminum polyethylene multilayer sheets by experiments and numerical simulations', *International Journal of Advanced Manufacturing Technology*, 114(7–8), pp. 1953–1973. doi: 10.1007/s00170-021-06910-0.

Ranjan, R. *et al.* (2016) 'Classification and identification of surface defects in friction stir welding: An image processing approach', *Journal of Manufacturing Processes*, 22, pp. 237–253. doi:

10.1016/j.jmapro.2016.03.009.

Reimann, M. *et al.* (2017) 'Refilling termination hole in AA 2198–T851 by refill friction stir spot welding', *Journal of Materials Processing Technology*, 245, pp. 157–166. doi: 10.1016/j.jmatprotec.2017.02.025.

Riahi, M. and Nazari, H. (2011) 'Analysis of transient temperature and residual thermal stresses in friction stir welding of aluminum alloy 6061-T6 via numerical simulation', *International Journal of Advanced Manufacturing Technology*, 55(1–4), pp. 143–152. doi: 10.1007/s00170-010-3038-z.

Richter-Trummer, V. *et al.* (2012) 'Influence of the FSW clamping force on the final distortion and residual stress field', *Materials Science and Engineering A*, 538, pp. 81–88. doi: 10.1016/j.msea.2012.01.016.

Rosado, L. S. *et al.* (2010) 'Advanced technique for non-destructive testing of friction stir welding of metals', *Measurement: Journal of the International Measurement Confederation*, 43(8), pp. 1021–1030. doi: 10.1016/j.measurement.2010.02.006.

Rosado, L. S. *et al.* (2014) 'Eddy currents testing probe with magneto-resistive sensors and differential measurement', *Sensors and Actuators, A: Physical*, 212, pp. 58–67. doi: 10.1016/j.sna.2014.03.021.

Rui-dong, F. *et al.* (2011) 'Improvement of weld temperature distribution and mechanical properties of 7050 aluminum alloy butt joints by submerged friction stir welding', *Materials and Design*, 32(10), pp. 4825–4831. doi: 10.1016/j.matdes.2011.06.021.

Saanouni, K. *et al.* (2004) 'Numerical prediction of discontinuous central bursting in axisymmetric forward extrusion by continuum damage mechanics', *Computers and Structures*, 82(27), pp. 2309–2332. doi: 10.1016/j.compstruc.2004.05.018.

Saeid, T., Abdollah-zadeh, A. and Sazgari, B. (2010) 'Weldability and mechanical properties of dissimilar aluminum-copper lap joints made by friction stir welding', *Journal of Alloys and Compounds*, 490(1–2), pp. 652–655. doi: 10.1016/j.jallcom.2009.10.127.

Sahlot, P. and Arora, A. (2018) 'Numerical model for prediction of tool wear and worn-out pin profile during friction stir welding', *Wear*, 408–409(December 2017), pp. 96–107. doi: 10.1016/j.wear.2018.05.007.

Sahu, A. K. and Bag, S. (2021) 'Influence of current pulsation on solidification parameters during micro-plasma arc welding of thin sheet Alloy 718', *Welding in the World*, 65(12), pp. 2403–2419. doi: 10.1007/s40194-021-01191-3.

Sahu, P. K. *et al.* (2016) 'Influence of plate position, tool offset and tool rotational speed on mechanical properties and microstructures of dissimilar Al/Cu friction stir welding joints', *Journal of Materials Processing Technology*, 235, pp. 55–67. doi: 10.1016/j.jmatprotec.2016.04.014.

Sahu, P. K., Pal, S. and Pal, S. K. (2017) 'Al/Cu Dissimilar Friction Stir Welding with Ni, Ti, and Zn Foil as the Interlayer for Flow Control, Enhancing Mechanical and Metallurgical Properties', *Metallurgical and Materials Transactions A: Physical Metallurgy and Materials Science*, 48(7), pp. 3300–3317. doi: 10.1007/s11661-017-4093-y.

Salih, O. S., Ou, H. and Sun, W. (2022) 'Heat generation, plastic deformation and residual stresses in friction stir welding of aluminium alloy', *International Journal of Mechanical Sciences*, 238(October 2022), p. 107827. doi: 10.1016/j.ijmecsci.2022.107827.

Sandeep, R. and Natarajan, A. (2022) 'Application of machine learning approaches to predict joint strength of friction stir welded aluminium alloy 7475 and PPS polymer hybrid joint', *Proceedings of the Institution of Mechanical Engineers, Part C: Journal of Mechanical Engineering Science*, 236(16), pp. 9003–9011. doi: 10.1177/09544062221090082.

Santiago, D. H. *et al.* (2004) 'Numerical modeling of welded joints by the "Friction Stir Welding" process', *Materials Research*, 7(4), pp. 569–574. doi: 10.1590/s1516-14392004000400010.

Santos, M. J. and Santos, J. B. (2010) 'Lamb waves technique applied to the characterization of defects in friction stir welding of aluminum plates: Comparison with x-ray and ultrasonic C-scan', *Journal of Testing and Evaluation*, 38(5). doi: 10.1520/jte102397.

Santos, T. G., Miranda, R. M. and Vilaça, P. (2014) 'Friction Stir Welding assisted by electrical Joule effect', *Journal of Materials Processing Technology*, 214(10), pp. 2127–2133. doi: 10.1016/j.jmatprotec.2014.03.012.

de Saracibar, C. A. *et al.* (2014) 'Computational Modeling and Sub-Grid Scale Stabilization of Incompressibility and Convection in the Numerical Simulation of Friction Stir Welding Processes', *Archives of Computational Methods in Engineering*, 21(1), pp. 3–37. doi: 10.1007/s11831-014-9094-z.

De Saracibar, C. A. (2019) 'Challenges to be tackled in the computational modeling and numerical simulation of FSW processes', *Metals*, 9(5). doi: 10.3390/met9050573.

Saravanan, V. *et al.* (2016) 'Effect of shoulder diameter to pin diameter ratio on microstructure and mechanical properties of dissimilar friction stir welded AA2024-T6 and AA7075-T6 aluminum alloy joints', *International Journal of Advanced Manufacturing Technology*, 87(9–12), pp. 3637–3645. doi:

10.1007/s00170-016-8695-0.

Sato, Y. S. *et al.* (2004) 'FIB-assisted TEM study of an oxide array in the root of a friction stir welded aluminium alloy', *Scripta Materialia*, 50(3), pp. 365–369. doi: 10.1016/j.scriptamat.2003.10.008.

Sato, Y. S. *et al.* (2005) 'Characteristics of the kissing-bond in friction stir welded Al alloy 1050', *Materials Science and Engineering A*, 405(1–2), pp. 333–338. doi: 10.1016/j.msea.2005.06.008.

Schmidt, H. B. and Hattel, J. H. (2008) 'Thermal modelling of friction stir welding', *Scripta Materialia*, 58(5), pp. 332–337. doi: 10.1016/j.scriptamat.2007.10.008.

Schmidt, H. and Hattel, J. (2005) 'A local model for the thermomechanical conditions in friction stir welding', *Modelling and Simulation in Materials Science and Engineering*, 13(1), pp. 77–93. doi: 10.1088/0965-0393/13/1/006.

Scialpi, A. *et al.* (2008) 'Mechanical analysis of ultra-thin friction stir welding joined sheets with dissimilar and similar materials', *Materials and Design*, 29(5), pp. 928–936. doi: 10.1016/j.matdes.2007.04.006.

Scialpi, A., De Filippis, L. A. C. and Cavaliere, P. (2007) 'Influence of shoulder geometry on microstructure and mechanical properties of friction stir welded 6082 aluminium alloy', *Materials and Design*, 28(4), pp. 1124–1129. doi: 10.1016/j.matdes.2006.01.031.

Sedmak, A. *et al.* (2022) 'The effects of welded clips on fatigue crack growth in AA6156 T6 panels', *International Journal of Fatigue*, 165(May 2022). doi: 10.1016/j.ijfatigue.2022.107162.

Sen, M. and Puri, A. B. (2022) 'Formation of intermetallic compounds (IMCs) in FSW of aluminum and magnesium alloys (Al/Mg alloys) − A review', *Materials Today Communications*, 33(November), p. 105017. doi: 10.1016/j.mtcomm.2022.105017.

Senthil, S. M., Nathan, S. R. and Parameshwaran, R. (2021) 'Experimental investigation on joining process of aluminium alloy 6063-T6 pipes using hybrid friction stir welding', *Journal of the Brazilian Society of Mechanical Sciences and Engineering*, 43(7), pp. 1–9. doi: 10.1007/s40430-021-03054-w.

Shah, F. *et al.* (2022) 'Mechanical properties and weld characteristics of friction stir welding of thermoplastics using heat-assisted tool', *Welding in the World*, (0123456789). doi: 10.1007/s40194-022-01385-3.

Shankar, S. *et al.* (2019) 'Joint strength evaluation of friction stir welded Al-Cu dissimilar alloys', *Measurement: Journal of the International Measurement Confederation*, 146, pp. 892–902. doi: 10.1016/j.measurement.2019.07.019.

Shen, Z. *et al.* (2015) 'Interfacial microstructure and properties of copper clad steel produced using friction stir welding versus gas metal arc welding', *Materials Characterization*, 104, pp. 1–9. doi: 10.1016/j.matchar.2015.02.022.

Sheppard, T. and Jackson, A. (1997) 'Constitutive equations for use in prediction of flow stress during extrusion of aluminium alloys', *Materials Science and Technology*, 13(3), pp. 203–209. doi: 10.1179/mst.1997.13.3.203.

Sheppard, T. and Wright, D. S. (1979) 'Determination of flovv stress: Part 1 constitutive equation for aluminium alloys at elevated temperatures', *Metals Technology*, 6(June), pp. 215–223.

Shi, Q. Y. *et al.* (2008) 'Experimental study on distortion of Al-6013 plate after friction stir welding', *Science and Technology of Welding and Joining*, 13(5), pp. 472–478. doi: 10.1179/174329308X341924.

Siddiquee, A. N. and Pandey, S. (2014) 'Experimental investigation on deformation and wear of WC tool during friction stir welding (FSW) of stainless steel', *International Journal of Advanced Manufacturing Technology*, 73(1–4), pp. 479–486. doi: 10.1007/s00170-014-5846-z.

Simar, A. *et al.* (2012) 'Integrated modeling of friction stir welding of 6xxx series Al alloys: Process, microstructure and properties', *Progress in Materials Science*, 57(1), pp. 95–183. doi: 10.1016/j.pmatsci.2011.05.003.

Sinclair, P. C. *et al.* (2010) 'Heated friction stir welding: An experimental and theoretical investigation into how preheating influences process forces', *Materials and Manufacturing Processes*, 25(11), pp. 1283–1291. doi: 10.1080/10426914.2010.496122.

Singarapu, U., Adepu, K. and Arumalle, S. R. (2015) 'Influence of tool material and rotational speed on mechanical properties of friction stir welded AZ31B magnesium alloy', *Journal of Magnesium and Alloys*, 3(4), pp. 335–344. doi: 10.1016/j.jma.2015.10.001.

Singh, A. K. *et al.* (2019) 'Heat transfer modeling of dissimilar FSW of Al 6061/AZ31 using experimentally measured thermo-physical properties', *International Journal of Advanced Manufacturing Technology*, 105(1–4), pp. 771–783. doi: 10.1007/s00170-019-04276-y.

Singh, K., Singh, G. and Singh, H. (2018) 'Review on friction stir welding of magnesium alloys', *Journal of Magnesium and Alloys*, 6(4), pp. 399–416. doi: 10.1016/j.jma.2018.06.001.

Singh, V. P. *et al.* (2019) 'Parametric effect on dissimilar friction stir welded steel-magnesium alloys joints: a review', *Science and Technology of Welding and Joining*, 24(8), pp. 653–684. doi: 10.1080/13621718.2019.1567031.

Singh, V. P. *et al.* (2020) 'Recent research progress in solid state friction-stir welding of aluminium–magnesium alloys: A critical review', *Journal of Materials Research and Technology*, 9(3), pp. 6217–6256. doi: 10.1016/j.jmrt.2020.01.008.

Sinha, P. *et al.* (2008) 'Condition monitoring of first mode of metal transfer in friction stir welding by image processing techniques', *International Journal of Advanced Manufacturing Technology*, 36(5–6), pp. 484–489. doi: 10.1007/s00170-006-0854-2.

Sinha, P., Muthukumaran, S. and Mukherjee, S. K. (2008) 'Analysis of first mode of metal transfer in friction stir welded plates by image processing technique', *Journal of Materials Processing Technology*, 197(1–3), pp. 17–21. doi: 10.1016/j.jmatprotec.2007.06.013.

Skrzat, A. (2012) 'Application of coupled Eulerian-Lagrangian approach in metal forming simulations', *Scientific Letters of Rzeszow University of Technology - Mechanics*, 84(4/2012), pp. 25–35. doi: 10.7862/rm.2012.9.

Somasekharan, A. C. and Murr, L. E. (2004) 'Microstructures in friction-stir welded dissimilar magnesium alloys and magnesium alloys to 6061-T6 aluminum alloy', *Materials Characterization*, 52(1), pp. 49–64. doi: 10.1016/j.matchar.2004.03.005.

Stolarska, M. and Chopp, D. L. (2001) 'Modeling thermal fatigue cracking in integrated circuits by level sets and the extended finite element method', *International Journal of Engineering Science*, 51, pp. 943–960. doi: 10.1016/S0020-7225(03)00217-9.

Sudhagar, S., Sakthivel, M. and Ajith Arul Daniel, S. (2020) 'Application of image processing to radiographic image for quantitative assessment of friction stir welding quality of aluminium 2024 alloy', *Measurement: Journal of the International Measurement Confederation*, 152, p. 107294. doi: 10.1016/j.measurement.2019.107294.

Sun, G. *et al.* (2017) 'Fatigue modeling and life prediction for friction stir welded joint based on microstructure and mechanical characterization', *International Journal of Fatigue*, 98(December), pp. 131–141. doi: 10.1016/j.ijfatigue.2017.01.025.

Sun, Z. and Wu, C. S. (2018) 'A numerical model of pin thread effect on material flow and heat generation in shear layer during friction stir welding', *Journal of Manufacturing Processes*, 36(June), pp. 10–21. doi: 10.1016/j.jmapro.2018.09.021.

Systèmes, D. (2007) *Abaqus analysis user's manual*, *Simulia Corp. Providence, RI, USA*.

Tabatabaeipour, M. *et al.* (2016) 'Non-destructive ultrasonic examination of root defects in friction stir welded butt-joints', *NDT and E International*, 80, pp. 23–34. doi: 10.1016/j.ndteint.2016.02.007.

Tan, C. W. *et al.* (2013) 'Microstructural evolution and mechanical properties of dissimilar Al-Cu joints produced by friction stir welding', *Materials and Design*, 51, pp. 466–473. doi: 10.1016/j.matdes.2013.04.056.

Tan, M., Wu, C. and Shi, L. (2023) 'Formation Mechanism of Thicker Intermetallic Compounds in Friction Stir Weld Joints of Dissimilar AA2024 / AZ31B Alloys', *Materials*, 16(1), p. 51.

Tang, J. *et al.* (2020) 'Parallelized implementation of the finite particle method for explicit dynamics in GPU', *CMES - Computer Modeling in Engineering and Sciences*, 122(1), pp. 5–31. doi: 10.32604/cmes.2020.08104.

Tartakovsky, A. *et al.* (2006) 'Modeling of Friction Stir Welding (FSW) process with Smooth Particle Hydrodynamics (SPH)', *SAE Technical Papers*, (724). doi: 10.4271/2006-01-1394.

Tello, K. E., Gerlich, A. P. and Mendez, P. F. (2010) 'Constants for hot deformation constitutive models for recent experimental data', *Science and Technology of Welding and Joining*, 15(3), pp. 260–266. doi: 10.1179/136217110X12665778348380.

Testo.com (no date) *testo 868 - Thermal Imager Instruction manual*.

Thakur, A., Sharma, V. and Bhadauria, S. S. (2023) 'Improving tensile properties by varying the welding conditions of the passes of the double-sided friction stir welding of AZ31B magnesium alloy', *Materials Today Communications*, 34(November 2022), p. 105406. doi: 10.1016/j.mtcomm.2023.105406.

Thomä, M. *et al.* (2018) 'Ultrasound enhanced friction stir welding of aluminum and steel: Process and properties of EN AW 6061/DC04-Joints', *Journal of Materials Science and Technology*, 34(1), pp. 163–172. doi: 10.1016/j.jmst.2017.10.022.

Thomas, W.M.; Nicholas, E.D.; Needham, J. C.; Murch, M.G.; Templesmith, P.; Dawes, C. J. . (1991) 'Friction stir welding', *International patent application no. PCT/GB92102203 and Great Britain patent application*, 9125978.

Thomas, W. M. and Nicholas, E. D. (1997) 'Friction stir welding for the transportation industries', *Materials and Design*, 18(4–6), pp. 269–273. doi: 10.1016/s0261-3069(97)00062-9.

Tongne, A. *et al.* (2015) 'Banded structures in friction stir welded Al alloys', *Journal of Materials Processing Technology*, 221, pp. 269–278. doi: 10.1016/j.jmatprotec.2015.02.020.

Tutum, C. C. and Hattel, J. H. (2010) 'Optimisation of process parameters in friction stir welding based on residual stress analysis: A feasibility study', *Science and Technology of Welding and Joining*, 15(5),

pp. 369–377. doi: 10.1179/136217110X12707333260455.

Tutunchilar, S. *et al.* (2012) 'Simulation of material flow in friction stir processing of a cast Al-Si alloy', *Materials and Design*, 40, pp. 415–426. doi: 10.1016/j.matdes.2012.04.001.

Ulysse, P. (2002) 'Three-dimensional modeling of the friction stir-welding process', *International Journal of Machine Tools and Manufacture*, 42(14), pp. 1549–1557. doi: 10.1016/S0890-6955(02)00114-1.

Vakhrushev, A. *et al.* (2022) 'Norton-Hoff model for deformation of growing solid shell of thin slab casting in funnel-shape mold', *Journal of Iron and Steel Research International*, 29(1), pp. 88–102. doi: 10.1007/s42243-021-00734-8.

Valvi, S. R. *et al.* (2016) 'Prediction of microstructural features and forming of friction stir welded sheets using cellular automata finite element (CAFE) approach', *International Journal of Material Forming*, 9(1), pp. 115–129. doi: 10.1007/s12289-015-1216-0.

Verma, M. and Saha, P. (2023) 'Effect of micro-grooves featured tool and their depths on dissimilar micro-friction stir welding (μFSW) of aluminum alloys: A study of process responses and weld characteristics', *Materials Characterization*, 196(September 2022), p. 112614. doi: 10.1016/j.matchar.2022.112614.

Verma, S. *et al.* (2021) 'Prediction of tensile behavior of FS welded AA7039 using machine learning', *Materials Today Communications*, 26(December 2020), p. 101933. doi: 10.1016/j.mtcomm.2020.101933.

Verma, S., Gupta, M. and Misra, J. P. (2018) 'Performance evaluation of friction stir welding using machine learning approaches', *MethodsX*, 5(September), pp. 1048–1058. doi: 10.1016/j.mex.2018.09.002.

Verma, S., Misra, J. P. and Popli, D. (2022) 'Modeling of friction stir welding of aviation grade aluminium alloy using machine learning approaches', *International Journal of Modelling and Simulation*, 42(1), pp. 1–8. doi: 10.1080/02286203.2020.1803605.

Vijendra, B. and Sharma, A. (2015) 'Induction heated tool assisted friction-stir welding (i-FSW): A novel hybrid process for joining of thermoplastics', *Journal of Manufacturing Processes*, 20, pp. 234–244. doi: 10.1016/j.jmapro.2015.07.005.

Wan, L. *et al.* (2014) 'Mechanical Properties and Microstructure of 6082-T6 Aluminum Alloy Joints by Self-support Friction Stir Welding', *Journal of Materials Science and Technology*, 30(12), pp. 1243–1250. doi: 10.1016/j.jmst.2014.04.009.

Wang, H. *et al.* (2022) 'Effect of microstructure inhomogeneity on creep behavior of friction stir welding 7B50-T7451 aluminum alloy thick plate joint', *Materials Characterization*, 193(June), p. 112292. doi: 10.1016/j.matchar.2022.112292.

Wang, T. *et al.* (2019) 'Effect of reactive alloy elements on friction stir welded butt joints of metallurgically immiscible magnesium alloys and steel', *Journal of Manufacturing Processes*, 39(November 2018), pp. 138–145. doi: 10.1016/j.jmapro.2019.02.009.

Wang, X. *et al.* (2023) 'Prediction of M–A Constituents and Impact Toughness in Stir Zone of X80 Pipeline Steel Friction Stir Welds', *Acta Metallurgica Sinica (English Letters)*, 36(4), pp. 573–585. doi: 10.1007/s40195-022-01495-3.

Wang, Yubao *et al.* (2020) 'The identification of improved Johnson-Cook constitutive model in a wide range of temperature and its application in predicting FLCs of Al-Mg-Li sheet', *Journal of Materials Research and Technology*, 9(3), pp. 3782–3795. doi: 10.1016/j.jmrt.2020.02.005.

Wang, Z. (2014) 'Monitoring of GMAW weld pool from the reflected laser lines for real-time control', *IEEE Transactions on Industrial Informatics*, 10(4), pp. 2073–2083. doi: 10.1109/TII.2014.2349360.

Wang, Z. Bin *et al.* (2016) 'An overview of smoothed particle hydrodynamics for simulating multiphase flow', *Applied Mathematical Modelling*, 40(23–24), pp. 9625–9655. doi: 10.1016/j.apm.2016.06.030.

Watanabe, T., Takayama, H. and Yanagisawa, A. (2006) 'Joining of aluminum alloy to steel by friction stir welding', *Journal of Materials Processing Technology*, 178(1–3), pp. 342–349. doi: 10.1016/j.jmatprotec.2006.04.117.

Wen, Q., Li, W. Y., Wang, W. B., *et al.* (2019) 'Experimental and numerical investigations of bonding interface behavior in stationary shoulder friction stir lap welding', *Journal of Materials Science and Technology*, 35(1), pp. 192–200. doi: 10.1016/j.jmst.2018.09.028.

Wen, Q., Li, W. Y., Gao, Y. J., *et al.* (2019) 'Numerical simulation and experimental investigation of band patterns in bobbin tool friction stir welding of aluminum alloy', *International Journal of Advanced Manufacturing Technology*, 100(9–12), pp. 2679–2687. doi: 10.1007/s00170-018-2750-y.

Withers, P. J. *et al.* (2008) 'Recent advances in residual stress measurement', *International Journal of Pressure Vessels and Piping*, 85(3), pp. 118–127. doi: 10.1016/j.ijpvp.2007.10.007.

Withers, P. J. and Bhadeshia, H. K. D. H. (2001a) 'Residual stress part 1 - Measurement techniques', *Materials Science and Technology*, 17(4), pp. 355–365. doi: 10.1179/026708301101509980.

Withers, P. J. and Bhadeshia, H. K. D. H. (2001b) 'Residual stress part 2 - Nature and origins', *Materials Science and Technology*, 17(4), pp. 366–375. doi: 10.1179/026708301101510087.

Woo, W. *et al.* (2006) 'Texture analysis of a friction stir processed 6061-T6 aluminum alloy using neutron diffraction', *Acta Materialia*, 54(15), pp. 3871–3882. doi: 10.1016/j.actamat.2006.04.018.

Woo, W. *et al.* (2008) 'Microstructure, texture and residual stress in a friction-stir-processed AZ31B magnesium alloy', *Acta Materialia*, 56(8), pp. 1701–1711. doi: 10.1016/j.actamat.2007.12.020.

Woo, W. *et al.* (2011) 'Neutron diffraction measurements of residual stresses in friction stir welding: A review', *Science and Technology of Welding and Joining*, 16(1), pp. 23–32. doi: 10.1179/136217110X12731414739916.

Woo, W. and Choo, H. (2011) 'Softening behaviour of friction stir welded Al 6061-T6 and Mg AZ31B alloys', *Science and Technology of Welding and Joining*, 16(3), pp. 267–272. doi: 10.1179/1362171811Y.0000000016.

Wu, Q. *et al.* (2020) 'Residual stresses in wire-arc additive manufacturing – Hierarchy of influential variables', *Additive Manufacturing*, 35(May). doi: 10.1016/j.addma.2020.101355.

Xia, H. *et al.* (2022) 'In situ SEM study on tensile fractured behavior of Al/steel laser welding-brazing interface', *Materials and Design*, 224, p. 111320. doi: 10.1016/j.matdes.2022.111320.

Yaduwanshi, D. K., Bag, S. and Pal, S. (2014) 'Effect of Preheating in Hybrid Friction Stir Welding of Aluminum Alloy', *Journal of Materials Engineering and Performance*, 23(10), pp. 3794–3803. doi: 10.1007/s11665-014-1170-x.

Yaduwanshi, D. K., Bag, S. and Pal, S. (2015) 'Hybrid Friction Stir Welding of Similar and Dissimilar Materials', in *Advances in Material Forming and Joining*, pp. 29–47. doi: 10.1007/978-81-322-2355-9_17.

Yaduwanshi, D. K., Bag, S. and Pal, S. (2016) 'Numerical modeling and experimental investigation on plasma-assisted hybrid friction stir welding of dissimilar materials', *Materials and Design*, 92, pp. 166–183. doi: 10.1016/j.matdes.2015.12.039.

Yaduwanshi, D. K., Bag, S. and Pal, S. (2018) 'On the effect of tool offset in hybrid-FSW of copper-aluminium alloy', *Materials and Manufacturing Processes*, 33(3), pp. 277–287. doi: 10.1080/10426914.2017.1279309.

Yan, D. *et al.* (2011) 'Predicting residual distortion of aluminum alloy stiffened sheet after friction stir welding by numerical simulation', *Materials and Design*, 32(4), pp. 2284–2291. doi: 10.1016/j.matdes.2010.11.032.

Yang, C. *et al.* (2020) 'Microstructure and mechanical properties of double-side friction stir welded 6082Al ultra-thick plates', *Journal of Materials Science and Technology*, 41, pp. 105–116. doi: 10.1016/j.jmst.2019.10.005.

Yang, C., Wu, C. S. and Gao, S. (2022) 'Computational fluid dynamics model of AA6061 friction stir welding with considering mechanical anisotropy', *Materials Today Communications*, 32(May), p. 103991. doi: 10.1016/j.mtcomm.2022.103991.

Yang, C., Wu, C. and Zhao, J. (2021) 'Numerical Prediction of Intermetallic Compounds Thickness in Friction Stir Welding of Dissimilar Aluminum/Magnesium Alloys', *Acta Metallurgica Sinica (English Letters)*, 34(10), pp. 1375–1385. doi: 10.1007/s40195-021-01238-w.

Yao, Z. *et al.* (2012) 'Acoustic softening and residual hardening in aluminum: Modeling and experiments', *International Journal of Plasticity*, 39, pp. 75–87. doi: 10.1016/j.ijplas.2012.06.003.

Yau, Y. H. *et al.* (2013) 'Temperature distribution study during the friction stir welding process of Al2024-T3 aluminum alloy', *International Journal of Minerals, Metallurgy and Materials*, 20(8), pp. 779–787. doi: 10.1007/s12613-013-0796-2.

Yazdipour, A. and Heidarzadeh, A. (2016a) 'Dissimilar butt friction stir welding of Al 5083-H321 and 316L stainless steel alloys', *International Journal of Advanced Manufacturing Technology*, 87(9–12), pp. 3105–3112. doi: 10.1007/s00170-016-8705-2.

Yazdipour, A. and Heidarzadeh, A. (2016b) 'Effect of friction stir welding on microstructure and mechanical properties of dissimilar Al 5083-H321 and 316L stainless steel alloy joints', *Journal of Alloys and Compounds*, 680, pp. 595–603. doi: 10.1016/j.jallcom.2016.03.307.

Ye, P. *et al.* (2023) 'Texture and High Yield Strength of Rapidly Solidified AZ31 Magnesium Alloy Extruded at 250 °C', *Materials*, 16(8). doi: 10.3390/ma16082946.

You, J. *et al.* (2023) 'Improving the microstructure and mechanical properties of Al-Cu dissimilar joints by ultrasonic dynamic-stationary shoulder friction stir welding', *Journal of Materials Processing Technology*, 311(October 2022), p. 117812. doi: 10.1016/j.jmatprotec.2022.117812.

Yu, M. *et al.* (2012) 'Modelling of entire friction stir welding process by explicit finite element method', *Materials Science and Technology (United Kingdom)*, 28(7), pp. 812–817. doi: 10.1179/1743284711Y.0000000087.

Zamani, S. M. M. *et al.* (2021) 'Friction stir welding of Al-SiC composite sheets: a numerical

simulation of residual stresses', *The International Journal of Advanced Manufacturing Technology*, 116, pp. 3717–3729. doi: 10.1016/j.matdes.2015.07.071.

Zandsalimi, S., Heidarzadeh, A. and Saeid, T. (2019) 'Dissimilar friction-stir welding of 430 stainless steel and 6061 aluminum alloy: Microstructure and mechanical properties of the joints', *Proceedings of the Institution of Mechanical Engineers, Part L: Journal of Materials: Design and Applications*, 233(9), pp. 1791–1801. doi: 10.1177/1464420718789447.

Zapata, J., Toro, M. and López, D. (2016) 'Residual stresses in friction stir dissimilar welding of aluminum alloys', *Journal of Materials Processing Technology*, 229(2016), pp. 121–127. doi: 10.1016/j.jmatprotec.2015.08.026.

Zeng, X. H., Xue, P., Wang, D., Ni, D. R., Xiao, B. L. and Ma, Z. Y. (2018) 'Effect of Processing Parameters on Plastic Flow and Defect Formation in Friction-Stir-Welded Aluminum Alloy', *Metallurgical and Materials Transactions A: Physical Metallurgy and Materials Science*, 49(7), pp. 2673–2683. doi: 10.1007/s11661-018-4615-2.

Zeng, X. H., Xue, P., Wang, D., Ni, D. R., Xiao, B. L., Wang, K. S., *et al.* (2018) 'Material flow and void defect formation in friction stir welding of aluminium alloys', *Science and Technology of Welding and Joining*, 23(8), pp. 677–686. doi: 10.1080/13621718.2018.1471844.

Zhai, M., Wu, C. S. and Su, H. (2020) 'Influence of tool tilt angle on heat transfer and material flow in friction stir welding', *Journal of Manufacturing Processes*, 59(September), pp. 98–112. doi: 10.1016/j.jmapro.2020.09.038.

Zhang, C. *et al.* (2012) 'Modelization and comparison of Norton-Hoff and Arrhenius constitutive laws to predict hot tensile behavior of Ti-6Al-4V alloy', *Transactions of Nonferrous Metals Society of China (English Edition)*, 22(SUPPL.2), pp. s457–s464. doi: 10.1016/S1003-6326(12)61746-4.

Zhang, C. *et al.* (2019) 'A study on microstructure and mechanical properties of micro friction stirwelded ultra-thin al-1060 sheets by the shoulderless tool', *Metals*, 9(5). doi: 10.3390/met9050507.

Zhang, H. W., Zhang, Z. and Chen, J. T. (2007) '3D modeling of material flow in friction stir welding under different process parameters', *Journal of Materials Processing Technology*, 183(1), pp. 62–70.

Zhang, L. *et al.* (2011) 'Friction Stir Welding of Al Alloy Thin Plate by Rotational Tool without Pin', *Journal of Materials Science and Technology*, 27(7), pp. 647–652. doi: 10.1016/S1005-0302(11)60120-5.

Zhang, Z. *et al.* (2011) 'Coupled thermo-mechanical model based comparison of friction stir welding processes of AA2024-T3 in different thicknesses', *Journal of Materials Science*, 46(17), pp. 5815–5821. doi: 10.1007/s10853-011-5537-1.

Zhang, Z. and Chen, J. T. (2008) 'The simulation of material behaviors in friction stir welding process by using rate-dependent constitutive model', *Journal of Materials Science*, 43(1), pp. 222–232. doi: 10.1007/s10853-007-2129-1.

Zhang, Z. and Zhang, H. W. (2009) 'Numerical studies on controlling of process parameters in friction stir welding', *Journal of Materials Processing Technology*, 209(1), pp. 241–270. doi: 10.1016/j.jmatprotec.2008.01.044.

Zhao, C. and Liu, X. (2020) 'Computational Analysis on Weld Formation Mechanism during Self-Reacting Friction Stir Welding', *Journal of Manufacturing Science and Engineering*, pp. 1–15. doi: 10.1115/1.4048856.

Zhao, C. and Liu, X. (2021) 'An alternative pressure-dependent velocity boundary condition for modeling self-reacting friction stir welding', *International Journal of Advanced Manufacturing Technology*, 117(5–6), pp. 1601–1613. doi: 10.1007/s00170-021-07589-z.

Zhao, J. *et al.* (2023) 'Evolution of microstructures and intermetallic compounds at bonding interface in friction stir welding of dissimilar Al/Mg alloys with/without ultrasonic assistance', *Journal of Materials Science & Technology*, 139, pp. 31–46. doi: 10.1016/j.jmst.2022.08.025.

Zhao, Y. *et al.* (2016) 'Influence of cooling conditions on joint properties and microstructures of aluminum and magnesium dissimilar alloys by friction stir welding', *International Journal of Advanced Manufacturing Technology*, 83(1–4), pp. 673–679. doi: 10.1007/s00170-015-7624-y.

Zhao, Y. *et al.* (2019) 'Investigation of void formation in friction stir welding of 7N01 aluminum alloy', *Journal of Manufacturing Processes*, 37(September 2018), pp. 139–149. doi: 10.1016/j.jmapro.2018.11.019.

Zheng, Q. *et al.* (2017) 'Effect of plunge depth on microstructure and mechanical properties of FSW lap joint between aluminum alloy and nickel-base alloy', *Journal of Alloys and Compounds*, 695, pp. 952–961. doi: 10.1016/j.jallcom.2016.10.213.

Zheng, S. *et al.* (2017) 'Non-destructive investigation of aluminum alloy hemmed joints using neutron radiography and X-ray computed tomography', *NDT and E International*, 91(March), pp. 32–35. doi: 10.1016/j.ndteint.2017.06.004.

Zhou, C., Yang, X. and Luan, G. (2006) 'Effect of kissing bond on fatigue behavior of friction stir

welds on Al 5083 alloy', *Journal of Materials Science*, 41(10), pp. 2771–2777. doi: 10.1007/s10853-006-6337-x.

Zhou, L. *et al.* (2012) 'New technique of self-refilling friction stir welding to repair keyhole', *Science and Technology of Welding and Joining*, 17(8), pp. 649–655. doi: 10.1179/1362171812Y.0000000058.

Zhu, Y. *et al.* (2016) 'Simulation of material plastic flow driven by non-uniform friction force during friction stir welding and related defect prediction', *Materials and Design*, 108, pp. 400–410. doi: 10.1016/j.matdes.2016.06.119.

Zhu, Z. *et al.* (2017) 'A finite element model to simulate defect formation during friction stir welding', *Metals*, 7(7), p. 256.

Zina, N. *et al.* (2019) 'Numerical Simulation on the Effect of Friction Stir Welding Parameters on the Peak Temperature, Von Mises Stress, and Residual Stresses of 6061-T6 Aluminum Alloy', *Journal of Failure Analysis and Prevention*, 19(6), pp. 1698–1719. doi: 10.1007/s11668-019-00766-z.

Zuo, L. *et al.* (2022) 'Investigation on tool wear in friction stir welding of SiCp/Al composites', *Wear*, 498–499(February), p. 204331. doi: 10.1016/j.wear.2022.204331.

List of Publications out of present work

International Journals

1. Das, D., Bag, S., Pal, S. and Sharma, A., (2023), "Material Defects in Friction Stir Welding through Thermo–Mechanical Simulation: Dissimilar Materials with Tool Wear Consideration" **Materials (MDPI)**, 16(1), 301.

2. Das, D., Bag, S., and Pal, S. (2023), "Tailoring mass scaling approach for the prediction of defects in friction stir welding using coupled Eulerian-Lagrangian approach" **Materials Today Communications** (Elsevier), 35, 105646.

3. Das, D., Bag, S., Pal, S., and Amin, M. R., (2022), "A finite element model for the prediction of chip formation and surface morphology in friction stir welding process" **Journal of Manufacturing Science and Engineering** (ASME), 144(4), 041015.

4. Das, D., Bag, S., & Pal, S. (2021). "A finite element model for surface and volumetric defects in the FSW process using a coupled Eulerian–Lagrangian approach". **Science and Technology of Welding and Joining** (Taylor & Francis), 26(5), 412-419.

5. Das, D., Bag, S., and Pal, S., (2021), "Investigating surface defect by tool-material interaction in friction stir welding using coupled Eulerian-Lagrangian approach". **Manufacturing Letters** (Elsevier), 30, 23-26.

6. Das, D., Bag, S., and Pal, S., "A physics-informed machine-learning model of dissimilar friction stir welding to tailor residual stress using CEL approach" **Journal of Materials Engineering and Performance** (*Under Review*).

7. Kumar, A. **Das, D.,** Raj, N. D., Bag, S., Srivastava, V. C., (2023), "Comparison of machine learning performance for the prediction of melting efficiency and bead geometry in wire arc additive manufacturing process." **Archives of Metallurgy and Materials (PAS)** *(Accepted)*.

8. Kumar, B., Sahu, A. K., **Das, D.,** & Bag, S., (2023), "Probing the thermal stability and microstructural-mechanical behaviour of laser-welded 17-4 PH stainless steel." **Archives of Metallurgy and Materials (PAS)** *(Accepted)*.

9. Das, D., Bag, S., and Pal, S., "Phenomenological model subtleties for Defect Prediction in Friction Stir Welding." (*Under Preparation*).

Book chapters

10. Das, D., Bag, S., and Pal, S., (2023), "A phenomenological model for the prediction of defects in similar and dissimilar friction stir welding" **Welding & Joining, and Additive Materials Joining Techniques** in **Comprehensive Materials Processing – 2nd Edition [CMP-2E] (Elsevier).**

11. Das, D., Bag, S., and Pal, S., (2023), "Finite element simulation of tunnel defect in friction stir welding of pure copper: Effect of tool geometry" **Lecture Notes in Mechanical Engineering (Springer),** Selected proceedings of 2nd International Conference on Advances in Mechanical Engineering and Material Science (ICAMEMS-2023).

12. Das, D., Bag, S., and Pal, S., (2020), "Phenomenological Modelling of Surface Morphology and Defect for Friction Stir Welded Aluminium Alloy." **Next Generation Materials and Processing Technologies (Springer Singapore)**, Selected proceedings of Conference on Research and Developments in Material Processing, Modelling and Characterization (RDMPMC 2020).

13. Das, D., Bag, S., Pal, S, & Amin, MR. "Prediction of Surface Profile in Friction Stir Welding Using Coupled Eulerian and Lagrangian Method" **Proceedings of the ASME 2020 International Mechanical Engineering Congress and Exposition (IMECE-2020), (ASME).** Volume 11: Heat Transfer and Thermal Engineering. Virtual, Online. November 16–19, 2020. V011T11A035.

Referred Conferences

14. Das, D., Bag, S., & Pal, S. "CEL based physics-informed ML algorithms to predict thermo-mechanical responses of dissimilar FSW" Poster presentation during **Research and Industrial Conclave (RIC-2023)**, IIT Guwahati. May 14-16, 2023. (3rd best departmental poster presentation award in RIC-2023).

15. Das, D., Bag, S., & Pal, S. "Mechanistic modelling of the FSW process with CEL and ML algorithms with a focus on defect prediction" 3 min thesis presentation during **Research and Industrial Conclave (RIC-2023)**, IIT Guwahati. May 14-16, 2023.

16. Das, D., Pal, S., & Bag, S. "A coupled eulerian-lagrangian approach for the holistic modelling of the surface defect in dissimilar FSW process" **24th International Conference On Advances In Materials And Processing Technologies (AMPT-2023)**. September 13-16, 2023.

17. Das, D., Bag, S., & Pal, S. "Investigation of Material Flow to Predict Defect Formation in Friction Stir Welding " **Proceedings of the 27th National and 5th International ISHMT-ASTFE Heat and Mass Transfer Conference (IHMTC-2023)**. December 14-17, 2023.

Patents (Utility and Design)

18. Das, D., Bag, S., & Pal, S., (2022), "Multi-utility FSW tool shank with interchangeable tool probe". Indian Patent, **Application Number: 202231049902**.

19. Das, D., Bag, S., & Pal, S., (2023), "FSW tool with modified tool shoulder". Indian Patent, **Application Number: 202331012303**.

20. Das, D., Bag, S., & Pal, S., (2023), "Friction stir welding tool". Indian Patent, **Application Number: 385291-001**.

21. Das, D., & Bag, S., (2022), "An economical and portable μ-FSW setup". Indian Patent, **Application Number: 202231048830**.

22. Das, D., & Bag, S., (2023), "Micro friction stir welding machine". Indian Patent, **Application Number: 385292-001**.